Dipl.-Ing. Bernhard Mayr-Mittermüller

Numerical modeling of high temperature processes under oxygen enriched conditions

Dissertation

to achieve the university degree of

Doctor of Engineering Sciences

submitted to

Graz University of Technology

Faculty of Mechanical Engineering and Economical Science

Supervisors:

Univ.-Prof. Dipl-Ing. Dr.techn. Christoph Hochenauer
Prof. Dr. Chungen Yin

Institute of Thermal Engineering

Graz, October 2017

Affidavit

I declare that I have authored this thesis independently, that I have not used other than the declared sources/resources, and that I have explicitly indicated all material which has been quoted either literally or by content from the sources used. The text document uploaded to TUGRAZonline is identical to the present PhD thesis.

Date

Signature

Abstract

This thesis investigates the effect of oxygen-enhanced combustion (OEC) and oxy-fuel combustion on high temperature processes by means of experiments and numerical simulations. In OEC and oxy-fuel combustion, nitrogen is reduced or removed from the oxidizer, which results in a higher flame temperature and higher radiation intensities. Due to the lower amount of nitrogen, the combustions system's flue gas losses are reduced, and more heat can be used to maintain melting or heating in industrial processes. Because of the higher energy demands of oxygen production, the use of OEC is mainly restricted to applications that require high temperatures and demand high amounts of energy, such as the melting or reheating of metals.

Experiments were conducted on a lab-scale furnace for temperatures above 1000 °C, and using different oxidants (N_2/O_2 mixtures) in order to demonstrate the beneficial effect of OEC on high temperature processes. In all of the experiments, natural gas (NG) was used as fuel. The experiments showed that as the oxygen concentration in the oxidizer increases, the furnace efficiency also increases, and the highest increase in furnace efficiency was obtained with oxygen concentrations between 21 (air) and 30 Vol%. The data gathered from the experiments was subsequently used to evaluate different numerical approaches to model combustion, turbulence, and radiation, in terms of their applicability for OEC and oxy-fuel conditions. The main goal of this project was to find and develop time-efficient Computational Fluid Dynamics (CFD) models, which are applicable for a wide range of oxygen enrichments, up to oxy-fuel combustion. Furthermore, this thesis also explores the limits of such numerical models under OEC and oxy-fuel conditions. The steady laminar flamelet model (SFM) was used as combustion model, due to its low computational demands, in conjunction with a skeletal reaction mechanism that considers 17 species and 25 reactions. This reaction mechanism was used because it is applicable for both, oxy-fuel and air-fuel conditions. The radiative heat transfer in the furnace was modelled using the Discrete Ordinates model (DO), and the radiative properties of the flue gas were calculated using the Weighted Sum of Grey Gases Model (WSGGM). The results of the CFD simulations of the lab-scale furnaces showed close agreement with the measured gas temperatures and heat fluxes. The simulations found OEC to have the same beneficial

effect on furnace efficiency as the experiments. This investigation also revealed that the SFM is not capable of calculating oxy-fuel flames with a low shear rate between the oxidizer and the fuel.

For a better understanding of the heat transfer in reheating furnaces, a new model was developed, which makes it possible to determine the amount of gas and wall surface radiation in furnaces. This model was then used to assess a lab-scale furnace. The investigation revealed that wall surface radiation has by far the highest influence on the heat flux to the thermal load, while gas radiation has only a small one. Beyond that, this investigation revealed that, in the lab-scale furnace, as the oxygen concentration in the oxidizer increases, the radiation emitted by the solid bodies is reduced, due to the higher absorption rates of flue gas.

The applicability of these numerical models was also tested for bigger furnace dimensions (optical thickness). The CFD models were used to investigate a pusher-type reheating furnace as well as a walking hearth type furnace, which are both used for reheating steel billets. The pusher-type reheating furnace operated under air-fuel conditions, and the walking hearth type furnace under air-fuel conditions and oxygen enrichment of 25 Vol%. In the simulation of the pusher-type reheating furnace, the coupling of the gas phase combustion and the transient reheating of the billets was considered, by means of a new approach, which treats the billets as a fluid with a very high viscosity. This is justified due to the special arrangement of the billets, which are placed close together without any gaps between them. The advantage of this approach is that the reheating of the billets and the gas phase combustion can be calculated in one steady-state simulation, which makes this approach numerically efficient. The simulations and the measurements taken by the furnace's control system were in close agreement with each other. Additionally, an iterative approach from existing literature was used to couple the gas phase combustion and the transient reheating in the pusher-type furnace in order to verify the results of the proposed model.

For the walking hearth type furnace, the amount of wall surface and gas radiation was calculated using the developed model in this thesis. Again, the investigation showed that the wall surface radiation has the biggest impact on the total heat flux, while gas radiation has only a minor one. In contrast to the investigation of the lab-scale furnaces where the gas radiation reduces the heat flux to the thermal load under OEC, in industrial scale furnaces, the gas radiation increases the heat flux to the billets.

Based on the experiments and the CFD simulations, a zero/one dimensional thermodynamic model was developed that can be used to determine the influence of OEC on the heat

transfer, gas, and wall temperatures in a furnace. The model uses simple thermodynamic correlations, which makes it very time efficient (with calculation times of a few seconds), and therefore mean that it can be used in Microsoft Excel. This model was used to calculate the heat flux to the thermal load and the main temperatures (gas and wall) in the lab-scale furnace and the industrial scale furnaces. The results were compared with both experimental measurements and the results of the CFD calculations. The thermodynamic model showed good agreement with the measurements and the results of the CFD calculations, considering its simplicity. Thus, this model shows high potential for use to quickly determine the effects of OEC on industrial furnaces.

Kurzfassung

In dieser Arbeit wird die Auswirkung von sauerstoffangereicherter Verbrennung auf Hochtemperaturprozesse mittels Experimenten und numerischen Simulationen untersucht. In sauerstoffangereicherten Verbrennungen wird der Anteil des Stickstoffes im Oxidator reduziert bzw. entfernt. Dadurch werden höhere Flammentemperaturen sowie eine höhere Strahlungsintensität erreicht. Zusätzlich werden (durch den geringen Anteil an Stickstoff im Abgas) die Abgasverluste reduziert, wodurch mehr Energie im Prozess verfügbar ist, um zum Beispiel mehr Gut zu schmelzen oder aufzuheizen. Sauerstoffangereicherte Verbrennung wird hauptsächlich für Prozesse verwendet, die hohe Temperaturen benötigen und einen hohen Energieverbrauch haben. Typische Anwendungen sind das Schmelzen und Wiedererwärmen von Metallen.

Um den positiven Effekt sauerstoffangereicherter Verbrennung von Erdgas auf Hochtemperaturprozesse zu zeigen, wurden Experimente für Gastemperaturen über 1000 °C in einem Versuchsofen durchgeführt. Die Experimente zeigten den positiven Effekt von sauerstoffangereicherter Verbrennung auf den Ofenwirkungsgrad. Der Wirkungsgrad des Ofens stieg für Sauerstoffanreicherung zwischen 21 und 30 Vol% am stärksten an. Die gemessenen Daten wurden anschließend verwendet, um verschiedene Verbrennungsmodelle, Strahlungsmodelle und Turbulenzmodelle auf ihre Anwendbarkeit für die Simulation von sauerstoffangereicherter Verbrennung zu überprüfen. Das Hauptziel dieser Arbeit war die Entwicklung von effizienten numerischen Modellen, welche für die Berechnung von Luft- sowie Reinsauerstoff-Verbrennungen von Erdgas verwendet werden können. Zusätzlich werden in dieser Arbeit die Grenzen der Anwendbarkeit dieser Modelle untersucht. Um den Rechenaufwand gering zu halten, wurde als Verbrennungsmodell hauptsächlich das Steady laminar Flamelet Model (SFM) in Verbindung mit einem skeletal Reaktionsmechanismus verwendet, welcher 17 Spezies und 25 Reaktionen berücksichtigt. Dieser Reaktionsmechanismus wurde gewählt, da er sowohl für die Berechnung von Luftverbrennungen als auch für die Berechnung von sauerstoffangereicherten Verbrennungen uneingeschränkt verwendet werden kann. Für die Berechnung des Strahlungstransportes in den Öfen wurde das Discrete Ordinates Model (DO) verwendet. Die Strahlungseigenschaften des Rauchgases wurden mittels dem Weighted Sum of Grey Gases Model (WSGGM) berechnet. Die Ergebnisse der

CFD-Simulation der Versuchsöfen zeigten eine gute Übereinstimmung mit den gemessenen Temperaturen und Wärmeströmen. So wie die Experimente, zeigten auch die Simulationen den positiven Effekt sauerstoffangereicherter Verbrennung auf den Wirkungsgrad der Öfen. Ein weiteres Ergebnis dieser Untersuchungen ist, dass das SFM bei der Berechnung von Reinsauerstoffflammen mit einer geringen Scherrate zwischen Oxidator und Brennstoff unrealistische Temperaturen in der Flame berechnet. In dieser Arbeit wurde eine neue Methode entwickelt, die es ermöglicht, den Anteil der Gas- und Festkörperstrahlung am gesamten Wärmestrom zu bestimmen. Diese Methode wurde angewendet, um den Anteil der Gas- und Festkörperstrahlung in den Versuchsöfen zu bestimmen. Die Berechnung mit dieser Methode zeigte, dass der Großteil des Wärmestromes auf die thermische Last im Versuchsofen von den Wänden abgestrahlt wird und nur ein kleiner Teil vom Rauchgas. Weiters zeigte sich, dass mit zunehmender Sauerstoffanreicherung die Festkörperstrahlung durch das Rauchgas verringert wird.

Die Anwendbarkeit dieser Modelle wurde auch an Industrieöfen (höhere optische Dichte) getestet. Die CFD-Modelle wurden verwendet, um zwei Wiedererwärmunsgöfen zu untersuchen. Es handelt sich dabei um einen Stoßofen und um einen Hubbalkenofen. Der Stoßofen wurde für konventionelle Luftverbrennung untersucht, der Hubbalkenofen für Luftverbrennung und eine Sauerstoffanreicherung von 25 Vol%. Für die Simulation des Stoßofens wurde ein neuer Ansatz entwickelt, der es ermöglicht, die Gasphasenverbrennung und die instationäre Wiedererwärmung der Knüppel in einer stationären Simulation zu berechnen. In diesem Ansatz werden die Knüppel als ein Fluid mit einer hohen Viskosität betrachtet, was in diesem Fall zulässig ist, da die Knüppel bei diesem Ofentyp Seite an Seite platziert sind. Der Vorteil von diesem Ansatz ist, dass nur eine stationäre Berechnung durchgeführt werden muss, was diesen Ansatz sehr rechenzeiteffizient macht. Die Ergebnisse der Simulation und die Messungen zeigten eine sehr gute Übereinstimmung. Für die Berechnung des Hubbalkenofens wurde ein iterative Ansatz aus der Literatur verwendet, um die Gasphasenverbrennung und das Aufheizen der Knüppel zu berechnen. Für beide Öfen wurde der Anteil der Gas- und Festkörperstrahlung am gesamten Wärmestrom auf die Knüppel bestimmt. Wiederum zeigte sich, dass die Festkörperstrahlung den höchsten Anteil am gesamten Wärmestrom auf die Knüppel hat und die Gasstrahlung nur einen kleinen Beitrag zum Wärmestrom auf die Knüppel liefert. Im Gegensatz zu den Berechnungen des Versuchsofen erhöht die Gasstrahlung den Wärmestrom auf die Knüppel.

Basierend auf den Experimenten und den Simulationen wurde ein 0-D bzw. 1-D thermodynamisches Modell entwickelt. Mit diesem Modell ist es möglich, den Einfluss von Sauerstoffanreicherung auf die Wärmeübertragung, die Gastemperatur und die Wandtem-

peratur in einem Ofen sehr rechenzeiteffizient zu bestimmen. Das 0-D bzw.1-D Modell verwendet einfache thermodynamische Korrelationen und kann deshalb mit einer Software wie Microsoft Excel mit Rechenzeiten im Sekundenbereich gelöst werden. Alle im Zuge dieser Arbeit untersuchten Öfen wurden mit diesem Modell berechnet und die Ergebnisse mit den Ergebnissen der CFD-Simulationen sowie den Messungen verglichen. Die Ergebnisse des thermodynamischen Modells zeigten eine sehr gute Übereinstimmung mit den Messungen bzw. den Ergebnissen der CFD-Simulationen, vor allem unter Berücksichtigung der Einfachheit des Modells. Damit ist das Modell sehr gut geeignet, die Auswirkung von Sauerstoffanreicherung auf industrielle Öfen rasch zu bestimmen.

Acknowledgements

This PhD thesis is the result of a research project between Messer Austria GmbH and the Institute of Thermal Engineering. Therefore, I would like to thank the team at Messer Austria GmbH for their financial support and for the opportunity to use the test facility in Gumpoldskirchen for my experiments. Specifically, I would like to thank Dr. Martin Demuth for his valuable input and for his continuous supervision of the project. Furthermore, I would like to thank Davor Spoljaric for the financial support of this project. I would also like to extend my thanks to the Austrian Research Promotion Agency (FFG) for funding the project, which provided the financial basis of this thesis.

During my time at the Institute of Thermal Engineering, I gained deep insight into experimental issues and numerical simulations, especially through countless talks with my colleagues at the Institute. Therefore, I would like to thank all of my colleagues at the Institute for their help, input, and constructive feedback. Specifically, I would like to thank Dr. Rene Prieler and Johannes Wurm for the numerous conversations, in which many ideas were born and problems were solved at an early stage. I would also like to express my gratitude to my supervisor at the Institute, Prof. Christoph Hochenauer, for his valuable insights during the project and the writing of this thesis, and for giving me the opportunity to do my PhD at the Institute. Special thanks also go to Prof. Yin for agreeing to review and supervise the writing of this thesis.

I would also like to sincerely thank my parents for enabling me to study and always supporting my decisions. Finally, I would like to express my deepest gratitude to my wife, Katharina, for supporting and motivating me during the writing of this thesis and throughout my studies. This thesis would not have been possible without her help and support.

List of Publications

The following publications are the basis of this thesis and were written during my PhD study. Parts of the publications which are used in this thesis are marked by footnotes at the beginning of the particular section.

1. B. Mayr, R. Prieler, M. Demuth, M. Potesser, and C. Hochenauer. “CFD and experimental analysis of a 115 kW natural gas fired lab-scale furnace under oxy-fuel and air–fuel conditions.” In: *Fuel* 159 (2015), pp. 864–875

2. B. Mayr, R. Prieler, M. Demuth, and C. Hochenauer. “The usability and limits of the steady flamelet approach in oxy-fuel combustions.” In: *Energy* 90 (2015), pp. 1478–1489

3. B. Mayr, R. Prieler, M. Demuth, L. Moderer, and C. Hochenauer. “CFD analysis of a pusher type reheating furnace and the billet heating characteristic.” In: *Applied Thermal Engineering* 115 (2017), pp. 986–994

4. B. Mayr, R. Prieler, M. Demuth, M. Potesser, and C. Hochenauer. “Computational analysis of a semi-industrial furnace fired by a flat flame burner under different O_2/N_2 ratios using the steady laminar flamelet approach.” In: *Journal of the Energy Institute* 90.4 (2017), pp. 602–612

5. B. Mayr, R. Prieler, M. Demuth, and C. Hochenauer. “Comparison between solid body and gas radiation in high temperature furnaces under different oxygen enrichments.” In: *Applied Thermal Engineering* 127 (2017), pp. 679–688

Contents

List of Figures

List of Tables

Acronyms

CARS	Coherent Anti-Stokes Raman Spectroscopy.
CAS	Cryogenic Air Separation.
CCS	Carbon Capture and Storage.
CFD	Computational Fluid Dynamics.
CPU	Central Processing Unit.
CSTR	Continuous Stirred Tank Reactor.
CV	Control Volume.
DNS	Direct Numerical Simulation.
DO	Discrete Ordination Model.
EDC	Eddy Dissipation Concept Model.
EDM	Eddy Dissipation Model.
EES	Engineer Equation Solver.
EPR	Electron Paramagnetic Resonance.
EWB	Exponential Wide Band Model.
FGM	Flamelet Generated Manifold.
FID	Flame Ionization Detector.
FVM	Finite Volume Method.
HITEMP	High-Temperature Molecular Spectroscopic Database.
HITRAN	High-Resolution Transmission Molecular Absorption Database.
IFRF	International Flame Research Foundation.
ISAT	In-Situ Adaptive Tabulation.
JL	Jones and Lindstedt.

LBL	Line by Line Model.
LDV	Laser Doppler Velocimetry.
LES	Large Eddy Simulation.
LHV	Lower Heating Value.
LOX	Liquefied Oxygen.
NDIR	Non Dispersive Infrared.
NG	Natural Gas.
OEC	Oxygen Enriched Combustion.
PDF	Probability Density Function.
PFR	Plug Flow Reactor.
RANS	Reynolds-Averaged Navier-Stokes.
RSM	Reynolds Stress Model.
RTE	Radiative Transport Equation.
S2S	Surface to Surface Model.
SFM	Steady Flamelet Model.
UDF	User Defined Function.
VSA	Vacuum Swing Adsorption.
WD	Westbrook and Dryer.
WSGGM	Weighted Sum of Grey Gases Model.

List of Symbols

Sign	**Description**	**Unit**
A, B	Model parameter EDM	[-]
A	Surface	$[m^2]$
C_d	Model parameter SFM	[-]
C_g	Model parameter SFM	[-]
$C_{1\epsilon}$	Model parameter turbulence model standard $k-\epsilon$, realizable $k-\epsilon$	[-]
C_1	Model parameter turbulence model standard $k-\epsilon$, realizable $k-\epsilon$	[-]
$C_{2\epsilon}$	Model parameter turbulence model standard $k-\epsilon$, realizable $k-\epsilon$	[-]
C_2	Model parameter turbulence model standard $k-\epsilon$, realizable $k-\epsilon$	[-]
$C_{3\epsilon}$	Model parameter turbulence model standard $k-\epsilon$, realizable $k-\epsilon$	[-]
C_μ	Model parameter turbulence model standard $k-\epsilon$, realizable $k-\epsilon$	[-]
$D_k, D_{k,T}$	Mass diffusion coefficient laminar/tubulent and thermal (Sorot) diffusion	$[\frac{m^2}{s}]$
Da	Dammköhler number	[-]
G_b	Generation of turbulent kinetic energy due to gradients of the mean velocity	$[\frac{kg}{s^3m}]$
G_k	Generation of turbulence due to buoyancy	$[\frac{kg}{s^3m}]$
G	Incident radiation	$[\frac{W}{m^2}]$
H	Enthalpy	$[J]$
I	Identity matrix	[-]
I	Radiation intensity	$[\frac{W}{sr}]$
M	Molar mass	$[\frac{kg}{kmol}]$

Sign	Description	Unit
Pr_ϵ	The effective Prandtl number for the transport of the turbulent dissipation rate ϵ	[-]
Pr_k	The effective Prandtl number for the transport of the turbulence kinetic energy k	[-]
Pr_t	Turbulent Prandtl number	[-]
T	Mole combustion product per mole fuel	$[K]$
U^*	Dimensionless velocity	[-]
U_τ	Friction velocity	$[\frac{m}{s}]$
X_i	Mole combustion product per mole fuel	$[\frac{mole_i}{mole_f}]$
X	Mole fraction	[-]
Y_i^*	Fine scale mass fraction	[-]
Y	Mass fraction	[-]
Z_i	Element mass fraction of element i	[-]
Γ	Diffusion coefficient	$[\frac{m^2}{s}]$
Ω	Direction vector	[degree, rad]
α, a	Absorption coefficient	$[\frac{1}{m}]$
α	Parameter for PDF generation	[-]
$\bar{c}_p$	Averaged specific heat capacity	$[\frac{J}{kg\,K}]$
β	Parameter for PDF generation	[-]
β	Thermal expansion coefficient	$[\frac{1}{K}]$
χ	Scalar dissipation	$[\frac{1}{s}]$
$\delta_{i,j}$	Kronecker delta	[-]
δ	Single dirac PDF	[-]
$\dot{M}$	Molar flow	$[\frac{mol}{s}]$
$\dot{Q}_{Air}$	Heat flux of the combustion air	$[W]$
$\dot{Q}_{CH_4}$	Heat flux of the fuel	$[W]$
$\dot{Q}_{Flue\,gas}$	Heat flux of the flue gas	$[W]$
$\dot{Q}_{LHV}$	Heat flux due to the lower heating value	$[W]$
$\dot{Q}_{Load}$	Heat flux to a thermal load like billets	$[W]$
$\dot{Q}_{O_2}$	Heat flux of the additional oxygen	$[W]$
$\dot{Q}_{Wall}$	Heat loses through the walls	$[W]$
$\dot{Q}_{billet}$	Heat flux to the billet	$[W]$
$\dot{Q}_{fuel}$	Heat input of the fuel	$[W]$
$\dot{Q}_{fuel}$	Thermal heat input	$[W]$

Sign	**Description**	**Unit**
$\dot{Q}_{rad,gas}$	Heat flux due to gas radiation	$[W]$
$\dot{Q}_{rad,total}$	Total radiative heat flux	$[W]$
$\dot{Q}_{rad,wall}$	Heat flux due to solid body radiation	$[W]$
$\dot{Q}_{radiation,p}$	Heat flux to the plate due to thermal radiation	$[W]$
$\dot{Q}_{tot,p}$	Total heat flux to the plate	$[W]$
$\dot{m}$	Mass flow	$[\frac{kg}{s}]$
$\dot{q}$	Heat flux density	$[\frac{W}{m^2}]$
ϵ	Emission coefficient	[-]
ϵ	Turbulent dissipation rate	$[\frac{m^2}{s^3}]$
$\eta_{furnace}$	Efficiency of the furnace	[-]
κ	Karman constant	[-]
λ_t	Turbulent heat conductivity	$[\frac{W}{mK}]$
λ	Oxidizer-fuel equivalence ratio	[-]
λ	Thermal conductivity	$[\frac{W}{m\,K}]$
μ, μ_T	Dynamic viscosity and turbulent viscosity	$[\frac{kg}{ms}]$
ν', ν''	Stoichiometric coefficients of the reactant and products	[-]
ν_i	Volume fraction	[-]
ν	Kinematic viscosity	$[\frac{m^2}{s}]$
ω	Production/destruction rate (source or sink term)	$[\frac{W,kg,N}{m^3}]$
$\overline{\phi}$	Mean value of a transport value	[-]
$\overline{f'^2}$	Mixture fraction variance	[-]
$\overline{f}$	Mean mixture fraction	[-]
ϕ'	Fluctuating value of a transport value	[-]
$\phi_{N_2\,oxi}$	Volume fraction of nitrogen in the oxidizer	[-]
$\phi_{O_2\,oxi}$	Volume fraction of oxygen in the oxidizer	[-]
ϕ	Instantaneous value of a transport value	[-]
ϕ	Phase function	[-]
π	Geometrical value	
ρ, ρ_∞	Density and density at the inlet	$[\frac{kg}{m^3}]$
σ_S	Scattering coefficient	$[\frac{1}{m}]$
σ	Stefan-Boltzmann constant	$[\frac{W}{m^2\,K^4}]$
τ^*	Time scale	$[s]$
τ	Stress tensor	$[\frac{N}{m^2}]$

Sign	**Description**	**Unit**
$\varphi_{radiation,p}$	Proportion of the radiative heat flux on the total heat flux	[-]
$\vec{J}$	Diffusion flux	$[\frac{kg}{m^2 s}]$
$\vec{g}, g_i$	Gravitational vector or component i of the gravitational vector	$[\frac{m}{s^2}]$
$\vec{r}$	Direction vector	[-]
$\vec{s}$	Direction vector	[-]
ζ^*	Length fraction	[-]
a, α, h	Heat transfer coefficient	$[\frac{W}{m^2\,K}]$
$a_{\epsilon,i}$	Emissivity weighting factor	[-]
$b_{\epsilon,i,j}$	Emissivity gas temperature polynomials	[-]
c_{mp}	Molar heat capacity	$[\frac{J}{kmol\,K}]$
c_p	Specific heat capacity	$[\frac{J}{kg\,K}]$
e	Specific energy	$[\frac{J}{kg}]$
f	Mixture fraction	[-]
k	Turbulent kinetic energy	$[\frac{m^2}{s^2}]$
l	Length	$[m]$
n	Refractive index	[-]
$p(f)$	Probability density function of the mixture fraction	[-]
p	Pressure	$[\frac{N}{m^2}]$
t	Time	$[s]$
$u, v, w, \vec{v}$	Velocity components and vector for the Cartesian coordinate system	$[\frac{m}{s}]$
$x, y, z, \vec{x}$	Coordinates and vector for Cartesian coordinate system	$[m]$
y^+, y^*	Dimensionless normal wall distance	[-]

1. Introduction[1]

Global warming as a result of climate change is the greatest challenge mankind must face in the future. The greenhouse gas that most contributes to climate change as a result of human activities is CO_2, and the combustion of fossil fuels is the main source of CO_2 emissions. Fossil fuels are responsible for 85% of global energy generation [6], and it is likely that this situation will remain unchanged for several decades [7]. CO_2 is also emitted by chemical reactions within the furnace load, such as during the production of cement clinker. In cement clinker production, only 32% of the total amount of CO_2 in the flue gas is emitted by combustion, while 68% is formed through the calcination process [8]. In the glass industry, 30 to 36% of the overall CO_2 in the flue gas is produced by the chemical reactions in the glass bath during the melting process [9]. The issues of the availability and cost of fuel also have to be taken into account, as they are major factors for many industries. Therefore, in the future, the main focus will be on reducing fuel consumption, counteracting the problem of rising fuel prices, and reducing CO_2 emissions. One way to effectively reduce fuel consumption and CO_2 emissions in industrial processes or power plants is to use oxy-fuel combustion with or without Carbon Capture and Storage (CCS). In CCS, carbon dioxide is removed from the flue gas and stored, for example, in empty gas fields. CCS processes can be subdivided into pre- and post-combustion capturing, as well as Oxygen Enriched Combustion (OEC) and oxy-fuel combustion [10]. In post-combustion capturing processes, CO_2 is removed from the flue gas by different measures, including adsorption, absorption by chemical solvents, and cryogenic separation [11–13]. In pre-combustion processes, steam reforming is used to convert the fuel to a syngas which primarily consists of CO and H_2. With additional steam, the CO is further converted to CO_2 and H_2, which increases the concentration of H_2 in the syngas. The CO_2 is then removed from the syngas, and H_2 can be used as the fuel for combustion. Some technical and economic surveys have shown that CCS is a promising technology for the future [14–16]. CO_2 emissions can be reduced even further by using biomass as fuel, or by replacing some of the fossil fuels with biomass. The co-firing of biomass with coal under oxygen-enriched or oxy-fuel conditions has been extensively investigated by Bhuiyan

---

[1] Parts of this section have already been published in [1–4]

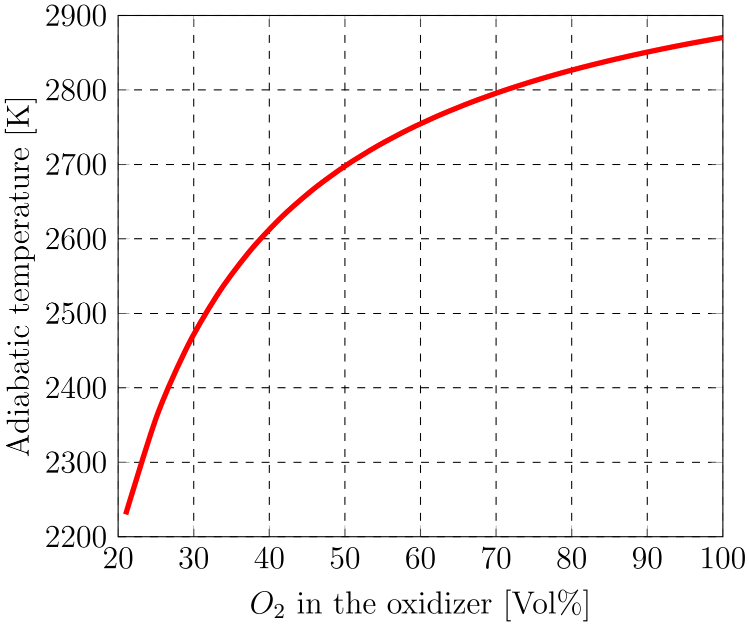

Figure 1.1.: Adiabatic flame temperature for combustion of methane with different O_2/N_2 mixtures as oxidant [21]

and Naser [17–19] and Álvarez et al. [20]. This thesis investigates oxy-fuel and OEC by means of experiments and numerical simulations in terms of their applicability for high temperature processes, without consideration of CCS. The effects of oxy-fuel combustion and OEC on process efficiency and heat transfer in industrial furnaces are of particular interest in the following sections.

1.1. Oxy-Fuel and Oxygen-enriched Combustion (OEC)

In oxy-fuel and OEC, the O_2 concentration in the oxidizer is increased from 21 Vol% up to 100 Vol%. This leads to a higher combustion temperatures due to the smaller amount (or the absence) of N_2. Nitrogen absorbs a high amount of the energy released by the chemical reaction in the flame. In Figure 1.1, the adiabatic flame temperatures for the combustion of methane with different O_2/N_2 mixtures is shown. For air combustion (21 Vol% O_2) the adiabatic flame temperature is approximately 2230 K. Increasing the oxygen in the oxidizer leads to a higher adiabatic flame temperature, with a maximum of 2890 K at 100 Vol% oxygen in the oxidizer. The higher flame temperature under oxy-fuel or OEC conditions also has an impact on the heat transfer inside a furnace or a boiler. The main mode of heat transfer in boilers and furnaces is thermal radiation. The higher flame temperatures reached under oxy-fuel or OEC lead to a higher radiation intensity, which subsequently results in a higher heat transfer. Additionally, the radiative heat transfer is improved, due to the fact that concentration of H_2O and CO_2 in the flue gas are increased, and, therefore, the radiative properties of the flue gas are enhanced. Because of these effects, use of oxy-fuel or OEC entails the following benefits [22]:

- Due to the smaller amount of N_2 in the flue gas, the heat losses through the flue gas are reduced, and the efficiency of the furnace is improved.
- Due to the higher heat fluxes, the productivity of the process can be improved. This also makes the process more flexible: if higher productivity is needed, only the oxygen in the oxidizer must be increased.
- Due to the higher concentration of CO_2 in the flue gas, and the smaller flue gas volume, it is easier to separate the CO_2 from the rest of the flue gas in a CCS process.

The higher flame temperature and higher heat flux can also lead to problems, including damage to the refractory lining as a result of overheating. Therefore, special care must be taken to distribute the temperature evenly in furnaces using oxy-fuel or OEC. In boilers using oxy-fuel combustion, flue gas recirculation is carried out in order to lower the flame temperature [23]. Wall et al. [24] investigated the effect of flue gas recirculation on the combustion process. Further investigations of using oxy-fuel with flue gas recirculation in power generation can be found in Chen et al. [25], Scheffknecht et al. [26] and Yin and Yan [27]. Because of the higher temperatures in OEC, NO_x formation can increase unless the burner design is adapted, which is a problem when it comes to retrofitting existing boilers or furnaces. The biggest drawback of oxy-fuel and OEC is the high energy demands of O_2 production, which results in additional costs. Methods of producing oxygen are described in Section 1.1.2. While it has some drawbacks, the advantages of this technology make it extremely attractive for processes with high flue gas temperatures, limited production rates, small thermal efficiencies, and for CCS technologies.

1.1.1. The Use of Oxygen-enhanced Combustion in High Temperature Processes

In many industries, high gas temperatures are required for processes such as annealing, melting, and reheating of metals. The high energy demands of such processes are mainly fulfilled by fossil fuels. To cope with rising fuel prices and environmental regulation, OEC is now commonly used to optimize such processes. For example more than half of the world's copper, lead, and nickel is produced using OEC [22]. Oliveira et al. [28] analysed the fuel-saving potential of oxy-fuel and air preheating in a metal reheating furnace with simple energy balances, for a temperature level of 1200 °C. Their investigation showed that fuel consumption can be reduced by 46% if oxygen is used instead of non-preheated air. As the pre-heated temperature of the combustion air increases, the fuel-saving potential of oxy-fuel combustion decreases. If the combustion air is preheated to 400 °C, the fuel-saving potential of oxy-fuel combustion decreases to 28%, and at a pre-heating temperature of 800 °C, fuel savings are only 8%. Oliveira et al. also carried out an economic evaluation of oxy-fuel combustion, taking into account the costs of oxygen production and storage. This analysis revealed that oxy-fuel combustion is more economical if the combustion air is not pre-heated. In the case where the combustion air was pre-heated to 400 °C, oxy-fuel combustion showed no costs savings. Moreover, at a pre-heating temperature of 800 °C, air combustion remains more economical than oxy-fuel combustion. Experiments performed by Bělohradsky et al. [29, 30], using a test furnace with a 750 kW natural gas burner, also demonstrated the fuel-saving potential of OEC. The furnace showed an efficiency of 60% under the air-fuel conditions, while the efficiency increased to 78% with an enrichment of 38 Vol% oxygen in the oxidizer. Prieler et al. [31] investigated a natural gas fired lab-scale furnace with different oxygen enrichments in the oxidizer. Their investigation also showed an increase in furnace efficiency from 44% at 25 Vol% O_2 to 67% at 100 Vol% O_2. Prieler et al. [32] used numerical simulations to show that the fuel input in an 18 MW reheating furnace can be reduced by 8% if an oxygen enrichment of 25 Vol% is used, and that this method results in the same product quality and the same productivity. Wu et al. [33] investigated air-fuel combustion and OEC with 30 Vol% oxygen in the oxidizer on a lab-scale furnace in terms of the time needed to heat the furnace to a temperature of 1200 °C using either OEC or air-fuel combustion. Their analysis revealed that there was a significantly higher heating rate between 700 °C and 1200 °C for OEC (30 Vol% O_2) compared to air-fuel combustion. Subsequently, they performed an experiment where the furnace operated at a temperature of 1200 °C in steady-state under OEC (30 Vol% O_2) and air-fuel conditions. In this experiment, fuel savings of 26.1% were identified for operation with 30 Vol% oxygen in the oxidizer, due to the higher heat fluxes to the wall.

1.1.2. Production and Storage of Oxygen

The production of oxygen is an energy demanding process, and poses a significant problem for the use of OEC and oxy-fuel in industrial processes. There are four common methods to produce oxygen, which differ in terms of their production capacity and the purity of the oxygen produced [22]:

- Delivery and storage of Liquefied Oxygen (LOX): This method is used when only small quantities of oxygen are needed. Oxygen is produced at a central facility and delivered to the customer, usually in liquid form. The advantage of LOX is that the capital costs of on-site oxygen production can be avoided, and the oxygen has a high purity of 99.5%. LOX is economically efficient if purchasing only a small amount of oxygen.

- Vacuum Swing Adsorption (VSA): In this method, air is pressed through a bed of zeolite, which preferentially adsorbs nitrogen. Thus, the amount of nitrogen in the air is reduced, while the oxygen concentration in the air increases, making it easier to capture the oxygen. Two zeolite drums are used concurrently; one for the adsorption of nitrogen, while the second is regenerated by lowering the pressure to create a mild vacuum, to be used again in its turn. With VSA technologies, it is only possible to produce oxygen with a purity of 93%, and production rates are limited to 185 t/d. The advantage of this system over LOX is that the cost per unit of oxygen is significantly lower.

- Cryogenic Air Separation (CAS): This method is used when high amounts of oxygen are required. Using this method, the components of air are cooled down and liquefied. In this process, the different boiling points of nitrogen (-196 °C) and oxygen (-183 °C) are used to separate them from the ambient air through distillation. Huge amounts of energy are necessary to cool down the air to about -196 °C. CAS provides the purest oxygen, with the potential to reach 99.9% purity, but for standard applications, a purity of 99.5% is used.

- Membrane gas separation: In this method, oxygen is produced by means of membrane separation. As a result of different pressure levels on the two sides of the membrane, air is dissolved and can diffuse through the membrane. MIEC membranes (Mixed Ionic and Electronic Conductor), with a fluorite or perovskite structure are commonly used [34]. The permeation of oxygen through the membrane is determined by the selectivity of the membrane. On the other side of the membrane, an oxygen-enriched gas mixture is produced, which can be used for further applications, such as combustion. The energy demand for this technology is very high, and production rates are low. Therefore, this method is mainly used for lab-scale applications [35, 36].

1.2. Optimisation of High Temperature Processes

In evaluating high temperatures processes, it is difficult to perform experiments, and the significance of such experiments is limited. Because such processes and the furnaces in which they occur are embedded in a production process which depends on the operation of the furnaces, it is nearly impossible to carry out such experiments. Any downtime of the furnaces leads to high costs. In the past, expensive test runs were necessary in order to determine the effect of different operating conditions on the efficiency and product quality of heating processes. The increase in computational power in recent years means that it is now possible to perform numerical simulations of industrial processes with a reasonable standard of accuracy and in a short period of time. Computational Fluid Dynamics (CFD) is useful to investigate the heat transfer characteristics, fluid flow, and reaction kinetics inside a furnace operating under high temperature. The numerical simulations made possible by CFD provide detailed insight into the temperature, species, and heat flux distribution in the furnace, which could not be gained by experiments, due to high temperatures or limited accessibility. Beside CFD calculations, high temperature furnaces can also be described by reactor networks. In these reactor networks, the furnace is subdivided into small reactors, where each of these represents a specific region of the furnace. In each reactor, the temperature, species concentration, and flow field is calculated by solving a set of detailed chemical reactions. A combination of Plug Flow Reactors (PFRs) and Continuous Stirred Tank Reactors (CSTRs) are used. A PFR is used to describe chemical reactions for continuous flows: the flow domain is subdivided into infinitely thin plugs, where set of chemical reactions is solved in each plug for different temperatures and species concentrations. CSTR is the simplest reactor, in which it is assumed that the species and temperatures are evenly distributed. Based on this assumption, the chemical reactions are solved. The advantage of this approach is that the calculation times are much shorter than those of CFD calculations. This approach was used by Ponsich et al. [37] to calculate the species concentration in a glass melting furnace. The results of this calculation were subsequently compared to CFD calculations. Using both CFD and a reactor network calculation is referred to as a hybrid method. The fluid flow and the main species, including H_2O, CO_2, O_2, are calculated by the CFD calculation. Based on this calculation, the reactor network calculation is performed using a detailed reaction mechanism. The advantage of this approach is that it reduces the calculation time in comparison to a CFD simulation using a detailed reaction mechanism. This approach was used by Falcitelli et al. [9] for the calculation of NO_x formation rates in two glass melting furnaces.

1.2.1. Lab-scale Furnaces

Many experiments and numerical investigations have been carried out for a huge variety of operating conditions in lab-scale furnaces. Leicher and Giese [38] performed experiments and numerical simulation of oxy-fuel Natural Gas (NG) flames in a lab-scale furnace for use in glass melting furnaces. Detailed species and temperature measurements were taken and compared with the results of a CFD simulation. Furu et al. [39] determined the heat transfer to aluminium samples in a small-scale furnace by means of experiments and numerical simulations of air-fuel and oxy-fuel conditions. Yin et al. [40] investigated a 0.8 MW furnace operating under oxy-fuel conditions. The furnace was investigated using numerical simulations, which were then compared with detailed in-flame temperature and species measurements. Different global mechanisms were tested in terms of their applicability for oxy-fuel combustion, and a refined version of the Jones and Lindstedt (JL) reaction mechanism was proposed for use in oxy-fuel combustion. Prieler et al. [31, 41] investigated a lab-scale furnace for oxygen concentrations of 21 to 100 Vol% oxygen in the oxidizer, using both experiments and numerical simulations. In the numerical simulations, different reactions mechanisms were tested under both air-fuel and oxy-fuel conditions. These investigations have shown that it is possible to numerically calculate the local thermo-physical properties of lab-scale furnaces using either oxy-fuel or OEC.

1.2.2. Industrial-scale Furnaces

The focus of this thesis is on the furnaces used for high temperature applications, such as reheating furnaces and melting furnaces; therefore, in this section, only high temperature applications are discussed. In steel plants, reheating furnaces are one of the largest consumers of energy [42, 43]. Such reheating furnaces are used to raise the temperature of the steel - mostly introduced in billet or slab form - to a desired level, in order to prepare the steel for subsequent processing, such as through rolling mills. The optimisation of such furnaces is therefore of great interest to the industry, and many investigations have been carried out on this topic, mainly using numerical calculations. There are a variety of approaches to modelling reheating furnaces used in scientific literature, ranging all the way from simple 1D simulations to complex 3D-CFD simulations. One of the first investigations of this topic resulted in the simplified models of Zhang et al. [44, 45], in which the geometry of the furnace was simplified, and the billets were treated as a single slab placed on the furnace floor. Kim et al. [46] performed more complex three-dimensional simulations that considered turbulent combustion and radiative heat transfer in order to predict the heat flux to the billets, in steady state, and in which the surface temperatures were fixed based on experimental data. Kim and Huh [47] performed another steady-state analysis of the heat transfer to the slabs, and calculated the temperature profile of the slabs using a finite difference solver. Hsieh et al. [48] used a similar method as Kim and Huh to calculate the combustion in a turbulent flow with a more complex geometry. Other simplified models divide the furnace into zones with different wall and gas temperatures. In [49], the furnace was modelled as a radiating medium, and the temperature of the billets was calculated using the transient heat conduction equation. More recent work on this topic has been carried out by Han and Chang [42] and Han et al. [50]. In their studies, detailed 3D transient simulations were performed. The movement of the billets was simulated by moving the temperature field in the billets from one positon to the next until the end of their residence time in order to reach a periodically transient solution. An entirely different approach was proposed by Martín et al. [51], in which a low computational-cost model was developed. This approach consists of a pre-processing phase, where a database of heating curves is created by means of 2D numerical simulations. The heating curves are calculated for different heat inputs and different residence times of the thermal load. In the next step, this database is used to develop a surrogate model, which uses High Order Singular Value Decomposition and interpolation techniques. This surrogate model is then used to predict the behaviour of the furnace for various furnace operating conditions: different residence times of the thermal load and varying the power input of the burners. The results of these calculations were compared to the results of the numerical simulations of the first step, and showed close agreement. The biggest advantage of the surrogate model is its fast calculation time of only a few milliseconds.

The majority of the works described above focus on simplified steady-state simulations with a certain lack of accuracy, but fast calculation times. Other, more complex models solve the reheating process in transient simulations, which provide more accurate results, but also require more calculation time. Generally, it is possible to state that, for transient simulations, the complexity of the furnace model must be reduced in order to achieve reasonable calculation times. Recently, new CFD approaches have been proposed which reduce the calculation time necessary. Prieler et al. [52] proposed a new iterative and numerically-efficient solution strategy for reheating furnaces. Combustion in the gas phase was done using a steady-state simulation, while the transient reheating of the billet was performed in a separate, transient simulation. The heat flux to the billets is calculated using the gas phase simulation, and the new surface temperature of the billets is calculated with this heat flux in the transient simulation. This is done iteratively until the convergence criterion is reached. Prieler et al. used the Steady Flamelet Model (SFM) with a skeletal mechanism so as to keep the calculation time to a minimum. Casal et al. [53] proposed a new method of conducting a 3D simulation of the periodically transient reheating process of steel billets in a steady-state simulation. They introduced source terms to the energy transport equation in the billet regions in order to transform the transient movement of the billets into a steady-state simulation, thereby significantly reducing the calculation time, and preventing information from being lost. The simulation results were compared with data from the furnace control system of the reheating furnace, and showed good agreement. It is also important to mention recent work using mathematical models based on the zone method. Tan et al. [54] and Emadi et al. [55] used the zone method to simulate transient furnace behaviour in production, transient temperature fields, and heat flux to the billets. Li et al. [56] used the finite volume method with an alternating direction implicit algorithm to determine the transient temperature field inside a reheating furnace.

1.3. Aim of This Thesis

The present study will investigate the effect of oxy-fuel and OEC on high temperature applications, both experimentally and using CFD simulations. The experiments in this work were conducted on a lab-scale furnace with a water-cooled copper plate serving as the thermal load. The experiments were conducted for oxygen concentrations between 21 Vol% and 100 Vol% oxygen in the oxidizer, and for two gas temperatures of 1070 °C and 1200 °C. In order to observe the fuel reduction potential of OEC and oxy-fuel combustion, the gas temperature (whether 1070 °C or 1200 °C) was set at a distinct temperature measurement point in the furnace, and the fuel input was adapted for the different oxygen concentrations. Special emphasis is placed on the heat transfer to the thermal load in the lab-scale furnace for the different oxygen enrichments. Furthermore, a semi-industrial furnace equipped with a flat flame burner was investigated with different oxygen concentrations, also using both experiments and numerical simulations. The experiments were conducted for oxygen concentrations from 21 Vol% up to 37 Vol%. The gas temperature was measured at different points in the furnace, and the surface temperature of the burner quarl was also measured. The main objectives of the experiments conducted herein are to:

- Prove the fuel saving potential of OEC for high temperature processes (above 1000 °C) compared to air-fuel combustion.
- Provide experimental data (temperature, heat flux) to validate the CFD models.

The aim of this thesis is to develop numerical models which are applicable for all kinds of oxygen enrichment, for both lab-scale and industrial-scale furnaces, with low computational demand and high accuracy. The numerical CFD simulations performed herein were carried out using the commercial software ANSYS Fluent.

In the first step, 3-D CFD simulations of the furnaces investigated experimentally were performed, in order to evaluate different combustion models, radiation models, and reaction mechanisms in terms of their applicability in oxy-fuel and OEC conditions. The results of the CFD simulations were subsequently compared to the experiments performed within this thesis, and with additional experimental data from existing literature. Furthermore, this thesis also explores the limits of the CFD models investigated. To gain a better understanding of the heat transfer in high temperature furnaces, a CFD model was developed, which makes it possible to determine the amount of heat flux that occurs as a result of either gas radiation, wall surface radiation, or convection to a thermal load. This model was then used to determine the amount of each mode of heat transfer that occurs in lab-scale furnaces and industrial-scale furnaces. The aims of this numerical study can be summarized as follows:

- Investigate the applicability of different combustion and radiation CFD models and reaction mechanisms in terms of their applicability under OEC;
- Validate the CFD models with experimental data;
- Reveal limitation of the CFD models for OEC conditions;
- Develop a CFD model which can determine the amount of gas and wall surface radiation on the total heat flux to a thermal load.

The validated CFD models were then used to investigate an industrial scale pusher-type reheating furnace. For this purpose, a numerically-efficient method was developed which makes it possible to calculate the combustion process, flow field, and species concentrations, as well as the periodically transient reheating of the billets in one steady-state simulation. The results of this simulation were compared with measurements of the furnace control system. The goals of this part of the thesis are to:

- Develop a numerically-efficient method to couple the transient reheating of the steel billets and gas phase combustion in one steady-state simulation;
- Simulate an industrial-scale pusher-type reheating furnace using the model; developed to couple the gas phase combustion and the transient reheating of the billets;
- Compare the results of the simulation with measurement data.

Based on the validated CFD simulations, both a 0-D and a 1-D thermodynamic model were developed in this thesis, which make it possible to estimate the effect of OEC on the heat transfer to a load in a furnace. Due to the simplicity of this model, the calculation time is very low compared to CFD simulations. With the thermodynamic model, the gas temperature, the wall temperature, and the heat flux to a thermal load are calculated using simple thermodynamic correlations. The results obtained with this thermodynamic model were compared with the solution of the CFD simulation, using the validated models, and compared to measurements. Like the CFD model, the thermodynamic model is applicable for both large- and small-scale furnaces, and for all kinds of oxygen enrichments. The aims of this section are to:

- Develop a thermodynamic model which calculates the heat flux to a load, as well as the gas and wall temperatures in a furnace, using simple thermodynamic correlations;
- Validate the thermodynamic model by comparing the results of the calculations with experimental data and with the results of the CFD simulations;
- Check the applicability of the thermodynamic model for lab-scale and industrial-scale furnaces, and for OEC and air-fuel conditions.

2. Overall Modelling Strategy and the Key Sub-Models

This chapter describes the overall modelling strategy and the most important governing transport equations, turbulence models, combustion models, reaction mechanisms, and radiation models used for the numerical simulation of reactive flows. More detailed information about the numerical modelling of turbulent reactive flows can be found in Ferziger and Falcitelli [57], Poinsot and Veynante [58] and Moukalled et al. [59]. This chapter also describes one model that makes it possible to distinguish between the total radiative heat flux into gas and wall surface radiation, in addition to presenting an iterative approach to calculating the reheating of billets or slabs in a reheating furnace.

2.1. Overall Modelling Strategy

To receive accurate simulation results the model must take into account the major physical effects as radiative heat transfer, homogeneous chemical reactions, etc. The results of the model must be validated by measurements to verify if the results are reliable. The overall modelling strategy used in this thesis can be seen in Figure 2.1. The furnace model can be subdivided into the following sub-models: flow modelling, turbulence modelling, homogeneous reaction model/combustion modelling and radiative heat transfer models. The results of the model was compared with measurements performed in this thesis. In the following sections the different sub-models are described in detail.

2.2. Flow Modelling

In most commercial CFD codes, the Finite Volume Method (FVM) is used for the discretization of the governing transport equations. The basic idea of the FVM is that the fluid domain is subdivided into finite Control Volumes (CVs); for each CV, the conservation

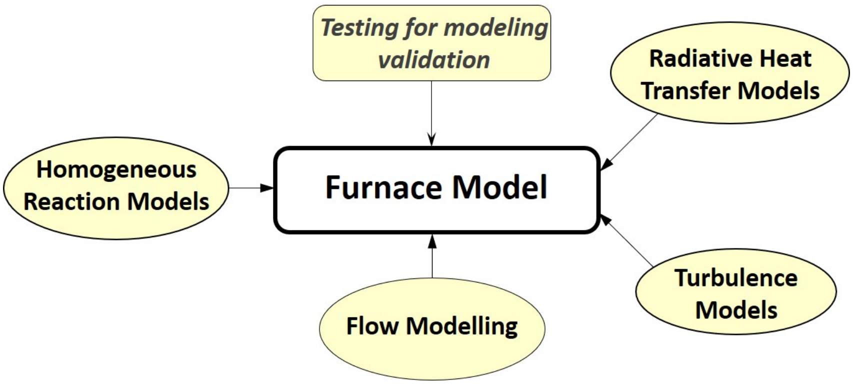

Figure 2.1.: Overall modelling strategy

equations for mass, momentum, energy, and species are applied and solved by numerical methods. The transport equation for the variable ϕ is given in Eq. 2.1 in its integral form and in Eq. 2.2 in its differential form. In this equations, the $\vec{v}$ is the velocity vector, Γ stands for the diffusion coefficient, $\vec{n}$ is the vector normal to the surface of the CV and ω_ϕ stands for the mass sink or source of the variable ϕ. The first term on the left-hand side of these equations represents the time dependent variation of the variable ϕ in the CV, while the second term stands for the convective flux of the variable ϕ over the surface of the CV. The first term of the right-hand side of the equation stands for the diffusion flux of the transport variable over surfaces of the CV, and the last term represents the generation or destruction of ϕ [59].

$$\frac{\partial}{\partial t}\int\limits_{V_{CV}} \rho\phi \, \mathrm{d}V_{CV} + \int\limits_{S_{CV}} \rho\phi\vec{v}\cdot\vec{n}\, \mathrm{d}S_{CV} = \int\limits_{S_{CV}} \Gamma\nabla\phi\cdot\vec{n}\, \mathrm{d}S_{CV} + \int\limits_{V_{CV}} \omega_\phi \, \mathrm{d}V_{CV} \tag{2.1}$$

$$\frac{\partial\left(\rho\phi\right)}{\partial t} + \nabla\cdot\left(\rho\phi\vec{v}\right) = \nabla\cdot\left(\Gamma\nabla\phi\right) + \omega_\phi \tag{2.2}$$

2.2.1. Conservation of Mass

In Eq. 2.3, the conservation equation for mass is given, also referred to as the continuity equation. These equations have to be satisfied by each phase in a flow with different phases. Therefore, due to chemical reactions, the mass exchange between the different phases can lead to source or sink terms on the right-hand side of the continuity equation for the different phases.

$$\frac{\partial\rho}{\partial t} + \nabla\cdot\left(\rho\vec{v}\right) = 0 \tag{2.3}$$

2.2.2. Conservation of Momentum

In Eq. 2.4, the conservation of momentum is given. In this equation, τ stand for the stress tensor and $\vec{g}$ is the gravitational vector. Again, the terms on the left-hand side stand for the transient and convective change of the momentum in the CV. The terms on the right-hand side represent the forces due to pressure, normal and shear stresses and gravitation.

$$\frac{\partial\left(\rho\vec{v}\right)}{\partial t}+\nabla\cdot\left(\rho\vec{v}\vec{v}\right)=-\nabla p+\nabla\cdot\tau+\rho\vec{g} \tag{2.4}$$

The stress tensor, given in Eq. 2.5, is a 3 x 3 matrix for a three-dimensional Cartesian coordinate system, where τ_{ii} stands for the normal stresses (including pressure) and τ_{ij} for the resulting shear stresses on the CV.

$$\tau=\begin{pmatrix}\tau_{xx} & \tau_{xy} & \tau_{xz}\\ \tau_{yx} & \tau_{yy} & \tau_{yz}\\ \tau_{zx} & \tau_{zy} & \tau_{zz}\end{pmatrix} \tag{2.5}$$

In this thesis only Newtonian fluids are investigated. For a Newtonian fluid, the stresses can be expressed by a linear function of the strain rate, as shown in Eq. 2.6, where μ is the dynamic viscosity and I the identity matrix.

$$\tau=\mu\left[\left(\nabla\vec{v}+\left(\nabla\vec{v}\right)^{T}\right)-\frac{2}{3}\left(\nabla\cdot\vec{v}\right)I\right] \tag{2.6}$$

Furthermore, the flow is assumed to be incompressible, and the material properties, such as density and viscosity, are assumed to be constant. In this context, incompressible means that the density does not change due to changing pressure ($\rho\neq f(p)$), but still changes because of changing temperatures ($\rho=f(T)$). This assumption is justified because the velocities of the flows investigated in this thesis are below a Mach number of 0.3. In Eq. 2.7, the conservative equation for a Newtonian, incompressible fluid and with constant material properties is given.

$$\frac{\partial\left(\rho\vec{v}\right)}{\partial t}+\nabla\cdot\left(\rho\vec{v}\vec{v}\right)=-\nabla p+\mu\nabla^{2}\vec{v}+\rho\vec{g} \tag{2.7}$$

2.2.3. Conservation of Energy

The conservation equation for energy is given in Eq. 2.8, where e stands for the total energy (see Eq. 2.9), λ is the thermal conductivity, h_k and $\vec{J}_k$ are the enthalpy and the diffusion flux of the component k which passes through the surface of the CV (see Eq. 2.10

and 2.11). The diffusion flux $\vec{J_k}$ is calculated using Eq. 2.11, where the diffusion and diffusion due to the Soret effect are considered. In this equation, the D_k and $D_{k,T}$ are the diffusion coefficients and S_{C_t} is the turbulent Schmidt number. ω_e represents the source term which has to be determine by the combustion model and the radiative model in the CFD calculation.

$$\frac{\partial\left(\rho e\right)}{\partial t}+\nabla\cdot\left(\rho\vec{v}e\right)=-\nabla\cdot\left(p\vec{v}\right)+\nabla\cdot\left(\tau\cdot\vec{v}\right)-\nabla\cdot\left(\lambda\nabla T\right)-\nabla\cdot\sum_k h_k\vec{J_k}+\omega_e \tag{2.8}$$

$$e=h-\frac{p}{\rho}-\frac{\vec{v}}{2} \tag{2.9}$$

The first term on the left-hand side of Eq. 2.8 again stands for the time dependent variation of the energy inside the CV, and the second term represents the convective energy fluxes over the surfaces of the CV. On the right-hand side, the terms stand for the energy resulting from the pressure and stresses on the CV, the energy flux due to thermal conductivity, and the enthalpy by diffusion flux of the component k, respectively.

$$h_k=\int_{T_0}^{T} c_p\,\mathrm{d}T \tag{2.10}$$

The energy equation can also be written in terms of temperature by inserting Eq. 2.9 and Eq. 2.10 into Eq. 2.8.

$$\vec{J_k}=-\left(\rho D_k+\frac{\mu_t}{S_{C_t}}\right)\cdot\nabla Y_k-D_{k,T}\cdot\frac{\nabla T}{T} \tag{2.11}$$

2.2.4. Conservation Equation for Species

In Eq. 2.12 the conservation equations for the species k in a multi species flow is given. Again the terms on the left hand side stands for the transient and the convective part and on the right-hand side the terms stand for the species transport due to diffusion and ω_{Y_k} for the source or the sink term of the species k. This source term has to be provided by the combustion models.

$$\frac{\partial\left(\rho Y_k\right)}{\partial t}+\nabla\cdot\left(\rho Y_k\vec{v}\right)=-\nabla\cdot\vec{J_k}+\omega_{Y_k} \tag{2.12}$$

2.3. Turbulence Modelling

In the majority of industrial applications, the flow is turbulent. This must be taken into account in any numerical calculations. A turbulent flow is defined by the unsteady, three-dimensional fluctuation of its velocity components [57]. This fluctuation affects both the energy and mass transfer, as well as the mixing process in systems with different components. Such fluctuations arise from eddies, which are formed by the shear stresses that result from different velocities in the flow or between the flow and the walls. In a turbulent flow, different length scales of eddy structures can be observed. The larger eddy structures contain the highest kinetic energy of the fluid flow. After some time, these larger eddies break up into smaller eddies due to energy dissipation. On the smallest length scale, also called the Kolmogorov scale, the energy dissipates into thermal energy. The transport of energy from the large scale eddies to the smallest turbulent structure is called energy cascade [60]. In a CFD calculation, these energy cascade must be considered, otherwise the calculation would be unrealistic. Three different approaches to these calculations have been developed. The first of these is the Direct Numerical Simulation (DNS) approach. Using this method, the conservation equations (Navier-Stokes equations) presented in the previous section can be used for the calculation of turbulent flows without any changes. Only the size of the grid must resolve the smallest turbulent structures, which means that the entire energy cascade has to be calculated. This approach can not be used for technical applications due to the very long calculation times. The second approach is referred to as Large Eddy Simulation (LES). Since larger eddies have the highest influence on fluid flow, these eddies should be resolved by the CFD calculation. In an LES calculation, the structures that are smaller than the computational grid are modelled, and the larger structures are calculated. Therefore, the computational grid is coarser than that of the DNS. The calculation times are still quite high for industrial applications, since for both the DNS and the LES approaches the transient Navier-Stokes equations must be solved. The last and most commonly used approach for modelling turbulent flow is to use the so called Reynolds-Averaged Navier-Stokes (RANS) equations. This approach, which models the whole energy cascade and does not consider time dependent fluctuations, was also used in this thesis. In Figure 2.2, the energy cascade depending on the wave length is shown, in addition to how much of the energy cascade is resolved by each approach. The wave length k is the inverse of the turbulent length scale l. In Figure 2.2, l_0 stands for the integral length scale, which represents the large eddies, and l_k stands for the Kolmogorov scale, which represents the smallest eddies. The RANS equations are derived from the Navier-Stokes equations (see Eq. 2.3 and 2.7) by Reynolds-averaging them using Eq. 2.13.

$$\phi = \overline{\phi} + \phi' \tag{2.13}$$

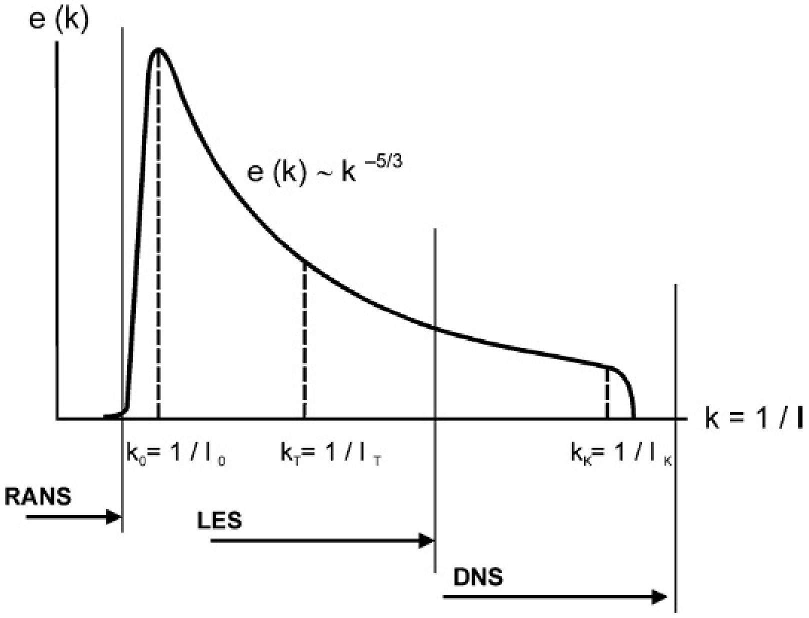

Figure 2.2.: Energy cascade depending on the length scale and the resolution of the different approaches [60]

The instantaneous value of a variable ϕ can be decomposed into a mean value $\overline{\phi}$ and a fluctuating value ϕ'. The mean value of a statistical steady-state fluid flow is defined as shown in Eq. 2.14.

$$\overline{\phi} = \lim_{t \to \infty} \frac{1}{t} \int_0^t \phi \,\mathrm{d}t \tag{2.14}$$

The RANS equations for momentum and mass conservation are given in Eq. 2.15 and 2.16 for an incompressible medium. As a result of the Reynolds-averaging, a new unclosed term so called Reynolds stresses arise in the momentum equation. These Reynolds stresses must be modelled by turbulence models.

$$\frac{\partial \rho}{\partial t} + \nabla \cdot \left(\rho \overline{\vec{v}}\right) = 0 \tag{2.15}$$

$$\frac{\partial \left(\rho \overline{\vec{v}}\right)}{\partial t} + \nabla \cdot \left(\rho \overline{\vec{v}}\,\overline{\vec{v}}\right) = -\nabla \overline{p} + \nabla \cdot \tau - \nabla \cdot \underbrace{\left(\rho \overline{\vec{v}'\vec{v}'}\right)}_{Reynolds\,stresses} + \rho \vec{g} \tag{2.16}$$

In turbulent flows with a gaseous medium, the fluctuation of temperature or pressure can lead to varying densities. Due to this density variation, the mass cannot be conserved by means of the Reynolds-averaging method. To overcome this problem, only mass-weighted averaged (Favre averaged) values are used in the calculation. The additional Reynolds stresses can be calculated using zero-, one - and two-equation turbulence models based on the Boussinesq approach, or by modelling the components of the stress tensor resulting in the Reynolds Stress Model (RSM). In this thesis, only two-equation models and the RSM were used for turbulence modelling. Therefore, these models are described in the next sections in more detail.

2.3.1. Standard k-ϵ Model

The standard k-ϵ model is a two- equation model proposed by Launder and Spalding [61]. Thanks to its robustness, the standard k-ϵ model is used in a wide range of applications. For this reason, it was also used in this thesis. The standard k-ϵ model assumes that the Reynolds stresses are proportional to the local mean-velocity gradients. This method was first proposed by Boussinesq, and is therefore denoted as the Boussinesq hypothesis. In Eq. 2.17, the relations for the calculation of the Reynolds stresses with the Boussinesq approach are shown, where μ_t is the turbulence viscosity, k is the turbulent kinetic energy and δ_{ij} is the Kronecker delta. The turbulence viscosity is not a property of the fluid (unlike the molecular viscosity), and it can therefore vary, not only from fluid flow to flow, but also over the domain of a particular fluid flow. This turbulence viscosity must be provided by the turbulence model.

$$- \rho \overline{\vec{v}'\vec{v}'} = \mu_t \left(\nabla \vec{v}\right) - \rho \frac{2}{3} k \delta_{i,j} \tag{2.17}$$

In the standard k-ϵ model, the turbulence viscosity is calculated using Eq. 2.18, where ϵ is the dissipation rate and C_μ a empirical model constant.

$$\mu_t = \rho C_\mu \frac{k^2}{\epsilon} \tag{2.18}$$

The turbulence model solves two additional transport equations for the dissipation rate ϵ and the kinetic energy k. These equations are given in Eq. 2.19 and Eq. 2.20, using the Einstein notation. The variables G_k and G_b represent the generation of turbulent kinetic energy due to velocity gradients (see Eq.2.21) and buoyancy effects (see Eq. 2.22), with the turbulent Prandtl number P_{r_t}. In Eq. 2.23, the calculation of the thermal expansion coefficient is defined.

$$\frac{\partial}{\partial x_i}\left(\rho k u_i\right) = \frac{\partial}{\partial x_j}\left[\left(\mu + \frac{\mu_t}{Pr_k}\right)\frac{\partial k}{\partial x_j}\right] + G_k + G_b - \rho\epsilon \tag{2.19}$$

$$\frac{\partial}{\partial x_i}\left(\rho \epsilon u_i\right) = \frac{\partial}{\partial x_j}\left[\left(\mu + \frac{\mu_t}{Pr_\epsilon}\right)\frac{\partial \epsilon}{\partial x_j}\right] + C_{1,\epsilon}\frac{\epsilon}{k}\left(G_k + C_{3\epsilon} G_b\right) - C_{2\epsilon}\rho\frac{\epsilon^2}{k} \tag{2.20}$$

$$G_k = -\rho \overline{u_i' u_j'} \frac{\partial u_j}{\partial x_i} \tag{2.21}$$

Table 2.1.: Values of the model constants used in the k-ϵ model [61] [62].

Model constant	Value
C_μ	0.09
Pr_k	1.0
Pr_ϵ	1.3
$C_{1,\epsilon}$	1.44
$C_{2,\epsilon}$	1.92

$$G_b = \beta g_i \frac{\mu_t}{Pr_t} \frac{\partial T}{\partial x_i} \tag{2.22}$$

$$\beta = -\frac{1}{\rho} \left(\frac{\partial \rho}{\partial T} \right)_p \tag{2.23}$$

All other coefficients in Eq. 2.19 and Eq. 2.20 are empirical model constants and are defined by experiments. In Table 2.1, the values for these constants are given. The variable $C_{3\epsilon}$ in Eq. 2.20 is calculated by Eq. 2.24, where u and v are the velocity components perpendicular and parallel to the gravitational vector.

$$C_{3\epsilon} = \tanh \left| \frac{v}{u} \right| \tag{2.24}$$

2.3.2. Realizable k-ϵ Model

The realizable k-ϵ model is an improvement of the standard k-ϵ model and was proposed by Shih et al. [63]. The realizable k-ϵ model is, like the standard k-ϵ model, a two-equation model based on the Boussinesq hypothesis. The big difference between the models is the calculation of the turbulent viscosity, the turbulent Prandtl number, and the modified transport equation for the dissipation rate ϵ (see Eq. 2.25). The calculation of the variables in Eq. 2.25 are given in Eqs. 2.26 to 2.28.

$$\frac{\partial}{\partial x_i} (\rho \epsilon u_i) = \frac{\partial}{\partial x_j} \left[\left(\mu + \frac{\mu_t}{Pr_\epsilon} \right) \frac{\partial \epsilon}{\partial x_j} \right] + \rho C_1 S \epsilon - \rho C_2 \frac{\epsilon^2}{k + \sqrt{v \epsilon}} + C_{1\epsilon} \frac{\epsilon}{k} C_{3\epsilon} G_b \tag{2.25}$$

$$C_1 = max \left[0.43, \frac{\eta}{\eta + 5} \right] \tag{2.26}$$

$$\eta = S \frac{k}{\epsilon}, \; S = \sqrt{2 S_{ij} S_{ij}} \tag{2.27}$$

$$S_{ij} = \frac{1}{2} \left(\frac{\partial u_j}{\partial x_i} + \frac{\partial u_i}{\partial x_j} \right) \tag{2.28}$$

With the realizable k-ϵ model, the calculation of high stream curvatures and spreading rates in an axisymmetric jet is improved compared to the standard k-ϵ model [62]. This

Table 2.2.: Model constants used in the realizable k-ϵ model

Model constant	Value
Pr_k	1.0
Pr_ϵ	1.2
C_2	1.9
$C_{1,\epsilon}$	1.44

is because of the different formulation of the transport equation for the dissipation and the turbulent viscosities. In contrast to the standard k-ϵ model, where the C_μ is constant, the realizable k-ϵ model calculates this parameter based on an eddy viscosity formulation from Reynolds [64] and which can be found in [62]. All other model constants used in the realizable k-ϵ model can be found in Table 2.2. Again, these parameters are determined by experiments. Due to the broader applicability of the realizable k-ϵ model, it was primarily used in this thesis.

2.3.3. Reynolds Stress Model (RSM)

The Reynolds Stress Model (RSM) is the most advanced approach for modelling the Reynolds stresses in the RANS equations. In the RSM, the Reynolds stresses are determined by solving a transport equation for each component of the stress tensor. Therefore, seven additional equations (six stresses, one dissipation rate) must be solved, which makes this model more computationally demanding than the models presented above. The advantage of the RSM is that, in contrast to the eddy-viscosity approach in the k-ϵ model, it considers the anisotropic behaviour of a flow with rapid changes to the strain rate or high stream line curvature, etc. [57, 65, 66]. In Eq. 2.29, the transport equation for the Reynolds stresses is given, where $\tau_{ij} = \rho\overline{u_i' u_j'}$ represents the Reynolds stress tensor. In this equation, the terms for the turbulent diffusion, the dissipation tensor, and the pressure strain rate have to modelled, which is done using the dissipation rate. Due to the fact that the RSM is the most advanced turbulence model, it was used in this thesis as the reference turbulence model.

$$\begin{aligned}
&\underbrace{\frac{\partial \tau_{ij}}{\partial t}}_{time\,derivative} + \underbrace{\frac{\partial\left(\overline{u}_k \tau_{ij}\right)}{\partial x_k}}_{convective\,term} = -\underbrace{\left(\tau_{ik}\frac{\partial \overline{u}_j}{\partial x_k} + \tau_{jk}\frac{\partial \overline{u}_i}{\partial x_k}\right)}_{stress\,production\,term} + \underbrace{\frac{\partial}{\partial x_k}\left(\frac{\mu}{\rho}\frac{\partial \tau_{ij}}{\partial x_k}\right)}_{molecular\,diffusion} \\
&+ \underbrace{2\mu\overline{\frac{\partial u_i'}{\partial x_k}\frac{\partial u_j'}{\partial x_k}}}_{dissipation\,tensor} + \frac{\partial}{\partial x_k}\underbrace{\left(\rho\overline{u_i' u_j' u_k'} + \overline{p' u_i'}\delta_{jk} + \overline{p' u_j'}\delta_{ik}\right)}_{turbulent\,diffusion} - \underbrace{p'\left(\frac{\partial u_i'}{\partial x_j} + \frac{\partial u_i'}{\partial x_j}\right)}_{pressure\,strain}
\end{aligned} \tag{2.29}$$

2.3.4. Near-Wall Treatment Methods

Walls have a high influence on turbulent flow due to the high velocity gradients which occur near the wall and the viscose damping of the turbulence. Therefore, special attention must be paid to the modelling of the near wall region to gain an accurate numerical simulation.

Turbulent Boundary Layers

Experiments show that the near wall region can be subdivided into three layers: viscous sublayer, buffer layer and the fully turbulent region. In the viscous sublayer the viscous forces play the dominant roll in momentum or heat transfer and the flow is nearly laminar. In the fully turbulent layer the turbulence has the highest influence on the momentum and the heat transfer. The buffer layer is the transition layer between the viscous sublayer and the fully turbulent region. In this layer the turbulence and the viscosity have an equally big impact on the momentum or heat transfer. In Figure 2.3 the velocity profile of a turbulent flow near the wall is plotted in semi-log coordinates. Where U/U_τ stands for the dimensionless velocity and y^+ for the dimensionless normal wall distance. The velocity U_τ stands for the friction velocity and is defined as:

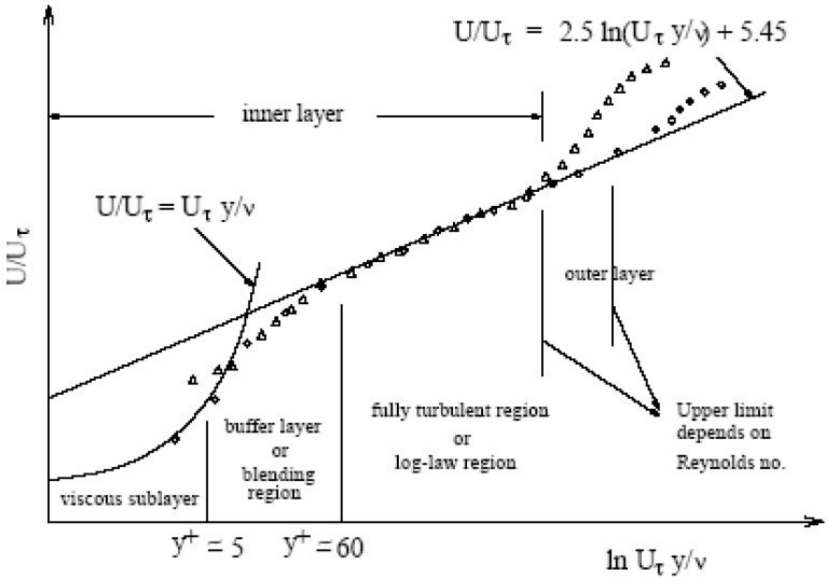

Figure 2.3.: Velocity profile of a turbulent boundary layer as a function of distance normal to the wall [62]

$$U_\tau = \sqrt{\frac{\tau_w}{\rho}} \tag{2.30}$$

and the normal wall distance y^+ is defined as:

$$y^+ = \frac{\rho U_\tau y}{\mu} \tag{2.31}$$

The dotted points in Figure 2.3 correspond to experimental data and the solid lines are the values calculated by the corresponding equations. In the viscous sublayer the dimensional velocity can be approximated by the following equation:

$$\frac{U}{U_\tau} = y^+ \tag{2.32}$$

and in the fully turbulent region the dimensional velocity can be approximated by the so called log-law:

$$\frac{U}{U_\tau} = \frac{1}{\kappa} \ln \left(y^+ \right) + B \tag{2.33}$$

where κ stands for the so called Karman constant with a value of 0.41 and B is an empirical constant related to the thickness of the viscous sublayer, for a flat plate this value is ~ 5.45. For the buffer layer none of this correlations show good results, therefore this region should be avoided.

Modelling Near-Wall Regions

There are generally two approaches to model the near wall region. The first approach are the so called wall functions. In this approach the viscous sublayer is not resolved by the numerical grid, instead semi-empirical formulations are used to describe the viscous effected region. In the second approach the numerical grid resolves the viscous sublayer all the way down to the wall. In this thesis wall functions are used to model the near-wall regions because the focus of this thesis is on models with a low computational demand. Therefore, only the wall function approach will be described in this thesis.

The wall functions provide functions and laws for the mean velocity, temperature and turbulence quantities near the wall. In ANSYS Fluent different wall-function approaches are available:

- Standard wall function
- Non-Equilibrium wall function
- Enhanced wall function

In this thesis the standard wall function was used in all simulation and will therefore be further explained.

Momentum: In the standard wall function the mean velocity near the wall is calculated similar to Eq. 2.32 and 2.33 with a different formulation for y^+ and U/U_τ. In the standard wall function the mean velocity U^* is defined as

$$U^* = \frac{U_p C_\mu^{\frac{1}{4}} k_p^{\frac{1}{2}}}{\frac{\tau_w}{\rho}} \tag{2.34}$$

and the normal wall distance y^* is defined as

$$y^* = \frac{\rho C_\mu^{\frac{1}{4}} k_p^{\frac{1}{2}} y_p}{\mu} \tag{2.35}$$

where U_p stands for the mean velocity at the near-wall node P, k_p for the turbulent kinetic energy at the near-wall node P, C_μ is an empirical model constant from the turbulence model and y_p the normal distance from point P to the wall. With these formulations the log-law for the fully turbulent region can be rewritten to

$$U^* = \frac{1}{\kappa} \ln \left(E y^* \right) \tag{2.36}$$

and for the viscous sublayer to

$$U^* = y^* \tag{2.37}$$

In ANSYS Fluent the log-law (Eq. 2.36) is employed when the normal wall distance y^* is > 11 and the laminar stress-strain relationship (Eq. 2.37) is used for normal wall distances < 11. The standard wall function is applicable for y^* values between $15 <$ and < 300 whereby the upper limit strongly depends on the overall Reynolds number. For the simulations conducted in this thesis the y^* was between 20 and 300.

Turbulence: For the $k - \epsilon$ model and the RSM the k-equation is solved in the whole domain including the near-wall region. At the wall a zero gradient boundary condition ($\frac{\partial k}{\partial n} = 0$) is applied for the k-equation. The dissipation rate ϵ and the production of the kinetic energy G_k is calculated in the wall-adjacent cells by the local equilibrium hypothesis. The local equilibrium hypothesis states that the production of k and the dissipation rate ϵ are equal in the wall-adjacent cell. Therefore, the production of turbulent kinetic energy (G_k) is based on logarithmic law and can be calculated by the following correlation

$$G_k \approx \tau_w \frac{\partial U}{\partial y} = \tau_w \frac{\tau_w}{\kappa k_p^{\frac{1}{2}} y_p} \tag{2.38}$$

In contrast to k-equation the ϵ-equation is not solved at the wall-adjacent cells. Therefore, the ϵ value in the wall adjacent cell is calculated by the following correlation

$$\epsilon = \frac{C_\mu^{\frac{3}{4}} k_p^{\frac{3}{2}}}{\kappa y_p} \tag{2.39}$$

2.4. Combustion Modelling

In combustion modelling, the use of correct models for chemical kinetics and turbulent chemistry interaction is necessary in order to achieve an accurate simulation. The selection of the turbulence/chemistry interaction model has a significant impact on the calculation time and the solution. Three main models are available in most commercial CFD codes to describe the turbulence/chemistry interaction: the Eddy Dissipation Model (EDM), the Eddy Dissipation Concept Model (EDC), and mixture fraction models, like the SFM. In the following section, these models will be described in detail.

2.4.1. Eddy Dissipation Model (EDM)

The EDM is based on the assumption that the time scale of the chemical reaction is infinitely fast compared to the mixing time. Therefore, the combustion process can be reduced to a simple mixing problem. This approach is also called the “mixed is burnt” approach [67] and was first proposed by Magnussen and Hjertager [68]. The EDM predicts the net production rate of a species k in mixing-limited combustion. In the EDM, the characteristic value for the calculation of the production rate is the large eddy mixing time scale ($\frac{\epsilon}{k}$). To predict the net production rate of the species k, the minimum values of Eq. 2.40 (reactant mixing rate) and Eq. 2.41 (production mixing rate) are defined as the species source term.

$$\omega_{k,r} = \nu'_{k,r} M_k A \rho \, \frac{\epsilon}{k} \, min \left(\frac{Y_R}{\nu'_{R,r} M_R} \right) \tag{2.40}$$

$$\omega_{k,r} = \nu'_{k,r} M_k A B \rho \, \frac{\epsilon}{k} \, \frac{\sum_p Y_p}{\sum_j^k \nu''_{j,r} M_j} \tag{2.41}$$

In Eq. 2.40 and 2.41, Y stands for the mass fraction, ν' for the stoichiometric coefficient of reactants, ν'' for the stoichiometric coefficient of products, and M stands for the molecular weight. The subscripts r stands for the reaction, R for the reactant, and P for the product species. The variables A and B are model parameters and, have for a conventional combustion, the values 4.0 and 0.5, respectively. For different combustion regimes, these values can be adapted. In this thesis, the standard values are used. A big drawback of the EDM is that a maximum of two reactions can be considered because multi step reaction mechanism are based on the Arrhenius rate, which can be significantly different for each reaction. In the EDM, all reactions have the same turbulent rate, and, therefore the model should only be used with a global reaction mechanism which considers a maximum of two reactions [62]. This restriction means that no dissociation effects can be considered with the EDM. In oxy-fuel combustions, the consideration of dissociation effects is necessary, otherwise the temperature is massively overestimated (see section 2.4.4). Therefore, the EDM is deemed to be unsuitable for oxy-fuel combustion.

2.4.2. Eddy Dissipation Concept (EDC)

The EDC model is an improvement of the EDM model, and is based on the work of Magnussen [69]. With the EDC model, multi-step mechanisms can be used for the calculation of combustion processes. This makes it possible to consider radical formation and dissociation effects, both of which are necessary for the calculation of oxy-fuel combustions. Therefore, the EDC is mainly used by researchers for the calculation of oxy-fuel flames (e.g. [40, 70, 71]). The EDC assumes that the reaction takes place in fine scales, where the whole chemical reaction mechanism is solved for each iterations step. In Eq. 2.42 and Eq. 2.43, the definition of the length scale and the time scale is shown, where C_ζ is the volume fraction constant and C_t is the time scale constant, with values of 2.1377 and 0.4082, respectively [72].

$$\zeta^* = C_\zeta \left(\frac{\mu \epsilon}{\rho k^2} \right)^{\frac{1}{4}} \tag{2.42}$$

$$t^* = C_t \left(\frac{\mu}{\rho \epsilon} \right)^{\frac{1}{2}} \tag{2.43}$$

The source term for a species is calculated by Eq. 2.44, where Y_i^* represents the fine scale mass fraction.

$$\omega_k = \frac{\rho \left(\zeta^*\right)^2}{t^* \left[1 - \left(\zeta^*\right)^3\right]} \left(Y_i^* - Y_i\right) \tag{2.44}$$

The big drawback of the EDC is its high calculation time, which is due to the computationally demanding chemistry integration in each iteration step. Pope [73] proposed a method called In-Situ Adaptive Tabulation (ISAT), which reduces the calculation time for the chemistry integration with each iteration step. Although the ISAT method reduces the calculation time of the EDC, it still takes ten times longer than both the EDM and the SFM.

2.4.3. Steady Laminar Flamelet Model (SFM)

Another possibility for simulating combustion with detailed mechanisms is the SFM model. In this model, a turbulent flame can be represented by an ensemble of small one-dimensional laminar diffusion flamelets [74]. The flamelets are created by calculating one- dimensional counter flow diffusion flames. Such counterflow diffusion flames can be easily calculated with detailed chemical kinetics, and can be compared with measurements. The advantage of this model is that the thermochemical state of the fluid can be described by only one parameter, called mixture fraction. The mixture fraction is defined as the mass fraction of all fuels (C, H,...) and all oxidizer elements (O,...) in all species (H_2O, CO_2, CO, O, OH,...). In Eq. 2.45, the definition of the mixture fraction is shown, where Z_i, $Z_{i,ox}$ and $Z_{i,fuel}$ are the mass fractions of the element i in the oxidizer and the fuel.

$$f = \frac{\dot{m}_{fuel}}{\dot{m}_{fuel} + \dot{m}_{ox}} = \frac{Z_i - Z_{i,ox}}{Z_{i,fuel} - Z_{i,ox}} \tag{2.45}$$

The benefit of this approach is that the source terms from the chemical reactions in the transport equation of the mean mixture fraction can be avoided due to mass balance on the atomic level. The introduction of the mixture fraction reduces the chemistry to a simple mixing problem [58, 60, 62]. In Eqs. 2.46 - 2.48 the flamelet equations are given, where χ stands for the scalar dissipation rate, ω_k for the reaction rate of species k, H_k for the specific enthalpy of the species k, a_s for the strain rate, and ρ_∞ for the density of the fluid at the inlet. For the assumption of chemical equilibrium in the flamelet, the scalar dissipation rate has a value of 0.

$$\rho \frac{\partial Y_k}{\partial t} = \frac{1}{2} \rho \chi \frac{\partial^2 Y_k}{\partial f^2} + \omega_k \tag{2.46}$$

$$\rho \frac{\partial T}{\partial t} = \frac{1}{2} \rho \chi \frac{\partial^2 T}{\partial f^2} - \frac{1}{c_p} \sum_k H_k \omega_k + \frac{1}{2 c_p} \rho \chi \left[\frac{\partial c_p}{\partial f} + \sum_k c_{p,k} \frac{\partial Y_k}{\partial f} \right] \frac{\partial T}{\partial f} \tag{2.47}$$

$$\chi = \frac{a_s}{4\pi} \frac{\left(\sqrt{\frac{\rho_\infty}{\rho}} + 1 \right)^2}{2\sqrt{\frac{\rho_\infty}{\rho}} + 1} \exp \left\{ -2 \left[erfc^{-1} (2f) \right]^2 \right\} \tag{2.48}$$

For turbulent flows, the governing equations are only solved for Favre-averaged values. Therefore, the mean value of the different scalars is predicted by a Probability Density Function (PDF). The PDF is the probability that the instantaneous fluid value is equal to the averaged value at the same place in the flow field [58, 60, 62]. The PDF is also generated before the CFD calculation, based on the results of the flamelet calculation. Therefore, the shape for the PDF must be presumed. A commonly used PDF shape is the β-PDF, which is also used in all simulations performed in this thesis. Averaged values $\overline{\phi_i}$, like temperature, density, etc., were calculated with Eqs. 2.49 to 2.53. For the calculation of $p(f)$, the mixture fraction variance f'^2 is needed with $f' = f - \overline{f}$.

$$\overline{\phi} = \int_0^1 p(f)\phi(f, \overline{H})\, \mathrm{d}f \tag{2.49}$$

$$p(f, H) \approx p(f) \cdot \delta(H - \overline{H}) \tag{2.50}$$

$$p(f) = \frac{f^{\alpha-1}(1-f)^{\beta-1}}{\int_0^1 f^{\alpha-1}(1-f)^{\beta-1}\, \mathrm{d}f} \tag{2.51}$$

$$\alpha = \overline{f}\left(\frac{\overline{f}(1-\overline{f})}{\overline{f'^2}} - 1\right) \tag{2.52}$$

$$\beta = (1-\overline{f})\left(\frac{\overline{f}(1-\overline{f})}{\overline{f'^2}} - 1\right) \tag{2.53}$$

The advantage of this approach is that the chemistry calculations can be pre-processed and stored in look-up tables, and only two additional transport equations have to be solved for the mean mixture fraction $\overline{f}$ and mixture variance $\overline{f'^2}$. This means that the density, temperature, and mass fraction only depend on the mixture fraction and enthalpy (for non-adiabatic conditions). Furthermore, this leads to a significant reduction in the calculation time. The transport equations for the mean mixture fraction and mixture fraction variance are given in Eqs. 2.54 and 2.55, where μ_t stands for the turbulent viscosity; C_g and C_d are model constants. Additionally, the energy equation is given in Eq. 2.56, where $\overline{H}$ stands for the mean enthalpy, k_t for the turbulent conductivity, and $\omega_{\overline{H}}$ is the source term for enthalpy, for example, due to thermal radiation.

$$\frac{\partial}{\partial t}\left(\rho\overline{f}\right) + \nabla \cdot \left(\rho\vec{v}\overline{f}\right) = \nabla \cdot \left(\frac{\mu_t}{Pr_t}\nabla\overline{f}\right) \tag{2.54}$$

$$\frac{\partial}{\partial t}\left(\rho\overline{f'^2}\right) + \nabla \cdot \left(\rho\vec{v}\overline{f'^2}\right) = \nabla \cdot \left(\frac{\mu_t}{Pr_t}\nabla\overline{f'^2}\right) + C_g\mu_t\left(\nabla\overline{f}\right)^2 - C_d\rho\frac{\epsilon}{k}\overline{f'^2} \tag{2.55}$$

$$\frac{\partial}{\partial t}\left(\rho\overline{H}\right) + \nabla \cdot \left(\rho\vec{v}\overline{H}\right) = \nabla \cdot \left(\frac{\lambda_t}{c_p}\nabla\overline{H}\right) + \omega_{\overline{H}} \tag{2.56}$$

Borghi diagram

The Borghi diagram was used to evaluate if the SFM can be used for the calculation of oxy-fuel flames. The Borghi diagram can be used to estimate different combustion regimes of premixed turbulent combustions [75]. Although, in this thesis only turbulent diffusion flames are investigated, the Borghi diagram is used to roughly estimate the dominating combustion regime. The use of the SFM model is valid if the chemistry is much fast then the mixing process. The Damköhler number (Da) represent the ratio of the flow time scale to the chemical time scale and can be calculates using Eq. 2.57. In Eq. 2.57, v_L stands for the laminar flame speed, l_F for the laminar flame thickness, v' for the turbulent intensity and l_t for the turbulent length scale. From this equation it can be seen that the use of the SFM model is valid for Damköhler numbers higher then one. In Figure 2.4 the Borghi diagram is shown, where Re_{l_t} stands for the turbulent Reynolds number (definition see Eq. 2.58) and Ka for the Karlovitz number (definition see Eq. 2.59). The Kalovitz number stands for the ratio of the chemical time scale (t_F) and the Kolmogorov time scale (t_K). In this diagram the ratios of l_t/l_f and v'/v_L for the furnaces investigated in this thesis which operates under oxy-fuel conditions (VO2, IFRF furnace) are shown. Under oxy-fuel conditions the flame speed has the highest value and the Re number has the lowest value compared to air-fuel combustion. Therefore, the furnaces which operates under oxy-fuel were used to evaluate if the SFM can be used. If the SFM can be used for oxy-fuel conditions it is also valid for air-fuel conditions. Because under air-fuel conditions the Re number is far higher then under oxy-fuel conditions, due to the higher flow rates. It can be seen that for both furnaces the calculated ratios of l_t/l_f and v'/v_L results in a Damköhler number higher then one. Therefore, the use of the SFM is appropriate for this furnaces operating under oxy-fuel conditions.

$$Da = \frac{t_t}{t_F} = \frac{v_L \cdot l_t}{v' \cdot l_F} \tag{2.57}$$

$$Re_{l_t} = \frac{v' \cdot l_t}{v_l \cdot l_F} \tag{2.58}$$

$$Ka = \frac{t_F}{t_K} \tag{2.59}$$

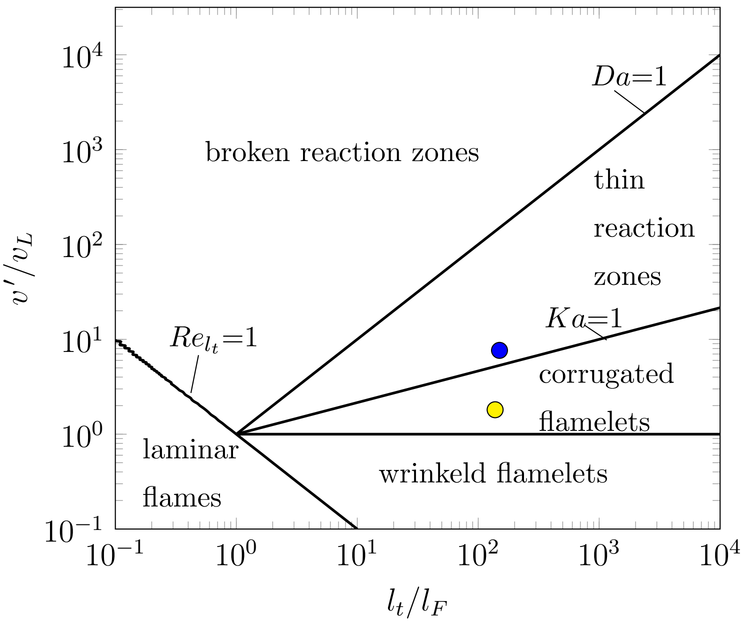

Figure 2.4.: Borghi diagram: VO2 furnace 🟡, IFRF furnace 🔵. Adapted from [75]

2.4.4. Reaction Mechanisms and Their Applicability for OEC

In literature, many chemical reactions mechanisms can be found for the combustion of different hydrocarbons with air. For oxy-fuel or OEC conditions, hardly any reaction mechanisms are available that have been specially designed or tested for these conditions. In oxy-fuel and OEC conditions, it is necessary to use detailed reaction mechanisms, because of the higher temperatures and dissociation process that must be taken into account [21, 40]. In this thesis only furnaces are investigated which are fired by NG. In Figure 2.5, the adiabatic flame temperature for the combustion of methane calculated with a detailed reaction mechanism (GRI3.0) is compared with a simple one-step global reaction mechanism for different oxygen concentrations in the oxidizer. It can clearly be seen that the detailed and the one-step mechanisms predict similar adiabatic flame temperatures for air-fuel conditions, but, with increasing oxygen concentrations in the oxidizer, the adiabatic flame temperature is massively overestimated by the one-step mechanism due to its neglect of dissociation effects. Prieler [21] and Prieler et al. [41] evaluated different detailed reaction mechanisms in terms of their application for oxy-fuel and OEC with the SFM. For this purpose, four detailed reaction mechanisms were investigated: the GRI3.0, DRM19, smooke46, and skeletal25. The GRI3.0 [76] is one of the most comprehensive and frequently-used reaction mechanisms for the combustion of NG. It consists of 325 reactions and considers 53 species (see Appendix A.3), including the formation of NO_x. This mechanism has been widely validated against experiments and data from literature on air-fuel combustion. The DRM19 [77] was derived from the GRI3.0 for methane air

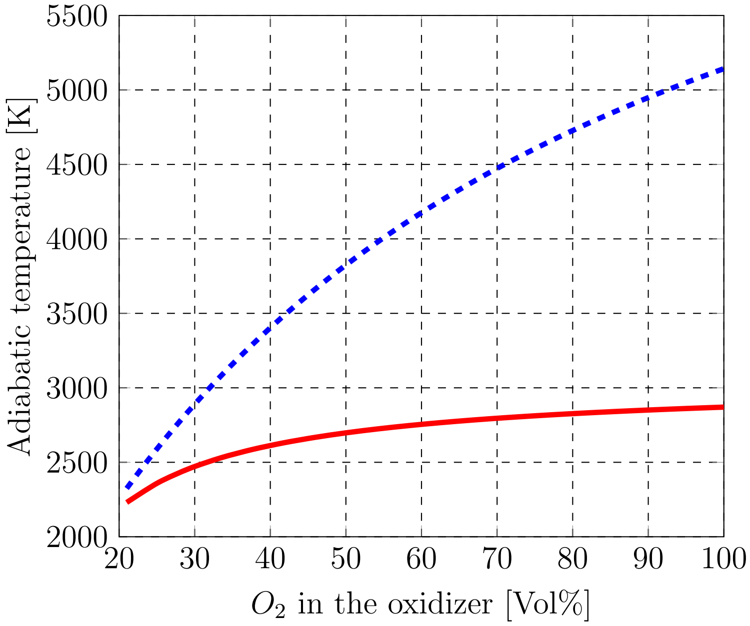

Figure 2.5.: Adiabatic flame temperature for combustion of methane with different O_2/N_2 mixtures calculated with a detailed reaction mechanism GRI3.0 (—) and 1 step (- - -) reaction mechanism [21]

combustion using reduction techniques. The mechanism considers 84 reactions and 19 species, and was tested against the GRI3.0 for a wide range of pressures and equivalence ratios under air-fuel conditions. The smooke46 mechanism was proposed by Smooke et al. [78], consists of 17 species, and considers 46 reactions (see Appendix A.1). This mechanisms was tested against experiments with counter diffusion flames, using diluted air as oxidant. The skeletal25 mechanism was developed by Peeters [79] in a PhD thesis. It consists of 25 reactions and considers 17 species (see Appendix A.2). This mechanism is an adaptation of the mechanism proposed by Smooke and Giovangigli [80]. In skeletal25, the pressure-dependent reaction (R13) has been adapted for atmospheric conditions. The investigation by Prieler et al. [41] revealed that up to an oxygen concentration of 30 Vol% oxygen in the oxidizer, all reaction mechanisms predict the same temperature and species concentrations for the combustion of methane. For higher oxygen concentrations, every reaction mechanism except skeletal25 predicted unrealistic flame temperatures and species concentrations. Prieler [21] concluded that the skeletal25 reaction mechanism is able to better predict the flame temperature under oxy-fuel and OEC conditions due to its faster conversion of the intermediate species CO to the products H_2O and CO_2. In this thesis, the smooke46 and the skeletal25 reaction mechanisms were mainly used for combustion simulations with the SFM model. A global four-step reaction mechanism proposed by Yin et al. [40] was also used in this thesis, in combination with the EDC model. This global mechanism is an adapted version of the JL [81] global four-step reaction mechanism, using

Table 2.3.: Kinetic parameters of the refined JL reaction mechanism by Yin et al. [40]

No.	Reactions	Rate equation $[kmol/(m^3 Ts)]$	A	b	E
1	$CH_4 + 0.5\,O_2 \longrightarrow CO + 2\,H_2$	$\frac{d[CH_4]}{dt} = AT^b \exp^{-E/(RT)} \cdot [CH_4]^{0.5}[O_2]^{1.25}$	$4.4 \cdot 10^{11}$	0	$1.26 \cdot 10^8$
2	$CH_4 + H_2O \longrightarrow CO + 3\,H_2$	$\frac{d[CH_4]}{dt} = AT^b \exp^{-E/(RT)} \cdot [CH_4][O_2]$	$3.0 \cdot 10^8$	0	$1.26 \cdot 10^8$
3	$H_2 + 0.5\,O_2 \longleftrightarrow H_2O$	$\frac{d[H_2]}{dt} = AT^b \exp^{-E/(RT)} \cdot [H_2][O_2]^{0.5}$ (forward)	$5.69 \cdot 10^{11}$	0	$1.465 \cdot 10^8$
4	$CO + H_2O \longleftrightarrow CO_2 + H_2$	$\frac{d[CO]}{dt} = AT^b \exp^{-E/(RT)} \cdot [CO]^{0.5}[H_2O]$ (forward)	$2.75 \cdot 10^9$	0	$8.36 \cdot 10^7$

the original H_2 oxidation model proposed by Marinov et al. [82]. In Table 2.3, the the kinetic parameters of the refined JL reaction mechanism are given.

2.5. Radiation Models

Radiative heat transfer in an participating medium consist of absorption, emitting and scattering. In Figure 2.6 a ray is shown passing through a participating medium. The radiation intensity I of the ray is gained by emission and in-scattering and is reduced by absorption and out-scattering. The change of the radiation intensity of a ray passing through a absorbing, emitting, and scattering medium is described by the Radiative Transport Equation (RTE), given in Eq. 2.60, in direction $\vec{s}$ at position $\vec{r}$:

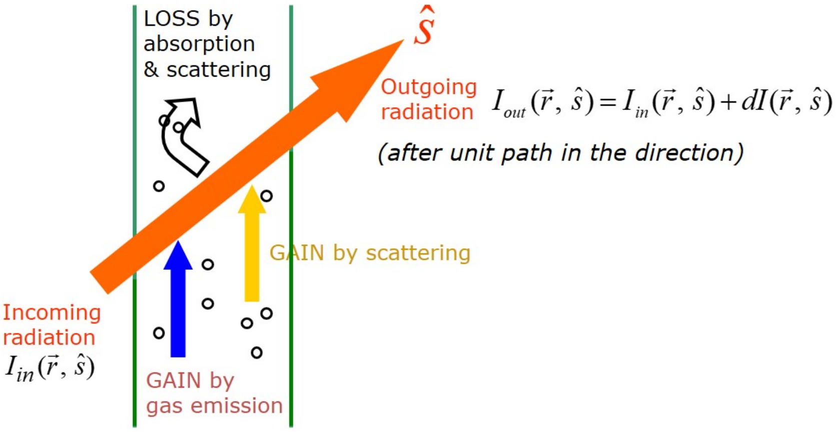

Figure 2.6.: Radiative heat transfer in an participating medium. Adapted from [62]

$$\nabla \cdot (I(\vec{r}, \vec{s})\,\vec{s}) + \underbrace{(a + \sigma_s) I(\vec{r}, \vec{s})}_{absorption/scattering\,loses} = \underbrace{a n^2 \frac{\sigma T^4}{\pi}}_{gas\,emission} + \underbrace{\frac{\sigma_s}{4\pi} \int_0^{4\pi} I(\vec{r}, \vec{s}\,')\Phi(\vec{s} \cdot \vec{s}\,')\, \mathrm{d}\Omega}_{in-scattering} \tag{2.60}$$

where a stands for the absorption coefficient of the flue gas, σ for the Stefan-Boltzmann constant, σ_s for the scattering coefficient of the flue gas, I for the radiation intensity, and T for the local temperature. Due to the use of natural gas as fuel, and, hence, the assumption of a low particle concentration, scattering can be neglected ($\sigma_s = 0$). Therefore, Eq. 2.60 reduces to:

$$\nabla \cdot \left(I\left(\vec{r}, \vec{s}\right) \vec{s}\right) + aI\left(\vec{r}, \vec{s}\right) = an^2 \frac{\sigma T^4}{\pi} \tag{2.61}$$

The RTE can be solved using the P1 model [83, 84] or the Discrete Ordination Model (DO) [85, 86], which are both described in detail in the following sections.

2.5.1. The P1 Model

In the P1 model, the general equation of radiative heat transfer is transformed by the method of spherical harmonics into a set of simultaneous partial differential equations. The first approaches were closely related to the neutron transport and to the radiative transfer of stars. The P1-approximation is the lowest order calculation of the method of spherical harmonics. The method of spherical harmonics is very popular because of the fact that it produces a relatively simple set of partial differential equations. On the other hand, its disadvantages are that low order approximations like the P1 are only right with near isotropic radiative intensity, and that the P1 does not give the correct result in case of optically thin media [87]. Generally, P1 model over predicts the radiative heat flux in many cases [62]. Porter et al. [88] and Prieler et al. [41] showed that the P1 model over predicts heat flux under oxygen-enriched conditions (with a high optical thickness). The higher order approximations are more time consuming. The radiative intensity is integrated over all directions, which leads to the diffusion equation of the RTE as given in Eq. 2.62, where G is the incident radiation (definition see Eq. 2.63) and $\nabla \cdot q_{rad}$ is the radiative heat flux. The result of the radiative heat flux from the Eq. 2.62 is used as a source or sink term in the energy equation.

$$-\nabla \cdot q_{rad} = aG - 4an^2 \sigma T^4 \tag{2.62}$$

$$G = \int_0^{4\pi} I(\vec{r}, \vec{s}') \, \mathrm{d}\Omega \tag{2.63}$$

2.5.2. Discrete Ordinates Model (DO)

The DO model calculates the radiative heat transfer by solving the RTE (see Eq. 2.61) for different solid angles, $\vec{s}$. The method presented here was first used for the calculation of neutron transport. Later, like the P_1-Approximations, it became established as a solution for radiation heat transfer problems. In the last thirty years, the DO has been adapted for general radiative heat transfer problems. The model is characterized by the variation of the direction of the RTE. The idea is that the transfer equation be solved for a discrete direction for the solid angle $\vec{s}$ of the angular space 4π. The DO method can be subdivided into the following steps:

- Angular discretization of the spherical envelop around the each cell-center
- Angular discretization of the RTE
- Spatial discretization of the RTE
- Solve the discretized RTE equations

In this work, each octant was discretized with 4 x 4 solid angels, which results in an total of 128 directions for which the RTE must be solved [62, 87].

The P1 model should be used for optical thicknesses of > 1 and the DO model for optical thicknesses lower then one [62, 87]. Definition of the optical thickness can be seen in Eq. 2.64, where a is the absorbing coefficient, σ_s the scattering coefficient and s the mean beam length or beam length.

$$(a + \sigma_s)\,\dot{s} \tag{2.64}$$

The beam length is calculated by Eq. 2.65, where V stands for the gas volume and A for the surrounding surface of the gas volume.

$$s = 3.6\frac{V}{A} \tag{2.65}$$

The typical optical thicknesses of the furnaces investigated in this thesis are between 0.34 and 0.87. Therefore, the DO model was mainly used as radiation model in this thesis.

2.5.3. Radiative Properties of the Flue Gas

In reactive flows, the modelling of the radiative properties is of high importance, especially in oxy-fuel or oxygen-enriched conditions. For the stoichiometric combustion of methane, the amounts of H_2O and CO_2 in the flue gas can vary from low amounts – under air-fuel conditions – with volume fractions of 0.19 for H_2O and 0.095 for CO_2, to high concentrations for oxy - fuel combustion, with volume fractions of 0.66 and 0.33 for H_2O and CO_2, respectively. Bearing in mind that most numerical models were developed for air-fuel conditions, the applicability of these models for OEC must be investigated. Combustion gases, such as H_2O, CO_2, CO and SO_2 absorb and emit radiation only over certain wave lengths, known as absorption bands. Between these bands, the gases do not absorb or emit radiation. In Figure 2.7, the pressure-based spectral absorption coefficient of CO_2 is shown as a function of the wavelength, and the different absorption bands can be seen clearly. To calculate the absorption bands of gases, there are a variety of models available in literature. These include:

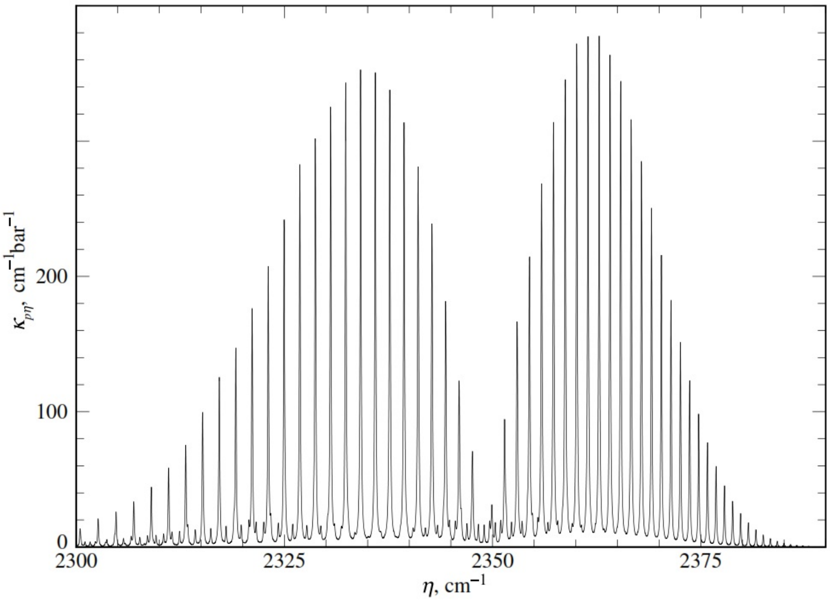

Figure 2.7.: Pressure based spectral absorption coefficient for small amount of CO_2 in nitrogen, at p=1 bar, T=296 K. [87]

- The Line by Line Model (LBL)
- Band models
- Global methods

These models differ in their accuracy and their calculation time, and will be described in the following sections.

The Line by Line model (LBL)

For the LBL calculation, detailed knowledge of every single spectral line is required. This information can be collected from different high-resolution spectroscopic databases, like the High-Resolution Transmission Molecular Absorption Database (HITRAN), a published database, such as the High-Temperature Molecular Spectroscopic Database (HITEMP), in many different version [89–92]. Using such databases, with strongly variegating values for the absorption coefficient, means that the radiative transfer equation need to be solved for millions of different wave numbers, and needs to be integrated over the entire spectrum. This high computational demand makes this model inapplicable for CFD calculations with desktop computers available today. Therefore, this model is mostly used for theoretical calculations, or as a benchmark for simpler models.

The Exponential Wide Band Model (EWB)

The Exponential Wide Band Model (EWB) is a simpler model than the LBL. The EWB assumes that there is a limited number of strong absorbing bands in the infrared part of the spectrum which contribute to absorption of the flue gas. The number of bands can be further reduced by only considering strong bands, instead of single lines. The EWB assumes the exponential function of the line intensity around a band's centre. In Figure 2.8, the assumed band shapes of the EWB are shown. Although it is a simpler approach than the LBL model, the calculation time is still high, and this model is therefore used primarily for calculations of lab-scale furnaces.

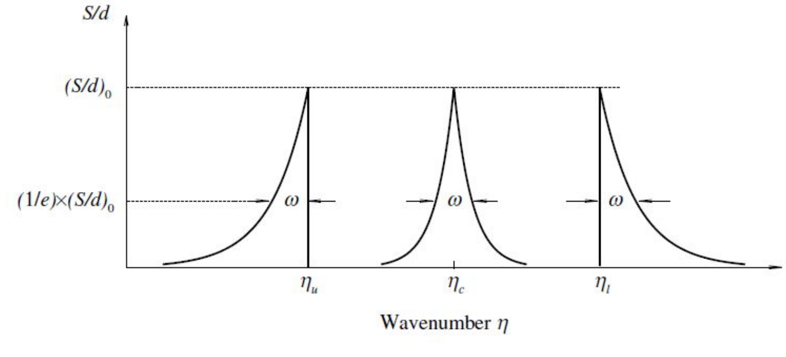

Figure 2.8.: Bands for the exponential wide band model [87]

Becher et al. [93] compared different LBLs (HITEMP2010 [92], HITEMP1995 [89], HITRAN2008 [91], HITRAN2004 [90]) and band models (EM2C [94], RADCAL [95], EWB [96]) with gas cell experiments under oxy-fuel conditions. Their comparison showed that the HITEMP2010 is the most accurate with regard to concentration and temperature.

Weighted Sum of Grey Gases Model (WSGGM)

The Weighted Sum of Grey Gases Model (WSGGM) is one of the simplest models for the calculation of radiative properties. It was first proposed by Hottel and Sarofim [97]. In this model, the radiative properties of the flue gas are considered as a mixture of fictive grey gases. The emissivity of the gas mixture is calculated by the sum of the emissivity of all fictive grey gases combined with a weighting factor, as displayed in Eq. 2.66. In this equation, $a_{\epsilon,i}$ stands for the emissivity weighting factor, a_i is the absorption coefficient of i-th fictive gas, p is the sum of all partial pressures of all absorbing gases and s is the path length.

$$\epsilon = \sum_{i=0}^{I} a_{\epsilon,i}(T)(1 - e^{-a_i ps}) \tag{2.66}$$

These emissivity weighting factors are calculated using Eq. 2.67, where $b_{\epsilon,i,j}$ stands for the emissivity gas temperature polynomial coefficient. These coefficients are derived from more accurate models, like the LBL or the EWB, using a regression scheme [98].

$$a_{\epsilon,i} = \sum_{j=1}^{J} b_{\epsilon,i,j} T^{j-1} \tag{2.67}$$

This thesis mainly uses the coefficients from Smith et al. [98], but other coefficients were also investigated.

Evaluation of WSGGM Coefficient

The WSGGM from Smith et al. [98] was originally derived for conventional air combustion. The coefficients are valid for H_2O/CO_2 ratios of 1 and 2, path lengths up to 10 m, and for temperatures between 600 and 2400 K. They were derived from a banded model (EWB). Yin [99] showed that, for large beam lengths, the WSGGM from Smith et al. produces large errors in comparison with the EWB. Yin et al. [100] compared Smith et al.'s WSGGM for different H_2O/CO_2 ratios (0.125, 1, 2), path lengths, and temperatures, with the EWB for oxy-fuel conditions. The WSGGM showed a high deviation for small H_2O/CO_2 ratios (which corresponds to oxy-fuel combustion with flue gas recycling) and large beam lengths. For a H_2O/CO_2 of 2, which is the case for the oxy-fuel combustion of CH_4, the WSGGM only showed a higher deviation for larger beam lengths. Similar investigations have been carried out by Becher et al. [101], who compared the WSGGM of Smith et al. with the very accurate LBL model (HITEMP2010). The WSGGM showed a maximum deviation of 59% under oxy-fuel conditions. For this reason, many new WSGGMs have recently been published for oxy-fuel condition [100, 102–107]. Yin et al. [40] calculated a 0.8 MW

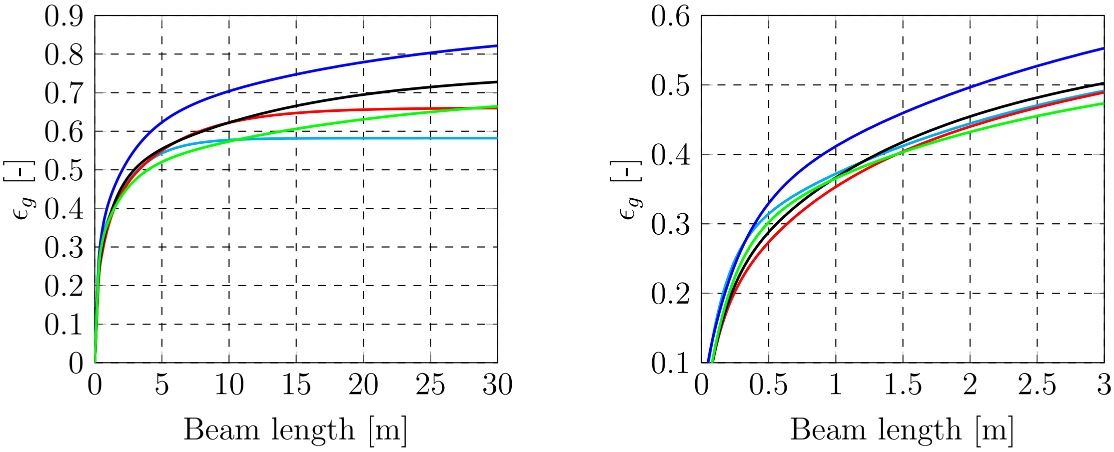

Figure 2.9.: Gas emissivity calculated with different WSGGMs for oxy-fuel conditions and different beam lengths (T_g=1500 k, p=1 bar): Smith et al. [98] (—), Kangwanpongpan et al. [102] (—), Krishnamoorthy [107] (—), Johansson et al. [103] (—), Yin et al. [100] (—)

furnace and a 609 MW boiler with two different WSGGMs. The simulation showed that the different WSGGMs make a negligible difference for small-scale furnaces because of the small beam length. For bigger furnaces and boilers, the WSGGMs showed a higher deviation from each other. Furthermore, Yin [108] used CFD calculations to compare the effect of grey and non-grey calculations of the radiative properties of the flue gas on the same boiler. The results of this investigation showed that the heat flux to the wall is over-predicted, and the gas temperature was under predicted by the grey calculation when compared to the non-grey calculation. Figure 2.9 shows the gas emissivity for oxy-fuel conditions calculated with different WSGGMs for different beam lengths and a typical gas temperature, which is representative of the furnaces investigated in this thesis. It is possible to see that the different WSGGMs differ more significantly from each other for beam lengths greater than 3 m. For beam lengths under 3 m, the difference between the WSGGMs is smaller than for higher beam lengths. Typical beam lengths for the furnaces investigated in this thesis are between 0.5 and 3 m. In this range, the WSGGMs show a negligible difference between each other. This has also been proven by many variant calculations for all of the furnaces investigated in this thesis. The different WSGGMs calculate similar gas emissivities for the investigated furnaces. Thus, the WSGGM from Smith et al., which is standard in the CFD code ANSYS Fluent, was primarily used in the simulations conducted in this thesis.

2.5.4. Determination of Gas and Wall Surface Radiation[1]

With Eq. 2.61, only the total radiation heat flux to a thermal load inside a furnace can be calculated, which is a combination of gas and wall surface radiation. In industrial furnaces, it is useful to know the quantities of the different heat fluxes emerging from convection, gas, and wall surface radiation in order to achieve the optimal design of the furnace. The heat flux arising from convection and the total radiation heat flux can be calculated in a standard CFD simulation of a furnace. To quantify the amount of gas and wall surface radiation in a furnace simulation, an additional calculation must be performed. The starting point for this calculation is the converged solution of the furnace simulation, from which the heat fluxes due to convection and (total) radiation are known. In this calculation, only the equation for the DO model is calculated anew; all other governing equations, such as the momentum, energy, turbulence model, and combustion model equations, were frozen. To calculate the amount of wall surface radiation, the absorption coefficient of flue gas is set to zero, which reduces Eq. 2.61 to:

$$\nabla \cdot \left(I\left(\vec{r}, \vec{s}\right) \vec{s} \right) = 0 \tag{2.68}$$

This means that the radiation intensity does not change over the direction $\vec{s}$. Hence, the calculated radiation intensity is the radiation emitted by the furnace walls (solid bodies).

Due to the fact that the energy equation is not calculated anew in this calculation, the heat flux arising from wall surface radiation, can not be calculated from the energy equation. Therefore, the radiative heat flux must be calculated directly from the DO equation. Figure 2.10 shows how the DO model calculates the radiative heat flux density to an opaque and diffuse wall, where $\dot{q}_{in}$ is the incident radiative heat flux density, which is defined in Eq. 2.69.

$$\dot{q}_{in} = \int_{\vec{s}\cdot\vec{n}>0} I_{in} \vec{s} \cdot \vec{n} d\Omega \tag{2.69}$$

At an opaque wall, a part of the incident radiation is absorbed, and the other part is reflected ($\dot{q}_{reflected\, diffuse}$). Additionally, the wall also emits radiation ($\dot{q}_{emission}$). The difference between absorbed incident radiation ($\epsilon_w \dot{q}_{in}$) and the emitted radiation ($n^2 \epsilon_w \sigma T_w^4$) is the radiative heat flux density of the wall ($\dot{q}_{rad}$). The equation to calculate the radiative heat flux density to a wall is given in Eq. 2.70. ϵ_w stands for the emission coefficient of the wall, and T_w for the wall temperature.

$$\dot{q}_{rad} = \epsilon_w \dot{q}_{in} - n^2 \epsilon_w \sigma T_w^4 \tag{2.70}$$

---

[1] Parts of this section have already been published in [5]

Using Eq. 2.70, it is possible to calculate the heat flux density arising solely from wall surface radiation. The difference between the heat flux density arising only from wall surface radiation and the total radiative heat flux density (gas and wall surface radiation) is the heat flux density resulting from gas radiation.

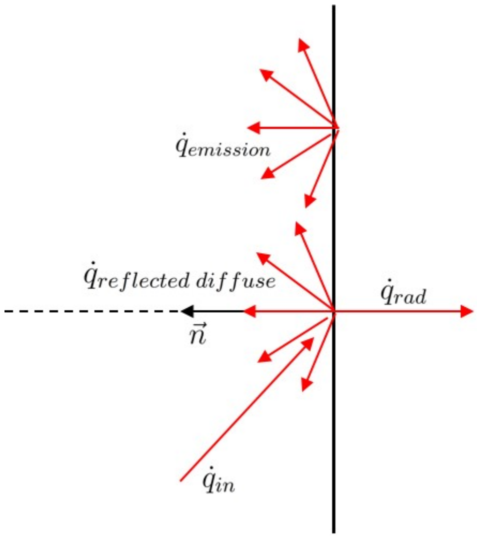

Figure 2.10.: Radiative heat transfer to an opaque and diffuse wall [62]

2.5.5. Solution Procedure for the Calculation of the Billet Temperature in a Reheating Furnace

In this thesis, an iterative approach was used for the calculation of the billet temperatures in an industrial reheating furnace in order to couple the gas-phase combustion and the periodically transient reheating of the billets. This procedure was recently proposed by Prieler et al. [52], and was tested for air-fired conditions as well as oxygen-enriched conditions [32]. The procedure consists of two simulations: a steady-state simulation of the gas phase combustion, and a transient simulation of the reheating of the billets. From the simulation of the gas phase combustion, the heat flux to the billets is calculated. This calculated heat flux is used as a boundary condition for the transient simulation. From this transient simulation, new surface temperatures for the billets are calculated, which are the new boundary conditions for the steady-state simulation of the gas phase combustion in the next iteration step. The temperature boundary condition for the billets in the first steady-state simulation was assumed to increase in a linear manner with the furnace length, from the temperature at the beginning to the estimated temperature at the end of the furnace. For the following iteration step, an arithmetically averaged temperature profile of the temperature profile from the previous iteration and the newly calculated temperature profile of the billets is calculated, and this is used as a boundary condition in the steady-state simulation of the gas phase combustion. This can be seen as an under- relaxation factor of 0.5. Without this averaging, the simulation would calculate unrealistically high temperatures at the corners and edges of the billets. The mean deviation of the temperature in all computational cells (transient billet simulation) from one iteration to the next was used as the convergence criterion. The solution was considered as convergent when the change in temperature between two simulations was below 1%. In Figure 2.11, the scheme for the solution procedure is shown. Further information about this process can be found in [52].

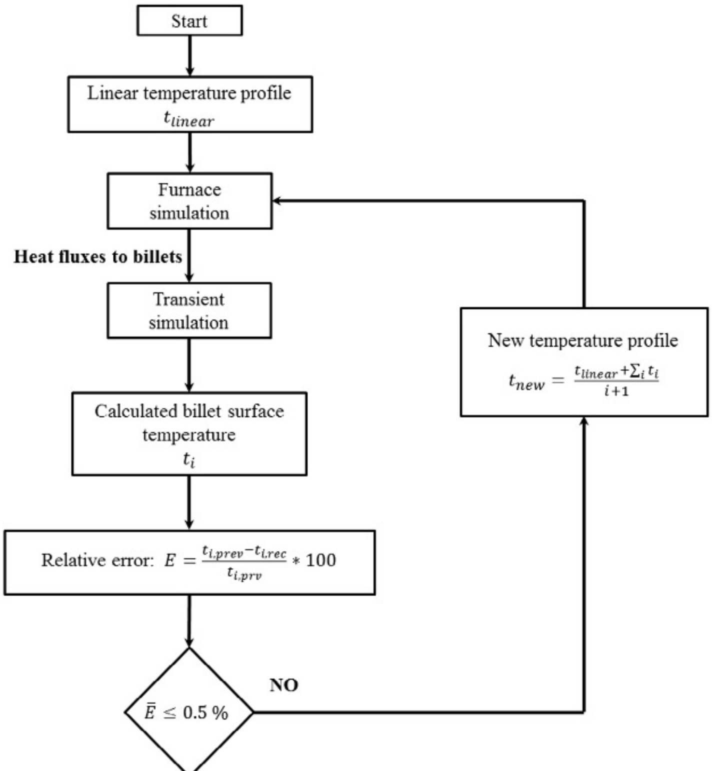

Figure 2.11.: Scheme of the iterative approach [52]

3. Lab-scale Furnaces: Testing and Modelling

This chapter will discuss the solutions of the numerical simulations carried out in this thesis, using the models outlined in Chapter 2. In combustion simulations, the calculation of the chemical kinetics is a time-consuming and computationally-demanding process. Therefore, in this thesis, combustion models with low computational demand, such as the SFM, were used. The sections of Chapter 3 are concerned with the validation of numerical models for oxy-fuel and OEC, as well as the determination of their limits. The numerical models will be validated by comparing the results of the simulations with experimental data from lab-scale furnaces. The main goal of this thesis is to find numerically efficient models that are applicable for all kinds of oxygen concentrations in the oxidizer, ranging from air-fuel to oxy-fuel conditions. Additionally, the method described in Section 2.5.4 is used to determine the amount of wall surface and gas radiation in the investigated furnaces for the different conditions.

3.1. Lab-scale Furnace VO2[1]

In this section, the numerical simulation of the lab-scale furnace VO2, described in Section 3.1.1, is presented. The solutions of the simulations are then compared to experimental data in order to validate the numerical models for oxy-fuel and OEC conditions. For the simulation of the lab-scale furnace, mainly models with low computational demand were used. Furthermore, the amount of gas and wall surface radiation in the lab-scale furnace was determined by means of the numerical method presented in Section 2.5.4.

---

[1] Parts of this section have already been published in [1]

Table 3.1.: Natural gas input in the experiments for different oxidizers [1]

	Water cooled plate alone		Water cooled plate + shielding	
O_2 in the oxidizer [Vol%]	T2=1200 °C NG input [kW]	T2=1070 °C NG input [kW]	T2=1200 °C NG input [kW]	T2=1070 °C NG input [kW]
100	57.2	36.1	40.7	27.9
45	79.4	45.2	67.2	40.6
30	94.1	55.3	80	47.5
25	114.9	62.3	86.5	51.5
21	-	73.9	91.7	61.1

3.1.1. Description of the Lab-scale Furnace VO2

The first experiments were executed on a natural gas fired lab-scale furnace called VO2, with a thermal input of between 28 and 115 kW, depending on the oxygen concentration in the oxidizer and the temperature level (see Table 3.1). This lab-scale furnace is equipped with three “Messer Oxipyr-Flex” burners. The internal dimensions of the combustion chamber are 0.77 x 0.75 x 0.99 m, this corresponds to a path length of 0.5 m, and the chamber is surrounded by 0.2 m of ceramic insulation. The bottom of the furnace is made of bricks. The burners are lowered 70 mm into the insulation, as can be seen in Figure. 3.1a. Figure. 3.1a also shows the different temperature measurement points (T1, T2, T3, T4). The temperature measurements were performed using four Type B thermocouples. The three thermocouples located above the burners were encapsulated by ceramic material. The top-wall distances for the different thermocouples are: T1: 50 mm, T2: 70 mm, T3: 65 mm. At the back wall, a standard thermocouple (T4) is located 0.52 m from the bottom, 40 mm from the side wall and 0.1 m from the back wall. In the experiments, the temperature inside the furnace was regulated at measurement point T2. Therefore, the term “temperature level” is defined as the temperature from the measurement point T2. Experiments were done for temperature levels of 1070 °C and 1200 °C. The measurement uncertainties for the thermocouples at these temperature levels are ±2.7 K and ±3 K for 1070 °C and 1200 °C, respectively. The thermocouples were calibrated with a thermocouple calibrator (Fluke 714B), and additional reference measurements were done with a quotient pyrometer (Keller Optix Q PT70). As a thermal sink, a water-cooled plate was placed inside the furnace. The plate has dimensions of 0.4 x 0.4 x 0.05 m, and was blackened before the experiment in order to minimise the reflection of thermal radiation. The water in- and outlet temperatures and the water mass flow were measured to determine the absorbed thermal power. The temperature of the copper plate was measured by three thermocouples on different positions. For the second experiment, a shielding was placed

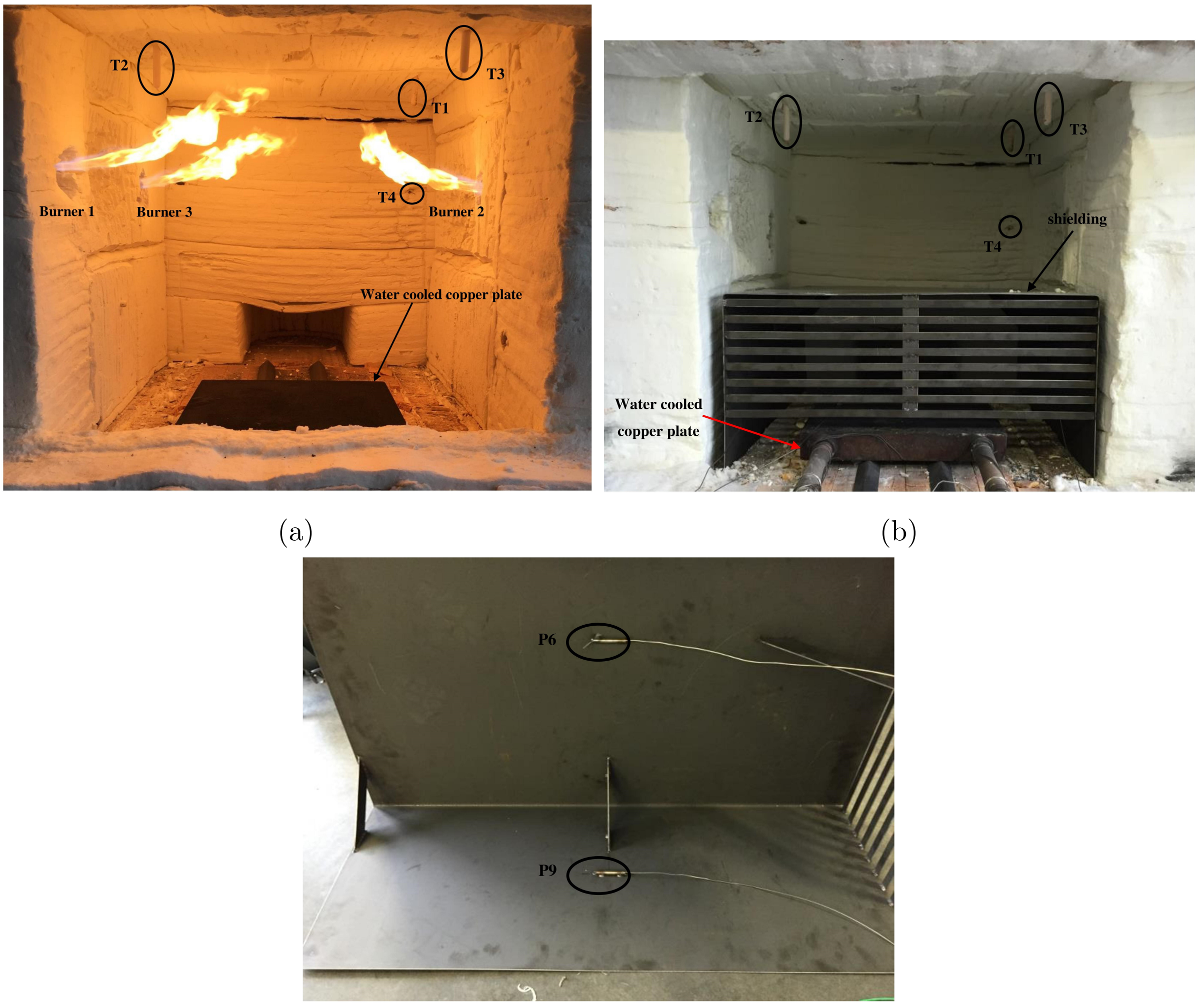

(a)

(b)

(c)

Figure 3.1.: Experimental-Setup VO2, (a) The lab-scale furnace with the water cooled copper plate and temperature measurement points, (b) Water cooled copper plate and shielding, (c) Positions of the thermocouples P6 and P9 under the shielding [1]

over the water-cooled copper plate to measure the heat flux without the hot zones of the flames and with a more uniform flue gas composition. The water-cooled copper plate with the shielding can be seen inside the furnace in Figure. 3.1b. The dimensions of the shielding were 0.92 x 0.7 x 0.35 m. In addition, three thermocouples were added to measure the temperature under the shielding. The thermocouples were located at the two side walls (P3 left wall, P9 right wall) and at the top wall (P6) of the shielding. The locations of the thermocouples P6 and P9 are shown in Figure. 3.1c. It is possible to see that each thermocouple is located in the middle of the shielding.

3.1.2. Boundary Conditions

In the simulations, pure methane was used as fuel, and a mixture of O_2 and N_2 was used as the oxidizer, depending on the oxygen enrichment. All inlets were modelled as mass flow inlets. The simulations were carried out for different experimental setups and oxygen concentrations, with fuel-oxidizer equivalence ratios between 0.925 and 0.989, which correspond to an oxidizer-fuel equivalence ratio λ between 1.081 and 1.011. This meant that the furnace was operated under slightly fuel-lean conditions. The inlet temperatures for fuel and oxidizer were set to 25 °C, and the inlet turbulent intensity was set to 5%. The hydraulic diameter for the fuel was set to 4 mm, and the hydraulic diameter for the oxidizer was set to 3 mm. A temperature boundary condition was applied at the water-cooled copper plate. The temperatures of the plate are known from the measurements (see Table 3.2), and the internal emissivity of the blackened copper plate was set to 0.9. The insulation and the bottom of the furnace, which are made of bricks, were modelled as solids, with thermal conductivities of 0.25 $\mathrm{W/(m\,K)}$ and 1 $\mathrm{W/(m\,K)}$, respectively (see Figure 3.2). The heat transfer from the outer wall to the ambient was modelled by a convective boundary condition (see Table 3.3). The numerical settings and the under-relaxation factors used for the simulations can be found in Appendix B.1.

3.1.3. Computational Grid

A high-quality numerical grid is essential in order to obtain an accurate solution, and the types of cells are of particular importance in combustion simulations [41]. Therefore, high-quality elements with low growth rates were used in the vicinity of the burner, where there are high temperatures and species concentrations. The grid of the furnace (fluid and solid) consists primarily of hexahedrons and wedges, due to their good numerical properties. For the setup, for which only the water-cooled plate was inside the furnace,

Table 3.2.: Temperature boundary condition for the water cooled copper plate in the lab-scale furnace VO2 [1]

	Water cooled plate alone		Water cooled plate + shielding	
O_2 in the oxidizer [Vol%]	T2=1200 °C T plate [°C]	T2=1070 °C T plate [°C]	T2=1200 °C T plate[°C]	T2=1070 °C T plate [°C]
100	158	131	133	124
45	185	142	165	124
30	191	152	172	125
25	185	157	172	126
21	-	166	174	132

Table 3.3.: Convective boundary condition in CFD at the outer wall of the lab-scale furnace VO2 [1]

Free stream temperature [K]	298.15
Heat transfer coefficient [W/(m^2 K)]	30
Radiation	
Internal emissivity	0.9

the grid was made up of 1,179,770 cells. The mesh quality was determined by a maximum aspect ratio of 32, and a minimum orthogonal quality of 0.1. For the setup with plate and shielding, the furnace was meshed with 2,518,501 cells. Again, the mesh quality was determined by a maximum aspect ratio of 35 and a minimum orthogonal quality of 0.146. Figure 3.2 presents a 3D model and the mesh of the furnace for the various configurations. Grid independency tests were performed for both models. For the setups with and without shielding grids, 4,970,929 and 4,395,637 cells were used for the grid independency test, respectively. A porous zone was set at the outlet to prevent reversed flows.

3.1.4. Results and Discussion

Effect of grid

The grid independency test was done for both cases with 100 Vol% O_2 in the oxidizer and a temperature level of 1200 °C. When only the plate was inside of the furnace, the fuel input was 57.2 kW; with the cooling plate and shielding, the fuel input was 40.7 kW. For the setup with the shielding, a mesh with 4,970,929 cells was used for the grid independency test, while for the setup with the water-cooled plate without shielding, a mesh with 4,395,637

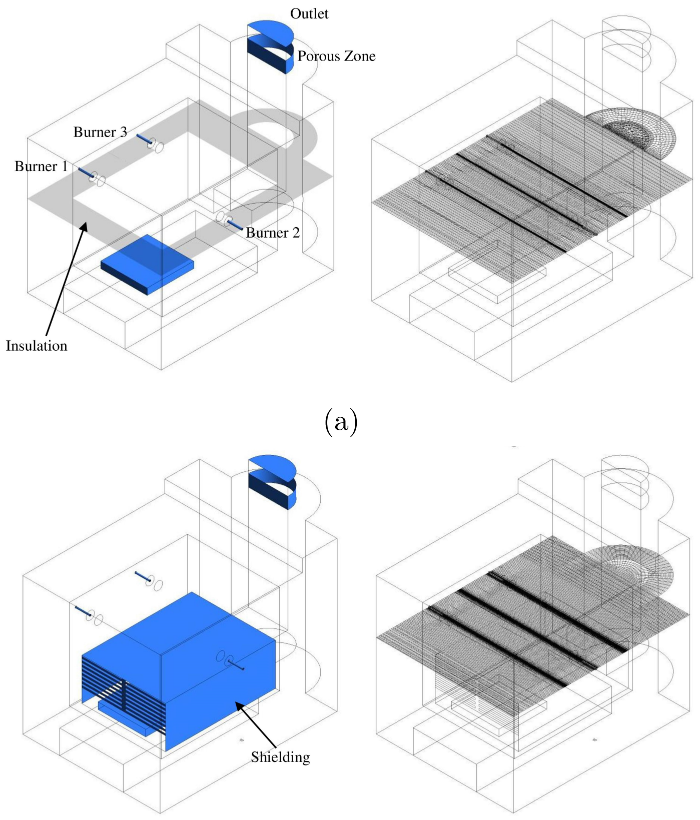

(a)

(b)

Figure 3.2.: 3D model and mesh of the different furnace configurations: (a) plate without shielding. (b) plate with shielding [1]

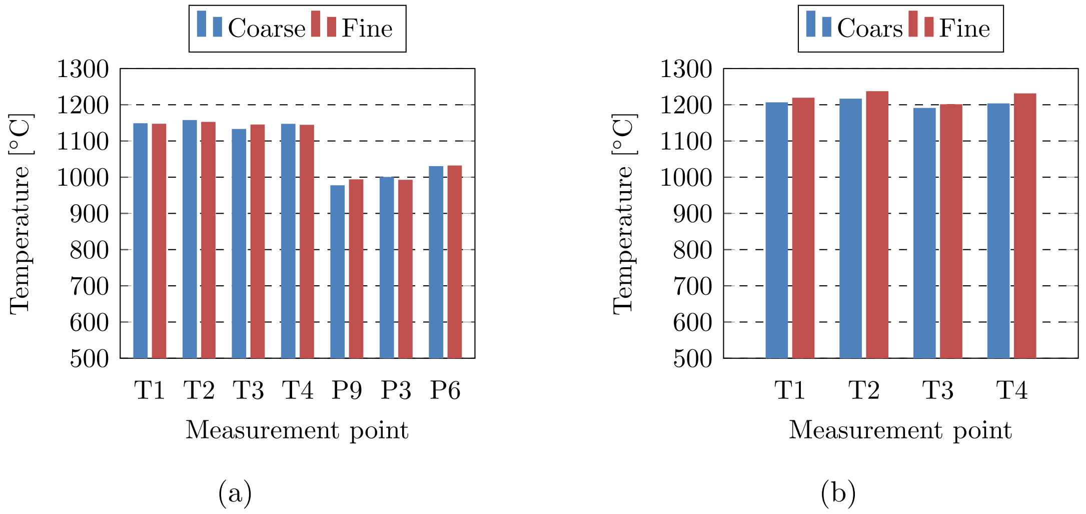

Figure 3.3.: Comparison between fine and coarse grid (SFM with skeletal25) (a) plate and shielding (b) plate without shielding [1]

cells was used. Figure 3.3 shows a comparison of the simulations with the fine and coarse grids. For both setups, the difference between the two grids is negligible; therefore, the coarse mesh was used for all further simulations.

Effect of Combustion Modelling

For the calculation of the chemistry and turbulent interaction in the furnace, two different models were used: the EDC and the SFM, in order to demonstrate the time-saving potential of the SFM model. For the EDC model, a refined version of the JL four-step mechanism was used. In contrast to the original JL mechanism, this refined mechanism uses the H_2 oxidation model proposed by Marinov et al. [82]. This model replaces the H_2 reaction in the JL mechanism. The refined JL mechanism was used by Kim et al. [109] and Yin et al. [40] for the simulation of natural gas flames under air-fuel and oxy-fuel conditions. The detailed mechanism skeletal25 was used for the simulations of the furnace with the SFM model. Using the SFM model, the calculation time can be reduced from 4 weeks, with the EDC, to 4 days on 8 Central Processing Unit (CPU) cores. As a result of the time saved using the SFM model, it was possible to perform calculations with different O_2 concentrations in the oxidizer, two temperature levels, and two different experimental setups, all within a short period of time. The temperature contours calculated with the SFM and the skeletal25 mechanism for different ratios of O_2/N_2 in the oxidizer are plotted in Figure 3.4. Additionally, in Figure 3.5, the volume fraction of the OH species is shown. It is possible to see that, for all enrichments of O_2 in the oxidizer, the flame shapes are well-predicted by the CFD calculation with the SFM and the skeletal25 mechanisms. The

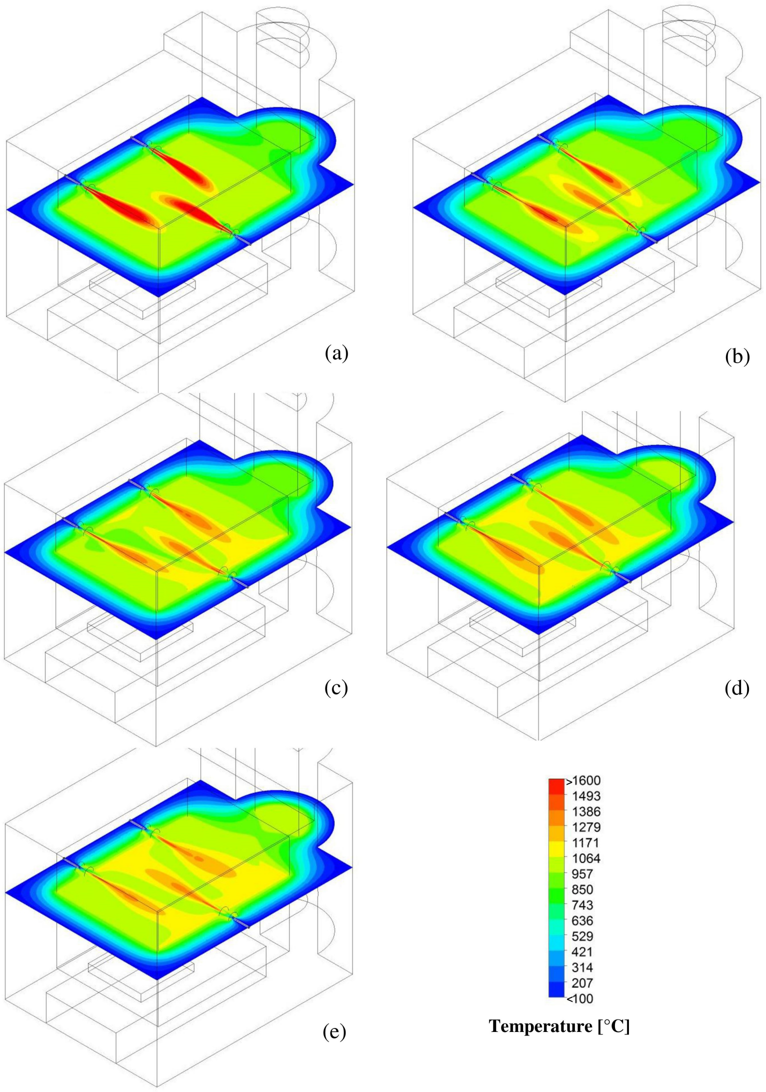

Figure 3.4.: Temperature contours of the furnace with water cooled plate for different O_2/N_2 ratios at a temperature level of 1070 °C (SFM with skeletal25): (a) 100 Vol% O_2; (b) 45 Vol% O_2; (c) 30 Vol% O_2; (d) 25 Vol% O_2; (e) 21 Vol% O_2 [1]

flame shapes were compared with photos of the flames and with calculations from other models, such as the EDC model (see Yin et al. [40]). Furthermore, it is also possible to see that, as the O_2 concentration in the oxidizer increases, the flames become shorter and the temperature distribution becomes more uniform. For an oxygen concentration of 100 Vol% oxygen in the oxidizer, the flame is deflected more upwards, due to the smaller exit velocity of the oxidizer as well as buoyancy effects. This leads to a higher temperature at the roof of the furnace. As the oxygen in the oxidizer decreases, the exit velocity of the oxidizer increases, and, therefore, the wall temperature on the opposite side of the burner is higher than the temperature at the wall and the roof. The volume fraction of the OH species increases as the O_2 concentration increases in the oxidizer, which is an indication

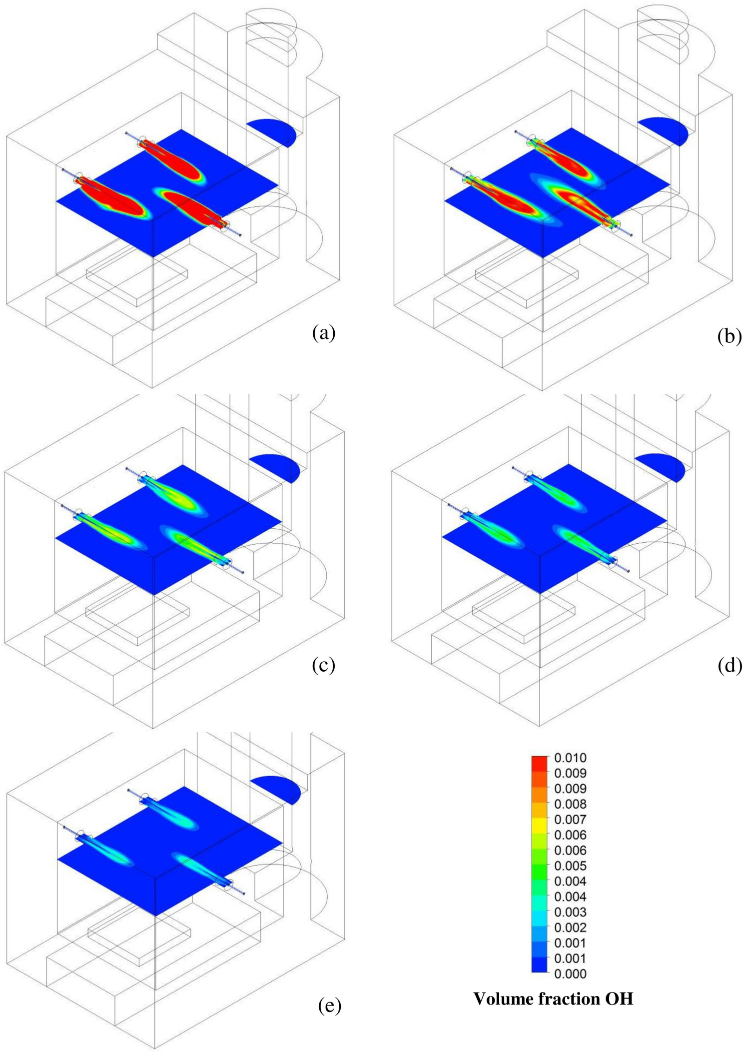

Figure 3.5.: OH Volume fraction contours of the furnace with water cooled plate for different O_2/N_2 ratios at a temperature level of 1070 °C (SFM with skeletal25): (a) 100 Vol% O_2; (b) 45 Vol% O_2; (c) 30 Vol% O_2; (d) 25 Vol% O_2; (e) 21 Vol% O_2 [1]

of higher chemical activity in the main combustion zone of the flame. This underlines the need for detailed chemical mechanisms in simulations of oxy-fuel combustions. The chemical mechanisms must include dissociation effects, due to the higher temperatures in oxygen-enriched combustion, which promote dissociation. If the dissociation effects are not included in the chemical mechanisms, the temperature in the main combustion zone of the flames is significantly overestimated (see Yin et al. [40]). Figure 3.6 shows the comparison between measurements and simulations for the experimental setup, where only the plate is inside the furnace and where there is a temperature level of 1070 °C. All simulated cases are in close agreement with the measurements. The maximum error occurs at T4 at an O_2 concentration of 21 Vol%, with a value of 80.5 K. The temperature for this measurement

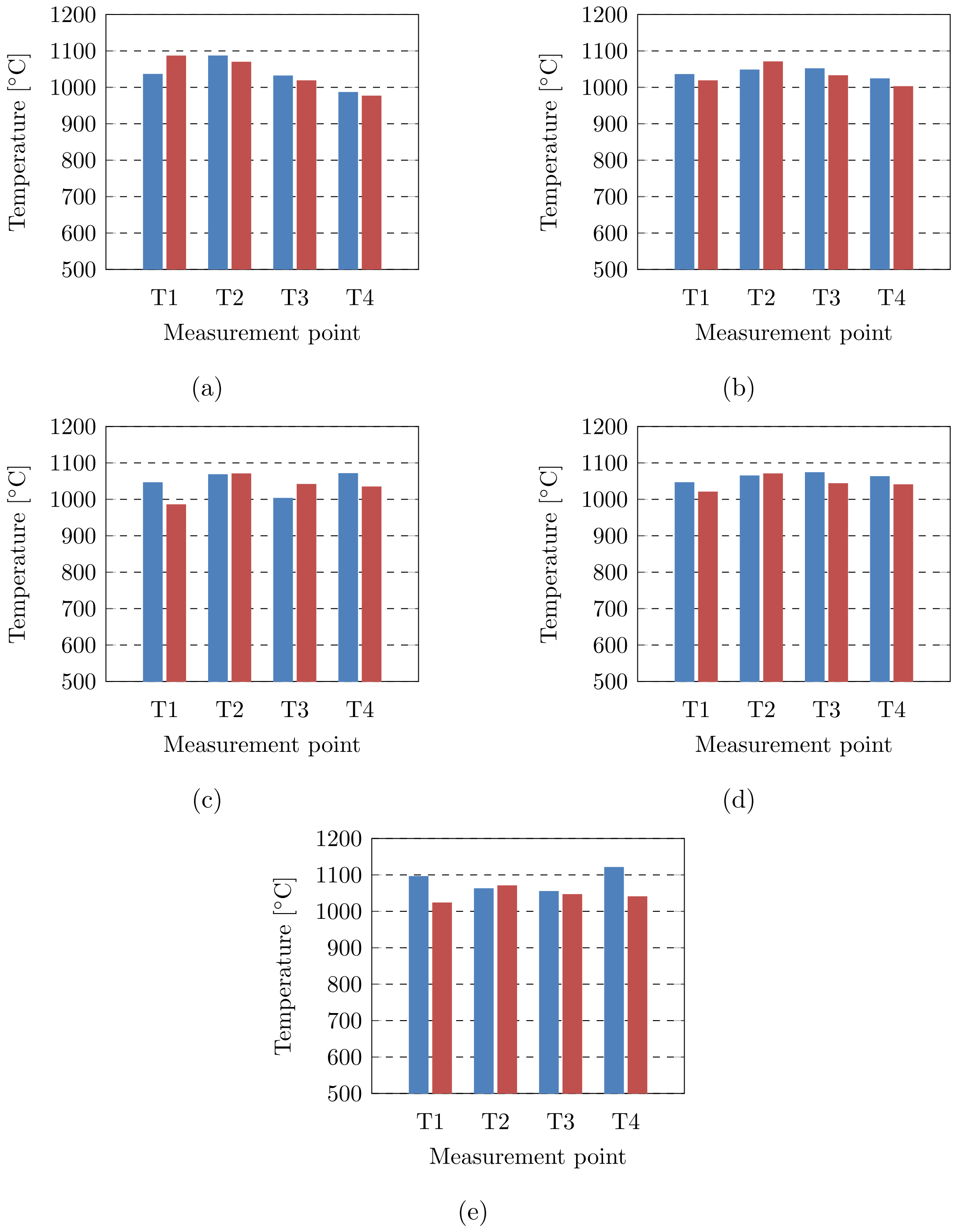

(a) (b) (c) (d) (e)

Figure 3.6.: Temperature comparison measurement (🟥)/CFD (SFM with skeletal25 🟦) for setup cooling plate only T=1070 °C: (a) 100 Vol% O_2; (b) 45 Vol% O_2; (c) 30 Vol% O_2; (d) 25 Vol% O_2; (e) 21 Vol% O_2 [1]

point is overestimated by the CFD simulation. This deviation between the measurements and the simulation was caused by air leaking in at the back of the furnace, which could not be prevented. The averaged error for all cases in Figure 3.6 is 24.5 K, which can be seen as sufficiently low for such high temperatures. Furthermore, the simulations predicted the temperature trends of the measurements well. Figure 3.7 shows the comparison between the measurements and simulation for the experimental setup with shielding and plate at the same temperature level of 1070 °C. The comparison again shows the same temperature trends as the measurements. Furthermore, it can be seen that the shielding leads to the hot zones, which occur above the shielding near the flame, being separated from the rest of the volume. Temperatures above the shielding are around 1070 °C; under the shielding, the temperatures are closer to 900 °C. The maximum error for these cases occurs at 25 Vol% O_2, at the measurement point P3, which is located under the shielding, with a value of 66 °C. The averaged error between simulations and experiments is 27 K for all cases and measurement points in Figure 3.7. Again, this is an acceptable degree of agreement between measurements and simulations for such high temperatures. For the temperature level of 1200 °C, the simulation was also able to well-predict the temperature trends of the measurements. For the experimental setup where the plate - without shielding - is inside the furnace, the maximum deviation between measurements and simulation was 104 K, and occurred at T4 for the case with 100 Vol% O_2. The leakage of air into the back of the furnace can again be seen as the reason for this deviation. The averaged error for all measurement points and O_2 enrichments is 43 K, which can be considered good agreement but, compared to the temperature level of 1070 °C, it is clear that the deviation has increased. For the setup where the plate and the shielding are inside the furnace at a temperature level of 1200 °C, the maximum error occurred at 30 Vol% O_2 at measurement point P3, with a value of 89 K. This measurement point is located under the shielding on the left wall. The average temperature deviation between the simulations and measurements for all measurement points and all O_2 enrichments is 28 K, which can again be deemed acceptable for such high temperatures. This comparison demonstrated that the temperature prediction of the SFM model with the detailed mechanism skeletal25 is sufficient for such high temperatures and setups. It is also possible to observe that the deviation increases with the temperature. However, the agreement between simulation and measurement is sufficient for these temperature levels.

Heat flux

Accurate prediction of the total heat flux is very important inside a furnace, especially in metal melting or reheating furnaces. The total heat flux on the plate is known from

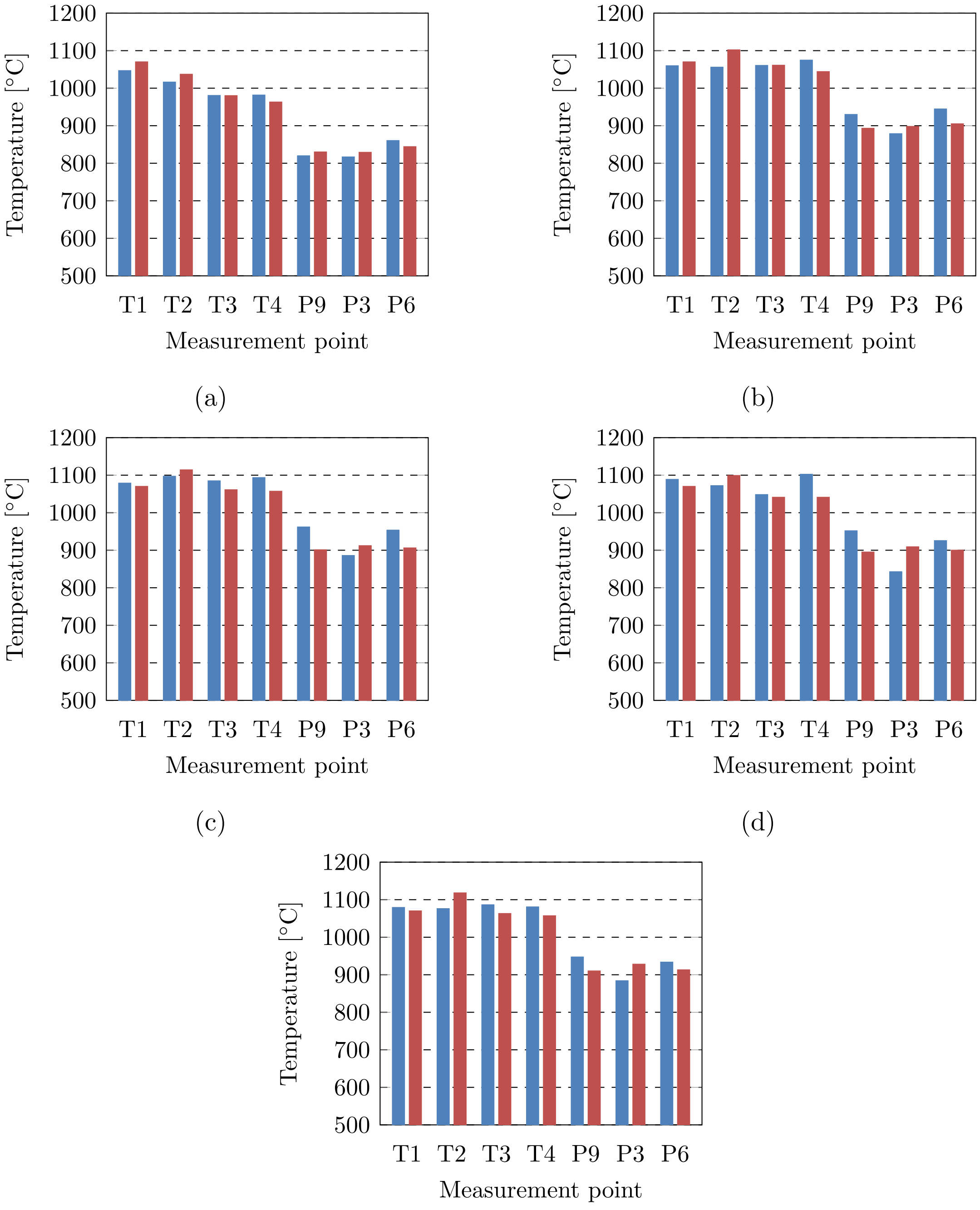

(a)

(b)

(c)

(d)

(e)

Figure 3.7.: Temperature comparison measurement (🟥🟥)/CFD (SFM with skeletal25 🟦🟦) for setup cooling plate only T=1070 °C: (a) 100 Vol% O_2; (b) 45 Vol% O_2; (c) 30 Vol% O_2; (d) 25 Vol% O_2; (e) 21 Vol% O_2 [1]

the experiments, where both in- and outlet temperatures as well as the mass flux of the water were measured. With this information, it is possible to calculate the total heat flux absorbed by the cooling plate. The radiation properties of the flue gas were predicted by the WSGGM model, using the coefficients from Smith et al. [98]. In Figure 3.8, the comparisons between measurements and experiments are depicted for the two different temperature levels and the two different experimental setups. In all cases, it can clearly be seen that, as the O_2 in the oxidizer increases, the fuel input decreases, whereby the decrease in the total heat flux is minor. Therefore, energy efficiency increases as the oxygen enrichment increases. Energy efficiency is defined as the fraction of the total heat flux to the plate $\dot{Q}_{tot,p}$ and the heat input of the fuel $\dot{Q}_{fuel}$ (see Eq. (3.1)).

$$\eta_{furnace} = \frac{\dot{Q}_{tot,p}}{\dot{Q}_{fuel}} \tag{3.1}$$

$$\varphi_{radiation,p} = \frac{\dot{Q}_{radiation,p}}{\dot{Q}_{tot,p}} \tag{3.2}$$

At a temperature level of 1200 °C, the furnace efficiency increases from 42% at 21 Vol% O_2 in the oxidizer to 65% at 100 Vol% O_2. At a temperature level of 1070 °C, the efficiency increases from 46% at 21 Vol% O_2 to 71% at 100 Vol% O_2. The furnace is more efficient at 1070 °C because the heat losses through the walls are smaller due to the lower temperature inside the furnace and the smaller mass flux of the flue gas. As the amount of oxygen in the oxidizer increases, the radiative heat flux to the plate also increases. For example, with the experimental setup with plate only, at a temperature level of 1070 °C, the percentage of the radiative heat flux $\dot{Q}_{radiation,p}$ on the total heat flux (see Eq. (3.2)) increases from 90% (21 Vol% O_2) to 95% (100 Vol% O_2). Comparison of the measurements and the simulations confirms that the heat flux trends can be predicted by the simulations. Furthermore, it is notable that the prediction of the heat flux is more accurate for lower temperature levels (1070 °C) than for higher temperature levels (1200 °C). The deviation between the measurements and the calculated solutions is in accordance with the investigation of Becher et al. [101]. In their investigation, they compared the WSGGM proposed by Smith et al. [98] with the very accurate LBL model, using the HITRAN2010 database. The comparison showed that, for a combustion atmosphere of natural gas with pure oxygen, the total emissivity calculated with the WSGGM had a maximum and minimum deviation from the LBL model of +16% and -8%, respectively, for a path length of 0.5 m, which corresponds to the path length of the lab-scale furnace. For this simulation, the maximum deviation of -12% between calculation and measurement is higher than that is accounted by Becher et al. This is because it was not possible to prevent air leaking into the furnace at 100 Vol% O_2 in the oxidizer. Additionally, the maximum temperature occurred in the furnace under 100 Vol% O_2 is with 2681 °C higher than the validity range given by Smith

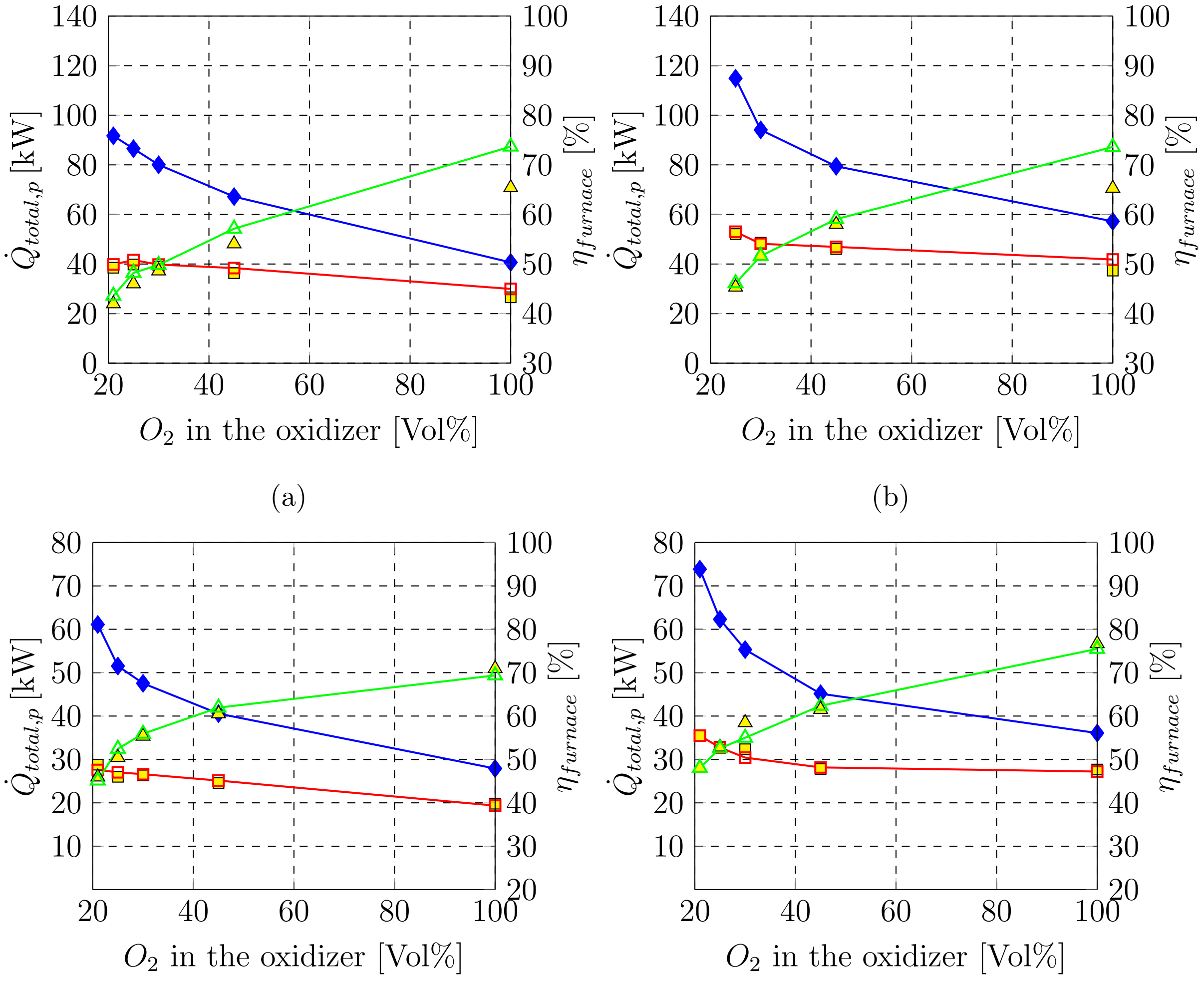

(a)

(b)

(c)

(d)

Figure 3.8.: Total heat flux to the plate for different oxygen concentration in the oxidizer; —◆— Fuel input; —□— Total heat flux to the plate (CFD, SFM with skeletal25); ■ Total heat flux to the plate (Measurement); —△— Efficiency (CFD, SFM with skeletal25); ▲ Efficiency (Measurement); (a) Plate and shielding T=1200 °C; (b) Plate only T=1200 °C; (c) Plate and shielding T=1070 °C; (d) Plate only T=1070 °C [1]

Table 3.4.: Breakdown of the total heat flux to the cooper plate into: gas, wall surface radiation and convection

	21 Vol% O_2	25 Vol% O_2	30 Vol% O_2	45 Vol% O_2	100 Vol% O_2
$\dot{Q}_{total,p}$ [kW]	35.48	32.74	30.42	28.16	27.21
$\dot{Q}_{conv,p}$ [kW]	3.46	3.09	2.28	1.75	1.42
$\dot{Q}_{rad\,total,p}$ [kW]	32.02	29.56	28.14	26.41	25.79
$\dot{Q}_{rad\,wall,p}$ [kW]	32.85	30.07	29.40	27.80	28.45
$\dot{Q}_{rad\,gas,p}$ [kW]	-0.83	-0.42	-1.26	-1.39	-2.66
$\dot{Q}_{rad\,wall,s2s}$ [kW]	32.8	30	29.79	27.76	28.2

et al. [98]. Furthermore, it is possible to note that the influence of the path length is insignificant for such small lab-scale furnaces, due to the fact that the errors between the experimental setup with and without shielding are nearly the same.

Comparison of gas and wall surface radiation[2]

In this section, the amount of gas and wall surface radiation on the total heat flux to the copper plate will be determined, using the method described in Section 2.5.4. The different heat fluxes calculated with this method are shown in Table 3.4. It is possible to see that convection has only a minor effect on the total heat flux, with a maximum of 3.46 kW for air-fuel conditions and a minimum of 1.42 kW under oxy-fuel conditions. The majority of the heat flux is transferred via radiative heat transfer. Splitting the total radiative heat flux ($\dot{Q}_{rad\,total,p}$) into solid body radiation ($\dot{Q}_{rad\,wall,p}$) and gas radiation ($\dot{Q}_{rad\,gas,p}$) reveals that nearly all of the radiative heat flux results from wall surface radiation. Even more significantly, the calculations show that the flue gas reduces the radiative heat flux from the walls. This means that without the flue gas and the same wall temperatures, more heat flux would be transferred to the plate. This was also verified by an additional calculation with the Surface to Surface Model (S2S) model ($\dot{Q}_{rad\,wall,s2s}$), which does not consider gas radiation in its calculations. Calculations using the S2S model showed similar heat fluxes due to radiation from the furnaces walls. Furthermore, the investigations show that the radiative heat flux from the furnace walls is reduced significantly as the oxygen concentration in the oxidizer increases. The reduction in the radiative heat flux from the furnace walls due to the flue gas occurs because the copper plate has a surface temperature of between 131 and 166 °C, which is relatively cold in comparison to the flue gas temperatures of over 1070 °C. The absorption coefficient of a flue gas consisting mainly

---

[2] Parts of this section have already been published in [5]

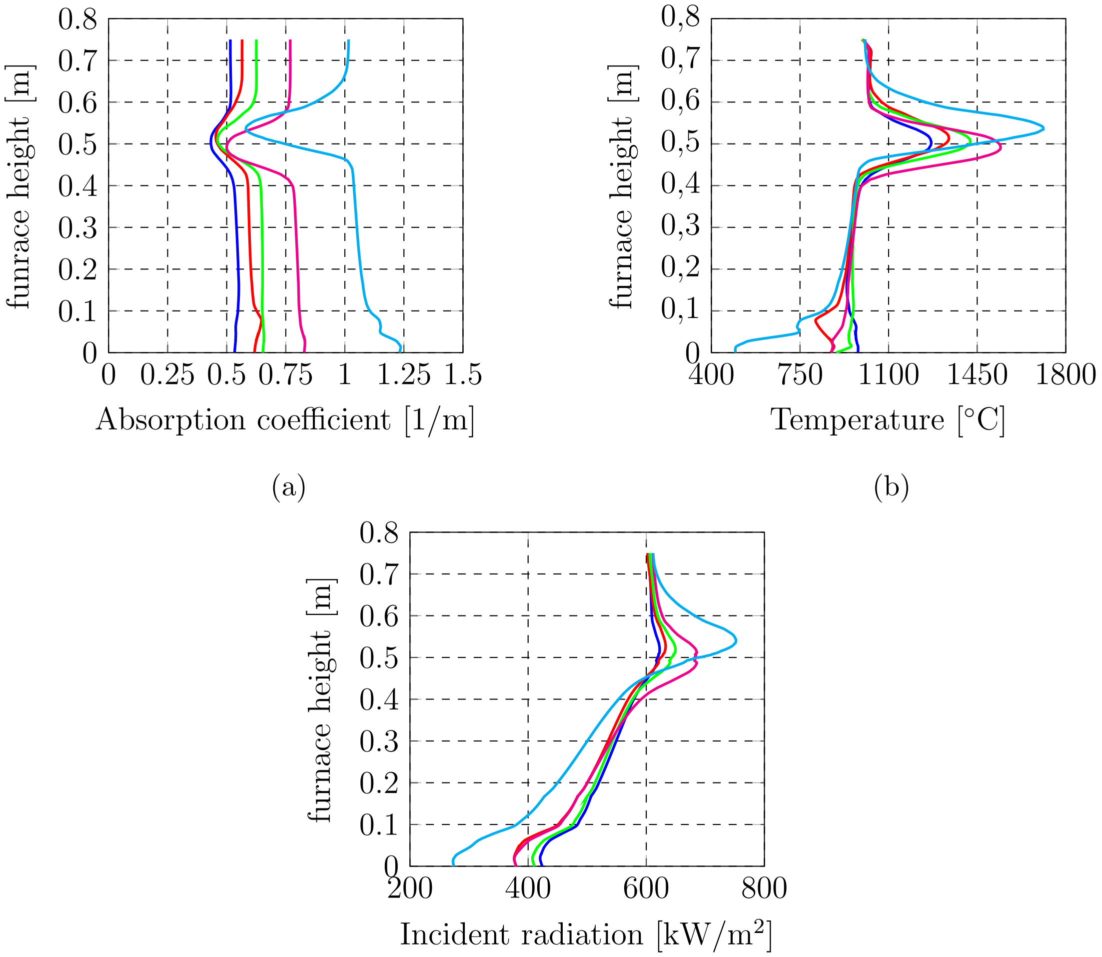

(a)

(b)

(c)

Figure 3.9.: Absorption coefficient (a), Temperature (b) and Incident radiation(c) for different oxygen concentration in the oxidizer in the lab scale furnace: 21 Vol% O_2 (——), 25 Vol% O_2 (——), 30 Vol% O_2 (——), 45 Vol% O_2 (——), 100 Vol% O_2 (——)

of CO_2 and H_2O has an inverse logarithmic dependency on the flue gas temperature [97]. This means that the absorption coefficient decreases as the gas temperature increases, and vice versa. Because of the low temperatures in the vicinity of the copper plate, the absorption coefficient is very high, and more of the radiative heat flux from the walls is absorbed by the flue gas. In Figure 3.9, the absorption coefficient, gas temperature, and the incident radiation are evaluated along the furnace height in the middle of the lab-scale furnace for the different oxygen concentrations in the oxidizer. The celling of the furnace is located at a height of 0.75 m and the bottom at 0 m. The burners are located at a height of 0.5 m. It can be clearly seen that the absorption coefficient of the flue gas is low when the flue gas temperature is high. Furthermore, the figure shows the influence of the oxygen concentration in the oxidizer on the absorption coefficient in the furnace. With increasing oxygen concentration in the oxidizer the absorption coefficient increases due to the higher concentration of CO_2 and H_2O. It can also be seen that with increasing oxygen concentration the maximum flue gas temperature increases and that the flue gas temperature near the plate (between furnace height 0 and 0.1 m in Figure 3.9b) becomes cooler. The reason for the lower flue gas temperature near the plate with a higher oxygen concentration is that the mass flux is also reduced, because N_2 is reduced with higher oxygen concentration. As a result the temperature of the flue gas near the copper plate is reduced further the higher the oxygen concentrations in the oxidizer, and this especially under oxy fuel conditions (100 Vol% O_2). Furthermore the influence of the thermal uplift can also be seen in Figure 3.9b. For oxygen concentrations of between 21 and 45 Vol% the maximum flue gas temperature occurs at a furnace height of 0.5 m, where the burners are located, under oxy fuel condition the maximum temperature was at 0.55 m. This is due to the thermal uplift, because under oxy fuel conditions the exit velocities of the burners are lower and the thermal uplift has a greater influence. With the low temperature near the plate and especially under oxy fuel conditions, the absorption coefficient increases drastically. In combination with the low temperature near the water cooled plate more radiative heat flux is absorbed by the flue gas components CO_2 and H_2O, and therefore lesser heat flux is transferred to the plate. This can also be seen in Figure 3.9c where the incident radiation is plotted along the furnace height for the different oxygen concentrations. In all cases the incident radiation becomes lower towards the furnace bottom. The reasons for this are the lower wall and the flue gas temperatures near the copper plate. The oxygen concentration also has a greater influence on the decline of the incident radiation towards the furnace bottom. As the oxygen concentration increases, the decline rate is also higher, reaching a maximum under oxy-fuel conditions, thus resulting in a lower radiative heat flux to the plate. In Figure 3.10, the incident radiation over the furnace height is displayed for oxygen concentrations of 21 Vol% and 100 Vol%. The incident radiation is shown with and without gas radiation for both oxygen concentrations. The maximum incident radiation with gas radiation under oxy-fuel conditions is significantly higher near the flame (at a furnace height of 0.5 m) than under air-fired conditions. Near the plate at the bottom of the furnace (furnace height 0-0.1 m), the incident radiation is higher under air-fuel conditions than under oxy-fuel conditions, due to the effects described above. Comparison of the incident radiation from wall surface radiation again shows that, under oxy-fuel conditions, the incident radiation at the bottom of the furnace would be higher than with gas radiation. This also means that the radiative heat flux to the plate would be higher without gas radiation. For air-fuel conditions, the same comparison between solid and gas radiation shows that, with gas radiation, the incident radiation is slightly higher than without gas radiation. The same investigation is performed in Section 4.1.5 and 4.3.4 for industrial scale furnaces.

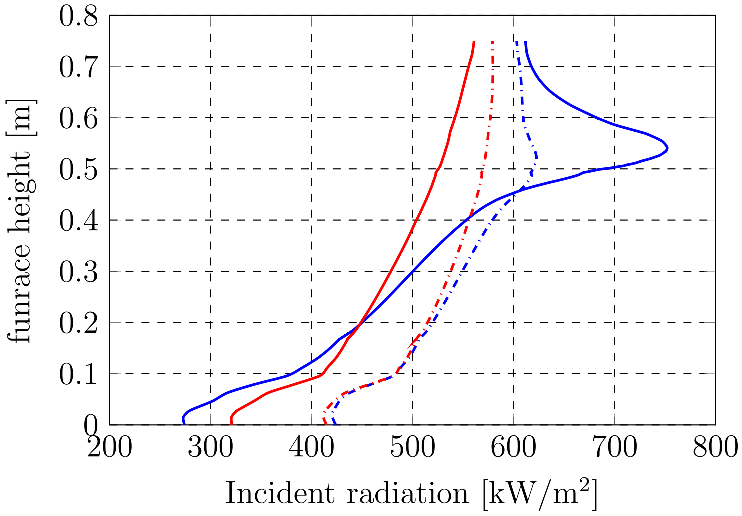

Figure 3.10.: Incident radiation from wall surface radiation for 21 Vol% O_2 in the oxidizer (-·-·-), Incident radiation from gas and wall surface radiation for 21 Vol% O_2 in the oxidizer (-·-·-), Incident radiation from wall surface radiation for 100 Vol% O_2 in the oxidizer (——), incident radiation from gas and wall surface radiation for 100 Vol% O_2 in the oxidizer (——)

3.1.5. Conclusion

Numerical investigations were conducted for a lab-scale furnace for two different experimental setups, two different temperature levels, and different O_2 concentrations in the oxidizer. The aim of these investigations was to use a detailed chemical mechanism capable of calculating OEC as well as air-fuel combustions. A further goal was to reduce the calculation time by using the SFM, which reduces the computational effort required for the chemistry integration. The EDC model with a 4-step mechanism, which has been widely used by other authors to simulate oxy-fuel combustions, was used as a benchmark in order to demonstrate the time-saving potential of the SFM approach. With the use of the SFM and the detailed mechanism skeletal25, the calculation time was reduced from 4 weeks with the EDC, to 4 days on an 8-core CPU. This significant reduction in time and computational costs makes this approach very interesting for the simulation of large furnaces. Using the SFM approach, it was possible to conduct simulations of the lab-scale furnace for O_2 concentration of between 21 Vol% and 100 Vol%, two temperature levels of 1070 °C, 1200 °C, and two experimental setups within a short period of time. The simulations were subsequently compared with temperature measurements taken from inside the furnace. The simulations and the measurements showed close agreement for the different O_2/N_2 ratios in the oxidizer. The averaged error for all measurement points for the different O_2 concentrations, experimental settings, and temperatures were between 24-43 K. This can be seen as an acceptable degree of agreement for high temperatures of between 1070 and 1200 °C. Furthermore, the total heat flux on a water-cooled plate was calculated using CFD and also these calculations were also compared with measurements. For the temperature level of 1070 °C, this comparison showed close agreement for the different O_2 concentrations in the oxidizer and experimental setups. For the temperature level of 1200 °C, the deviation between measurements and simulations was higher, especially for high oxygen concentrations in the oxidizer. Both the experiments and simulations showed that, as the O_2 concentration in the oxidizer increases, the efficiency of the furnace can be increased from 48% at 21 Vol% O_2 to 76% at 100 Vol% O_2, at a temperature level of 1070 °C. This demonstrates the potential of oxy-fuel or OEC to save fuel in furnaces with thermal loads.

This section has presented a novel CFD method to quantify the amount of wall surface and gas radiation on the total radiative heat flux to a load in a high temperature furnace under different oxygen enrichment conditions. To the best of our knowledge, this is a new finding. To determine the amount of wall surface and gas radiation, the RTE is calculated in an additional CFD calculation, where the absorption coefficient is set to zero, and all other conservation equations (energy, momentum,etc.) are frozen. An analysis of the lab-scale furnace with the method described above demonstrated that nearly all of the radiative heat flux to the load is emitted by the furnace walls (solid bodies), and only a minor part is emitted by the flue gas. Furthermore, the investigation revealed that as the oxygen enrichment in the oxidizer increases, the flue gas reduces the radiative heat flux from the walls, with a maximum reduction at 100% O_2. This is because the surface temperature of the copper plate is relatively cool (around 100 °C) in comparison to the temperature of the gas (around 1100 °C) in the furnace. This results in cooler flue gas temperatures near the plate than in the rest of the furnace. Due to the cooler flue gas temperatures, the absorption coefficient of the flue gas is higher near the plate than in the rest of the furnace. This is because the absorption coefficient of the flue gas increases as the gas temperature sinks. Additionally, the absorption coefficient of the flue gas increases as the oxygen concentration in the oxidizer increases due to the higher concentrations of H_2O and CO_2 in the flue gas. Furthermore, the mass flux, and, therefore, the velocity of the flue gas is lower under oxygen-enriched conditions, since less fuel is needed under oxygen-enriched conditions. Due to the lower velocities of the flue gas, the temperature of the flue gas is further reduced in the vicinity of the plate, which again results in the higher absorptivity of the flue gas for the reasons described above. The combination of these effects result in the radiative heat flux that is emitted from the furnace walls (solid bodies) being reduced by the flue gas, under oxygen-enriched conditions.

3.2. IFRF Furnace[3]

In this section, efficient numerical models are used for the simulation of the International Flame Research Foundation (IFRF) furnace, described in Section 3.2.1, in order to further validate these models for oxy-fuel conditions and to determine the limits of these models and the present operating conditions. Therefore, the different reaction mechanisms described in Section 2.4.4, are compared with both each other and experimental data. Additionally, different turbulence models and WSGGM coefficients are tested for these conditions.

3.2.1. Description of the IFRF Furnace

Together with industrial partners, the IFRF conducted the OXYFLAM project with the aim of gathering information about oxy-natural gas combustion [110]. The information gathered was used to optimize heat transfer and NOx-emission in oxy-natural combustion. One of the main objectives of the OXYFLAM project was to characterize oxy-natural gas flames of 1 to 2 MW of thermal input by means of detailed in-flame measurements. The measurements of the oxy-natural flame were performed on the horizontal IFRF furnace number 2, with two different configurations (OXYFLAM-1 and OXYFLAM-2). For the OXYFLAM-1 configuration, the furnace had bare walls, while in the OXYFLAM-2 configuration, a refractory lining was used. In both configurations, the furnace consisted of 13 water-cooled segments in which each of the elements was 300 mm wide. In the OXYFLAM-1 configuration, the thermal input was 1 MW and in the OXYFLAM-2 configuration, 0.78 MW. The lower heat input in the OXYFLAM-2 configuration was necessary in order to lower the temperature inside the furnace since the refractory lining reduced the heat losses to the atmosphere. Under both configurations, the furnace was operated at a pressure of 3 mm H_2O to prevent air leaking in. Further details regarding the furnace and the experiments conducted can be found in Lallemant et al. [110] and in Lallemant et al. [111].

In this thesis, the OXYFLAME-2 configuration was chosen as a test case. In that configuration, the furnace had a cross-section of 1.05 x 1.05 m and a length of 3.44 m (internal length), this corresponds to a path length of 0.86 m. Figure 3.11 shows a schematic drawing of the furnace. On the side wall of the furnace, there is a 1.7 m long slot, starting at the burner outlet. This slot is used to insert measurement equipment. In the rear part of the furnace, slots in the middle of each element provide access to the burner chamber. The

---

[3] Parts of this section have already been published in [2]

Table 3.5.: Operating conditions IFRF furnace [2, 40, 110]

Natural gas		Oxygen	
Mass flow [kg/h]	Temperature [°C]	Mass flow [kg/h]	Temperature [°C]
63	25	224.5	25

Table 3.6.: Fuel composition IFRF furnace [2, 40, 110]

Species	CH_4	C_2H_6	C_3H_8	C_4H_{10}	C_5H_{12}	CO_2	N_2	O_2
Natural gas composition in Vol%	86	5.4	1.87	0.58	0.14	1.79	4.01	0.21

burner is designed as a simple pipe-in- pipe burner. The NG was supplied by a 16 mm tube. Oxygen was fed through an annulus tube into a combustion chamber with an inner diameter of 28 mm and an outer diameter of 36 mm. The operating conditions of the IFRF furnace can be seen in Table 3.5. The NG used in the experiments consisted primarily of CH_4 (see Table 3.6), and the oxygen was of 99.9% purity [110].

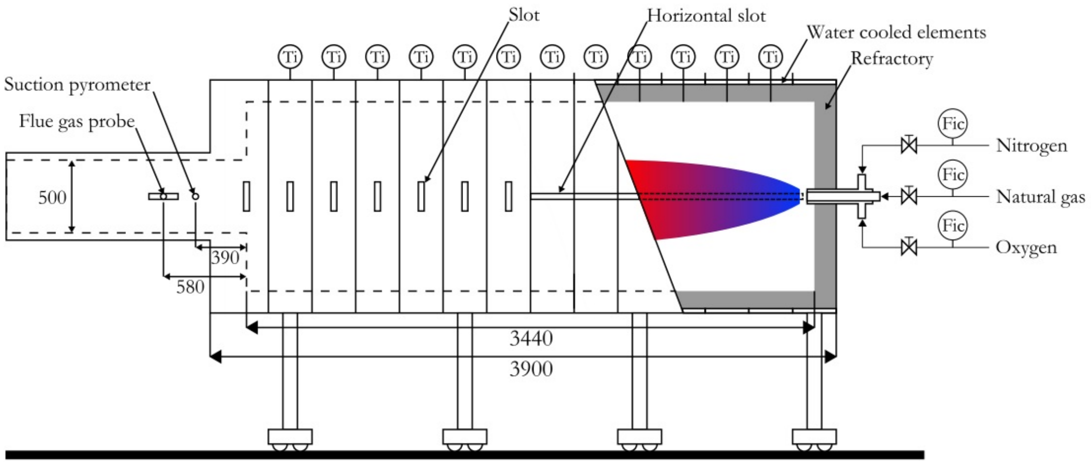

Figure 3.11.: Cross section of the IFRF furnace OXYFLAM-2 [110] [112]

Measurements

The following measurements are based on Lallemant et al. [110], Lallemant et al. [111] and Lallemant et al. [113], where more information about these measurements can also be found. On the side and top walls of the furnace, the wall temperatures were measured by 15 type B thermocouples along the axial distance of the burner (see Figure 3.11). The measurements revealed that the temperature of the top wall was 170 °C higher than the temperature of the side walls. This is due to the thermal uplift of the flame. At four positions along the burner axes (at 0.22, 0.82, 1.42 and 2.21 m downstream of the burner), detailed in-flame measurements for velocity, velocity fluctuation, temperature, and volume fraction of CH_4, O_2, CO, H_2, N_2, CO_2, NO and NOx were performed. The measurements were made from the centre line up to a radial distance of 0.45 m, at intervals of 0.01 m near the centre line, and 0.05 m at a radial distance of 0.45 m. The velocity in the burner chamber was measured by means of Laser Doppler Velocimetry (LDV). As seeding for the LDV, zirconium oxide particles were used, with a size range of 2-8 µm. The in-flame temperature measurements were performed with a water-cooled double venturi suction pyrometer equipped with a type B thermocouple. Due to the cooling of the pyrometer, the gas temperature dropped before the thermocouple. Hence, the pyrometer was calibrated with Coherent Anti-Stokes Raman Spectroscopy (CARS) temperature measurements. The measurements presented in Lallemant et al. [110] are not correct. Bollettini et al. [114] presented corrected temperature measurements, and these measurements were used for comparison in this thesis. Bollettini et al. [114] also stated that the double venturi suction pyrometer is difficult to use, and that the accuracy of the pyrometer is difficult to estimate. The gas species were measured by means of a gas sampling probe, a Non Dispersive Infrared (NDIR) sensor, Electron Paramagnetic Resonance (EPR) spectroscopy, chemiluminescence or Flame Ionization Detector (FID), depending on the species to be determined. Further information about the measurement techniques used can be found in Lallemant et al. [113].

3.2.2. Boundary Conditions

For the furnace simulation, pure methane was used as fuel. The methane mass flow was adapted to 55.42 kg/h in order to reach the same heat input as in the experiment (see Section 3.2.1). The fuel and the oxidizer streams were modelled as mass-flow inlets. The turbulent intensity was set to 20%. The high inlet turbulent intensity of 20% for the IFRF furnace was used because it was also used by the researchers of the IFRF [115] [114]. Additionally, the furnaces was calculated as having a turbulent intensity of 5%. The calculation showed that the inlet turbulent intensity has negligible impact on the solution. At the inlet of the fuel and the oxidizer, a turbulent velocity profile ($1/7^{th}$ power velocity profile law) was defined via a user-defined function in order to ensure that the flow is fully developed before it reaches the chamber. The inlet temperatures for the fuel and the oxidizer were set to 25 °C. The simulation of the IFRF was carried out with an equivalence ratio of 0.9871. That means that the furnace was operated under slightly fuel-lean conditions. The wall temperature of the IFRF-furnace was given by a function, which can be seen in Table 3.7. The numerical settings and the under-relaxation factors used for the simulations can be found in Appendix B.2.

Table 3.7.: Boundary condition for the IFRF furnace [2]

Mass flow-rate CH_4 [kg/h]	55.42
Mass flow-rate O_2 [kg/h]	224.49
Wall temperature [K]	$T(x) = 1700.6 + 212.59x - 46.669x^2$ (x: axial distance from the burner wall, [m])
Radiation	
Internal emissivity	0.7

3.2.3. Computational Grid

For the CFD simulation, two meshes were generated: a coarse and a fine mesh. The coarse mesh consists of 1 million hexahedron cells with a maximum skewness of 0.56 and a minimal orthogonal quality of 0.81. The mesh is fine near the burner due to the high velocity, species, and temperature gradients. For the fine mesh, 2.5 million hexahedron cells were used to model a quarter of the furnace, with a maximum skewness of 0.56 and a minimum orthogonal quality of 0.62. The two different meshes can be seen in Figures 3.12 and Figure 3.13.

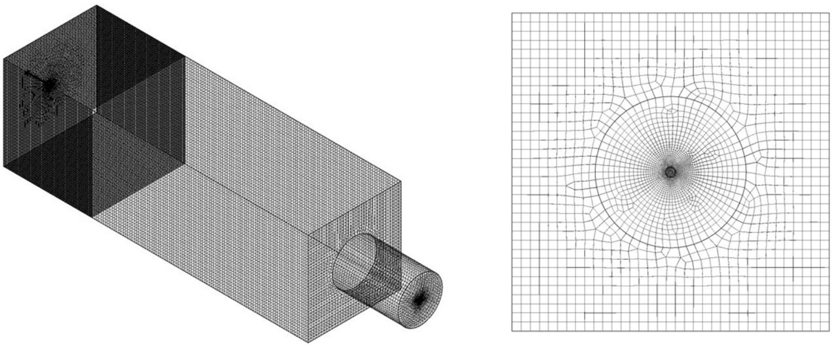

Figure 3.12.: Coarse mesh IFRF 0.8 MW [2]

3.2.4. Results and Discussion

Effect of the grid

Two simulations were carried out with the two different meshes in order to examine the grid independency of the solution for the IFRF furnace. The detailed mechanism (skeletal25) was used with the SFM approach for each of these simulations. The radiative properties of

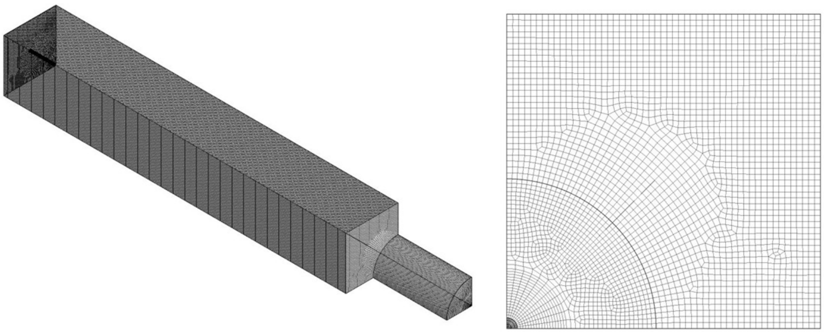

Figure 3.13.: Fine mesh IFRF 0.8 MW [2]

the flue gas were calculated with the WSGGM of Smith et al. [98]. The calculated volume fractions (dry) of CO_2, H_2, CO and O_2 for the different grid sizes are plotted in Figure 3.14 and were compared with the measurements. Figure 3.14 demonstrates that the size of the mesh has only a small influence on the solution. Therefore, the mesh with 2.5 million cells was used for all simulations of the IFRF 0.8 MW furnace.

Effect of combustion modelling

Three different models were used to calculate the chemistry turbulence interaction in the IFRF furnace: the EDM, EDC and the SFM models. For the EDM model, a simple 2-step mechanism [116] was used (see equation (3.3) and (3.4)). The EDC model used a refined version of the Jones and Lindsted 4-step mechanism [81]. The difference between the original JL 4-step and the refined mechanism is the use of the H_2 oxidation model proposed by Marinov et al. [82] in place of the reversible H_2 reaction in the original JL 4-step mechanism. This refined 4-step global mechanism has been used Yin et al. [40] and Kim et al. [109].

$$CH_4 + 1.5\,O_2 \longrightarrow CO + 2\,H_2O \tag{3.3}$$

$$CO + 0.5\,O_2 \longrightarrow CO_2 \tag{3.4}$$

Two detailed mechanisms, skeletal25 and smooke46, were used for the SFM model. Using the SFM, it was possible to reduce the calculation time from 4 weeks, with EDC, to 4 days on an 8-core CPU. The temperature profiles of the IFRF furnace for the different combustion models are plotted in Figure 3.15. It is possible to see that the shape of the flames from the EDC and the EDM models are quite similar. The major difference between these models is that the cold stream of CH_4 and O_2 extends further into the chamber with the EDC model. That means that the ignition of the CH_4/O_2 mixture is delayed. The SFM shows a totally different temperature profile than the EDC and the EDM. In Figure 3.15,

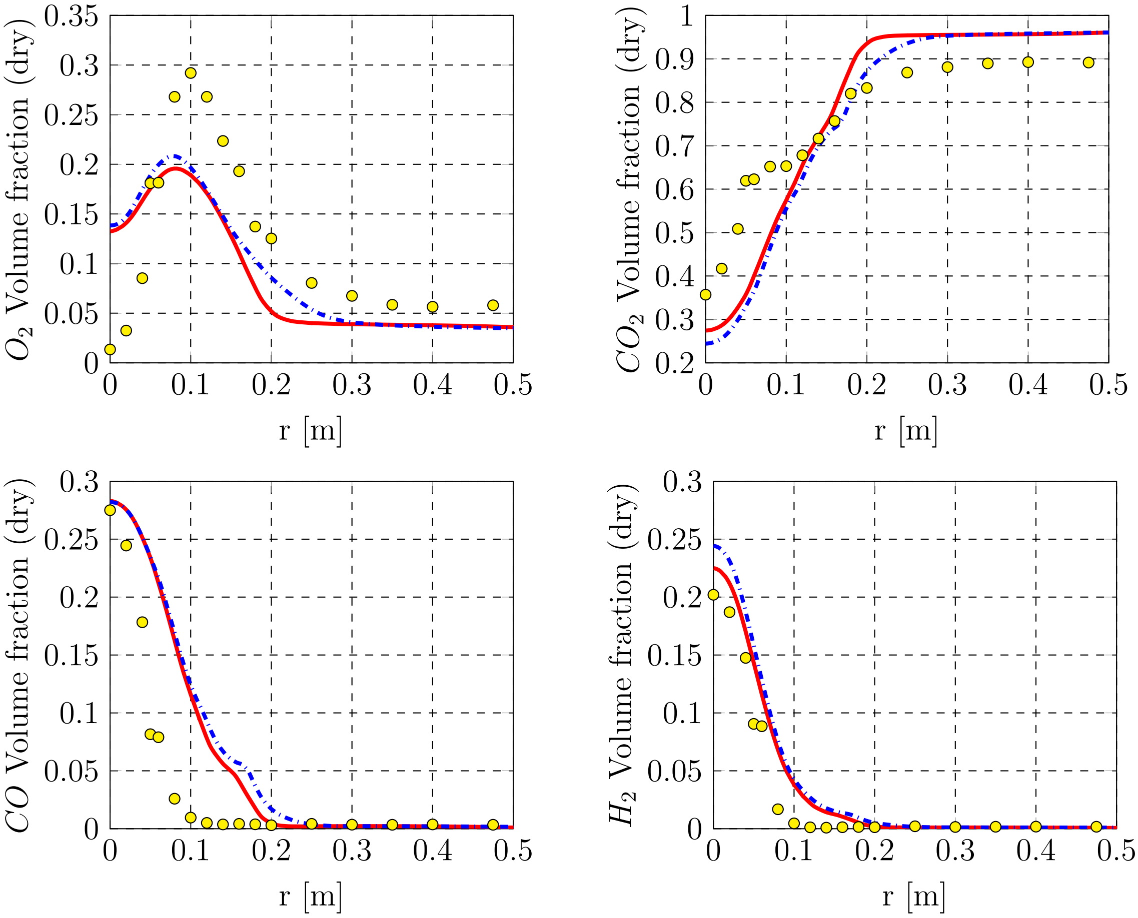

Figure 3.14.: Species predicted in the near-burner region (x=0.82 m) of the IFRF furnace for the fine and the coarse mesh: — coarse mesh, -·- fine mesh, ○ measurements [2]

it is possible to see that ignition of the CH_4/O_2 mixture is even more delayed than with the EDC model. That means that the mixing of the CH_4 and the O_2 stream is not good enough or cannot be calculated by the SFM. The shape and the temperature of the flame calculated by the SFM and the smooke46 mechanism are considerably different than those of the other models and mechanisms. The temperature calculated with the smooke46 is in a large area that is far too cold compared to the other simulations. The reason for the low temperatures is that, with the smooke46 mechanism, the ignition is even more delayed than with the skeletal25 mechanism; thus, the smooke46 mechanism is not suitable for oxy-fuel conditions [41]. To emphasise this fact, the different combustion models and mechanisms were compared with measurements at 0.22, 0.82 and 1.42 m from the burner in Figure 3.16, which shows that the EDM strongly overestimates the temperature at all measured lines. This was expected since the EDM is limited to using a 2-step mechanism, which is not able to account for radical formations or dissociation. The EDC model predicts the temperature near the burner well (x=0.22 m), but overestimates the temperature at x=0.82 and 1.42 m. The SFM with the skeletal25 mechanism underestimates the temperature near the burner and at x=0.82 m due to delayed ignition. The temperature calculated by the SFM at x=1.42 m is overestimated, but in the same range as the EDC. The SFM with the smooke46 mechanism underestimates the temperature at x=0.22 m in the same range as the SFM with the skletal25 mechanism. The temperatures calculated at x=0.82 and 1.42 m are nearly 1000 K lower than the measured temperatures. This indicates that ignition is delayed, and that the mechanism is not suitable for oxy-fuel combustion. In Figure 3.17, the species calculated by the different combustion models and mechanisms are

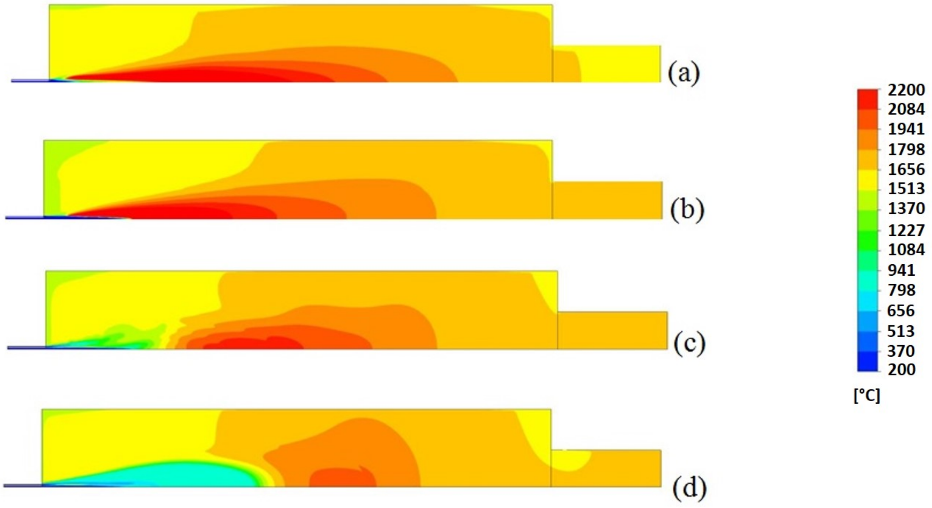

Figure 3.15.: Temperature profiles of the IFRF furnace for different combustion models; (a) EDM; (b) EDC; (c) SFM skeletal25; (d) SFM smooke46 [2]

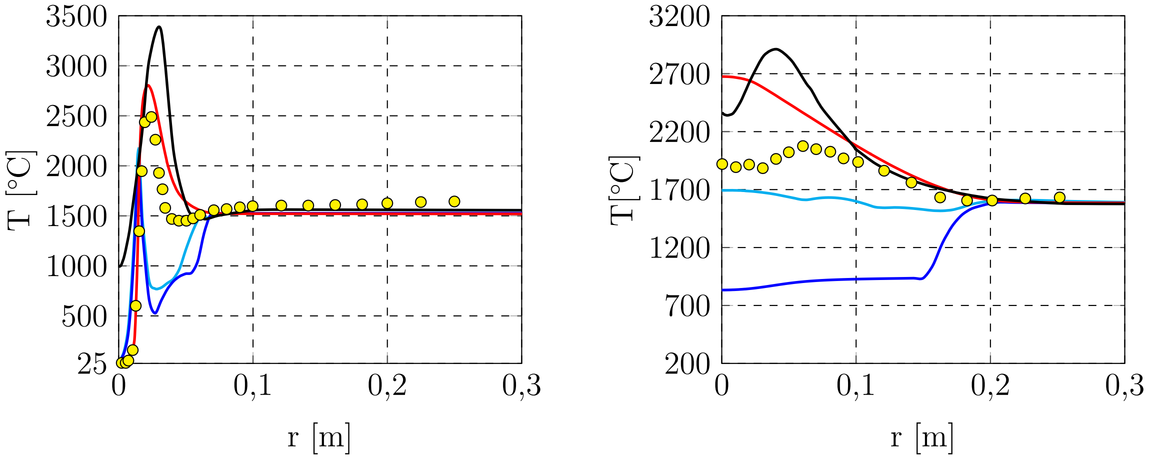

(a) Temperature at x=0.22 m

(b) Temperature at x=0.82 m

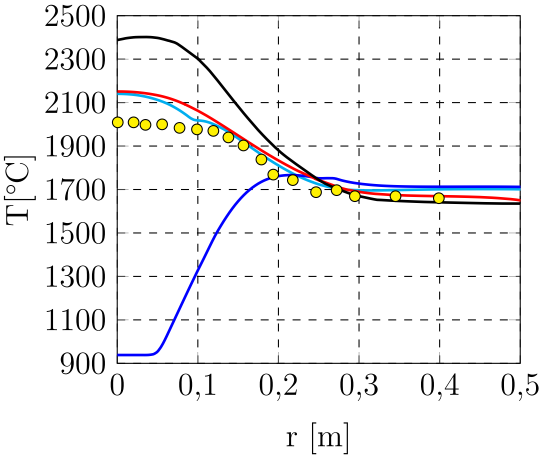

(c) Temperature at x=1.42 m

Figure 3.16.: Comparison of the temperature predicted by different combustion models in the IFRF furnace; EDC —; SFM skeletal25 —; SFM smooke46 —; EDM —; Measurements ● [2]

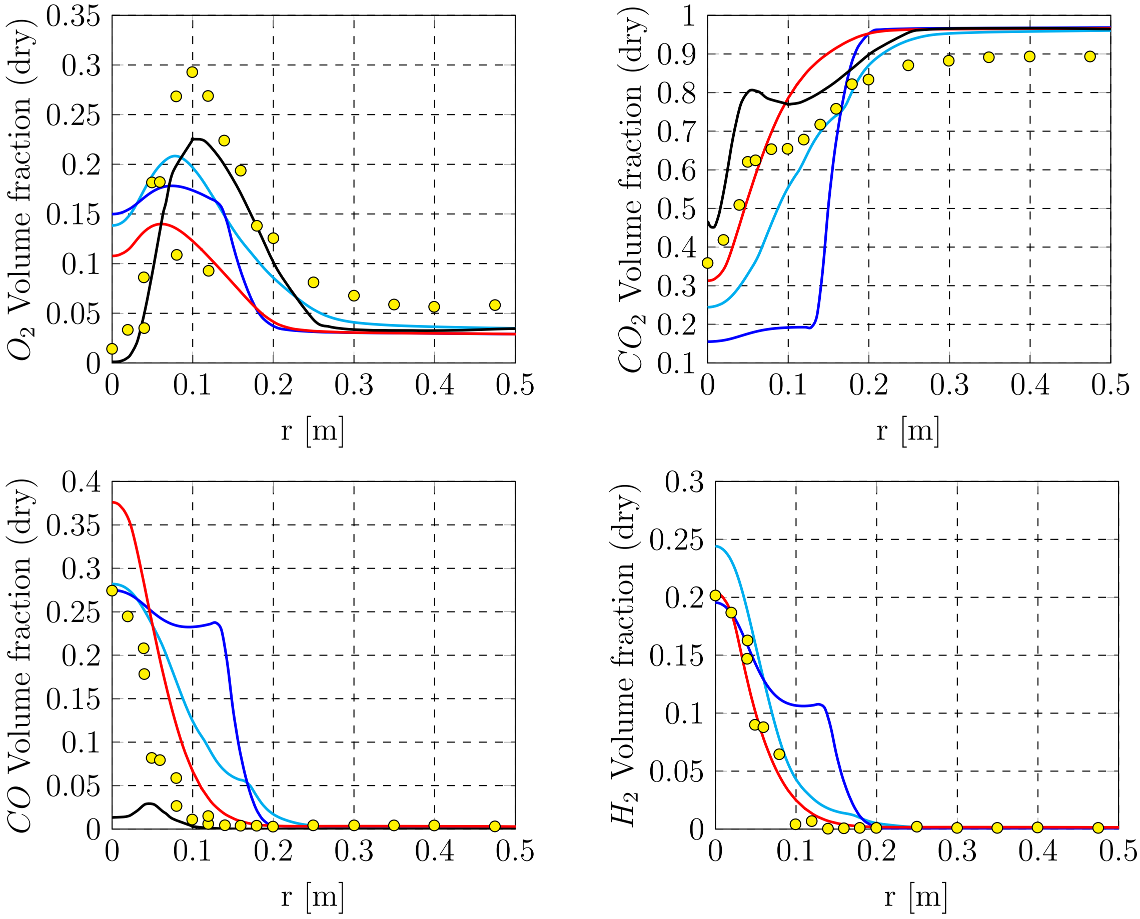

Figure 3.17.: Comparison of different species predicted by different combustion models in the IFRF furnace (at x=0.82 m): EDC —; SFM skeletal25 —; SFM smooke46 —; EDM —; Measurements ○ [2]

plotted against the results of the measurements. It is possible to see that the SFM with the smooke46 mechanism clearly fails to predict the CO_2 and the CO concentration in the IFRF furnace, which indicates once again that this mechanism is not suitable for simulating oxy-fuel combustion. The EDM also clearly fails to predict the CO concentration. The SFM with the skeletal25 mechanism is able to predict the trends of the different species in the same way as the EDC model. The measured values plotted are values averaged over 60 seconds. The gas analysers had an accuracy of 0.5% for the species CO, CO_2, O_2 and H_2. The sum of all measured species was between 97 and 108%, which indicates the high quality of the measurements [110]. The simulation of the VO2 furnace with the SFM and the skeletal25 showed a different flame shape compared to the IFRF furnace. The temperature profile of the VO2 furnace calculated by the SFM is plotted in Figure 3.18. There, one can clearly see that the ignition is not delayed, as in the simulation of the IFRF furnace. In Figure 3.19, that simulation is compared with measurements, and it is possible to see that the results are in good agreement with each other. The maximum temperature

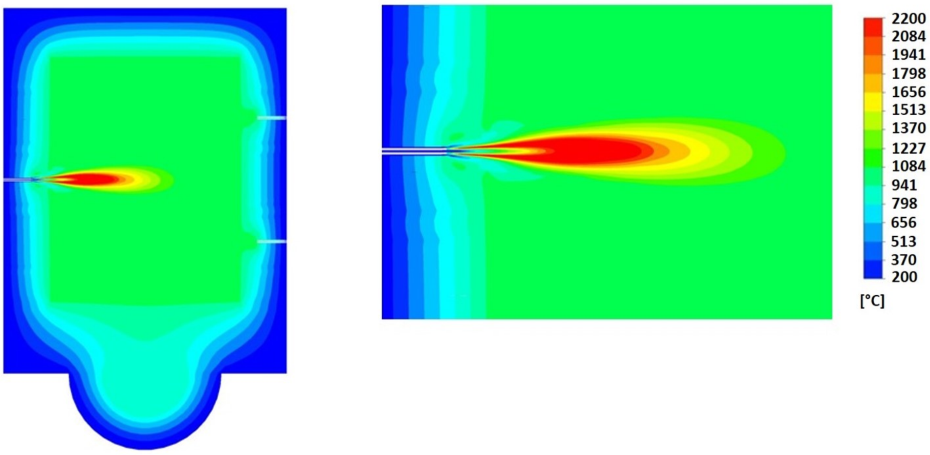

Figure 3.18.: Temperature profile of the VO2 calculated with the SFM and the skeletal25 [2]

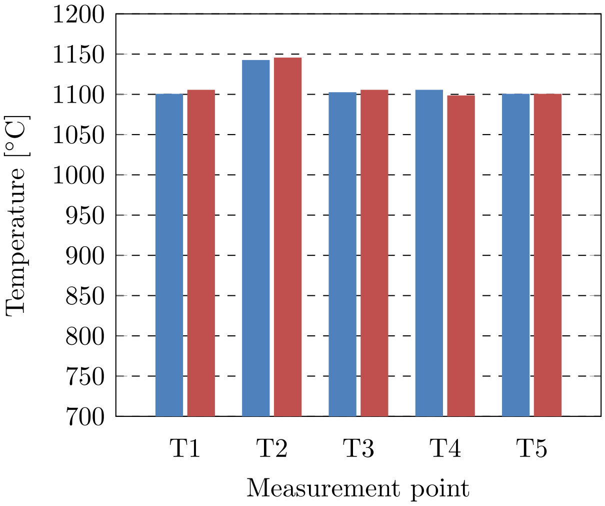

Figure 3.19.: Comparison between measurements and simulation of the VO2 furnace [2]

of 1142 °C was measured at T2, which is directly above the flame. The simulation shows only a 5 K deviation from the maximum temperature measured. Between T1 and T2, a difference of 43 K was measured. In the simulation, the temperature difference between T1 and T2 was calculated as being 41 K. The error of the thermocouples for this temperature range is thus 2.8 K. Furthermore, comparison shows that the computational model and the measurements are in good agreement for all points, and show the same temperature trends. This indicates that the SFM with skeletal25 works well for simulations of oxy-fuel combustion. However, the question remains as to why the SFM works for the VO2 furnace and not the IFRF furnace. The velocity profiles of the different furnaces are plotted in Figure 3.20. There, it is possible to see that, in the VO2 furnace, the velocity difference between the O_2 stream and CH_4 is far higher than in IFRF furnace. In the IFRF furnace, the O_2 and the CH_4 stream have nearly the same velocity. The fraction of the O_2 velocity to the CH_4 velocity is 0.21 in the VO2 furnace, whereas the velocity fraction in the IFRF furnace is 1.01, indicating that there is nearly no velocity difference between the O_2 and CH_4 stream in the IFRF furnace. Hence, with regard to the small shear rate between these two streams, the mixing is bad and cannot be calculated by the SFM approach. The strain rats for the two furnaces are plotted in Figure 3.21. This figure shows that the strain rate for the IFRF furnace is very high near the burner, but then decreases rapidly until there is hardly any strain rate between the O_2 stream and the CH_4 stream. This indicates that the mixing of the two streams is poor. In the VO2 furnace, the strain rate between the O_2 stream and CH_4 stream is also high at the beginning, but it does not decrease as fast as in the IFRF furnace. To improve the mixing between the two streams, the O_2 inlet in the IFRF furnace could be modified by changing the diameter in order to get the same velocity fraction of 0.21 as in the VO2 furnace. The calculations show a very similar flame shape to that of the VO2 furnace, as depicted in Figure 3.22. The SFM is able to calculate flames with high shear rates between the O_2 and CH_4 streams in good accordance with the measurements, but, if the shear rates are too low, the SFM fails to predict the temperature profile and the shape of the flame.

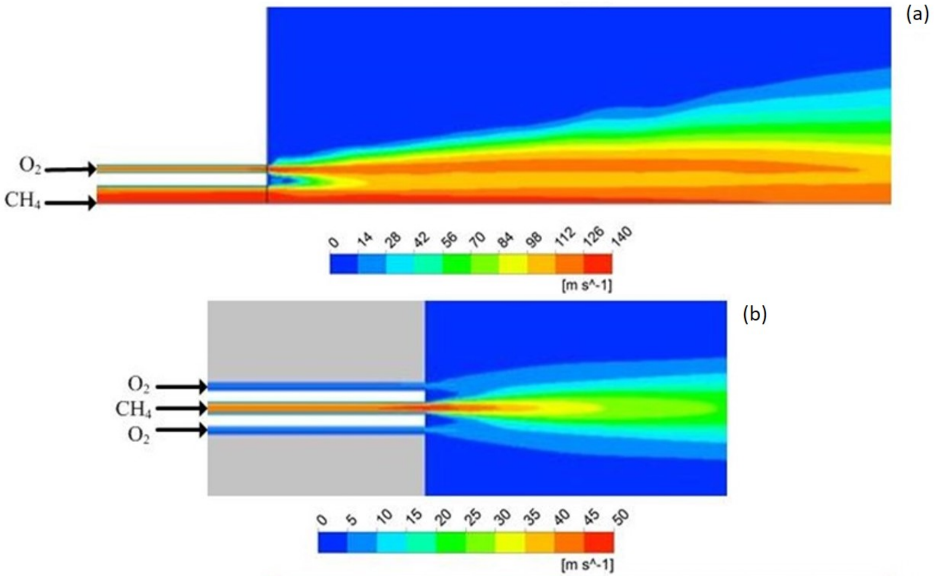

Figure 3.20.: Velocity magnitude calculated with the SFM (a) VO2-furnace (b) IFRF furnace [2]

Effect of turbulence modelling

To evaluate the influence of the turbulence model, further simulations of the IFRF were conducted, using three different turbulence models. These turbulence models are: the realizable k-ϵ (RKE), the standard k-ϵ (SKE) and the RSM. The results of the simulations

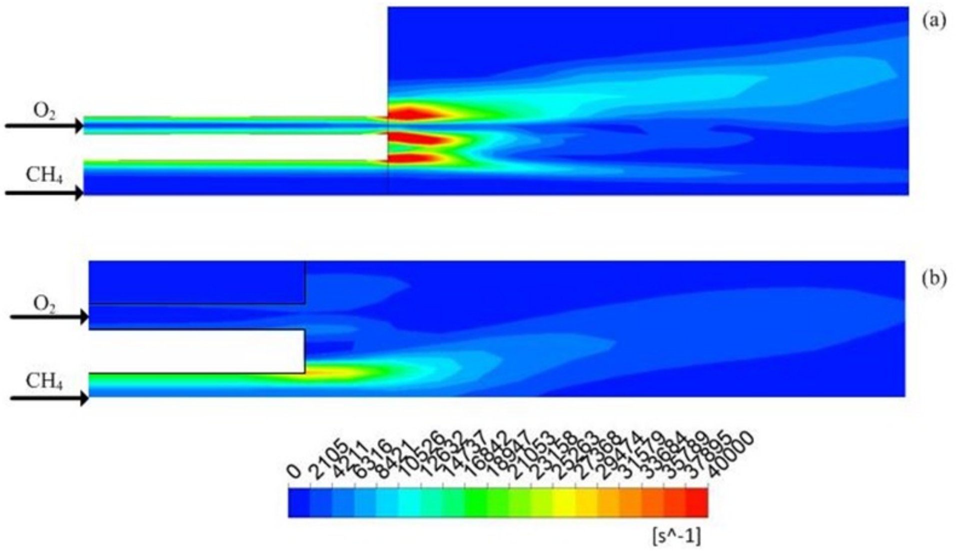

Figure 3.21.: Strain rate at gases inlet for the (a) IFRF furnace and the (b) VO2 furnace [2]

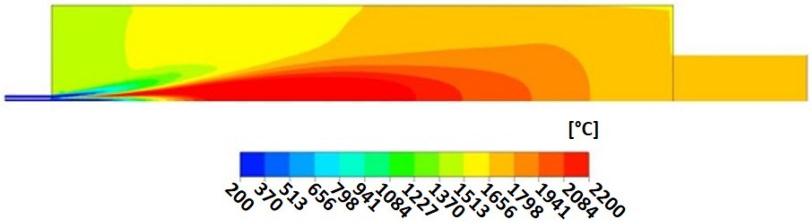

Figure 3.22.: Temperature profile of the IFRF furnace for a velocity ratio of 0.21 between the O2 and CH4 stream. [2]

with the SFM, the skeletal25 mechanism, and the different turbulence models are plotted in Figure 3.23. It is possible to see that, near the burner (x=0.22 m), the turbulence models have only a small influence on the solution, and the profiles are rather similar. At x=0.82 m, the SKE and the RSM improve the solution, but the temperatures are still too low. At x=1.42 m from the burner, the difference between the turbulence models is negligible. In Figure 3.24, the temperature plot of the IFRF furnace as calculated by the RSM and the SKE is shown. The shapes of the flame with the SKE and RSM are not considerably different than the shape calculated by the RKE.

Effect of radiation modelling

The DO was applied to solve the RTE in all cases. The radiative properties were calculated with the WSGGM, for which coefficients from three different authors were used. These included the coefficients of Smith et al. [98], Yin et al. [100] and Kangwanpongpan et al.

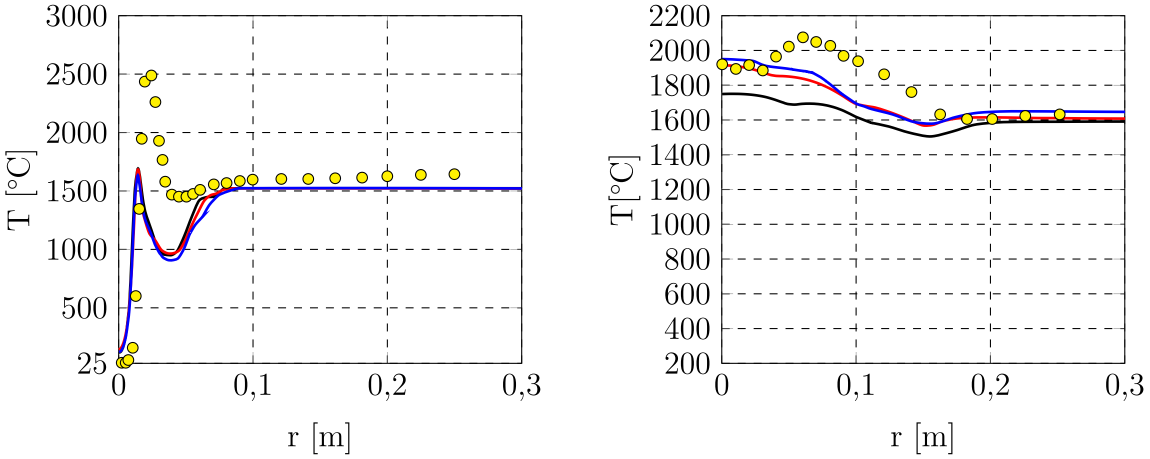

(a) Temperature at x=0.22 m

(b) Temperature at x=0.82 m

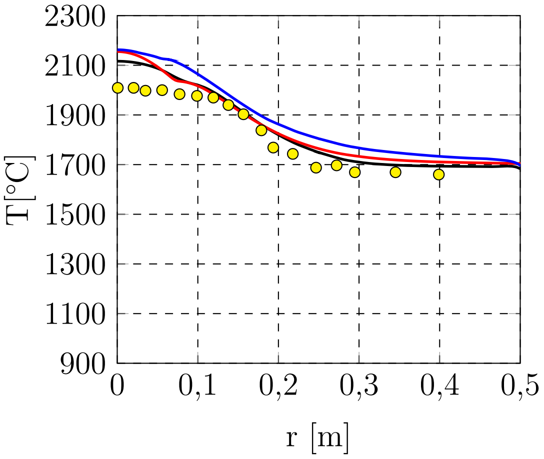

(c) Temperature at x=1.42 m

Figure 3.23.: Temperature predicted in the IFRF furnace by the SFM with skeletal25 and different turbulence models; RKE —; SKE —; RSM —; Measurements ● [2]

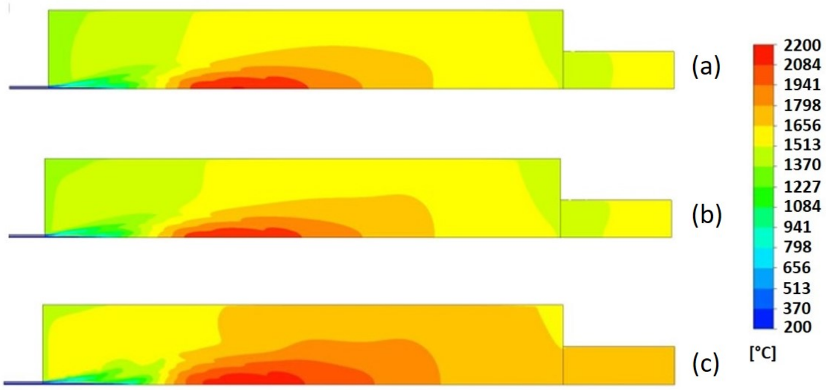

Figure 3.24.: Temperature profiles of the IFRF furnace calculated by the SFM with (a) RSM and (b) SKE. [2]

[102]. The coefficients from Yin et al. and Smith et al. were derived from the EWB model, with the difference that the coefficients of Yin et al. have a broader validation range. The WSGGM from Smith et al. is valid for a H_2O/CO_2 ratio of 1 and 2, path lengths of up to 10 m, and for temperatures between 600 and 2400 K. In comparison, the WSGGM from Yin et al. is valid for H_2O/CO_2 ratios between 0.125-4, and path lengths up to 60 m. Kangwanpongpan et al. derived the coefficients for the WSGGM from the highly accurate LBL (HITEMP2010) model. This WSGGM is valid for H_2O/CO_2 ratios between 0.125-4, and a maximum path length of 60 m. Unfortunately, Kangwanpongpan et al. did not derive coefficients for negligible H_2O and CO_2 concentrations arising near the burner. Therefore, the coefficients from Yin et al. were used. The three WSGGMs were implemented in the CFD code via User Defined Function (UDF). The temperatures calculated with the SFM, the skeletal25 mechanism, and the different WSGGMs are plotted in Figure 3.25. The figure clearly indicates that the different WSGGMs do not have any impact on the solution at all. This is because the beam length (about 0.8 m) of the IFRF furnace is too small to make a difference. The influence of the WSGGM is higher in furnaces with a longer beam length. Yin et al. [40] simulated a 609 MW utility boiler with a beam length of 11 m. They simulated the boiler with WSGGM coefficients from Smith et al. [98] and the coefficient from Yin et al. [100]. Their simulation showed that the absorption coefficient calculated by the two WSGGMs differs by about 120%, resulting in a temperature difference of 200 K.

3.2.5. Conclusion

In this section, the SFM approach was used with the skeletal25 and the smooke46 mechanisms in order to simulate a lab-scale furnace experimentally investigated by the IFRF.

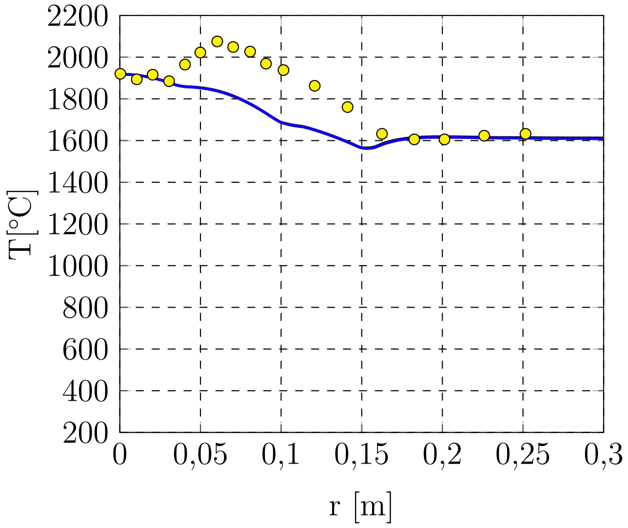

Figure 3.25.: Temperature profile in the IFRF furnace (x=0.82 m) calculated with the SFM and different WSGGM: Smith et al. [98] ——; Yin et al. [100] ——; Kangwanpongpan et al. [102] ——; Measurements ○ [2]

Furthermore, simulations of that furnace were conducted using the EDC and the EDM. The EDM used a simple 2-step mechanism, which highly overestimated the temperature in the furnace, due to its neglect of dissociation effects and radical formation, but did calculate the flame shape correctly. In the simulation with the EDC model, a 4-step mechanism was used, which showed good agreement with the measurements. However, the biggest drawback of the EDC is the long calculation time necessary, due to the computationally demanding chemistry integration. Therefore, it is difficult to simulate big furnaces with the EDC with reasonable accuracy in an appropriate amount of time. Use of the SFM reduced the calculation time from 4 weeks to 4 days on an 8-core CPU, and is therefore very interesting for simulations of large furnaces. In section 3.1, the SFM with the skeletal25 was shown to be in good accordance with the measurements, if the shear rate between the O_2 and CH_4 streams is high. The simulation and measurements deviated to a maximum of 5 K, which can be considered to be very good agreement for such high temperatures. When there is only small velocity difference between the O_2 and the CH_4 streams, resulting in a small shear rate, the SFM is neither able to predict the flame shape correctly, nor to predict the temperature. Simulations using the SFM with the smooke46 mechanism showed that the temperature in the furnace is highly underestimated; therefore, the smooke46 mechanism is not applicable for simulations of oxy-fuel conditions. The influence of the turbulence models on the solution with small shear rates and the SFM was also investigated. The standard k-ϵ, realizable k-ϵ and the RSM methods were used to evaluate the influence of turbulence. It was found that the impact of the different turbulence models on the solution is negligible, and that the turbulence models cannot improve the solution calculated with the SFM for small shear rates. Furthermore, the influence of the radiative properties on the solution was investigated by applying different WSGGMs from different authors. The simulations with the different WSGGMs showed that they have a negligible impact on the solution for such small furnaces, due to the small beam length, and a CO_2/H_2O fraction of 2 of the flue gas, due to the use of natural gas as fuel. These results show that the SFM can be used with the skeletal25 mechanism for oxy-fuel conditions with high shear rates, though it fails to correctly predict the flame shape for small shear rates.

3.3. Semi-industrial Furnace Burner Chamber[4]

The investigations in the previous sections of this chapter have established both the applicability and the limitations of the SFM with the skeletal25 reaction mechanism for jet flames under oxy-fuel and OEC conditions. This section will examine the applicability of the SFM for flat flame burners, which are commonly used in reheating furnaces, for different oxygen concentrations in the oxidizer. To this end, a semi-industrial furnace fired with a flat flame burner will be investigated by means of CFD simulations, and the results of these simulations will then be compared with experimental data.

3.3.1. Description Semi-industrial Furnace Burner Chamber

Subsequent experiments were performed on a natural gas fired semi-industrial furnace with a thermal input of 250 kW. This furnace was investigated for different oxygen enrichments in the oxidizer, ranging from 21 Vol% to 37 Vol%. The furnace is equipped with a flat flame burner, mounted at the front of the furnace. The internal dimensions of the furnace are 1.25 x 1.25 x 2.5 m, this corresponds to a path length of 0.9 m, and the chamber is surrounded by 0.2 m thick ceramic insulation. In Figure 3.26, the insulation and the position of the flat flame burner can be seen. Furthermore, the temperature measurement points (T1, T2, T3) are shown. The temperature measurements were carried out with three Type B thermocouples, which were encapsulated by ceramic material. The top-wall distance of the thermocouples was 60 mm. The first thermocouple (T1) was located 0.3 m, from the furnace door, the second thermocouple (T2) 0.97 m, and the third (T3) 1.47 m from the furnace door. The thermocouples were calibrated with a thermocouple calibrator (Fluke 714B), and additional reference measurements were made using a quotient pyrometer (Keller Optix Q PT70). The measurement uncertainties of the thermocouples are ±3.4 K

---

[4] Parts of this section have already been published in [4]

for temperatures above 1200 °C, which are typical temperatures encountered in the furnace. In addition to the gas temperature, the temperature of the quarl of the flat flame burner was also measured with a quotient pyrometer, from the opposite side of the furnace, where a window is located (see Figure 3.26). In Figure 3.27 shows the burner from the opposite side, as well as the different measurement points on the quarl.

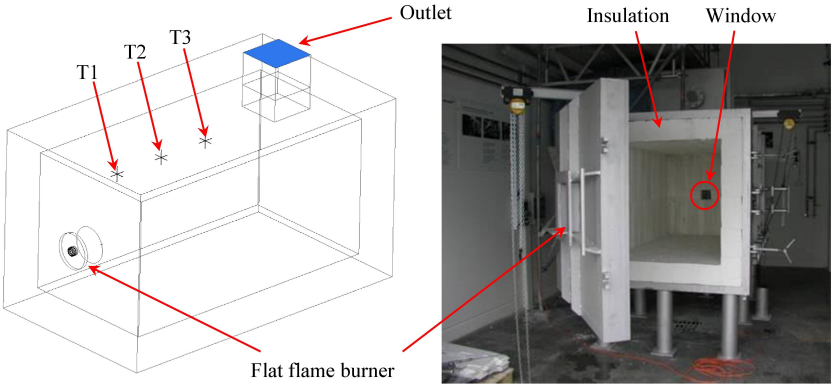

Figure 3.26.: 3D-model and picture of the Burner Chamber furnace [4]

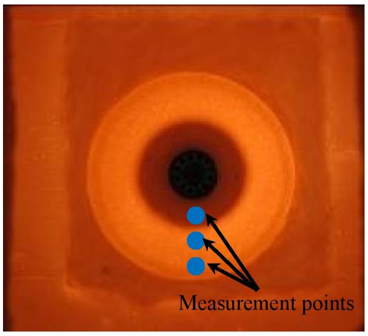

Figure 3.27.: Measurement points on the quarl of the Burner Chamber [4]

3.3.2. Boundary Conditions

For all simulated cases, pure methane was used as the fuel, and the oxidizer was a mixture of O_2, depending on the oxygen enrichment. All inlets in the simulations were modelled as mass flow inlets. The furnace was in operation during both the experiment and the simulations, under slightly fuel-lean conditions, with a fuel-oxidizer equivalence ratio of between 0.957 and 0.977, depending on oxygen enrichment. The temperatures of both fuel and oxidizer were set to 25 °C at the inlet, and the inlet turbulent intensity was set to 10%. The insulation of the furnace was modelled as solid, with a thermal conductivity of 1.25 W/(m K) and an emissivity of 0.95. At the outer wall, the heat transfer to the ambient was modelled as a convection boundary condition, with a free stream temperature of 25 °C and a heat transfer coefficient of 30 W/(m^2 K). The numerical settings and the under-relaxation factors used for the simulations can be found in Appendix B.3.

3.3.3. Computational Grid

In CFD simulations, the quality and the type of cells used for the computational mesh have a high impact on the resulting accuracy of the simulations. In this investigation, the furnace grid consists primarily of hexahedrons (fluid and solid) due to their good numerical properties. In the vicinity of the flat flame burner, the mesh consists primarily of tetrahedrons. The mesh used for the simulation is shown in Figure 3.28. The grid is composed of 2.2 million cells, with a maximum aspect ratio of 24 and minimum orthogonal quality of 0.24, which are sufficient for this investigation. A grid independency test was also performed with a grid consisting of 6.2 million cells.

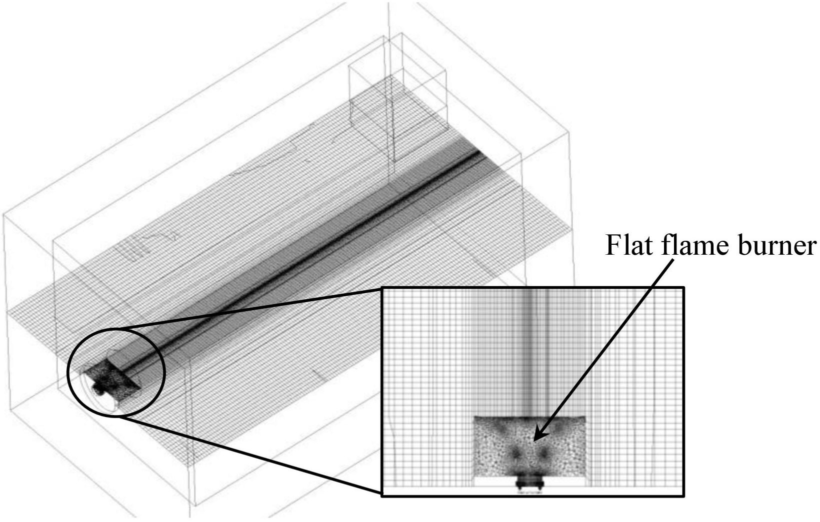

Figure 3.28.: Mesh of the investigated furnace burner chamber [4]

3.3.4. Results and discussion

Effect of the grid

Grid independency tests were performed in order to establish the extent of the influence of the grid on the solution. The simulations were carried out with two different grids: a coarse grid consisting of 2.2 million cells, and a fine grid of 6.2 million cells. The case with 21 Vol% oxygen in the oxidizer was used as a reference case. The results of the

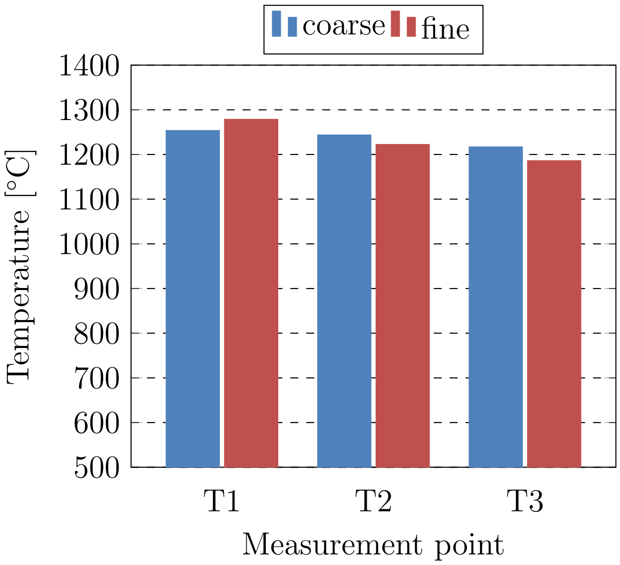

Figure 3.29.: Comparison between fine and coarse grid [4]

simulations with fine and coarse grids are shown in Figure 3.29. Comparison of the two grids shows that the difference between them is negligible. Thus, the coarse grid was used for all simulations.

Effect of combustion modelling

The SFM model was used to calculate the chemistry/turbulent interaction. Using the SFM model means that the calculation time can be dramatically reduced in comparison to calculations with the EDC model. Prieler et al. [41] and Mayr et al. [1] have shown that the SFM model makes it possible to reduce the calculation time from four weeks with the EDC, to four days with the SFM, even when a detailed mechanism is used. Furthermore, Prieler et al. [41] showed that not every detailed mechanism can be used with the SFM for the calculation of oxy-fuel jet flames. The investigation have shown, however, that the skeletal25 mechanism is applicable for all oxygen concentrations. This mechanism was thus also used for the investigation carried out in this section. The temperature plots calculated with the SFM and the skeletal25 mechanism for different ratios of oxygen and nitrogen, ranging from $21\%O_2$ to $37\%O_2$ are plotted in Figure 3.30. Additionally, the OH species are shown in Figure 3.31. It is possible to see that the flame of the flat flame burner is well-predicted by the SFM model with the skeltal25 mechanism for all oxygen enrichments. Furthermore, the temperature plots show that the flat flame burner is slightly too big for the chamber used because the flame is deflected at the side walls. It can also be seen that the maximum temperature of the flame inside the furnace increases as the oxygen concentration in the

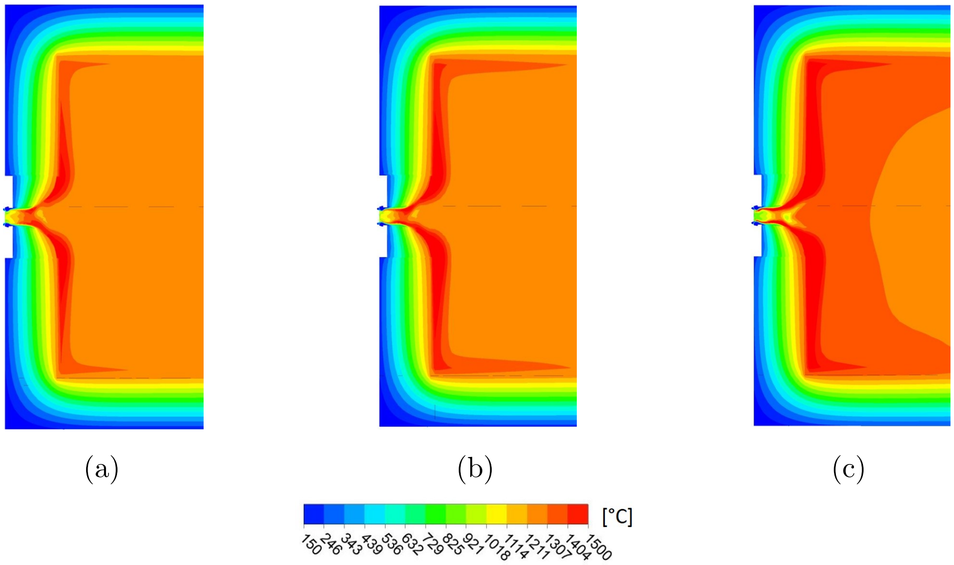
(a) (b) (c)

Figure 3.30.: Temperature contours for different oxygen concentrations (a) 21 Vol% O_2; (b) 24.5 Vol% O_2; (c) 37 Vol% O_2 [4]

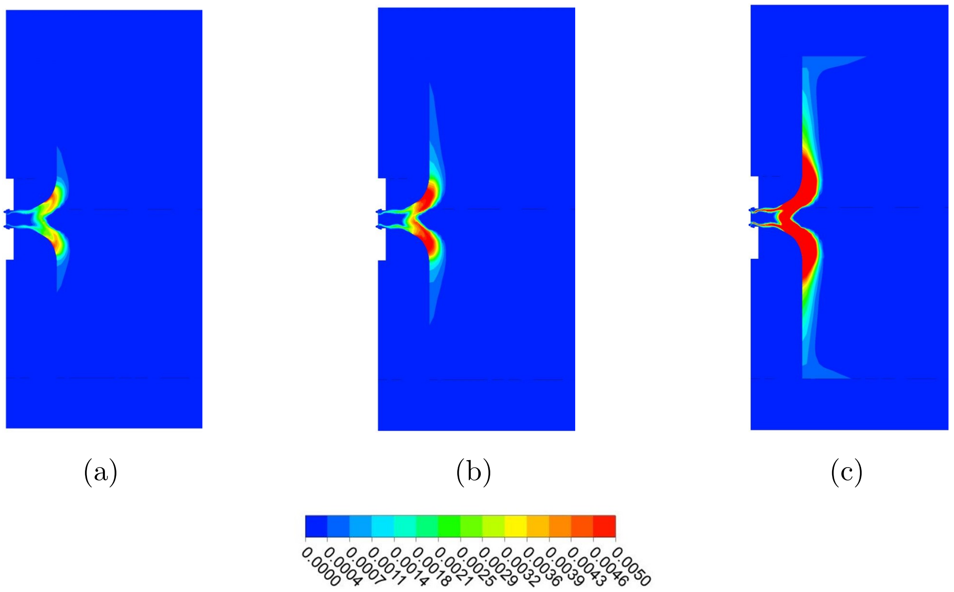
(a) (b) (c)

Figure 3.31.: OH-Volume fraction for different oxygen concentrations (a) 21 Vol% O_2; (b) 24.5 Vol% O_2; (c) 37 Vol% O_2 [4]

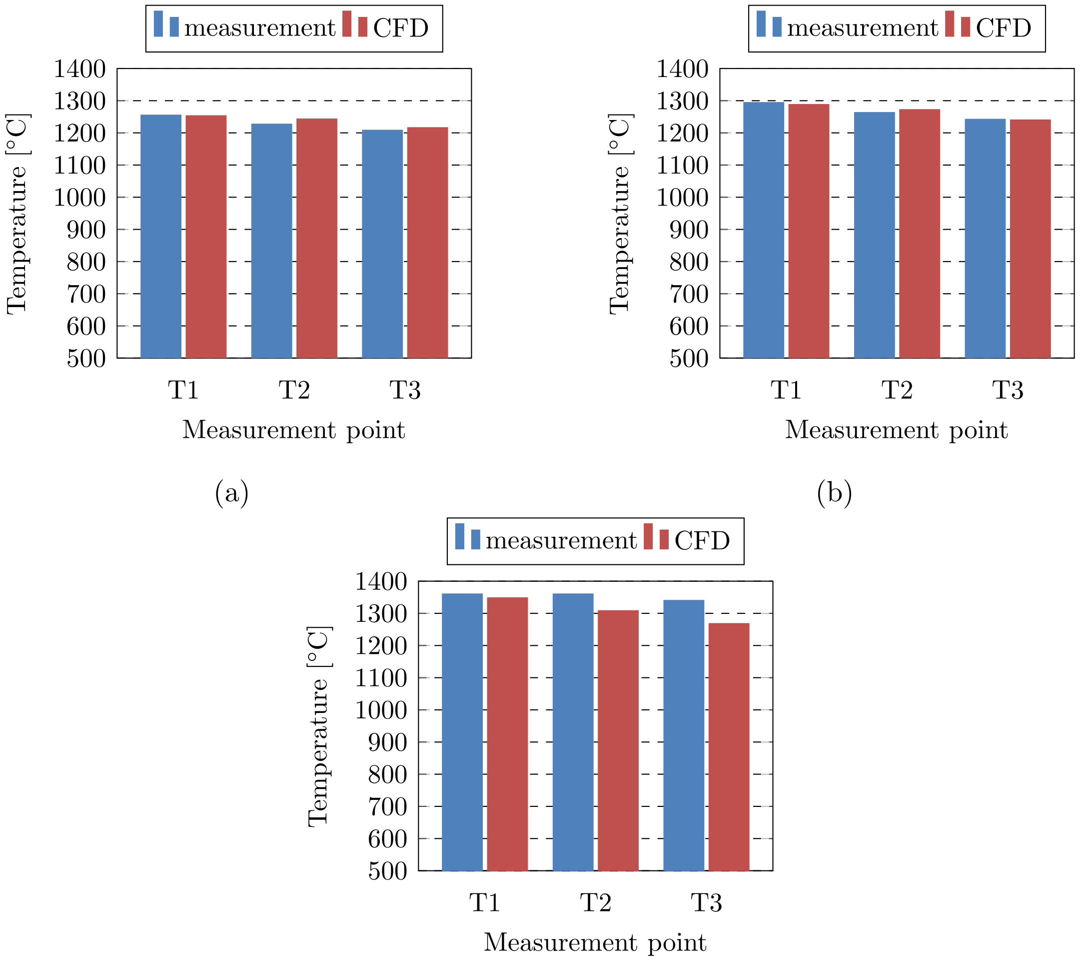

(a)

(b)

(c)

Figure 3.32.: Temperature comparison measurement/CFD: (a) 21 Vol% O_2; (b) 24.5 Vol% O_2; (c) 37 Vol% O_2 [4]

oxidizer increases. The volume fraction of the OH species also increases with the oxygen enrichment in the oxidizer, in the main combustion zone of the flame, which is indicative of higher chemical activity. This emphasises the need for a detailed chemical mechanism in simulations of oxy-fuel combustion. Due to the higher temperatures present during oxygen-enriched combustion, dissociation effects occur more often, and must be taken into account by the chemical mechanisms. Neglecting the dissociation effects leads to an over estimation of the temperature in the main combustion zone of the flame (see Yin et al. [40]). Global mechanisms, such as the Westbrook and Dryer (WD) mechanism, and the JL mechanism, do not consider OH radicals, and therefore can only be used for partial simulations of oxy-fuel flames. Figure 3.32 shows a comparison of the measurement and simulation results. All of the simulations are in close agreement with the measurements. For the case with 21% O_2 in the oxidizer, the maximum deviation between the measurements and simulations occurred at T2 (for position see 3.26) with 16.5 K, which can be considered

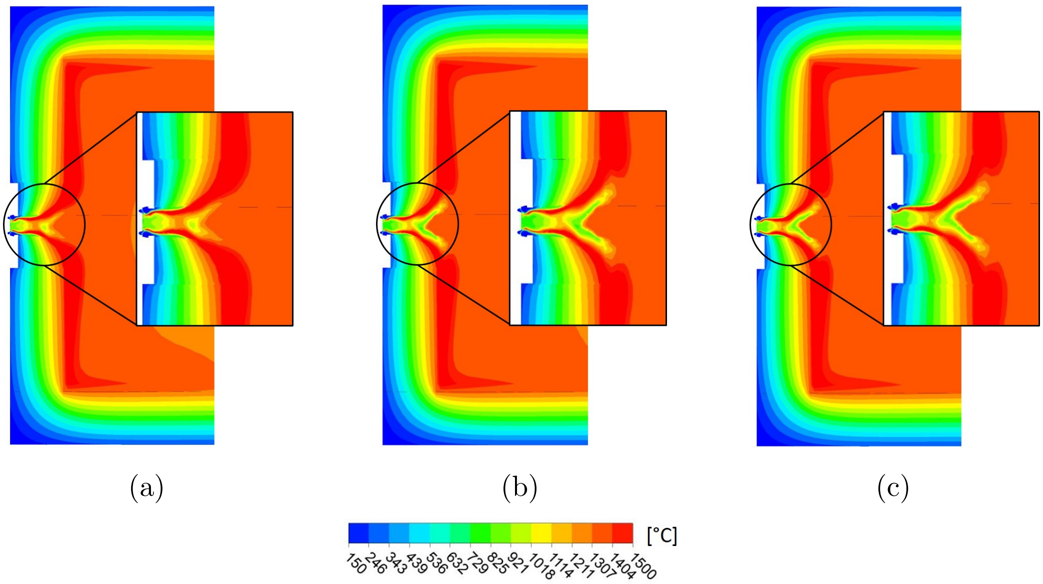
(a) (b) (c)

Figure 3.33.: Temperature contours for different detailed mechanism and 37 Vol% O_2: (a) skeletal25; (b) GRI 3.0; (c) smooke46 [4]

good agreement for such high temperatures. With 24.5% O_2 in the oxidizer, the maximum deviation also occurred at T2, but with only 9.5 K, which shows even better agreement. In the case with 37% O_2 in the oxidizer, the maximum deviation increases up to 72 K at measurement point T3 (for position see Figure 3.26). The reason for this higher deviation is that during the experiments, the flat flame burner exhibited some instability because this burner was originally developed for air-fuel conditions. For this reason, no investigations were carried out with higher oxygen concentrations in the oxidizer. However, the degree of error can still be deemed acceptable for such high temperatures. Additionally, the furnace was simulated with each of the two other detailed mechanisms and the SFM, in order to verify whether other mechanisms are applicable for oxygen concentrations higher than 30% O_2. The furnaces were simulated with the GRI 3.0 [76] and the smooke46 [78] mechanism. Prieler et al. [31] showed the smooke46 mechanism cannot be used with the SFM for jet flames with oxygen concentrations higher than 30% O_2 in the oxidizer. The results of the simulations conducted in this work are shown in Figure 3.33 for oxygen concentration of 37% O_2. The temperature fields calculated with the different mechanisms are very similar; however, in the vicinity of the burner, the smooke46 and the GRI 3.0 calculate slightly lower temperatures than the skeletal25. Thus, the difference between the mechanisms is not particularly great, and the smooke46 mechanism and GRI 3.0 can also be used to calculate flat flame burners with oxygen enrichments of up to 37% O_2. In Figure 3.34, the comparison between the measured and calculated surface temperatures of the quarl are shown, where x=0 refers to the inner side of the quarl and x=150 to its outer side. It is possible to note that the measured and the calculated surface temperatures for the

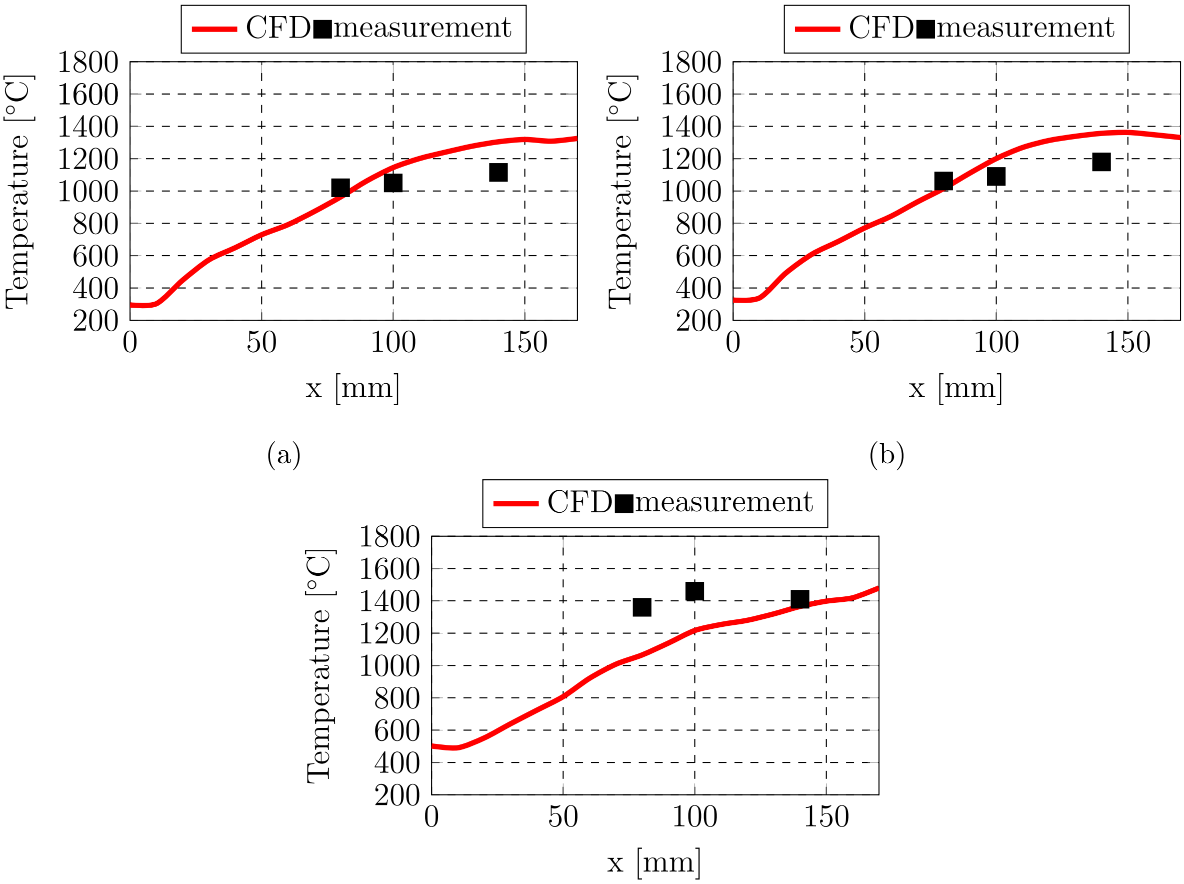

(a)

(b)

(c)

Figure 3.34.: Surface temperature comparison measurement/CFD of the quarl: (a) 21 Vol% O_2; (b) 24.5 Vol% O_2; (c) 37 Vol% O_2 [4]

cases with 21% and 24.5% O_2 in the oxidizer show reasonable accuracy, although they were measured from opposite sides of the furnace. The deviation is higher for the case with 37% O_2 in the oxidizer; the reason being that some instabilities occurred during the experiments of this case. However, it is nonetheless possible to conclude that the surface temperature of a quarl can be calculated with the SFM and the skeletal25 mechanism with reasonable accuracy, which is very important for furnaces which are retrofitted for oxygen-enhanced combustion in order to avoid overheating.

3.3.5. Conclusion

This section has presented the numerical and experimental investigations of a semi-industrial furnace with a flat flame burner for different O_2 concentrations in the oxidizer. Again, the SFM model, with the skeletal25 mechanism, was used to calculate the combustion. The simulations and measurements showed good agreement for the different

O_2/N_2 ratios in the oxidizer. Under air-fuel conditions, the simulation showed a maximum deviation of 16.5 K, which can be considered good agreement for temperatures above 1200 °C. For the case with an oxygen enrichment of 24.5% O_2, the deviation between the simulation and the measurements decreased to 9.5 K, which is even better agreement. The simulations showed a higher deviation, of 72 K, for an oxygen concentration of 37% O_2 in the oxidizer. As mentioned above, these results can be explained by the fact that the burner showed some instability during the investigation, but the error margin can still be considered acceptable for such high temperatures. Calculations with other detailed mechanisms, including the GRI 3.0 and the smooke46, showed slightly cooler regions in the vicinity of the burner for oxygen concentrations of 37.5%, but did not result in vastly different temperature profiles. It can thus be concluded that the GRI 3.0 and the smooke46 can be applied for a flat flame burner with oxygen concentration up to 37% O_2 in the oxidizer, a finding that is in contrast to other studies, which have shown that these mechanisms are not applicable for oxygen concentrations higher than 30% O_2 in the oxidizer for a jet flame. Moreover, the temperature of the quarl was measured and compared with the simulations. The simulations and the measurements showed reasonably good agreement for oxygen concentrations of 21% and 24.5% in the oxidizer. The simulations showed higher degrees of error for the case with the 37% oxygen in the oxidizer, which can also be accounted for by the instabilities that occurred during the experiment.

4. Industrial Furnaces: Testing and Modelling

In this chapter the numerically efficient and validated models were subsequently used to simulate and optimise different industrial scale furnaces for oxy-fuel and OEC conditions. In simulations of industrial-scale furnaces, the coupling of the gas phase combustion and the prediction of the reheating of the load are challenging and often time-consuming tasks. In this chapter, a new method is presented in which these two simulations are coupled in a numerically-efficient manner. Again, the method described in Section 2.5.4 is used to determine the amount of wall surface and gas radiation in the investigated furnaces.

4.1. Aluminium Melting Furnace

In this section, the validated and numerically efficient CFD models are used to investigate an industrial-scale, aluminium melting furnace. The furnace is operated with 70 Vol% O_2 in the oxidizer. In this section, the influence of using oxy-fuel combustion or different oxygen concentrations in the oxidizer on furnace efficiency and heat transfer is investigated. Additionally, the influence of a higher or lower heat input on the heat transfer will be investigated as well. Due to the use of numerically efficient models, such as the SFM model, the computational demand of this investigation is very low compared to other combustion models, such as the EDC model.

4.1.1. Description Aluminium Melting Furnace

The aluminium melting furnace has a capacity of 50 tonnes and is used to recycle aluminium scrap into aluminium alloys. The furnace is fired by four natural gas burners, which are located at the side wall of the furnace (see Figure 4.1). The molten aluminium is located in the lower part of the furnace, and the aluminium is fed into the furnace from the front of the furnace. The jet burners are slightly inclined towards the molten aluminium to increase the heat flux to the melting. The furnace works under oxygen-enriched conditions, with an O_2 concentration of 70 Vol% O_2 in the oxidizer. The furnace is operated under two different conditions called: " heating up" and "keeping warm". Under the operating condition "heating up" the thermal input was 2.4 MW, while under the operation condition "keeping warm", the thermal input was 0.7 MW. At the beginning of the cycle, the furnace is charged with molten aluminium and aluminium scrap. Subsequently the aluminium scrap is melted using the operation condition "heating up" and then kept warm (using the operation condition "keeping warm") until the molten aluminium is discharged. Then the cycle starts from the beginning. In this thesis, only the operation condition "heating up" was investigated. Inside the furnace, the gas temperature is measured by six thermocouples, which are surrounded by ceramic material. Both the flue gas temperature and the melting temperature were measured. In Figure 4.2, the positions of the measurement points are shown. Measurement points T2 to T6 are located in the ceiling of the furnace, and T1 is located at the back wall of the furnace. The measurement points T2, T3, T4 and T5 are located directly above the flames of the burners. Measurement point T6 monitors the wall temperature of the ceiling. The temperatures inside the furnace were measured over a time period of 1.4 hours at a measurement interval of 20 seconds.

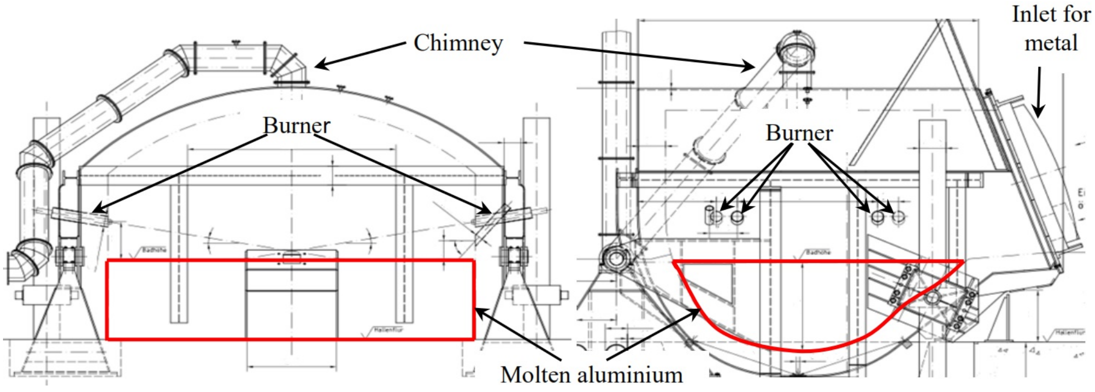

Figure 4.1.: Drawing of the Aluminium melting furnace

4.1.2. Boundary Conditions

In the CFD simulation, the gaseous phase and the refractory lining of the furnace were modelled, whereas the molten aluminium was not. Therefore, the surface of the molten aluminium was modelled as a wall with a temperature boundary condition. The temperature of the molten aluminium is known from the measurements of the melting temperature during the melting process (see Section 4.1.1). The emissivity of the molten aluminium

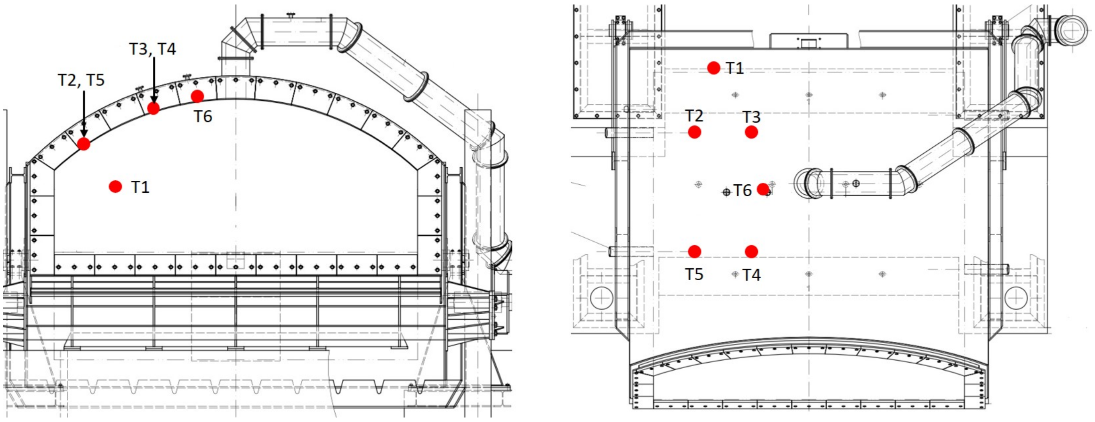

Figure 4.2.: Positions of the measurement points in the aluminium melting furnace

was set to 0.53, and the surface temperature was set to 805 °C. The refractory lining of the furnace was modelled as a solid with a thermal conductivity of between 0.6 and 1.3 W/(m K). On the outer wall of the refractory lining, a convective boundary condition to the atmosphere was applied, with a heat transfer coefficient of 15.35 W/(m^2 K) and a free stream temperature of 30 °C. Pure methane was used as fuel in all of the simulations. In Figure 4.3, the 3D model of the gaseous phase and the modelled refractory lining of the furnace is shown. The numerical settings and the under-relaxation factors used for the simulations can be found in Appendix B.4.

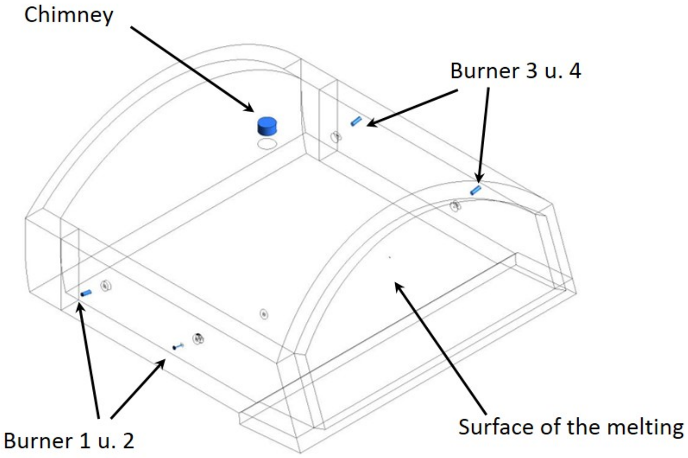

Figure 4.3.: 3D-Model of the aluminium melting furnace

4.1.3. Computational Grid

The grid of the furnace consists of 2.2 million cells, with a maximum aspect ratio of 19 and a maximum skewness of 0.89. The grid is dense near the burners, where the highest gradients for temperature, species concentration, and velocity occur. The mesh consists mainly of hexahedrons and tetrahedrons. In the vicinity of the burners, high-quality hexahedrons were used. In Figure 4.4, the mesh of the furnace can be seen. A grid independency test was also performed with a grid consisting of 7 million cells. Both meshes calculates similar results, therefore the the mesh with 2.2 million cells was used in all simulations.

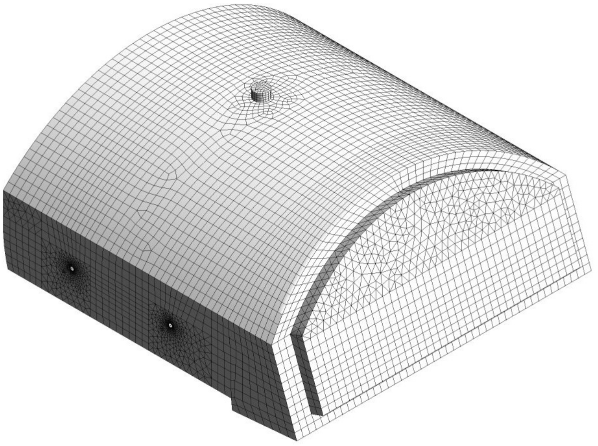

Figure 4.4.: Mesh of the aluminium melting furnace

4.1.4. Results and Discussion

In the simulation, the SFM was used as a combustion model along with the detailed reaction mechanism, skeletal25. In the numerical simulation, the operating condition “heating up” (see Section 4.1.1) was investigated. Under this operating condition, the heat input was 2.4 MW and the oxygen concentration in the oxidizer was 70 Vol%. The operating condition “heating up” is a transient process that takes place over a period of 1.4 hours. In Figure 4.5, the temperatures measured inside the furnaces are plotted over time (for the positions of the measurement points, see Figure 4.2). It is possible to see that the process is transient, but also that, at the end of the process, the measured temperatures have reached nearly steady conditions. Therefore, the furnace was simulated in a steady state, and the solutions of the furnace simulation were compared with the measurements at the end of the “heating up” process. The calculated temperatures in the furnace for an oxygen concentration of 70 Vol% are shown in Figure 4.6. One can see that the flames nearly touch each other in the middle of the furnace. This also has a high impact on the heat flux density to the melting, as seen in Figure 4.7, where the highest heat flux density appears in the middle of the furnace. This effect is also enhanced by the slight inclination of the burners towards the melting. The CFD calculation predicted a total heat flux of 1636 kW to the melting. In order to verify the CFD solution, the calculated

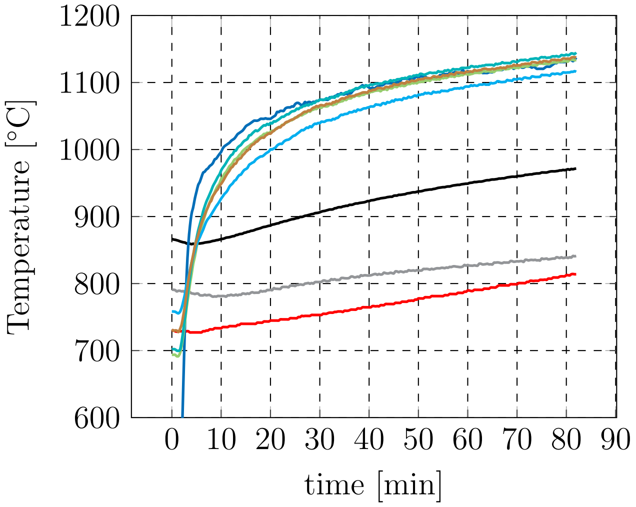

Figure 4.5.: Measured temperatures in the furnace for the operation condition “heating up”: $T_{melting}$ —, $T_{flue\,gas}$ —, T_1 —, T_2 —, T_3 —, T_4 —, T_5 —, T_6 — (Positions see Figure 4.2)

gas temperatures were compared to the measurements. In Table 4.1, the comparison between the measured and the calculated gas temperatures for the different measurement points (see Figure 4.2) is shown. It can be seen that the CFD simulation predicts the gas temperatures in the furnaces very well. The maximum deviation between the measurements and the CFD calculation is 59 K at measurement point, $T1$. The average deviation for all measurement points is 19 K, which can be considered good agreement, considering the high temperatures of 1000 °C in the furnace.

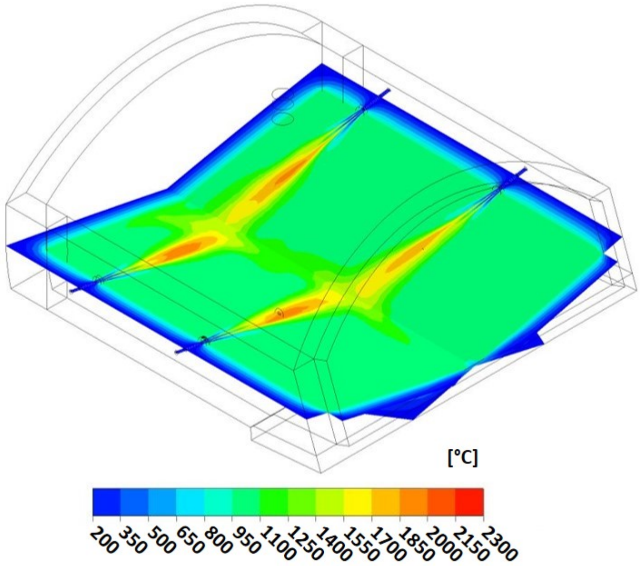

Figure 4.6.: Temperature plot of the aluminium melting furnace with 70 Vol% oxygen in the oxidizer

The verified model was subsequently used to investigate different operating conditions of

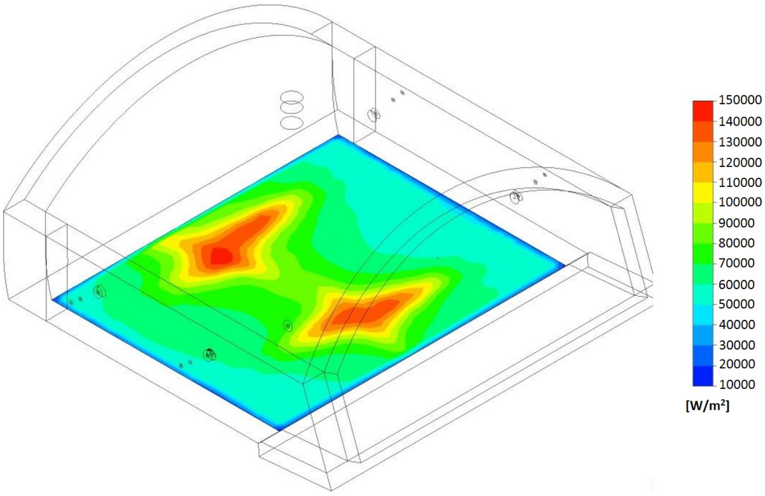

Figure 4.7.: Heat flux density to the melting

Table 4.1.: Temperatures inside the melting furnace, comparison CFD & Measurements (Positions of the measurement points see Figure 4.2)

	CFD [°C]	Measurement [°C]	ΔT [K]
$T1$	896	873	59
$T2$	1124	1128	4
$T3$	1125	1137	12
$T4$	1102	1111	9
$T5$	1084	1129	45
$T6$	965	965	0
$T_{flue\,gas}$	1124	1120	4

the furnace. Investigations were carried out in order to discover the influence of changing the oxygen enrichment from 70 Vol% to 100 Vol% and 50 Vol%, with a constant thermal input of 2.4 MW and the same residual oxygen content in the off-gas. Additionally, the influence of changing the thermal input from 2.4 MW to 3.2 MW and to 4 MW with the same oxygen enrichment of 70 Vol% oxygen in the oxidizer and the same residual oxygen content in the off-gas was investigated. No other boundary conditions were changed. In Figure 4.8, the calculated temperatures for the different oxygen concentrations are shown. The temperature in the furnace can be seen to increase as the concentration of oxygen in the oxidizer increases. Additionally, the predicted concentration of OH-radicals for the different cases are shown in Figure 4.9. With the increasing oxygen concentration, the OH-radical concentration also increases. The higher OH-radical concentration indicates that the chemical activity in the flames increases with the oxygen concentration in the oxidizer. The calculated heat flux densities to the molten aluminium for the different

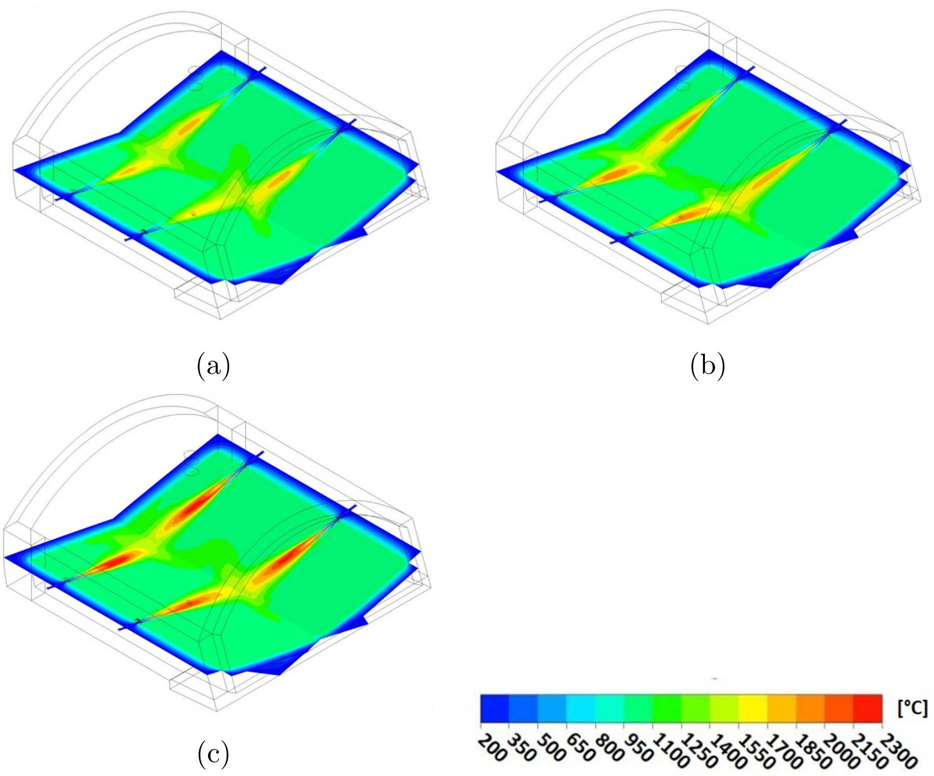
(a) (b) (c)

Figure 4.8.: Calculated temperatures in the melting furnace for different oxygen concentration in the oxidizer: (a) 50 Vol% O_2, (b) 70 Vol% O_2, (c) 100 Vol% O_2

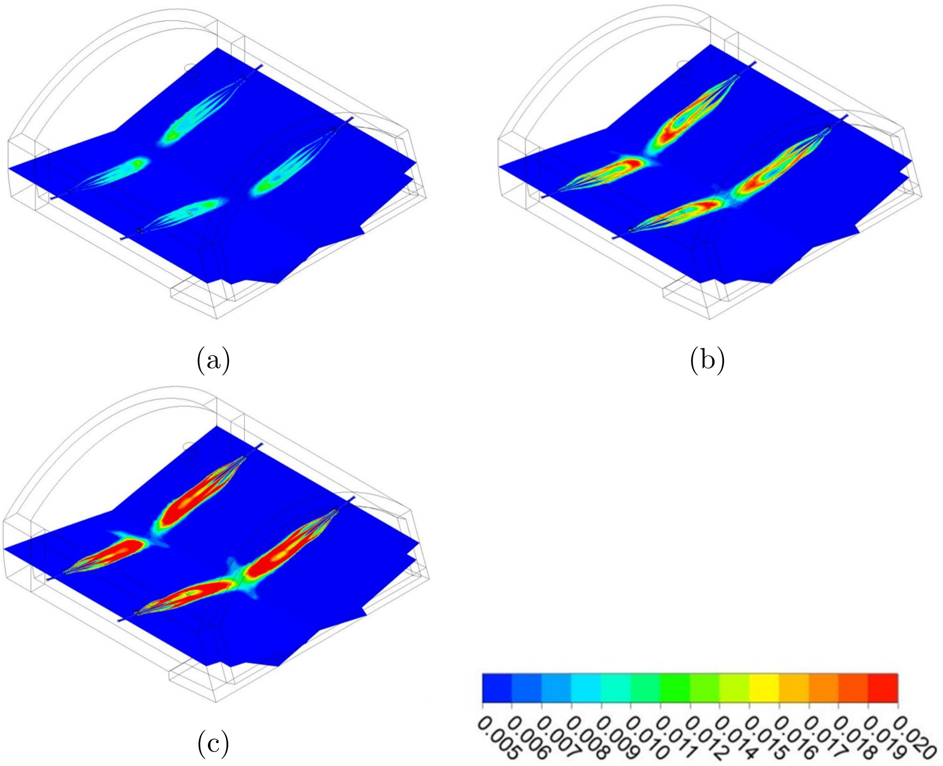
(a) (b) (c)

Figure 4.9.: Calculated OH-radical concentrations in the melting furnace for different oxygen concentration in the oxidizer: (a) 50 Vol% O_2, (b) 70 Vol% O_2, (c) 100 Vol% O_2

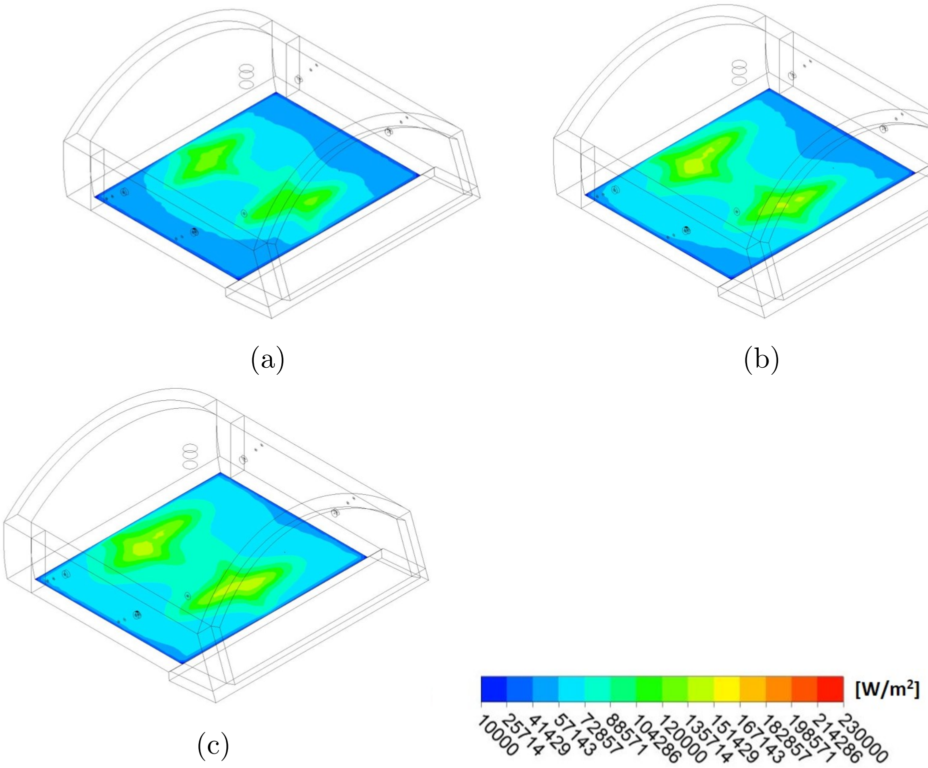

(a) (b) (c)

Figure 4.10.: Calculated heat flux density to the melting for different oxygen concentration in the oxidizer: (a) 50 Vol% O_2, (b) 70 Vol% O_2, (c) 100 Vol% O_2

oxygen concentrations in the oxidizer is shown in Figure 4.10. It can be seen that as the oxygen concentration increases, so does the heat flux density to the melting, which also becomes more uniformly distributed. For an oxygen concentration of 50 Vol%, the CFD calculation predicts a total heat flux of 1512 kW to the molten aluminium. The heat flux increases to 1636 kW and 1736 kW for 70 Vol% and 100 Vol% O_2, respectively. Therefore, the furnace efficiency increases from 63% for 50 Vol% oxygen in the oxidizer, up to 72% under oxy-fuel conditions. Furnace efficiency is defined as the fraction of the total heat flux to the molten aluminium and the thermal heat input of the fuel. In Figure 4.11, the calculated heat flux density to the molten aluminium is shown for the different thermal heat inputs. It can clearly be seen that the total heat flux density drastically increases with a higher thermal input. For a thermal heat input of 2.4 MW, the CFD calculation predicts a total heat flux of 1636 kW to the molten aluminium. With thermal inputs of 3.2 MW and 4 MW, the heat flux increases to 2187 kW and 2725 kW, respectively.

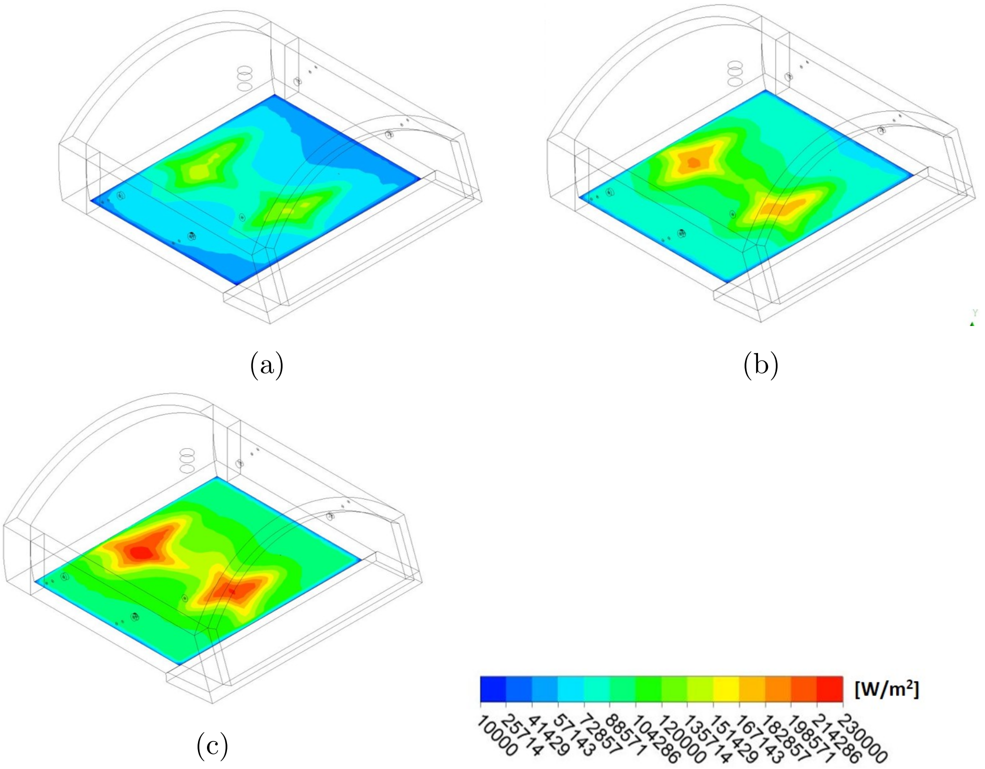

(a) (b)

(c)

Figure 4.11.: Calculated heat flux density to the melting for different thermal heat inputs: (a) 2.4 MW, (b) 3.2 MW, (c) 4 MW

4.1.5. Comparison of Gas and Wall Surface Radiation

In this section, the amounts of gas and wall surface radiation on the total heat flux to the molten aluminium will be determined using the method described in Section 2.5.4. The operating conditions with 50, 70 and 100 Vol% oxygen in the oxidizer were investigated with this method. In Figure 4.12, the calculated heat flux for the different operating conditions is shown. Furthermore, the amounts of wall surface radiation, gas radiation, and convection on the total heat flux to the molten aluminium are shown. It is possible to see that, for all oxygen enrichments, the majority of the heat flux is due to wall surface radiation, while only a minor part is due to gas radiation or convection. For an oxygen concentration of 70 Vol% in the oxidizer, the total heat flux to the molten aluminium is 1636 kW. At the same time, 1321 kW of the total heat flux is due to wall surface radiation, and only 313 kW comes from gas radiation and convection (66 kW from the 313 kW). In contrast to the investigation in Section 3.1.4 (where the flue gas reduced the radiation due to wall surface radiation with increasing oxygen in the oxidizer), here, the gas radiation increases the heat flux to the molten aluminium. This is because the gas volume of the aluminium melting furnace is far higher than that of the lab-scale furnace investigated in Section 3.1.4. Additionally, in the aluminium melting furnace, the

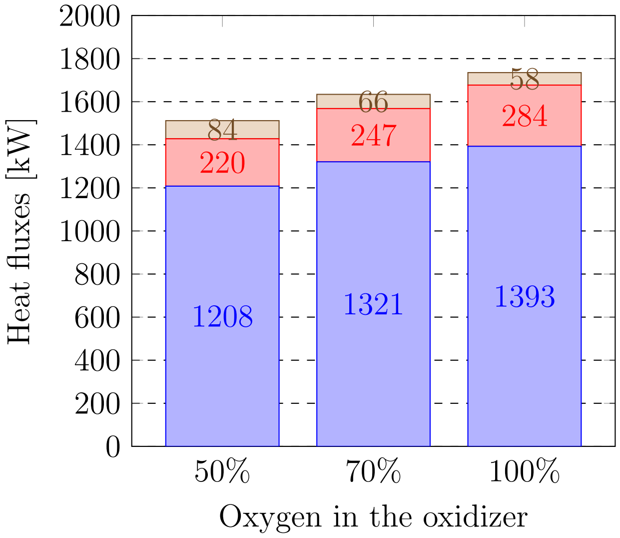

Figure 4.12.: Heat flux due to wall surface radiation (🟦), gas radiation (🟥) and convection (🟫) to the molten aluminium for different oxygen concentrations in the oxidizer

surface temperature of the molten aluminium is with 805 °C far higher than the surface temperature of the thermal load (around 100 °C) in the lab-scale furnace. Due to the higher temperature of the surface, the average temperature of the flue gas in the aluminium melting furnace is higher than that in the lab-scale furnace, which results in a higher radiative heat flux to the molten aluminium. It is the combination of these effects which explains why the gas radiation increases the total heat flux in the aluminium melting furnace. However, the biggest contribution to the total heat flux comes from wall surface radiation. This implies that the heat flux due to wall surface radiation must be correct predicted by the CFD simulation in order to calculate the correct total heat flux to a load. The surface temperature of the wall surface has the highest influence on the radiative heat transfer because the heat flux due to wall surface radiation has a power-of-four temperature dependency (T^4). Therefore, it is essential to correctly predict the surface temperatures of the refractory lining. This can only be achieved if the refractory lining is also modelled in the CFD calculation as solid body.

4.1.6. Conclusion

In this section, numerically efficient models have been used to investigate an industrial-scale aluminium melting furnace operating under OEC conditions. The solutions of the CFD calculations were subsequently compared to the measurements and showed good agreement for gas temperatures above 1000 °C, with a maximum deviation of 59 K and an averaged deviation of 19 K for all measurement points. The effect of different oxygen enrichments on the heat flux was investigated using CFD calculation. The CFD calculations showed that the heat flux to the melting increases as the oxygen concentration in the oxidizer increases, which the investigation of the lab-scale furnace (see section 3.1) also showed. Since the heat flux increases with the oxygen concentration in the oxidizer, the furnace efficiency increases as well, from 63% at an oxygen concentration of 50 Vol% in the oxidizer up to 73% at oxy-fuel conditions. The amount of wall surface and gas radiation on the total heat flux to the molten aluminium was also determined using the method described in Section 2.5.4. This investigation revealed that wall surface radiation has the biggest impact on the total heat flux to the molten aluminium, while gas radiation has only a small impact. In contrast to the investigation of the lab-scale furnace (see section 3.1.4), here, the gas radiation was responsible for increasing the total heat flux. This is because of the higher flue gas volume of the aluminium melting furnace, and the higher surface temperatures of the molten aluminium (805 °C) compared to the surface temperature of the thermal load (100 °C) in the lab-scale furnace. Additionally, the high amount of wall surface radiation on the total heat flux implies that it is crucial to correctly predict the heat flux due to wall surface radiation, in order for the total heat flux to be accurately predicted in the CFD simulation. The surface temperature of the refractory lining has the biggest influence on the heat flux due to wall surface radiation. Therefore, the surface temperature of the refractory lining must be calculated correctly in the CFD simulation. This can only be achieved if the refractory lining is also modelled in the CFD simulation. Furthermore, using the correct material properties for the refractory lining is also of great importance. In summary, this investigation has shown that an industrial-scale furnace operating under OEC can be calculated with the CFD models presented in this works.

4.2. Pusher-type Reheating Furnace[1]

In this section, CFD simulations are used to investigate a pusher-type reheating furnace. In reheating furnaces, the coupling of the gas phase combustion and the transient reheating of the billets is a challenging task. Therefore, this section presents a novel numerically efficient approach for the calculation of pusher-type reheating furnaces. The solutions of the simulation with the proposed approach were compared with measurements of the gas-phase temperatures from several points in the furnace. The temperature of the billets was compared to calculations done with an iterative approach as well as with temperature measurements on the furnace's outlet.

---

[1] Parts of this section have already been published in [3]

4.2.1. Description Pusher-type Reheating Furnace

The pusher-type reheating furnace is used to reheat low carbon steel billets from ambient temperatures to average temperatures of 1070 °C, before these are further processed to steel wire rods in the rolling mill. This furnace is 10 m long, 14 m wide, and about 1.8 m in height, this corresponds to a path length of 3 m. The refractory linings of the furnace are approximately 380 mm thick. The billets are 130x130 mm and approximately 13 m long. The billets are charged into the furnace by a pusher at the front, and are discharged by a peel bar machine at the side of the furnace (see Figure 4.13). The billets are heated by 36 swirl burners which are placed on the top of the furnace, and twelve jet burners, which are underneath the billets/skids. The burners are divided into six zones, which can be seen in Figure 4.13b, where zone 1 is inactive and therefore not modelled. The position of zone 1 is on the top wall before zone 2. In each of these zones, the thermal heat input can be individually controlled. Every zone has thermocouples to monitor the temperature inside the furnace and to control the furnace. The thermocouples for the swirl burners are 40 cm below the ceiling. The temperatures measured from these thermocouples were used to validate the simulations. Additionally, the average surface temperature of the billets was measured at the outlet during the discharging process by means of a stationary pyrometer, and measurements with a thermographic camera were performed in order to verify the calculated temperature distribution of the billets. In Figure 4.13, a 3D-model of the furnace shows the location of the swirl burners and jet burners. The skids that support the billets are shown in Figure 4.13b. These skids are water-cooled to preserve the mechanical properties of the material. The production capacity of the furnace is approximately 60 t/h. Each billet takes 7752 s (approximately 2 h) to pass through the furnace, which means that every billet spends 102 s in each position. The furnace has a thermal input of 18.6 MW and uses natural gas as fuel. The furnace also has a regenerator in order to recover energy from the flue gas. This energy is used to preheat the combustion air to a temperature of 340 °C.

4.2.2. Calculation of the Billet Movement

The movement of the billets in a reheating furnace is a periodically transient phenomenon. Because the billets in a pusher-type reheating furnace are placed side by side, without gaps between them, they can be considered as a continuum, and can therefore be modelled as a laminar, high-viscous medium with a constant velocity. The advantage of this approach is that the periodically transient movement of the billets can be transformed into a

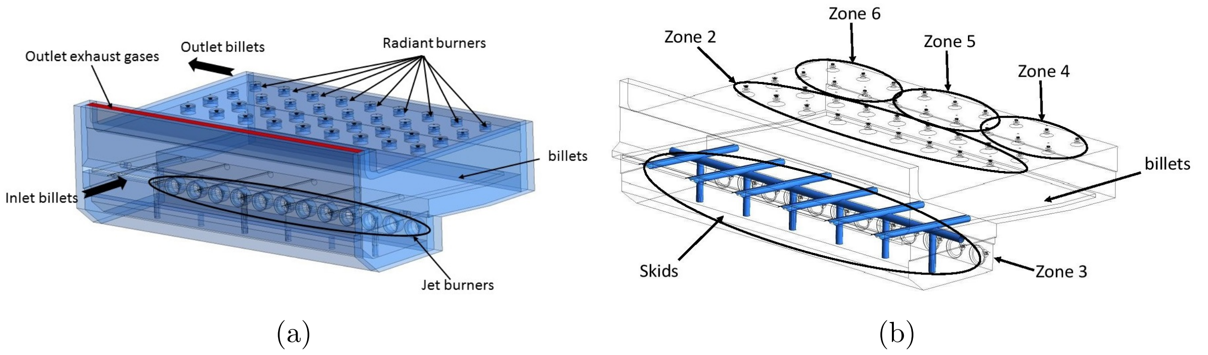

Figure 4.13.: 3D model of the reheating furnace (a) furnace with insulation (b) furnace with skids and the different burner zones [3]

steady-state simulation. Due to the fact that steady-state simulations are much faster than transient simulations, the computational time is greatly reduced.

4.2.3. Boundary Conditions

In the simulation, pure methane was used as fuel and preheated air was used as oxidizer. The combustion air is preheated to 340 °C by a recuperator. All inlets in the simulation were modelled as mass flow inlets. The furnace operates under fuel-lean conditions, with a fuel-oxidizer equivalence ratio of 0.862. The temperature at the fuel inlet was set to 25 °C, and the inlet turbulent intensity was set to 10%. The insulation of the furnace was modelled as solid, with a thermal conductivity of 0.7 W/(m K), and the emissivities of the walls and the billets were set to 0.6 and 0.55 respectively. At the outer wall, the heat transfer to the atmosphere was modelled as a convective boundary condition, with a free stream temperature of 25 °C, and a heat transfer coefficient of 15 $W/(m^2 K)$. At the skids, a heat flux boundary condition was employed; the heat flux to the skids is known from the absorbed energy of the cooling water. The thermal conductivity and the specific heat capacity of the billets change as the temperature increases, a fact which was also considered in the simulation. The properties were calculated with JMatPro [117] and implemented into the simulation via UDF. In Figure 4.14, the properties of the steel as dependent on the temperature can be seen. The wall between the gas phase and the fluid domain of the steel was modelled as a so called "two-sided wall". This means that each side of the wall is a distinct, infinitely thin wall zone, and that different thermal boundary conditions can be employed in each zone, or that individual zones can be coupled. If two zones are coupled, the solver calculates the heat transfer through the wall zones directly from the solution of the adjacent cell zones (gas-phase, steel fluid domain), where the heat transfer (whether radiation or convection) is calculated as for a normal wall [62]. In the

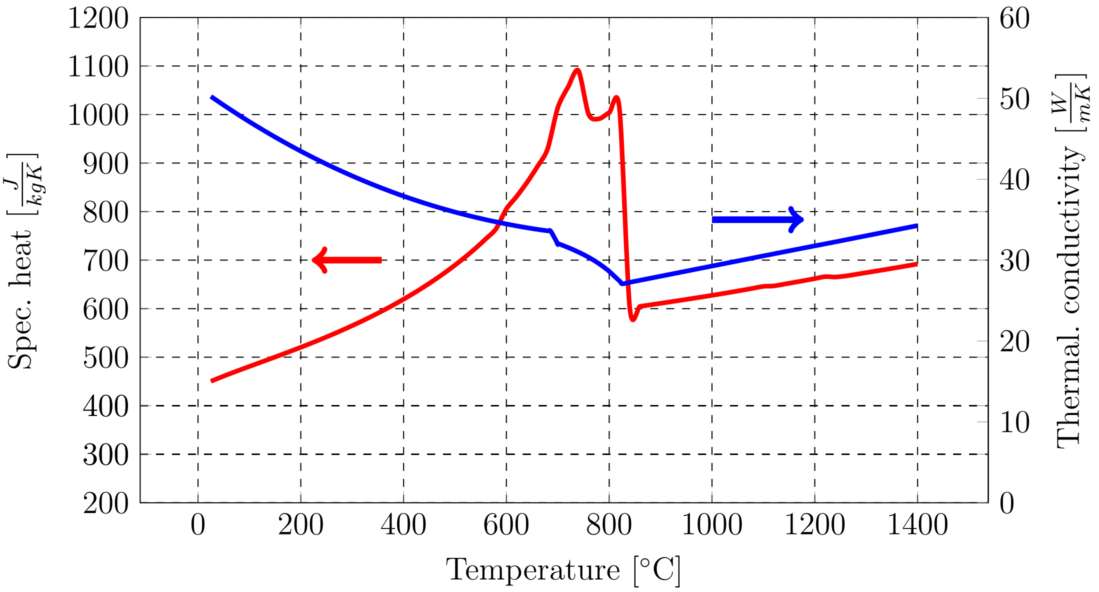

Figure 4.14.: Thermal conductivity (—) and specific heat capacity (—) of the steel temperature dependent [3]

present simulation, two wall zones were coupled. With this type of wall zone, it is also possible to have a no-slip condition on the gas-phase side, and to set the shear stress to 0 pascal on the side of the steel fluid domain so as to ensure a uniform velocity profile. Furthermore, the fluid domain of the steel was set to a laminar zone, and the viscosity was set to 10^5 kg/(m s). With these assumptions, the velocity in the fluid domain of the steel was uniform and had a constant velocity of 0.00123 m/s, which correspond to production capacity of 60 t/h. The numerical settings and the under-relaxation factors used for the simulations can be found in Appendix B.5.

4.2.4. Computational Grid

The computational grid of the furnace consists of 7,521,175 cells (tetrahedrons and hexahedrons) and includes the furnace walls, fluid domain of the steel fluid, and the gas phase. In Figure 4.15, the mesh of the pusher-type reheating furnace is shown. The grid is very dense in the vicinity of the burners, where the highest temperatures, velocity, and species gradients occur. Therefore, larger cells were used in regions where the temperature, velocity, and species gradients are low in order to conserve computational effort. Grid independency tests were performed with a mesh consisting of 10 million cells, but the difference between the two grids was negligible. Therefore, the coarser grid was used for the simulation.

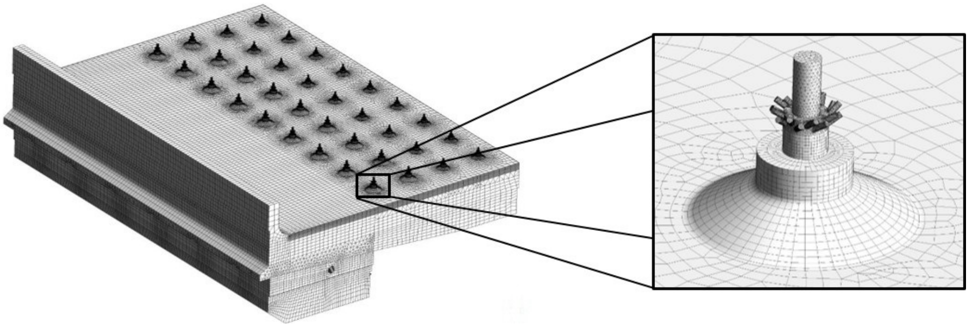

Figure 4.15.: Mesh of the pusher type reheating furnace

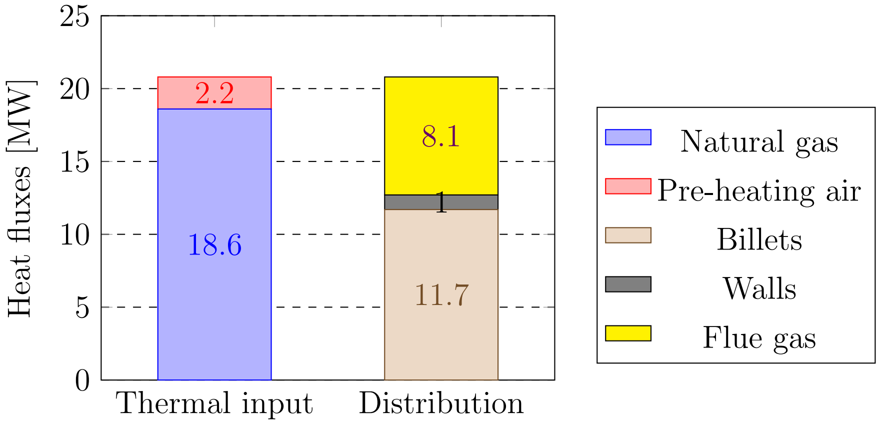

Figure 4.16.: Thermal input and heat fluxes in the furnace [3]

4.2.5. Results and Discussion

According to the furnace control system, the thermal input to the furnace was 18.6 MW. An additional 2.2 MW of heat input was added to the furnace through the preheating of the combustion air. The distribution of the heat fluxes in the furnace is shown in Figure 4.16. The CFD simulation calculated a heat transfer of 11.7 MW to the billets, which corresponds to a furnace efficiency of 62.9%. Furnace efficiency is defined as the fraction of the total heat flux to the billets $\dot{Q}_{billets}$ and the thermal heat input of the fuel $\dot{Q}_{fuel}$ (see Eq.4.1). The heat losses of the flue gas and the walls were 8.1 MW and 1 MW, respectively. Losses due to the skids are also included in the wall loses.

$$\eta_{furnace} = \frac{\dot{Q}_{billets}}{\dot{Q}_{fuel}} \tag{4.1}$$

Figure 4.17 shows the calculated temperatures inside the furnace, while Figure 4.17a shows a temperature plot through the swirl burners in zone 2. It is possible to see that the flames of the burners are closely attached to the ceiling of the furnace. The swirl burners form a continuous flame carpet, which is desirable in a reheating furnace in order to achieve the

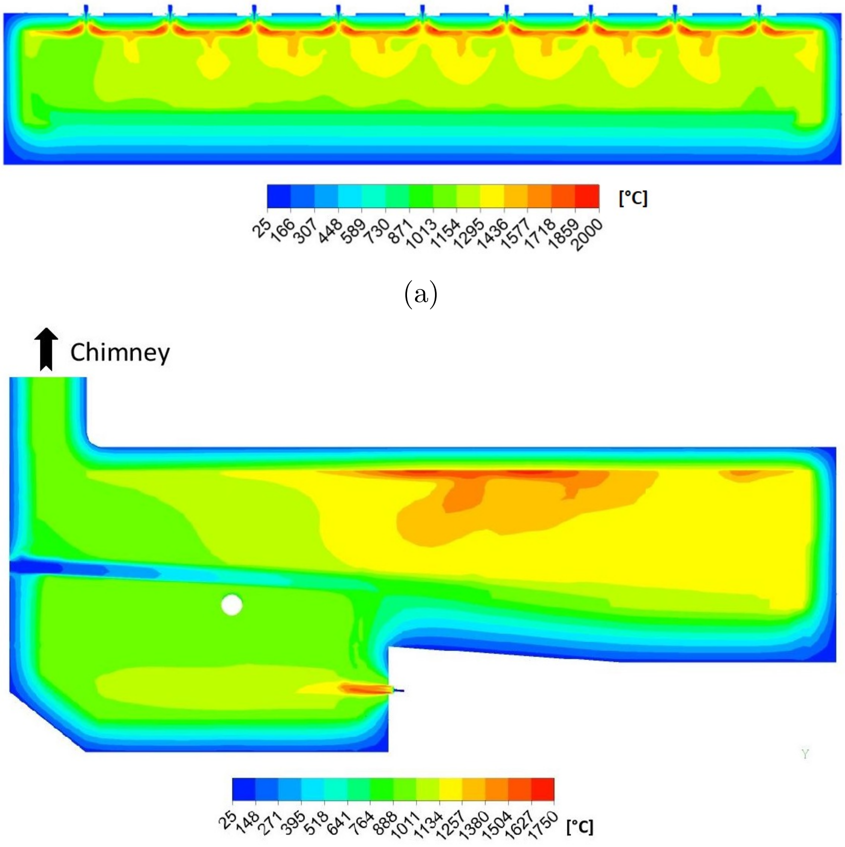

(a)

(b)

Figure 4.17.: Temperature plots of the furnace (a) Temperature plot swirl burners zone 2 (b) Temperature plots jet burners [3]

uniform reheating of the billets. Furthermore, it is evident that the realizable k-ϵ model is capable of calculating radiant burners. In Figure 4.17b, a temperature plot along the furnace axes is shown, where the jet burners below the billets can be seen. This temperature plot also shows that the gas temperature decreases towards the chimney of the furnace. In Table 4.2, the calculated temperatures were compared with the measured temperatures of the furnace control system. The calculations showed reasonable accuracy for such high temperatures, and for the complexity of the simulation. The maximum deviation between the measurements and the CFD calculations occurred in zone 5, with a temperature difference of 54 K. Bearing in mind the high temperatures inside the furnace, this can be deemed acceptable. Zone 2 had the smallest deviation between measurement and CFD calculation, with a temperature difference of only 5 K. The average deviation between the CFD calculations and the measurements, for all measurement points, is 38 K, which can considered good agreement for these temperatures. Therefore, the approach developed in this paper can be considered reasonably accurate in terms of the gas temperature. Figure 4.18 shows the calculated heat flux to the billets, from the upper and bottom sides of

Table 4.2.: Temperatures inside the furnace, comparison CFD & Measurements (Positions see section 4.2.1 and Figure 4.13b) [3]

	Zone 1	Zone 2	Zone 3	Zone 4	Zone 5	Zone 6
Measurement (°C)	1064	1278	845	1242	1233	1241
CFD (°C)	1102	1273	894	1205	1179	1192
ΔT (K)	38	5	49	37	54	49

the billets. On the top side of the billets, the maximum heat flux occurs in zone 2, which is also the zone with the highest heat input. Furthermore, the distribution of the heat flux is slightly asymmetrical, towards the billet outlet. On the bottom side of the billets, the shadows of the skids can be seen clearly. These shadows have a major impact on the temperature distribution in the billets. At the beginning, the heat flux is very high, due to the jet burners, which push the hot flue gas towards the billet inlet. The asymmetrical distribution of the heat flux also has an impact on the temperature distribution of the billets. Figure 4.19 shows the calculated temperature distribution of the billets. Like the heat flux, the temperature distribution is slightly asymmetrical towards the billet outlet. This is because the flows of all swirl burners rotate clockwise. As a result of the number of swirl burners in this furnace, the whole flow in the furnace has a slight clockwise rotation, which can be seen in Figure 4.20. Figure 4.20 displays the temperature and flow direction of the gas phase in the furnace at a height of 1 m. It is possible to see that the temperature distribution is slightly asymmetrical, due to the fact that cold flue gas is sucked back by the flow. Therefore, the temperature of the billets on the outlet side is slightly cooler than on the other side. This asymmetrical temperature distribution was also confirmed by the operator of the furnace. One option to overcome this problem would be for the flow of the swirl burner to rotate in alternating directions (clockwise or counter clockwise). The influence of the skids can also be seen on the top surface of the billets (see Figure 4.19). It can clearly be seen that the temperature of the billets is lower near the skids than in the rest of the billets, a phenomenon which is referred to as “skid marks”. The aim is for these skid marks to vanish at the end of the furnace because they can influence processing in subsequent processes. Figure 4.21 shows the surface-averaged heat flux and the volume averaged billet temperature over the furnace length. The heat flux at the beginning is very high, due to the fact that the billets are heated from both sides. At a furnace length of 3 m, the heat flux drops slightly due to the shadow of the supporting tube for the skids. This supporting tube is arranged along the total furnace width (see Figure 4.13b). The sharp decrease in heat flux at a furnace length of 4.5 m is due to the ending of the skids and the beginning of the solid underground. Therefore, the heat flux to the billets is smaller because the billets are only heated from above from this point on. Due to the

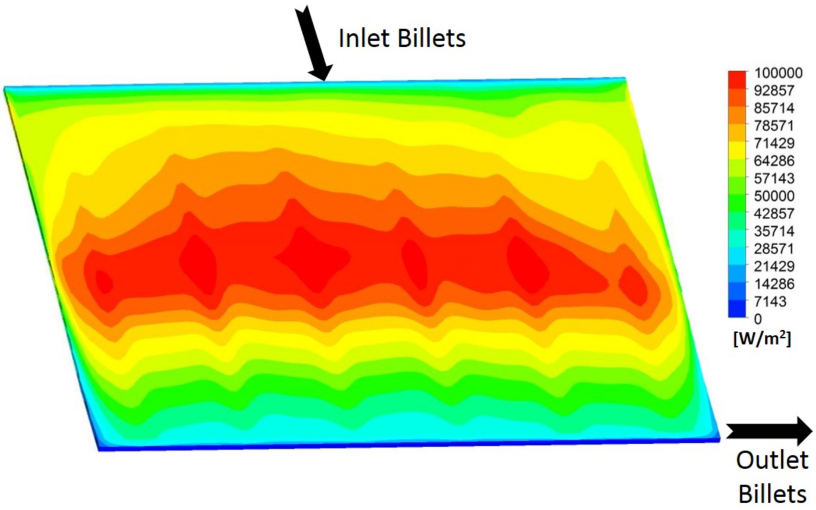

(a)

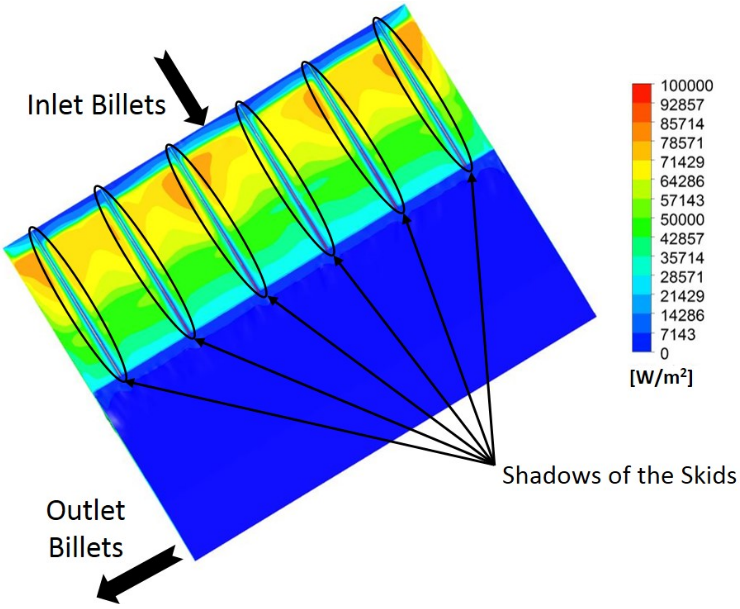

(b)

Figure 4.18.: Heat flux density (a) Top surface billets (b) Bottom surface billets [3]

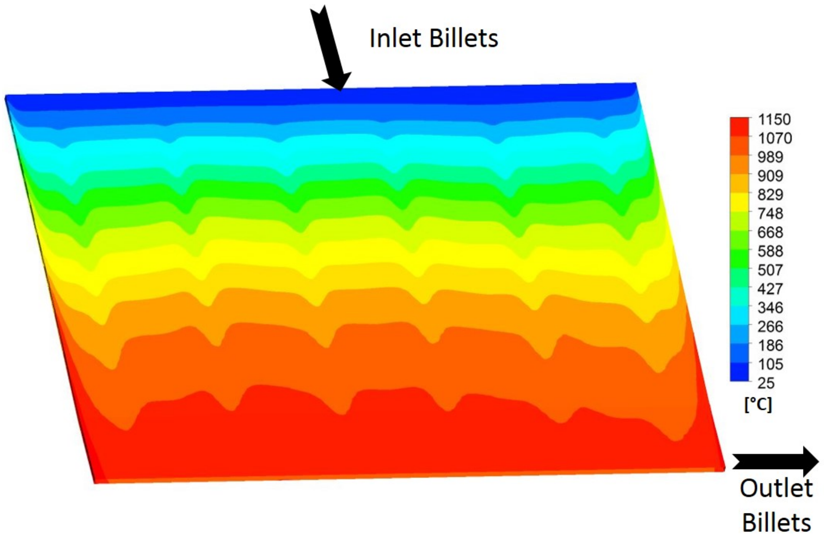

Figure 4.19.: Temperature distribution of the billets [3]

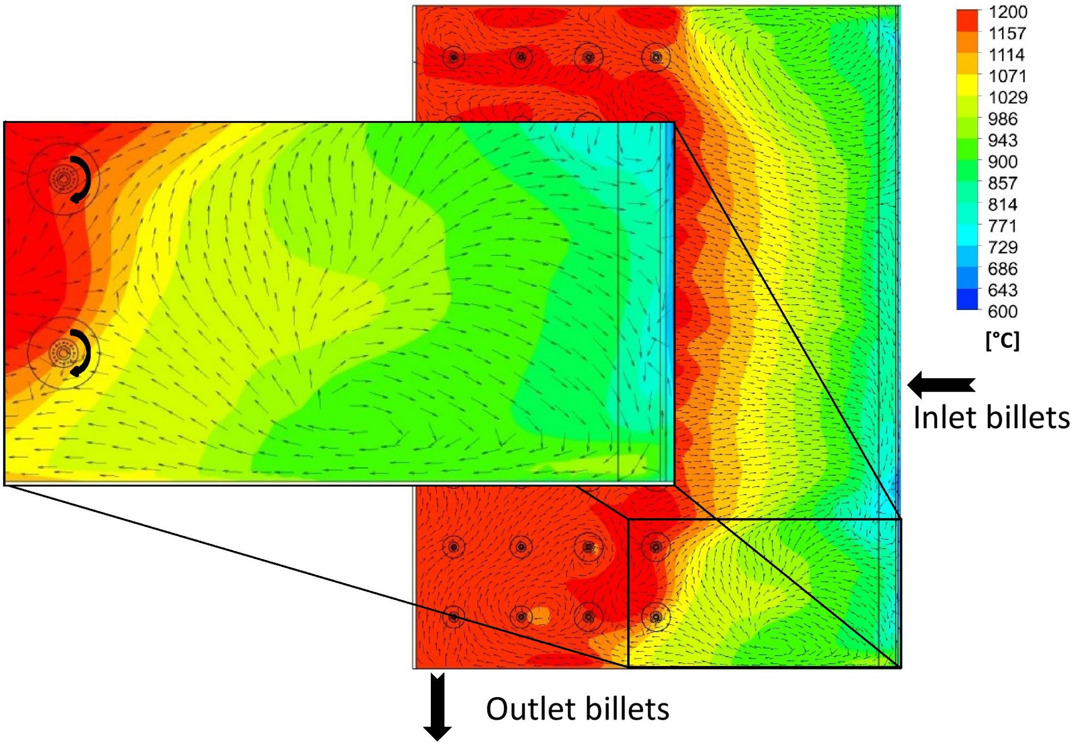

Figure 4.20.: Flow and temperature distribution of the gas phase in the furnace [3]

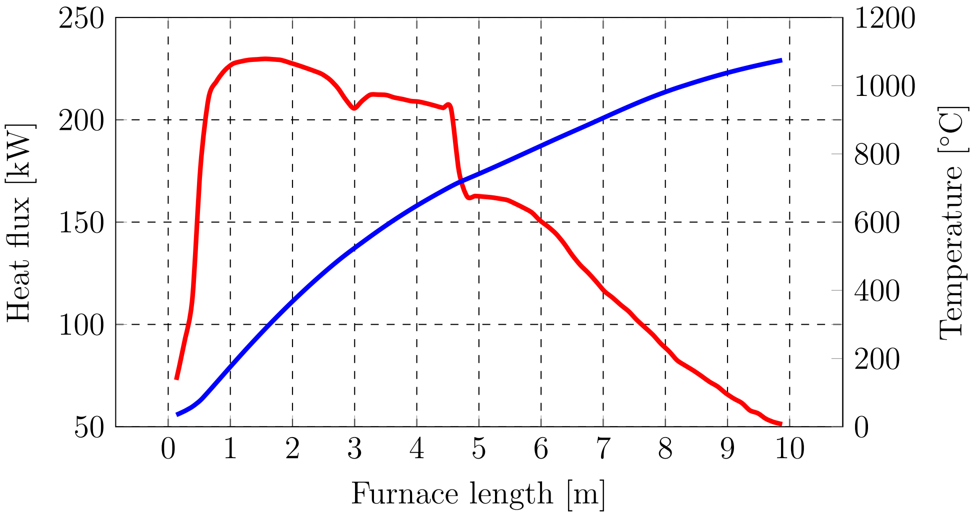

Figure 4.21.: Volume averaged temperature of the billet (—) and the surface averaged heat flux to the billets (—) over the furnace length [3]

increasing billet temperature, the heat flux decreases along the furnace's length. The core temperature of the billets at different positions in the furnace are displayed in Figure 4.22. The side of the billet outlet corresponds to the billet length 0 m. At the beginning, the temperature distribution in the billets is uniform, except on the edges of the billets. The higher temperatures on the edges of the billets are due to hot flue gas sweeping over the edges, from the burners located under the billets. Furthermore, the edges of the billets receive more heat flux due to radiation because they have more surface to interact with the furnace wall and the flue gas. Figure 4.22 clearly shows the influence of the shadow from the skids. The temperature in the billets near the skids (at billet lengths of 0.9 m, 3 m, 5.3 m, 7.5 m, 9.7 m and 11.9 m) is lower than the temperature in the rest of the billets, which is not desirable: the temperature of the billets should be evenly distributed. When the solid floor begins at a furnace length of 4.5 m, the temperature differences in the billets becomes more uniform with the furnace length, but the influence of the skids can still be seen at the end of the furnace. The distribution of the core temperature in the last billet is shown in Figure 4.23. It is possible to see that the temperature is asymmetrically distributed in the last billet. Furthermore, the influence of the skids on the temperature distribution is also evident. The averaged temperature in the last billet is about 1070 °C and the lowest temperature is 1026 °C, which corresponds to a maximum temperature difference of 44 K. The temperature asymmetry in the last billet was also confirmed by the furnace operator. On the outlet, the average surface temperature of the billet is measured by a pyrometer during the discharging process, which is placed on top of the furnace discharging door. This measured temperature is also an important control parameter for the whole process. The average surface temperature of 15 billets is used to verify the predicted temperature of the

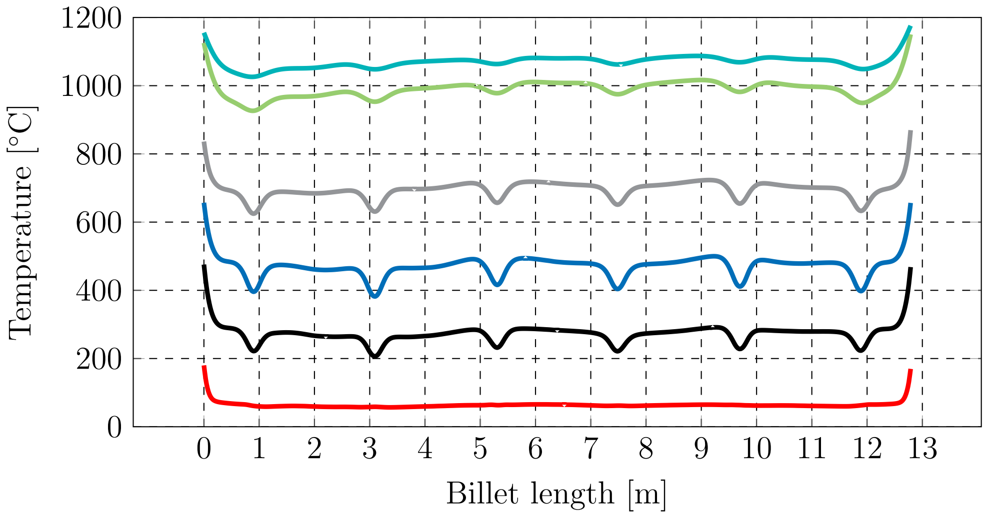

Figure 4.22.: Core temperature of the billets on different positions in the furnace: x=0.4 m (—), x=1.5 m (—), x=2.7 m (—), x=4.6 m (—), x=8.2 m (—), x=9.8 m (—) [3]

billets. The measured average surface temperature of the billets on the outlet was 1088 °C. The CFD calculation predicted an average surface temperature of 1115 °C at the outlet, which corresponds to a deviation of 27 K. Considering that the discharging process takes about 102 seconds, during which the surface of the billets cools down and the influence of the scale layer on the temperature measurement, a deviation of 27 K can be seen as good agreement. Additionally, the temperature distribution in the billets was calculated with the iterative approach from Prieler et al. [52] and then compared with the approach proposed in this work. A comparison of the two approaches can be seen in Figure 4.23. The figure shows that the two approaches result in similar trends for temperature distribution as well as temperature level. Furthermore, the influence of the skids is also visible, as it was with the proposed two-fluid approach. At 1069 °C, the average temperature calculated with the approach of Prieler et al. [52] is very similar to the temperature calculated with the approach proposed in this work. The lowest temperature calculated in the billet is 1010 °C, which corresponds to a temperature difference of 59 K to the average temperature. The highest temperature differences between the two models occurred at the edge of the billets, where the highest temperature gradients are located. Due to the iterative approach of the model by Prieler et al. [52], it is more difficult to obtain the exact same temperatures at the edge than with the two fluid approach, where the energy exchange between the gas phase and the billet is calculated simultaneously. Therefore, the temperature distribution in the billets should be more similar if a higher number of iterations were performed, but this would also result in an increase in calculation time. This comparison shows that the two-fluid approach is able to calculate temperature distribution in the same manner as an iterative approach that considers the billets as a solid. The advantage of the two-fluid

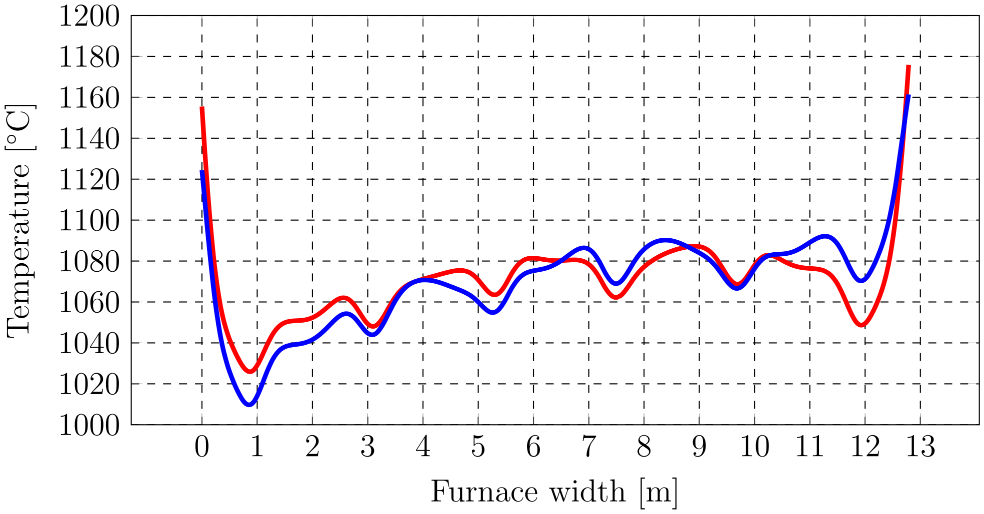

Figure 4.23.: Core temperature distribution in the last billet calculated with two different approaches: two fluid approach (▬), approach by Prieler et al. [52] (▬) [3]

approach is that the calculation times are far lower than those of an iterative approach, and the human effort required is also lower, due to fact that only one simulation case is needed. In a further step, measurements of the billet temperature at the outlet of the furnace were taken with a thermographic camera (FLIR T1030sc) in order to further verify the calculated temperature distribution of the billets with the proposed approach. In Figure 4.24, the measurement set-up can be seen. The thermographic camera is positioned at the outlet of the furnace, perpendicular to the billet at a distance of 2 m. The measuring range of the thermographic camera was set to between 300 °C and 2000 °C. Due to the close proximity of the furnace and the rolling mill, only a small section of the billets is visible at the outlet, and it is not possible to take an image of the whole billet at the outlet. Therefore, the thermographic camera was used to make a video of the discharging process of the billets. Subsequently, the measured temperature distribution was compared to the calculated temperature distribution at different positions. In Figure 4.25, the comparison between the measured and the calculated billet temperature distributions is shown. The measured values shown in Figure 4.25 are the average temperature values of a 100 cm^2 area on the billet surface. The measured temperature distribution, like the calculated temperature distribution, shows an asymmetrical temperature distribution. Furthermore, the measurement also shows lower billet temperatures near the position of the skids (at billet lengths of 0.9 m, 3 m, 5.3 m, 7.5 m, 9.7 m and 11.9 m), as it does in the calculation. This shows again that the proposed approach is capable of calculating the temperature distribution in the billets.

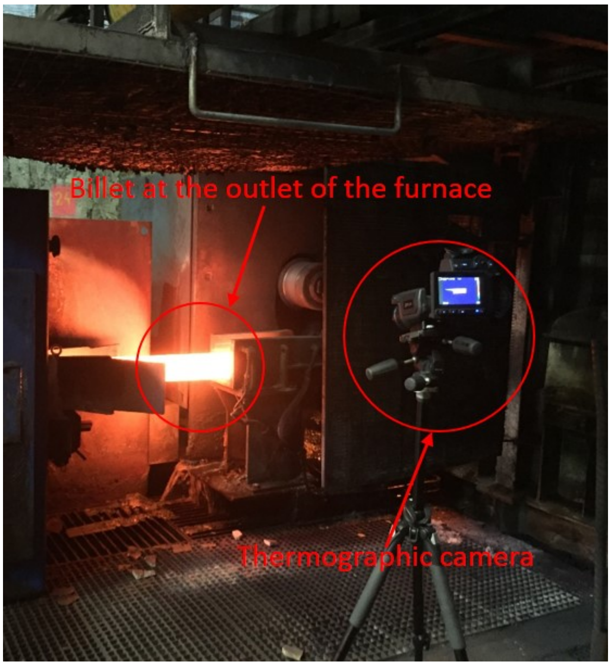

Figure 4.24.: Measurement set-up thermographic camera [3]

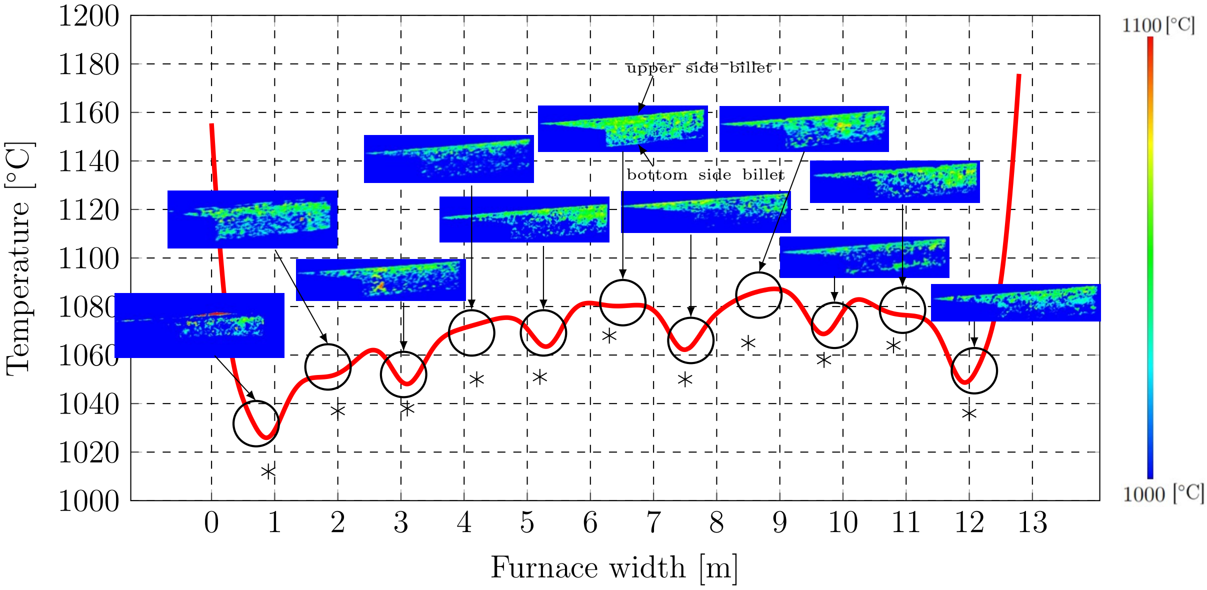

Figure 4.25.: Comparison between calculated and measured temperature distribution of the billet at the furnace outlet: calculated (━━), measured (∗) [3]

4.2.6. Conclusion

This section has presented a time-saving approach that converts the periodic transient reheating of steel billets in a reheating furnace into a steady-state simulation. This is done by modelling the steel billets as a fluid with high viscosity. For pusher-type reheating furnaces, this approach is justified due to the fact that the billets are placed side by side. Using this approach, calculation times can be significantly reduced compared to transient calculation methods. The simulation was compared to measurements from the furnace control system and showed good agreement with the measured gas temperatures. The average and maximum temperature deviations between the gas phase simulation and measurements were 38 K and 54 K, respectively. This can be deemed acceptable for temperatures above 1100 °C. The simulation revealed an asymmetrical temperature distribution in the billets along their length, which is due to the asymmetric flow in the furnace, where cold flue gas is drawn back into the furnace and the billets are cooled on one side. Additionally, the simulations showed that the skids have a major impact on the temperature distribution of the billets. The shadow of the skids generates skid-marks on the billets bottom surface. Furthermore, the simulation illustrated that these skid-marks do not vanish until the end of the furnace. The predicted averaged surface temperature of the billets at the outlet was compared with measurements at the outlet, and showed a maximum deviation of 27 K, which can be seen as good accordance. Additionally, a numerically efficient iterative approach from Prieler et al. [52] was used to verify the solution of the temperature distribution in the billets. The comparison showed that both approaches predicted similar trends with a maximum temperature deviation of 31 K. Measurements with a thermographic camera showed similar temperature distribution on the billets on the outlet of the furnace. These results prove that the proposed approach is capable of predicting the major operating conditions of the furnace, and can therefore be used to optimise the furnace's geometry or operating conditions without expensive test runs. Due to the low computational effort of this approach, this process can be carried out in a short period of time.

4.3. Walking Hearth Type Reheating Furnace[2]

In this section, a walking hearth type furnace is investigated using CFD calculations. The CFD calculations used in this section were originally performed by Prieler et al. [32] using the iterative procedure described in Section 2.5.5 to couple the gas phase combustion

---

[2] Parts of this section have already been published in [5]

and the transient reheating of the billets. Based on the results of these CFD simulations, the method proposed in Section 2.5.4 was used to determine the amount of gas and wall surface radiation in the industrial-scale reheating furnace for air-fuel and OEC conditions. The determination of the impact of wall surface and gas radiation on the total heat flux to the billets in an industrial scale furnace is the main finding of this section.

4.3.1. Description Walking Hearth Type Reheating Furnace[3]

The natural gas fired walking hearth type furnace is used to reheat low-alloy steel billets from ambient temperatures up to a process temperature of 1150°C for further processing in a rolling mill. The billets are 12 m in length and have a cross section of 0.12 x 0.12 m. The dimensions of the furnace are 17 x 13 x 1.6 m, this corresponds to a path length of 2.8 m, and it is fired by several flat flame burners located in the furnace ceiling. Because the furnace is symmetrical, only half of the furnace was modelled in the CFD simulation. In Figure 4.26, a 3D model of half of the furnace is shown. The furnace is subdivided into three different zones: the pre-heating zone, the heating zone, and the soaking zone. The heating and pre-heating zones are separated by a water-cooled wall over the total width of the furnace. In this investigation, the furnace was operated under air-fired conditions and with an oxygen concentration of 25 Vol% in the oxidizer. In both cases, the oxidizer was preheated to 310°C. The fuel input was 18.20 MW for air-fired conditions and 16.74 MW for 25 Vol% oxygen enrichment. This corresponds to a 8% reduction in fuel consumption. For both operating conditions, the productivity was 46.4 t/h. At this productivity rate, one billet takes 6400 s to pass through the furnace, and the billets remain in each position for 100 s. The billets were charged on the side of the flue gas outlet and discharged on the opposite side of the furnace. Both cases were investigated in [52] and [32], where more information about the furnace can also be found. In this thesis, the furnace was investigated in more detail with regard to the heat transfers due to gas and solid body radiation.

4.3.2. Boundary Conditions

All inlets for the fuel and the oxidizer were modelled as mass-flow inlets. At the inlets for fuel and oxidizer, the hydraulic diameters were set to 0.11 m and 0.0155 m, respectively. The turbulent intensity was set to 10% for both fuel and oxidizer inlet. On the outside of the furnace wall, a convective boundary condition was employed with a heat transfer

---

[3] Parts of this section have already been published in [5, 32, 52]

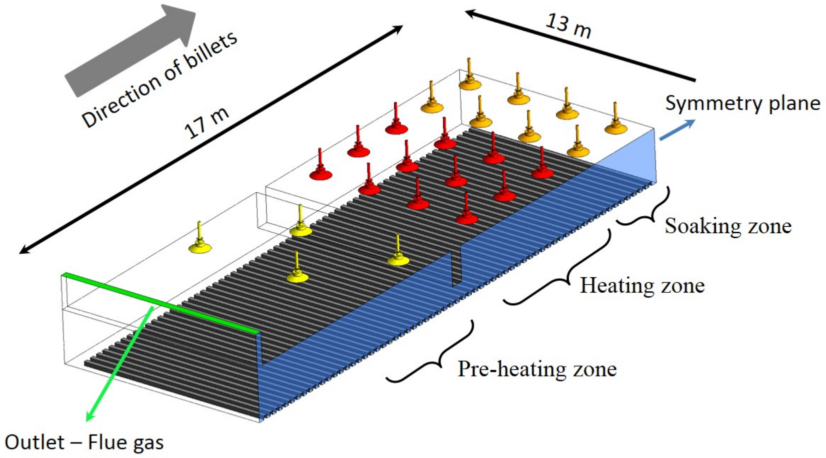

Figure 4.26.: Walking hearth type reheating furnace [52]

coefficient of 30 W/m^2K and a free stream temperature of 30°C. The emissivity of the furnace walls was set to 0.7 and the emissivity of the steel billets to 0.5. The equivalence ratios were 0.97 for both cases, which means that the furnace operated under slightly fuel-lean conditions [32]. More information about the numerical settings can be found in Prieler et al. [32].

4.3.3. Computational Grid

The computational grid for the whole furnace consists of 5,797,749 cells (hexahedrons and tetrahedrons). The maximum skewness of the mesh was 0.8, and the maximum aspect ratio was 19.8. Because the furnace is symmetrical, only half of the furnace has to be modelled in the simulation. Additionally, simulations using a mesh with 8,026,188 cells were performed in order to verify the influence of the computational mesh. The results of the simulation with the larger grid showed negligible differences for temperature, species concentration and heat flux in comparison to the smaller grid. The smaller grid was thus used in all simulations described in this thesis [32].

4.3.4. Results and Discussion

The furnace has a heat input of 18.2 MW under air-fuel conditions; with an oxygen enrichment of 25 Vol%, the heat input was reduced to 16.74 MW, which corresponds to fuel gas savings of 8%. The CFD calculation predicted a heat flux of 10.48 MW to the billets for air-fired conditions, and 10.28 MW for an oxygen enrichment of 25%. Due to the lower N_2 amount, the flue gas heat losses were reduced from 5.38 MW to 3.95 MW. Thus, the furnace efficiency increases from 57.6% under air-fired conditions to 61.4% under oxygen-enriched conditions. The majority of the heat flux is transferred via radiation (gas and wall surface radiation), while only a small amount is transferred via convection. Under air-fired conditions, 92.7% of the heat flux is transferred via thermal radiation, and only 7.3% via convection. Under oxygen-enriched conditions, 93.6% of the heat flux is transferred via radiation, and only 6.4% via convection [32]. Calculations with the method described in Section 2.5.4 were performed in order to determine the impact of wall surface and gas radiation on the total heat flux. In Figure 4.27, the different heat fluxes to the billets depending on position in the furnace are shown for the two different oxygen concentrations. The calculated total heat flux to the billets shows a similar trend for both cases: in the preheating zone (furnace length: 0 m to 8.5 m), the heat flux to the billets is lower under oxygen-enriched conditions than under air-fired conditions. This is due to the lower convective heat flux in the preheating zone, which drops from 447 kW under air-fired conditions, to 361 kW under oxygen-enriched conditions. Additionally, the flue gas temperature in the preheating zone drops from 810 °C under air-fired conditions to 778 °C under oxygen-enriched conditions. Due to the lower gas temperature under oxygen-enriched conditions, the heat flux due to gas radiation is also lower. In both cases, the investigation reveals that the majority of the total heat flux is due to wall surface radiation. Convection only has a higher share of the total heat flux at the furnace entry point of the billets (furnace length: 0 m), where it accounts for up to 17% of the total heat flux. After the billets enter the heating zone (furnace length: 8.5 m to 14 m), the total heat flux to the billets increases sharply, to its maximum of 260 kW. The higher total heat flux to the billets can be explained by the higher wall temperatures and gas temperatures of approx 1200 °C in the heating zone, compared to approx 800 °C in the preheating zone. This can also be seen in Figure 4.27, where, in both cases, a sharp rise in the amount of wall surface radiation can be seen at the beginning of the heating zone. Under oxygen-enriched conditions, the amount of wall surface radiation is higher in this section. This is because the billets entering the heating zone have a slightly lower surface temperature under oxygen-enriched conditions than under air-fired conditions, due to the lower total heat flux in the preheating zone, as mentioned above. The total heat flux in this section is thus higher under oxygen-enriched conditions than under air-fired conditions. In the soaking zone (furnace length: 14 m to 17 m), the heat flux to the billets decreases because, in this zone, the surface temperatures of the billets are nearly the same as those of the walls. The impact of gas radiation on the total heat flux in these zones stays nearly the same; therefore, the percentage of the gas radiation on the total heat flux increases. Gas radiation thus has the greatest impact on the total heat flux in the last part of the furnace.

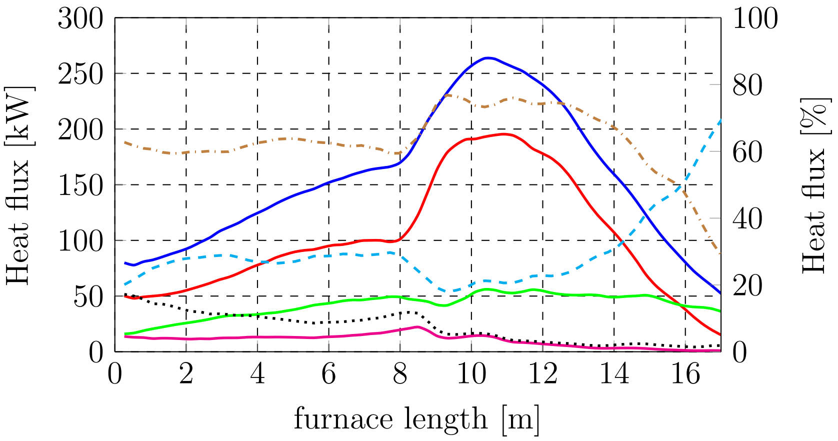

(a) 21 Vol% O_2 in the oxidizer

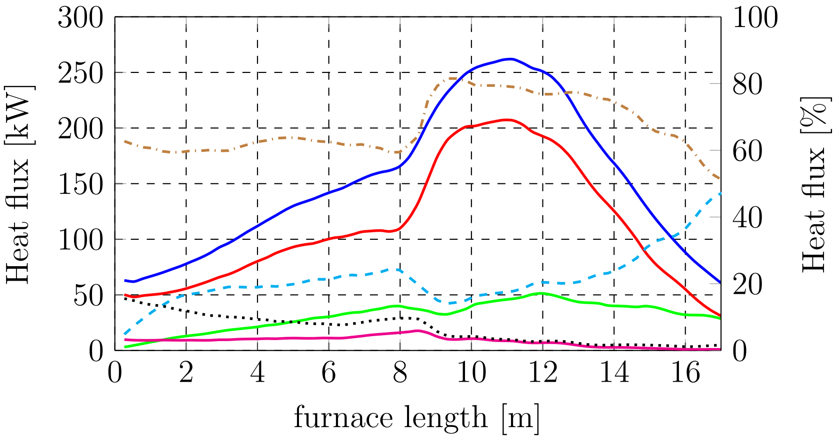

(b) 25 Vol% O_2 in the oxidizer

Figure 4.27.: Calculated heat flux to the billets depending on the position in the furnace: Total heat flux (——) [32], heat flux from wall surface radiation (——), heat flux from gas radiation (——), heat flux from convection (——), percentage of the wall surface radiation on the total heat flux (-·-·-), percentage of the gas radiation on the total heat flux (- - -), percentage of the convection on the total heat flux (······)[5]

At the end of the furnace, under air-fired conditions, 59.6% of the total heat flux is due to gas radiation and 28.6% due to wall surface radiation. With oxygen enrichment, 47.2% of the total heat flux is due to gas radiation and 51.2% is due to wall surface radiation. The higher amount of wall surface radiation under oxygen-enriched conditions can be explained by the fact that the surface temperatures of the billet are slightly lower at the end of the furnace, due to the slightly lower total heat flux of 0.2 MW to the billets. This is the first time, to the best of our knowledge, that the radiative heat flux to a billet is subdivided into wall surface and gas radiation.

4.3.5. Conclusion

This investigation of an industrial-scale reheating furnace has shown the beneficial effects of oxygen enrichment in the oxidizer. Heat input can be reduced by 8% when using an oxygen enrichment of 25 Vol% in the oxidizer, whereby the heat flux to the load remains virtually constant [32]. Using the method described in Section 2.5.4, this investigation has shown that the majority of the radiation heat flux in the reheating furnace is emitted by the furnace walls, while only a small part of it comes from the flue gas. It was found that gas radiation increases the total heat flux to the billets in the reheating furnace, as it did for the aluminium melting furnace (see Section 4.1.5), but in contrast to investigations of the lab-scale furnace (see Section 3.1). The reasons the gas radiation increases the total heat flux in industrial-scale furnaces are the same as described for the aluminium melting furnace, outlined in Section 4.1.5. Furthermore, this investigation has shown that gas radiation only has a significant impact on the total radiative heat flux when the wall temperatures and the surface temperatures of the billets are in nearly the same temperature range. This is valuable information for the design and optimisation of reheating furnaces, and, therefore, the proposed method can be used to optimise the design of future reheating furnaces.

5. Thermodynamic Furnace Model

In this chapter, a simplified one-dimensional thermodynamic model for calculating the heat transfer in reheating furnaces is developed. This model calculates the heat flux between the gas phase, furnace wall, and thermal load by means of simple correlations. These heat fluxes are then used to calculate the energy balance of the entire furnace. The model is not only useful for calculations of air-fired conditions, but also for calculations of oxygen-enriched and oxy-fuel conditions. Due to the simplicity of this model, the calculation times are very low, and calculations can be performed using a simple software like Microsoft Excel. The results of this model are then compared to the solutions of the CFD simulations and measurements presented in Chapter 3

5.1. Energy Balance of the Entire Furnace

In this section, the energy balance for the entire furnace is derived. As a first step, the system boundaries for the thermodynamic system have to be defined. For this system, the system boundaries were defined at the outer wall of the furnace insulation because the necessary values can be easily determined by measurements. On the system boundary, the different in- and outgoing heat fluxes are balanced. In Figure 5.1, a schematic drawing of the in- and outgoing heat fluxes is shown. The following heat fluxes are fed into the thermodynamic system: the heat flux of the combustion air ($\dot{Q}_{Air}$), the heat flux of the fuel CH_4 ($\dot{Q}_{CH_4}$), the heat flux of the pure oxygen (additional oxygen beside the oxygen supplied by the combustion air) supplied to the system ($\dot{Q}_{O_2}$), and the release of the chemical energy of the fuel, which is represented by the Lower Heating Value (LHV), and described as an additional heat flux to the system ($\dot{Q}_{LHV}$). The system's outgoing heat fluxes are: the heat flux of the flue gas ($\dot{Q}_{Flue\,gas}$), the heat losses through the walls ($\dot{Q}_{Wall}$), and the heat flux to the thermal load ($\dot{Q}_{Load}$). With these heat fluxes, it is possible to derive the energy balance of the entire furnace, which is given in Eq. 5.1.

$$0 = \dot{Q}_{Air} + \dot{Q}_{CH_4} + \dot{Q}_{O_2} + \dot{Q}_{LHV} - \dot{Q}_{Flue\,gas} - \dot{Q}_{Wall} - \dot{Q}_{Load} \tag{5.1}$$

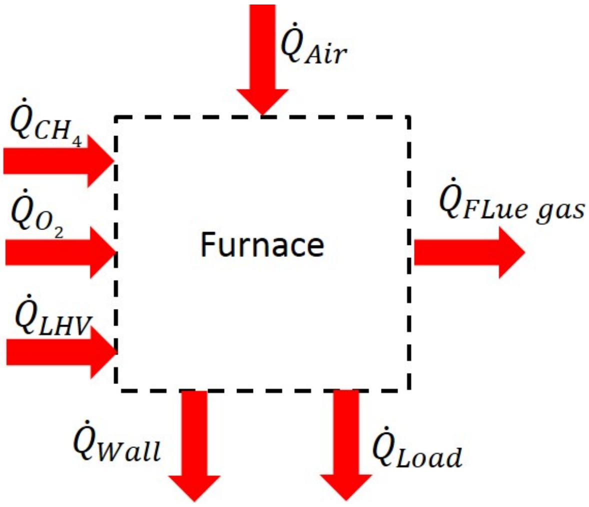

Figure 5.1.: Energy balance of the entire furnace

The variables in Eq. 5.1 are defined as follows:

$$\dot{Q}_{Air} = \dot{m}_{Air} \cdot \bar{c}_{p\,air}|_{T_0}^{T_{Air}} \cdot T_{Air} \tag{5.2}$$

$$\dot{Q}_{O_2} = \dot{m}_{O_2} \cdot \bar{c}_{p\,O_2}|_{T_0}^{T_{O_2}} \cdot T_{O_2} \tag{5.3}$$

$$\dot{Q}_{LHV} = \dot{m}_{CH_4} \cdot H_{LHV} \tag{5.4}$$

$$\dot{Q}_{CH_4} = \dot{m}_{CH_4} \cdot \bar{c}_{p\,CH_4}|_{T_0}^{T_{CH_4}} \cdot T_{CH_4} \tag{5.5}$$

$$\dot{Q}_{flue\,gas} = \dot{m}_{flue\,gas} \cdot \bar{c}_{p\,g}|_{T_0}^{T_g} \cdot T_g \tag{5.6}$$

The mass flows of the combustion air ($\dot{m}_{Air}$), the mass flow of the fuel methane ($\dot{m}_{CH_4}$) and the mass flow of the oxygen ($\dot{m}_{O_2}$) are input parameters of the calculation, and are therefore known. The temperatures of the different mass flows (T_{Air}, T_{O_2}, T_{CH_4}) are also input parameters for the calculation because these values are known from the furnace operating system or can be easily measured. The variable H_{LHV} stands for the LHV of the fuel methane, with a value of 50.013 MJ/kg. The specific heat capacity of each species is calculated by means of a polynomial approach. The polynomial used to calculate the specific heat capacity is shown in Eq. 5.7. The coefficients A to G were derived by means of polynomial fitting with the software Engineer Equation Solver (EES) [118]. In this software, a large database of the material properties of all kinds of species is available.

$$c_{p,i} = A + B \cdot T + C \cdot T^2 + D \cdot T^3 + E \cdot T^4 + F \cdot T^5 + G \cdot T^6 \tag{5.7}$$

The specific heat capacity has a strong temperature dependency, which must be taken into account in the calculations. Therefore, the heat capacity is averaged between a reference temperature (T_0) and the actual temperature of the species ($T_{Species}$), as shown in Eq. 5.8. As reference temperature $T_0 = 0$ °C was selected as a reference temperatures.

$$\bar{c}_{p,i}|_{T_0}^{T_{species}} = \frac{\int\limits_{T_0}^{T_{species}} c_{p,i}(T)\,\mathrm{d}T}{T_{Species} - T_0} \tag{5.8}$$

The mass flow ($\dot{m}_{flue\,gas}$) and the specific heat capacity ($\bar{c}_{p\,flue\,gas}|_{T_0}^{T_g}$) of the flue gas are not known and must be calculated. In order to calculate these values, the gas composition of the flue gas must be known. For the calculation of the flue gas composition, the fuel is assumed to be completely combusted, which is the case in nearly all reheating furnaces because of the high temperatures and an air-fuel ratio higher than one. In Eq. 5.9, the chemical equation for the combustion of methane for different oxidizers and oxidizer-fuel equivalence ratios (λ) is given.

$$CH_4 + 2\lambda\left(O_2 + \frac{\phi_{N_2\,oxi}}{\phi_{O_2\,oxi}}N_2\right) \longrightarrow CO_2 + 2H_2O + 2(\lambda-1)O_2 + 2\frac{\phi_{N_2\,oxi}}{\phi_{O_2\,oxi}}N_2 \tag{5.9}$$

It is possible to see that the flue gas mainly consists of N_2, CO_2, H_2O and of O_2, depending on the composition of the oxidizer. The oxidizer is assumed to be a mixture of oxygen ($\phi_{O_2\,oxi}$ volume fraction of oxygen in the oxidizer) and nitrogen ($\phi_{N_2\,oxi}$ volume fraction of nitrogen in the oxidizer). As an example, for air-fuel combustion, the ratio between oxygen and nitrogen ($\frac{\phi_{N_2\,oxi}}{\phi_{O_2\,oxi}}$) in the oxidizer is 3.76, therefore, the flue gas mainly consists of N_2, CO_2 and H_2O. In contrast, under oxy-fuel conditions, where the ratio between oxygen and nitrogen in the oxidizer ($\frac{\phi_{N_2\,oxi}}{\phi_{O_2\,oxi}}$) is zero, the flue gas consists mainly of H_2O and CO_2. With the known composition of the flue gas from Eq. 5.9, the mole fraction of the different species in the flue gas can be calculated with Eq. 5.10, where n_i stands for the mole of the different species and $n_{flue\,gas}$ for the sum of the moles of all species.

$$\nu_i = \frac{n_i}{n_{flue\,gas}} = \frac{n_i}{\sum\limits_{i=1}^{n} n_i} \tag{5.10}$$

The mole fraction of each species is needed to calculate the specific heat capacity of the flue gas, which can be calculated with Eq. 5.11.

$$c_{p,flue\,gas} = \frac{\sum\limits_{i=1}^{n} \nu_i\, c_{mpi}}{M_{flue\,gas}} = \frac{\sum\limits_{i=1}^{n} \nu_i\, c_{mpi}}{\sum\limits_{i=1}^{n} \nu_i\, M_i} \tag{5.11}$$

In this equation, c_{mpi} stands for the molar heat capacity and M_i for the molar mass of each species in the flue gas. All of the variables from Eqs. 5.1 to 5.6 have now been defined except for $\dot{Q}_{Wall}$ and $\dot{Q}_{Load}$. The calculation of these terms will be described in the next section.

5.2. Calculation of the Heat Transfer in the Furnace

The heat flux to the wall ($\dot{Q}_{Wall}$) and the thermal load ($\dot{Q}_{Load}$) in the furnace are calculated by an approach proposed by Jaklič et al. [119]. However, in contrast to their approach, where the input parameters, like wall temperature, were provided by measurements, in this model, these values are calculated by thermodynamic calculations. Therefore, this model can be considered a more general approach, which does not require temperature measurements of the wall or the gas temperatures in the furnace. For this reason, this model is ideal for use in design studies where no measurements are available. Jaklič et al. used the correlations by Hottel and Sarofim [97] to calculate the absorption and the emissivity coefficients of the flue gas, this model uses the WSGGM with the coefficient proposed by Smith et al. [98] to calculate these values.

In Figure 5.2, a schematic drawing of this approach can be seen. The furnace is divided into two thermodynamic systems (S_1 and S_2), which interact with each other. The thermodynamic system S_1 balances the heat fluxes at the wall, and the thermodynamic system S_2 balances the heat fluxes to the thermal load inside the furnace. In Figure 5.2, it is possible to see the different heat fluxes that are exchanged between the two thermodynamic systems and the gas phase. The heat flux between the gas phase and the wall is transferred both convectively ($\dot{q}_{conv_{gw}} \cdot A_w$) and radiatively ($\dot{q}_{rad_{gw}} \cdot A_w$). This is also the case for the heat flux between the gas phase and the thermal load. The heat flux between the wall and the thermal load is transferred via wall surface radiation ($\dot{q}_{rad_{ws}} \cdot A_w$), and is reduced by the amount which the gas phase absorbs ($\dot{q}_{abs_g} \cdot A_w$). For each thermodynamic system, an energy balance can be derived. In Eq. 5.12, the energy balance for the thermodynamic

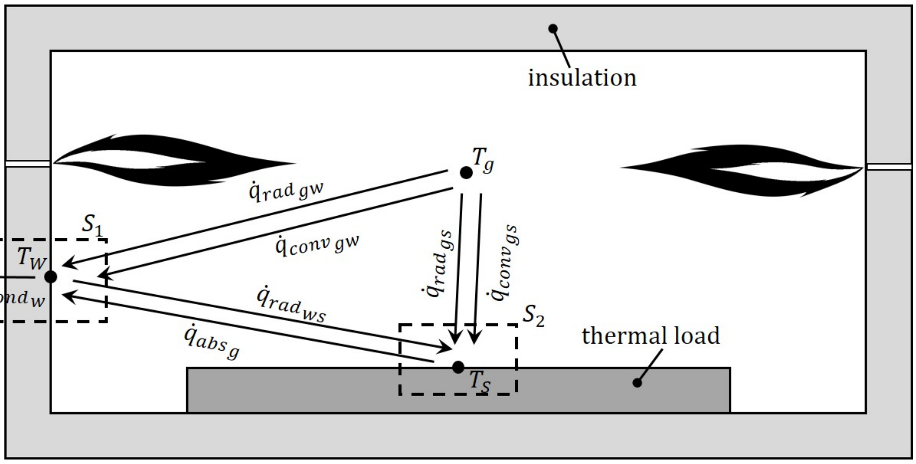

Figure 5.2.: Heat transfer inside the furnace. Adapted from [119]

system S_1 is shown.

$$0 = \dot{q}_{rad_{gw}} \cdot A_w + \dot{q}_{conv_{gw}} \cdot A_w - \dot{q}_{cond_w} \cdot \frac{A_w}{l_w} - \dot{q}_{rad_{ws}} \cdot A_s + q_{abs_g} \cdot A_s \tag{5.12}$$

The variables in Eq. 5.12 are defined as follows:

$$\dot{q}_{rad_{gw}} = \epsilon_g(T_g) \cdot \sigma \cdot T_g^4 - \alpha_g(T_g, T_w) \cdot \sigma \cdot T_w^4 \tag{5.13}$$

$$\dot{q}_{conv_{gw}} = a_{gw} \cdot (T_g - T_w) \tag{5.14}$$

$$\dot{q}_{rad_{ws}} = \frac{\epsilon_w \cdot \sigma \cdot T_w^4 - \epsilon_s \cdot \sigma \cdot T_s^4}{\frac{1}{\epsilon_s} + \frac{A_s}{A_w}\left(\frac{1}{\epsilon_w} - 1\right)} \tag{5.15}$$

$$\dot{q}_{abs_g} = \epsilon_g(T_w) \cdot \sigma \cdot T_w^4 - \alpha_g(T_w, T_s) \cdot \sigma \cdot T_s^4 \tag{5.16}$$

$$\dot{q}_{cond_w} = \lambda_w \cdot (T_w - T_{out}) \tag{5.17}$$

The radiative heat flux densities between the gas phase and the wall (see Eq. 5.13), as well as the wall and thermal load (see Eq. 5.15) are calculated by the Stefan-Bolzmann law. The Stefan-Bolzmann law states that the radiative heat flux emitted by a black body is proportional to the fourth power of the black body temperature ($\sigma \cdot T^4$). Real materials only emit and absorb a fraction of a black body. This is taken into account by the emissivity coefficient ϵ in the calculation. For solid bodies, a fixed value is used for the emissivity. The emissivity (ϵ_g) and the absorptivity (α_g) of the gas phase are calculated with the WSGGM and the coefficients from Smith et al. [98]. The heat losses through the furnace walls due to conduction are calculated using Eq. 5.17, where λ is the thermal conductivity of the furnace walls, and T_{out} the temperature of the atmosphere. The convective heat flux density to the wall from the gas phase is calculated using Eq. 5.14, where a_{gw} is the heat transfer coefficient. The convective heat transfer in high temperature furnaces is only minor, as the majority of the heat flux is transferred radiatively. Therefore, the heat transfer coefficient was assumed to be 10 W/(m^2 K), the same value as was used by Jaklič et al. [119].

In Eq. 5.18, the calculation of the total heat flux to the thermal load is shown. This equation was derived from the energy balance of the thermodynamic system S_2.

$$\dot{Q}_{load} = \dot{q}_{rad_{gs}} \cdot A_s + \dot{q}_{conv_{gs}} \cdot A_s + \dot{q}_{rad_{ws}} \cdot A_s - q_{abs_g} \cdot A_s \tag{5.18}$$

The variables $\dot{q}_{rad_{gs}}$ and $\dot{q}_{conv_{gs}}$ in Eq. 5.18 are the radiative and the convective heat flux density from the gas to the load, and are defined as follows:

$$\dot{q}_{rad_{gs}} = \epsilon_g(T_g) \cdot \sigma \cdot T_g^4 - \alpha_g(T_g, T_s) \cdot \sigma \cdot T_s^4 \tag{5.19}$$

$$\dot{q}_{conv_{gs}} = a_{gs} \cdot (T_g - T_s) \tag{5.20}$$

The variables $\dot{q}_{rad_{ws}}$ and q_{abs_g} are already known from Eq. 5.15 and Eq. 5.16.

5.3. Solution Strategy

Due to the mutual dependency of the different thermodynamic systems (entire furnace S_1, S_2) the calculations must be performed iteratively. In Figure 5.3, the iterative procedure for the calculation is shown. The gas temperature T_g nside the furnace is calculated by the energy balance for the entire furnace using Eqs. 5.1-5.6. In this system, the only unknown variable is the gas temperature; all other temperatures are known from the boundaries. The heat flux to the wall and the thermal load is assumed for the first iteration step because they are unknown. Therefore, the gas temperature is varied until the energy balance (Eq. 5.1) is satisfied, which is done by a solver embedded in the software Microsoft Excel. The calculated gas temperature is then used as an input parameter for the calculation of the two thermodynamic systems S_1 and S_2. With the calculated gas temperature T_g, the energy balance S_1 at the wall (using Eq.5.12-5.17) is solved by varying the wall temperature T_w until the energy balance is satisfied. From this calculation, the wall temperature T_w of the furnace is known.With the newly calculated gas temperature T_g and wall temperature T_w, the heat fluxes through the walls (using Eq.5.17) and to the the load (using Eq.5.15) are also calculated anew. Subsequently, the gas temperature T_g is used to calculate the total heat flux to the load, using Eq. 5.18. Due to the newly calculated heat fluxes through the wall and to the load, the energy balance of the entire furnace (see Eq.5.1) is imbalanced, and the gas temperature has to be calculated again. The solution process then starts from the beginning by recalculating Eq. 5.1. This is done until certain convergence criteria are reached. As convergence criteria, the error of both energy balances (S_1 and S_2) must be lower than 1% of the thermal input.

5.4. Calculation of High Temperature Furnaces

In this section, the model is used to calculate the lab-scale furnace VO2, described in Section 3.1.1 and numerically simulated in Section 3.1. The industrial scale aluminium melting furnace described in Section 4.1.1 and numerically simulated in Section 4.1 will also be calculated using this model. The results of the calculation with the model were compared to the results of the numerical simulation and measurements of the furnaces.

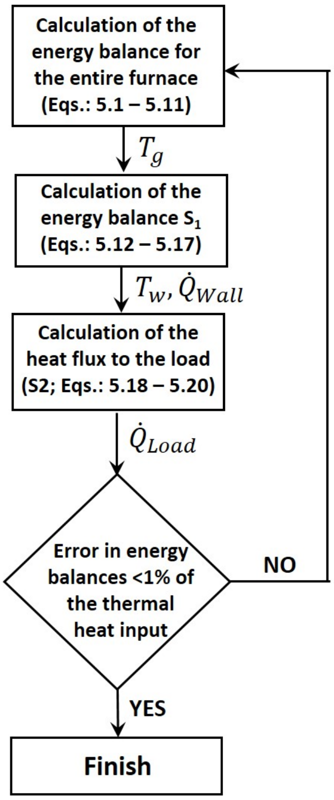

Figure 5.3.: Solution strategy for the simple furnace model

5.4.1. Lab-scale Furnace VO2

For the calculation of the lab-scale furnace VO2, the same boundary conditions were used as in the numerical simulation (see section 3.1.2). This section will consider only the configuration without the shielding. In Figure 5.4 and 5.5, the heat flux to the copper plate as calculated by the thermodynamic model is compared to the results of the numerical simulations and measurements for the temperature levels of 1070 °C and 1200 °C. The temperature level is defined as the temperature at measurement point T2 (see Figure 3.1 for the position of the measurement point). For both temperature levels, the thermodynamic model is able to predict the absolute value and the trends of the heat flux to the plate with the same accuracy as the CFD simulations and the measurements. For a temperature level of 1070 °C, the thermodynamic model predicts a heat flux of 37.42 kW for air-fuel conditions and 29.05 kW for oxy-fuel conditions. In the experiments under air-fuel conditions, a heat flux of 35.48 kW was measured, and while the measured heat flux under oxy-fuel conditions was 27.67 kW. The CFD simulation predicts a heat flux of 35.48 kW under air-fuel conditions and 27.21 kW under oxy-fuel conditions. The thermodynamic model can thus be seen to predict the same trends as measured in the experiments and the predicted by the CFD simulation. For a temperature of 1070 °C, the

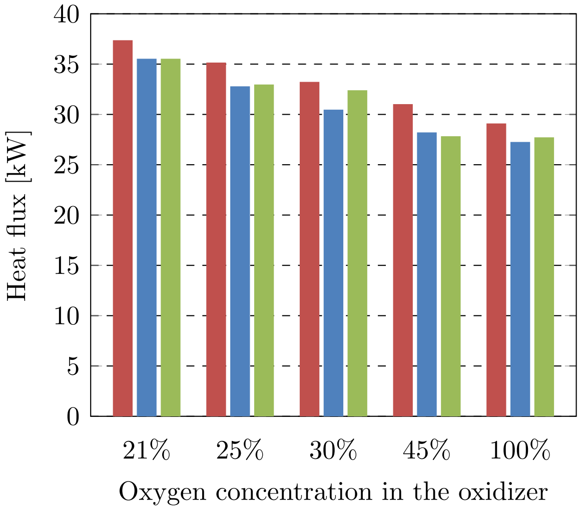

Figure 5.4.: Comparison of the heat flux to the load calculated with the thermodynamic model (🟥), the CFD simulation (🟦) and the measurements (🟩) for a temperature level of 1070 °C.

average deviation between the thermodynamic model and the measurements was 1.88 kW for all oxygen concentrations. At 1200 °C, the thermodynamic model predicts a heat flux of 57 kW for an oxygen enrichment of 25 Vol%, and a heat flux of 44.08 kW under oxy-fuel conditions. In the experiments of the same conditions, heat fluxes of 52.1 kW (25 Vol% O_2) and 47.45 kW (oxy-fuel) was measured. With 53.02 kW (25 Vol% O_2) and 41.82 kW (oxy-fuel), the simulation predicts similar values for the heat flux under the same conditions. The averaged deviation for all oxygen enrichments between the thermodynamic model and the measurements for a temperature level of 1200 °C was 3.77 kW. Considering the simplicity of the model, this can be seen as very good agreement. In Figure 5.6, the wall and gas temperatures calculated by the thermodynamic model for a temperature level of 1070 °C were compared to the temperatures calculated by the CFD simulation and to measurements. The gas temperature values calculated with the CFD simulation shown in Figure 5.6 are volume averaged values because the thermodynamic model only calculates one value for the gas temperature. For the same reason, the wall temperatures calculated by the CFD simulation, shown in Figure 5.6, are faced averaged values. From Figure 5.6, it is possible to see that the values and the trend of the gas temperature are predicted in the same way by both the thermodynamic model and the CFD simulation. For air-fuel conditions, the thermodynamic model predicts a gas temperature of 968 °C and the CFD calculation predicts a temperature of 1011 °C. In the experiments for air-fuel conditions, a gas temperature of 1044 °C was measured. For oxy-fuel conditions, the thermodynamic model predicts a temperature of 853 °C and the CFD calculation predicts a value of 844 °C. The averaged deviation between the CFD simulation and the thermodynamic model was 20 K for all oxygen concentrations, which can be seen as good agreement in consideration

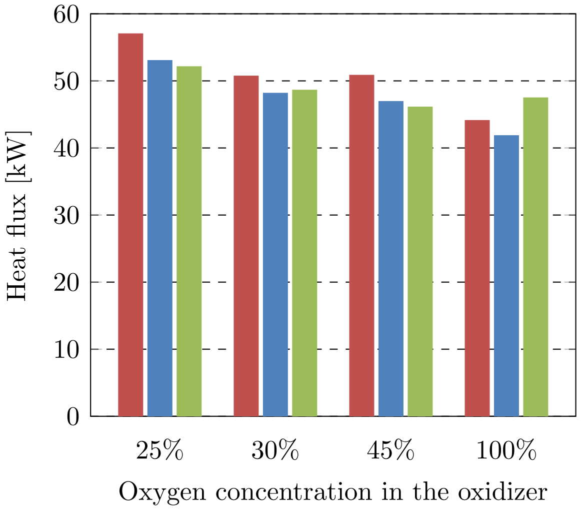

Figure 5.5.: Comparison of the heat flux to the load calculated with the simplified model (🟥), the CFD simulation (🟦) and measurements (🟩) for a temperature level of 1200 °C

of the model's simplicity. The wall temperatures calculated with the simplified model deviated more from the CFD simulation. For air-fuel conditions, the thermodynamic model predicts a wall temperature of 843 °C and the CFD calculations predicts a temperature of 976 °C. For oxy-fuel conditions, the thermodynamic model predicts a value of 781 °C and the CFD calculation predicts a wall temperature of 912 °C. This greater deviation can be explained by the fact that the three-dimensional effects in the corners of the furnace are neglected in the thermodynamic model. Furthermore, in the calculation of the wall temperature, all of the heat transfer calculation errors are cumulated, because the energy balance in Eq. 5.12 is solved by varying the wall temperature. The averaged deviation for the wall temperature between the CFD simulations and the simplified calculations was 126 K. Despite the somewhat higher deviation, the simplified model is able to predict the trend of the wall temperatures almost as well as the CFD simulation. For a temperature level of 1200 °C, the wall and gas temperatures calculated by the thermodynamic model are shown in Figure 5.7 and compared to the results of the CFD calculation and to measurements. The calculated temperatures showed a similar trend as for a temperature level of 1070 °C. Again, the gas temperature values and trends are similar predicted by the simplified model as by the CFD simulation. For an oxygen concentration of 25 Vol% in the oxidizer, the thermodynamic model predicts a gas temperature of 1075 °C, and the CFD simulation predicts a temperature of 1128 °C. In the experiments, a gas temperature of 1060 °C was measured for the same oxygen concentration. Under oxy-fuel conditions, the thermodynamic model predicts a gas temperature of 1047 °C and the CFD calculation a temperature of 1074 °C. The averaged deviation for the gas temperature between the numerical simulation and the simplified model was 24 K for all oxygen concentrations.

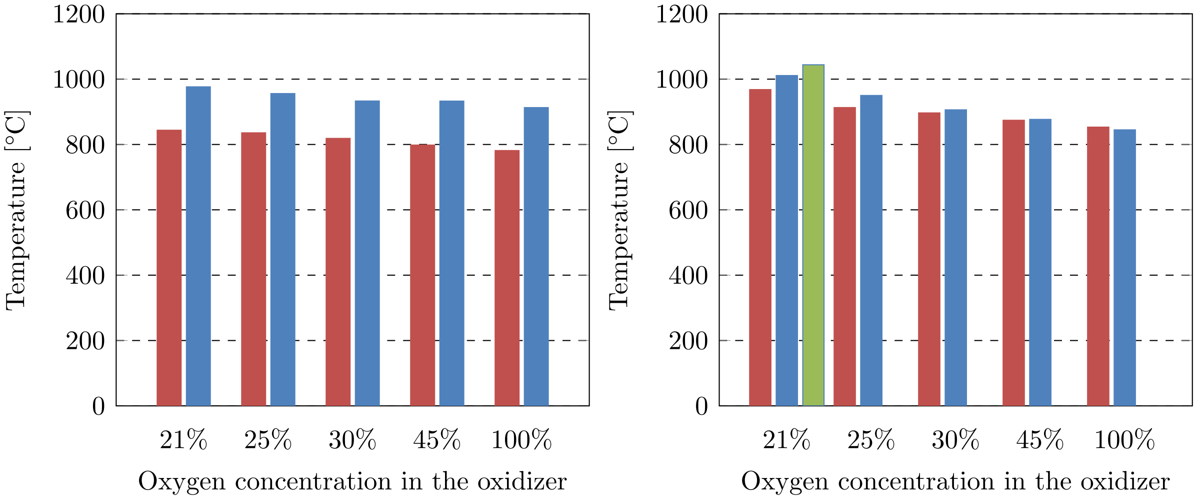

(a) Wall temperature

(b) Gas temperature

Figure 5.6.: Comparison between calculated temperatures with the simplified model (🟥), measurement (🟩) and the CFD calculation (🟦) for a temperature level of 1070 °C

Again, this can be seen as very good agreement considering the simplicity of the model. The calculated wall temperatures deviated more significantly, as they did for the temperature level of 1070 °C. The thermodynamic model predicts a wall temperature of 986 °C for an oxygen enrichment of 25 Vol%, and the CFD csimulation predicts a temperature of 1100 °C. For oxy-fuel conditions, the thermodynamic model calculates a wall temperature of 970 °C and the CFD calculation predicts a wall temperature of 1111 °C. The averaged deviation of the wall temperatures calculated by the thermodynamic model and the CFD simulation was 128 K. This comparison shows that the simplified model is able to predict the heat flux to a thermal load, the gas temperature, and the wall temperature of a lab-scale furnace almost as well as an advanced CFD simulation. In the next section, an industrial furnace will be investigated.

5.4.2. Aluminium Melting Furnace

For the calculation of the industrial scale furnace, the same boundary conditions were used as in the CFD simulation (see section 4.1.2). As in the previous section, the solutions of the thermodynamic model were compared to the CFD simulation performed in Section 4.1.4. In Figure 5.8, the heat flux to the melting as calculated with the thermodynamic model is compared to the heat flux predicted by the CFD simulation for different oxygen concentrations in the oxidizer. It is possible to see that the thermodynamic model predicts the heat flux to the melting for the different oxygen concentration in the oxidizer in a

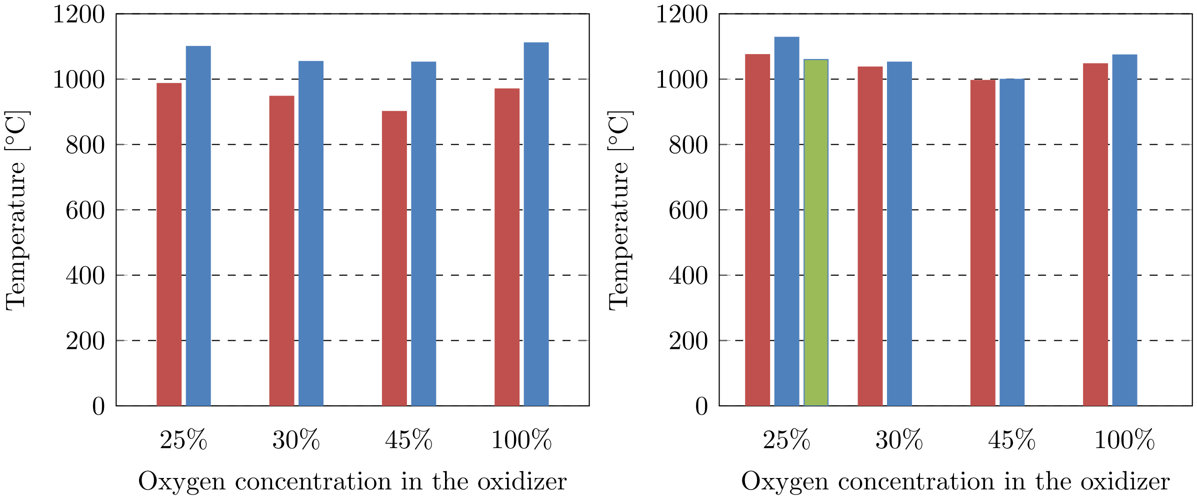

(a) Wall temperature

(b) Gas temperature

Figure 5.7.: Comparison between calculated temperatures with the simplified model (🟥), measurement (🟩) and the CFD calculation (🟦) for a temperature level of 1200 °C

similar way as the CFD simulation. The thermodynamic model predicts for an oxygen concentration of 70 Vol% in the oxidizer a heat flux of 1596 kW, the CFD calculation predicts a heat flux of 1636 kW. The averaged deviation between the simplified model and the numerical simulation was 43 kW for all oxygen concentrations, which can be seen as good agreement considering the scale of the furnace and the simplicity of the model. The wall and gas temperatures predicted by the thermodynamic model were also compared with the solution of the CFD simulation. In Figure 5.9, the comparison between the thermodynamic model and the CFD calculation is shown. The gas temperatures predicted by the numerical model are volume averaged values because the simplified model only calculates averaged values. For the same reason, the wall temperatures calculated by the numerical simulation are faced averaged values. As for the heat flux, the thermodynamic model can predict the temperature trends and values for all oxygen enrichments in the same way as the CFD simulation does. For an oxygen concentration of 70 Vol%, the thermodynamic model predicts a gas temperature of 1103 °C and the CFD calculation a temperature of 1124 °C. The averaged deviation between the thermodynamic model and the CFD simulation for the gas temperature was 16 K, which can be seen as very good agreement. For the wall temperature, the thermodynamic model calculates a wall temperature of 980 °C for an oxygen concentration of 70 Vol% in the oxidizer and the CFD calculation predicts a temperature of 965 °C. The averaged deviation between the thermodynamic model and the CFD simulation for the wall temperature was 18 K for all oxygen concentrations, which can be seen as good agreement. This demonstrates that the thermodynamic model is also able to calculate industrial scale furnace as well as a CFD

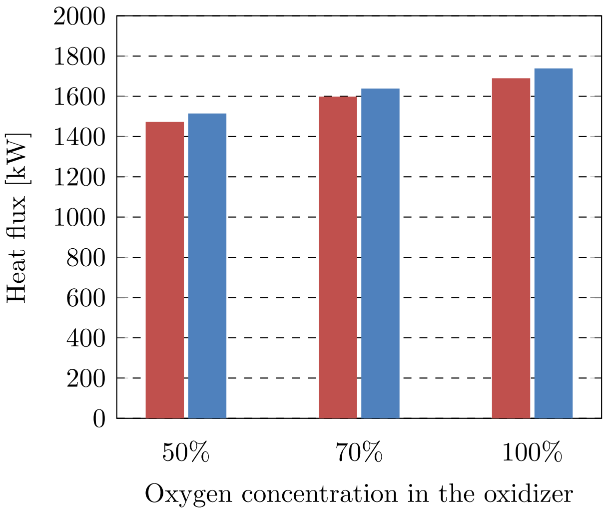

Figure 5.8.: Comparison of the heat flux to the melting calculated with simplified model (🟥) and the CFD calculation (🟦) for different oxygen concentrations in the oxidizer

simulation, bearing in mind its simple structure. To further validate the thermodynamic model, it was used to calculate the aluminium melting furnace for different thermal heat inputs, as done in the CFD simulations performed in Section 4.1.4, in order to show that the thermodynamic model is also able to calculate partial loads. The results of calculation with the thermodynamic model were compared to the results of CFD simulation. In Figure 5.10, the heat flux to the melting predicted by both the simplified model and the numerical simulation is shown for different thermal heat inputs. For a heat input of 2.4 MW, the thermodynamic model predicts a heat flux of 1596 kW and the CFD calculation predicts a heat flux of 1636 kW, which can be seen as good agreement. For a higher heat input of 3.2 MW, the thermodynamic model predicts a heat flux to the melting of 2116 kW, while the CFD simulations predicts a heat flux of 2187 kW. This shows that the thermodynamic model is able to predict the heat to the melting for different thermal heat inputs in a similar way as the CFD simulation. The averaged deviation in the heat flux between the CFD simulation and the thermodynamic model for all investigated heat inputs was 74 kW, which can again be seen as very good agreement. The wall and gas temperatures were also predicted by the thermodynamic model, and, as before, compared to the results of the CFD simulations. The calculated values of the thermodynamic model were compared to the volume averaged values for the gas temperature and the faced averaged wall temperatures of the CFD simulation. Figure 5.11 shows this comparison. The thermodynamic model is able to predict the temperature trends as well as the CFD simulation, and the total values are also well predicted. The thermodynamic model predicts a gas temperature of 1103 °C for a heat input of 2.4 MW, and the CFD calculation predicts a gas temperature of 1124 °C. The averaged deviation between the thermodynamic model and the CFD

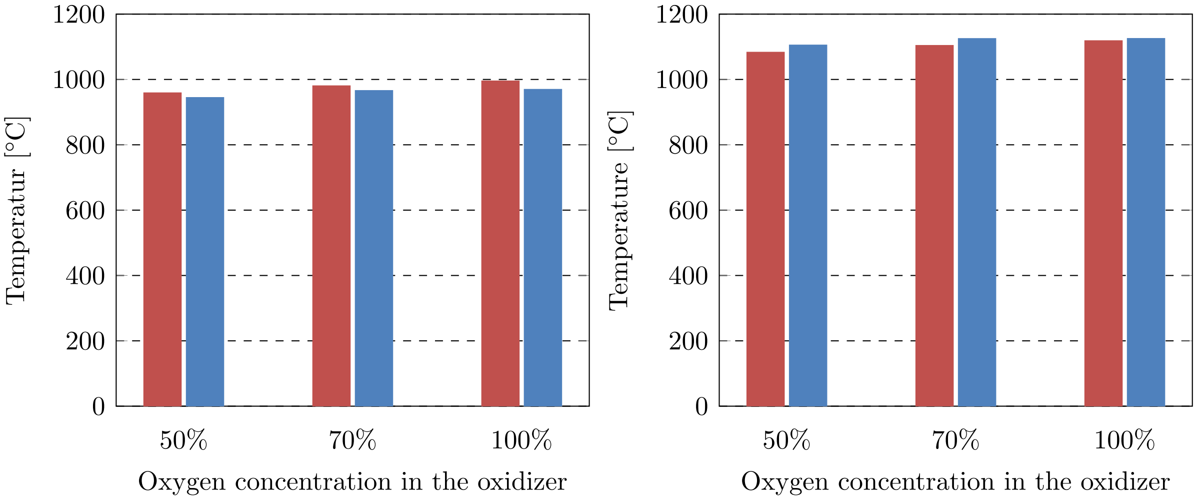

(a) Wall temperature

(b) Gas temperature

Figure 5.9.: Comparison between calculated temperatures with the simplified model (🟥) and the CFD calculation (🟦) in the aluminium melting furnace for different oxygen concentration in the oxidizer

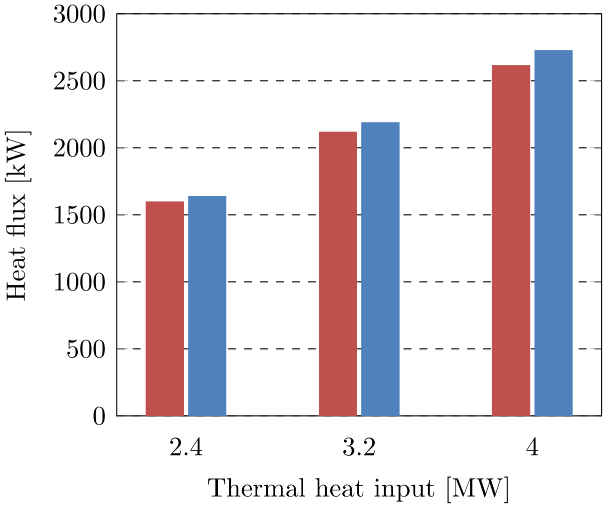

Figure 5.10.: Comparison of the heat flux to the melting calculated with simplified model (🟥) and the CFD calculation (🟦) for different thermal heat inputs

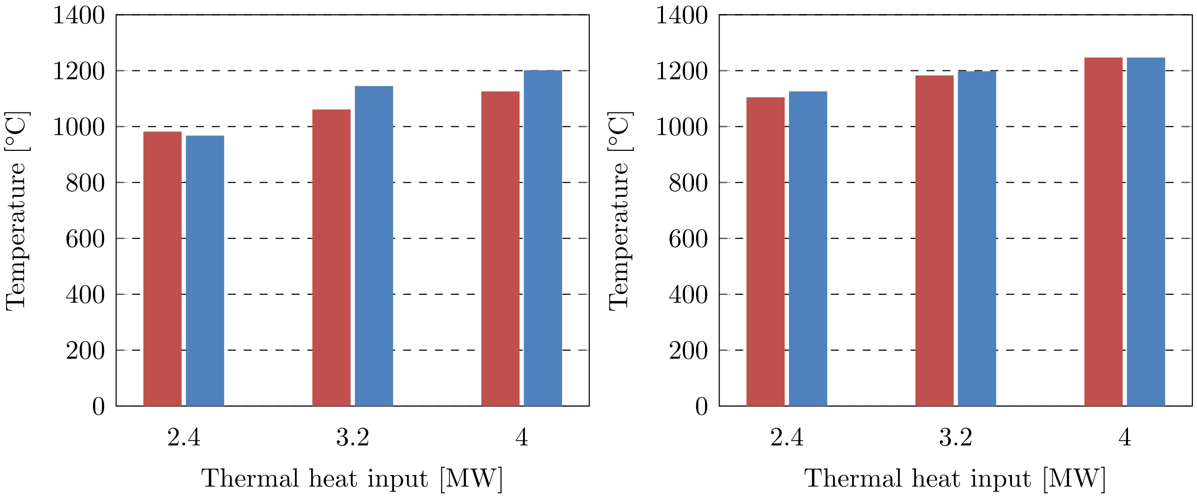

(a) Wall temperature

(b) Gas temperature

Figure 5.11.: Comparison between calculated temperatures with the simplified model (🟥) and the CFD calculation (🟦) in the aluminium melting furnace for different oxygen concentrations in the oxidizer

simulation, for all thermal heat inputs, was 12 K for the gas temperature. For the same thermal heat input of 2.4 MW, the thermodynamic model predicts a wall temperature of 980 °C and the CFD simulation predicts a temperature of 965 °C. The averaged deviation for the wall temperature for all heat inputs was 58 K, which is again very good agreement. This proves that the simplified model is capable of calculating industrial furnaces for different oxygen concentrations in the oxidizer and for different thermal heat inputs.

5.5. Thermodynamic Model for a Reheating Furnace

The thermodynamic model must be extended for the calculation of pusher-type reheating furnaces or walking hearth type furnaces. In these furnaces, the thermal heat input varies in the different zones, and the surface temperature of the billets (thermal load) changes over the furnace length. To calculate such furnaces, the furnace must be divided into sections. The different temperatures and heat fluxes must be calculated by solving the energy balances in each of these sections. Furthermore, the energy transfer to the next section must also be calculated. These calculations are not possible with the thermodynamic model used in Sections 5.1-5.3. Therefore, the energy balance for the entire furnace (see Eq. 5.1 and Figure 5.1) must be extended. In Figure 5.12, a schematic drawing of the thermodynamic system for such a section is shown. The thermodynamic system for the section is very similar to the thermodynamic system of the entire furnace (see Figure 5.1).

The only difference is that, in the thermodynamic system of the section, an additional heat flux, representing the incoming heat flux of the flue gas from the previous section ($\dot{Q}_{Flues\,gas_{in}}$), is added to the system. The radiative heat transfer from one section to another is neglected. This is due to the fact that, to calculate the radiative heat transfer from one section to another, viewing factors must be taken into account, which would significantly increase the complexity and the calculation time of the model. Therefore, the energy balance in Eq. 5.1 is extended by only adding the heat flux $\dot{Q}_{Flues\,gas_{in}}$. The total energy balance for a section of the furnace is given in Eq. 5.21.

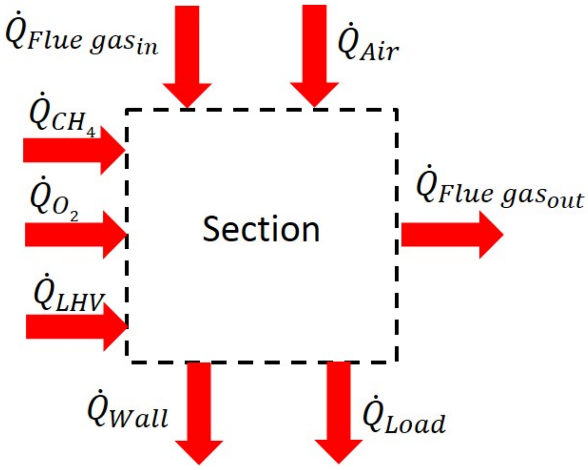

Figure 5.12.: Schematic drawing of the energy balance of a section of the furnace

$$0 = \dot{Q}_{Air} + \dot{Q}_{CH_4} + \dot{Q}_{O_2} + \dot{Q}_{LHV} + \dot{Q}_{Flues\,gas_{in}} - \dot{Q}_{Flue\,gas_{out}} - \dot{Q}_{Wall} - \dot{Q}_{Load} \tag{5.21}$$

The additional heat flux $\dot{Q}_{Flues\,gas_{in}}$ to the system is known from the previous section, where it is denoted as $\dot{Q}_{Flues\,gas_{out}}$. All other variables are calculated in the same way as for the energy balance of the entire furnace (see Eqs. 5.2 to 5.20). Thus, with this sectional model it is possible to investigate the effect of different oxidizer compositions in different zones of the furnace on the heat transfer in the furnace. To this end, the molar flows of the combustion species (H_2O, CO_2, N_2, O_2) are calculated and transferred from one section to the next. In the next section, the molar flow of the species arising from the combustion in that section, is added to the molar flow of the previous section. The molar flow of each species can be calculated with Eq. 5.22, where $\dot{M}_i$ stands for the molar flow of each species and X_i for the mole of each species arising from the combustion of one mole CH_4.

$$\dot{M}_i = \frac{\dot{m}_{CH_4}}{M_{CH_4}} \cdot X_i \tag{5.22}$$

The molar flow of each species is transferred from one section to the next. In the next section, the molar flow of the combustion products of CH_4 with the same or another oxidizer is added to the incoming molar flow. In each section, the molar fraction of each species can be calculated with the molar flows. In Eq. 5.23, the calculation of the molar fraction of one species using the molar flows is shown.

$$\nu_i = \frac{\dot{M}_i}{\sum\limits_{i=0}^{n} \dot{M}_i} \tag{5.23}$$

With this modified model, it is also possible to calculate reheating furnaces; such a calculation will be performed in the following section. With this thermodynamic model, the calculation time for a reheating furnace is a few seconds. In contrast, a CFD simulation of the same furnace takes a few days to converge, if numerically efficient models are used. If other, more computationally demanding models are used, calculation times can exceed a few weeks. Therefore, this thermodynamic model is a perfect tool for quick design studies.

5.5.1. Calculation of a Reheating Furnace

In this section, the walking hearth type furnace described in Section 4.3.1 is calculated by means of the extended thermodynamic model described above. To this end, the furnace must be divided into sections. In this case, the furnace was divided into five sections, which are shown in Figure 5.13. The calculation of the furnace with the thermodynamic model must be performed in the direction of the flue gas flow, otherwise the calculation has to be performed iteratively. Therefore, the first section is located at the outlet of the billets and the last section, at the chimney, where the flue gas is discharged from the furnace. For the calculation with the thermodynamic model, the same boundary conditions were used as in the CFD calculation (see Section 4.3.2). The surface temperatures of the billets along the

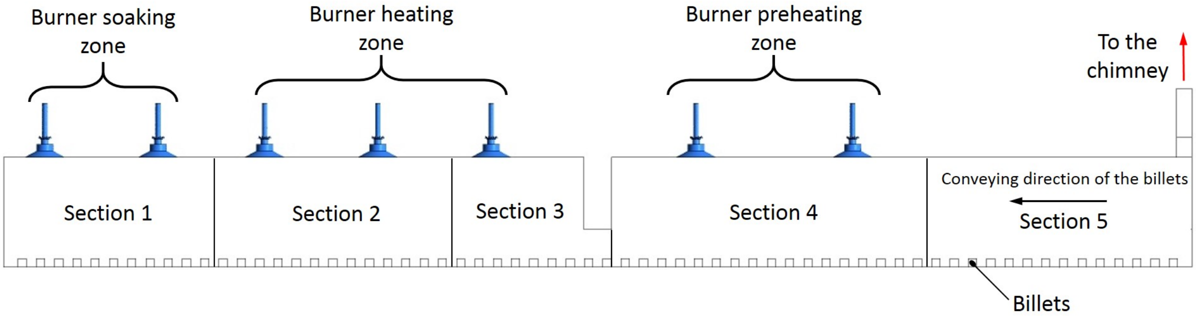

Figure 5.13.: Sectional division of the walking hearth type reheating furnace for the calculation with the simplified model

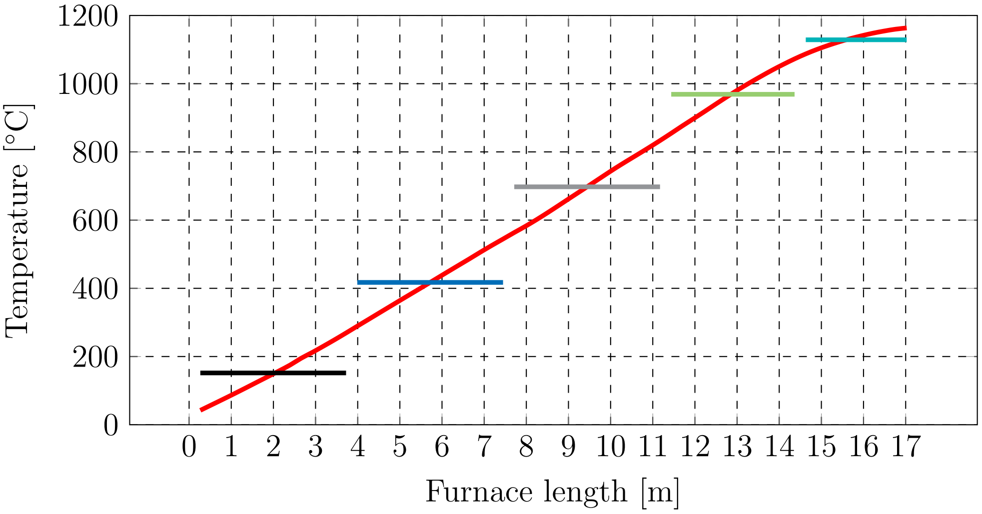

Figure 5.14.: Surface temperature of the billets in the different sections: Surface temperature of the billets from CFD (—), surface temperature section 1 (—), surface temperature section 2 (—), surface temperature section 3 (—), surface temperature section 4 (—), surface temperature section 5 (—)

furnace are an important input parameter to the calculation of the thermodynamic model. The surface temperatures of the billets along the furnace length, as calculated by the CFD simulation, are shown in Figure 5.14. The surface temperature of the billets can be seen to increase almost linearly along the furnace's length; only at the end of the furnace (furnace length 15 to 17) is the increase of the billet surface temperature not linear. This almost-linear behaviour is typical of reheating furnaces. Therefore, the surface temperatures of the billet in the furnace can be approximated very well by using a linear function between the in- and outlet temperatures of the billets. In this calculation, the surface temperatures of the billets in the different zones were taken from the CFD calculation. With a linear temperature profile, similar results are obtained, but for a better comparison between the CFD simulation and the thermodynamic model, the surface temperatures for the billet are taken from the CFD simulation. For the calculation with the thermodynamic model, the surface temperatures of the billets calculated by the CFD simulation were averaged for each zone. In Figure 5.14, the zone averaged surface temperatures of the billets are shown for the entire furnace. These temperatures were used for the calculation with the thermodynamic model. The heat fluxes, wall temperatures, and gas temperatures calculated by the simplified model were compared to the results of the CFD calculation. In Figure 5.15, the calculated heat flux to the billets in the different zones are shown. The trend of the heat flux in the reheating furnace can be predicted in a similar way with the simplified model as with the CFD calculation. The absolute values in each zone are also well predicted; only in section 5 is the difference between the simplified model and the

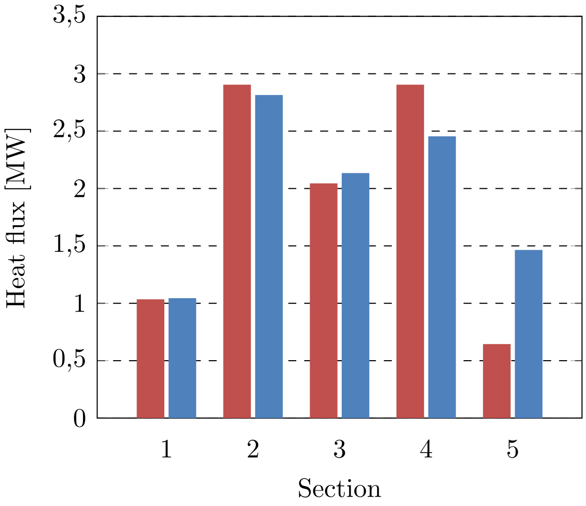

Figure 5.15.: Comparison of the calculated heat flux to the billets in the different sections with the simplified model (🟥) and the CFD simulation(🟦)

CFD simulation higher. This higher deviation can be explained by the fact that no burners are active in this zone. Therefore, the only energy source for this section comes from the heat flux ($\dot{Q}_{Flues\,gas_{in}}$) transported from the previous section into this one. Additionally, this section has a higher wall surface (because of the additional front wall of the furnace) resulting in higher heat losses to the atmosphere. Neglecting the radiative heat transfer from one section to the next also accounts for the higher deviation. Because of the cooler surface temperatures of the billets at the beginning of the furnace, the billets in this section receive a higher radiative heat flux from the walls in Section 4, where burners are located, and therefore higher wall temperatures arise. Considering the simplicity of the model, the results are still sufficient. In Figure 5.16, the wall and gas temperatures calculated with the thermodynamic model are compared with the averaged values from the CFD calculation. It is possible to see that they follow the same trends as the CFD calculation. In Section 5, the deviation between the CFD calculation and the thermodynamic model is higher, for the reasons explained above. The deviation of the wall temperatures is higher than that of the gas temperatures. This is due to the fact that the energy balance at the wall (see Eq. 5.12) is solved by varying the wall temperature. Hence, all of the errors made due to simplification of the model are cumulated in the wall temperature. Still, the results of the calculation are sufficient, considering the simplicity of the model. This comparison has shown that the simplified model can also be used for the calculation of industrial scale furnaces. The results of the model are sufficient for technical design studies, where the influence of oxygen enrichment in different zones is investigated. The thermodynamic model proposed thus provides a simple and easy way to estimate the wall and gas temperatures as well as the heat flux in the furnace.

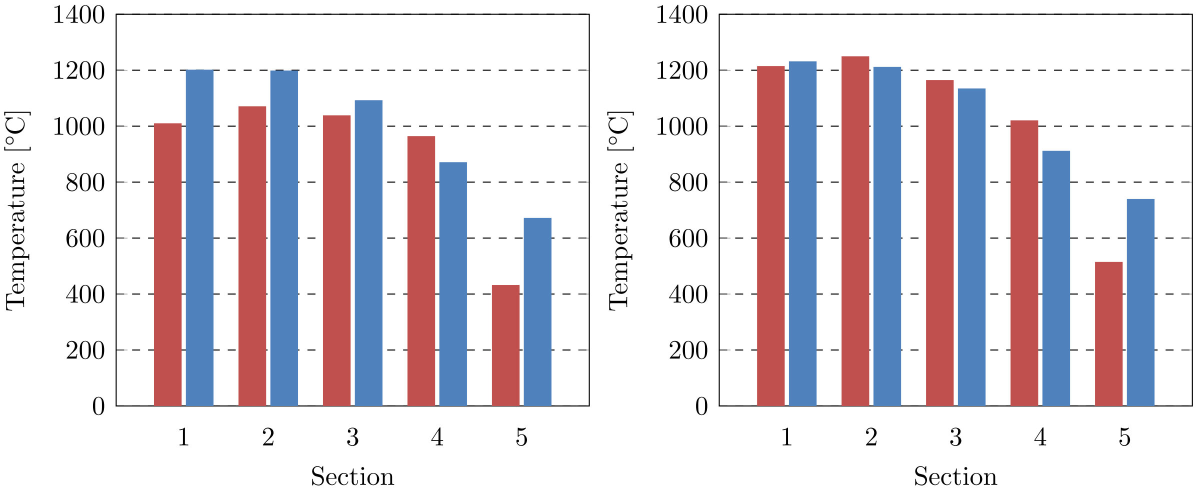

(a) Wall temperature

(b) Gas temperature

Figure 5.16.: Comparison between calculated temperatures with the simplified model (🟥) and the CFD calculation (🟦) in the different zones in the walking hearth type reheating furnace

5.5.2. Conclusion

In this section, a thermodynamic model is presented that is capable of calculating lab-scale and industrial-scale furnaces. This model uses simple thermodynamic correlations, which makes it very time efficient and easy to use. The thermodynamic model calculates all heat fluxes (heat flux to the wall and to the thermal load), gas temperature, and wall temperature in the furnace. Furthermore, the model can not only be used for air-fuel combustion, but also for oxygen-enriched or oxy-fuel conditions. The thermodynamic model was used to investigated a lab-scale furnace, which operates under different oxygen enrichments, where detailed measurements of the heat flux to a thermal load were available. This lab-scale furnace was also investigated by an advanced CFD simulations. The thermodynamic model showed good agreement with the measurements and the results of the CFD calculations. The averaged deviation between the heat flux calculated with the thermodynamic model and that measured was 1.88 kW, for an averaged heat flux level of 31.24 kW, which can be seen as very good agreement. The gas and wall temperatures calculated with the thermodynamic model showed a similar temperature trend as the CFD calculation. The averaged deviation for the gas temperature was 20 K, at a temperature level of nearly 1000 °C, which can be seen as very good agreement considering the simplicity of the model. With 126 K, the wall temperature showed a higher deviation from the results of the CFD calculation. This is due to the thermodynamic model's neglect of the three-dimensional heat conduction effects in the corners of the furnace. The thermodynamic model was also used to investigate an industrial scale aluminium melting furnace and a walking hearth type reheating furnace. For the aluminium melting furnace, the results of the calculations with the thermodynamic model showed close agreement to the results of the CFD calculation. This demonstrates that the thermodynamic model can also be used for industrial scale furnaces. In contrast to the aluminium melting furnace, the reheating furnace must be calculated in sections because the surface temperatures of the billets increase along the furnace's length and because of the different thermal heat inputs in the different zones of the furnace. Therefore, the thermodynamic model was extended for the calculation of a walking hearth type reheating furnace. The results of the calculations of the extended thermodynamic model were again compared to the results of CFD simulations. The comparison showed that the thermodynamic model can predict the trends for the heat flux, gas temperature, and wall temperature as well as an advanced CFD simulation. The greatest deviation between the CFD calculations and the calculations of the thermodynamic model occurred at the beginning of the furnace, where no burners are located. Thanks to the thermodynamic model's fast calculation time of only a few seconds, as well as its accuracy (considering its simplicity), it can be used to determine the effect of oxygen enrichment on the heat transfer, gas temperatures, and wall temperatures in any furnace. Additionally, the model can be used to perform case studies without the need to run expensive CFD calculations.

6. Conclusion and Outlook

In this work, the effect of OEC on industrial high temperature processes was investigated both experimentally and by means of numerical simulations. Only a few studies on OEC in high temperature process have been published in recent years. Most of the publications and studies deal with the oxy-fuel combustion of coal in power plants and CCS. Therefore, a novel CFD model was developed, which makes it possible to calculate industrial scale furnaces with little computational demand. A method was also presented which makes it possible to divide the heat flux to a thermal load into its convective, gas radiative, and wall surface radiative parts. Based on the experiments and the CFD simulations, a thermodynamic model was developed, that makes it possible to calculate the heat transfer, wall temperature, and gas temperature in a furnace by means of thermodynamic correlations for air-fuel and OEC conditions.

The experiments performed on the lab-scale furnace VO2 were done for temperature levels of 1070 and 1200 °C, which are typical of high temperature processes. The term temperature level is defined as the temperature measured at a certain measurement point in the furnace. The beneficial effects of OEC on furnace efficiency was also demonstrated by the experiments, which, were performed for oxygen concentrations between 21-100 Vol% in the oxidizer. These experiments showed that, for a temperature level of 1070 °C, the furnace efficiency increased from 48% under air-fuel conditions to 76% under oxy-fuel conditions. For a temperature level of 1200 °C, a similar trend was observed: under air-fuel conditions, furnace efficiency was 42% and increased to 65% under oxy-fuel conditions. This shows the fuel-saving potential of OEC in high temperature processes, like reheating furnaces.

The experimental data was subsequently used to validate the numerical models. The numerical simulations of the lab-scale furnace VO2 were performed with the commercial software package ANSYS Fluent. For the combustion simulation, the numerically efficient SFM method was used with the skeletal25 reaction mechanism, which considers 25 different reactions and 17 species. The RTE was solved using the DO model in combination with the WSGGM, using the coefficients of Smith et al. [98]. It has been shown in previous studies that the skeletal25 reaction mechanism is applicable for all kinds of oxygen enrichments, ranging from 21 Vol% up to 100 Vol%, especially in combination with the SFM. The simulations and the experiments of the lab-scale furnace VO2 showed close agreement with each other. The averaged error over all of the gas-temperature measurement points for the different O_2 concentrations, experimental settings, and temperatures was between 24-43 K. This can be seen as sufficient agreement for temperatures between 1070 and 1200 °C. Furthermore, the total heat flux to a water-cooled plate was calculated with CFD and the results were compared to measurements. This comparison showed close agreement for the temperature level of 1070 °C and all O_2 concentrations in the oxidizer. For the temperature level of 1200 °C, the deviation between measurements and simulations was slightly higher, especially for high oxygen concentrations in the oxidizer. The higher deviation at higher oxygen concentrations was due to fact that the furnace was not completely tight, allowing some air from the outside atmosphere to leak into the furnace.

A lab-scale furnace that was experimentally investigated by the IFRF, was also investigated using CFD simulations. This furnace was operated under oxy-fuel conditions, with a thermal input of 0.8 MW. In this furnace, detailed in-flame measurements of gas temperatures and species concentrations were performed. In the CFD simulation, the three main combustion models (EDM, EDC and SFM) were used. For the EDM, a simple two- step reaction mechanism was used, while for the EDC, a four-step mechanism was used, which was specially adapted for oxy-fuel conditions. For the SFM, the detailed skeletal25 mechanism and the smooke46 mechanism were used again. The CFD simulations revealed that the EDM overestimates the gas temperature, due to its neglect of dissociation effects. The EDC with the four-step mechanism showed good results for the gas temperature and the species concentrations, though it has the drawback of long calculation times. In contrast to the lab-scale furnace VO2 investigated before, the SFM with the skeletal25 predicted a different flame shape, and comparison with the measurements also revealed a higher deviation. The SFM with the smooke46 reaction mechanism was not able to correctly predict either the gas temperature or the species concentrations in the furnace. For the SFM with the skeletal25 reaction mechanism, it was found that the higher deviations originate from a limitation of the SFM under oxy-fuel conditions. If the shear rates between the oxidizer and the fuel are too low, the SFM calculates unrealistic flame temperatures and shapes. For higher shear rates between the oxidizer and the fuel, both the flame shape and the temperatures are predicted well. This limitation of the SFM for oxy-fuel conditions is a new finding, and constitutes important information about the proper use of the SFM under oxy-fuel conditions. The SFM was further investigated for flat-flame burners, which are commonly used in reheating furnaces. Therefore, experiments on a lab-scale furnace (burner chamber) were performed with a flat flame burner, for oxygen concentrations in the oxidizer ranging from 21 Vol% up to 37 Vol%. The heat input was set to 200 kW, while the oxygen concentration was adapted in these experiments. Again, the SFM with the skeletal25 reaction mechanism was used for the numerical investigation, and additional simulations were performed with the GRI3.0 and the smooke46 reaction mechanisms. The numerical simulation showed close agreement to the measured temperatures, with a maximum deviation of 16 K for gas temperatures above 1200 °C. The investigation revealed that the SFM in combination with detailed reaction mechanisms (GRI3.0, smooke46) other than the skeletal25 is capable of calculating the correct flame temperature and the correct shape of the flat flame burner for oxygen concentrations in the oxidizer up to 37 Vol%. This is in contrast to the findings of Prieler et al. [31], who showed that, for jet flames, all detailed reaction mechanisms except the skeletal25 fail to correctly predict the gas temperature for oxygen concentrations higher than 30 Vol%. In combination with the skeltal25 reaction mechanism, the SFM exhibited high accuracy and low computation demand for all investigated furnaces and all oxygen concentrations in the oxidizer (21 Vol%-100 Vol% O_2). It is therefore possible to conclude that the SFM in combination with the skeletal25 mechanism is the best choice for simulations of high temperature furnaces with different oxygen concentrations in the oxidizer.

In this thesis, the radiation models for solving the RTE and the models for calculating the radiative properties of the flue gas were also evaluated for use under oxy-fuel or OEC conditions. Comparison of the measured and calculated heat fluxes in the lab-scale furnace VO2 showed close agreement to each other. This proves that the DO, in combination with the WSGGM using coefficients from Smith et al. [98], is sufficient for calculating lab-scale furnaces under oxy-fuel and OEC conditions. Additionally, a method was developed which makes it possible to determine the amount of heat flux that emerges from convection, gas radiation, and wall surface radiation. This was done using one additional CFD calculation, where only one transport equation was calculated anew, and all other governing equations (energy, momentum, etc.) were frozen. Therefore, this method entails very low computational demand. This method was subsequently used to calculate the heat fluxes due to gas and wall surface radiation in the lab-scale furnace VO2. These calculations revealed that the majority of the total heat flux to the thermal load is due to wall surface radiation, and only a small amount occurs due to gas radiation or convection. Furthermore, the calculations showed that the flue gas reduces the heat flux to the thermal load with an increasing oxygen concentration in the oxidizer in the lab-scale furnace. This is because the absorption coefficient of the flue gas increases with the increasing oxygen concentration in the oxidizer. Additionally, the mass flux in the furnace is reduced with increasing oxygen concentrations in the oxidizer, which leads to a greater reduction of the flue gas temperatures near the thermal load. The lower flue gas temperatures further increase the absorption coefficient near the thermal load, which leads to a higher absorption of the radiative heat flux from the furnace walls.

The validated CFD models were subsequently used to investigate industrial-scale furnaces. First, an aluminium melting furnace was investigated for oxygen concentrations of 50, 70 and 100 Vol% in the oxidizer. The numerical simulation showed a higher heat flux to the melting with increasing oxygen concentrations, resulting in higher furnace efficiency, as seen for the lab-scale furnace. Furthermore, the heat flux due to gas and wall surface radiation was determined using the method developed in this thesis. The investigation showed that the majority of the heat flux in the aluminium melting furnace is due to wall surface radiation, as was found in the lab-scale furnace VO2. In contrast to the lab-scale furnace, the gas radiation increases the heat flux to the molten aluminium. This is due to the fact that the gas volume is higher in the aluminium melting furnace, and that the surface temperature of the molten aluminium is far higher than the surface temperature of the thermal load in the lab-scale furnace, which results in a higher gas temperature. Additionally, the high amount of wall surface radiation indicates that it is necessary to correctly predict the surface temperatures of the refractory lining (walls) in a furnace, due to the high temperature dependency of the heat transfer between solid bodies. Therefore, it is necessary to model the refractory lining in a CFD accurately, in order to calculate the correct surface temperatures, and, therefore, the correct heat flux.

Next, an industrial-scale pusher-type reheating furnace was investigated, which is used to raise the temperature of billets from ambient temperatures to 1100 °C. For this purpose, a novel and numerically efficient model was developed, which makes it possible to calculate the gas phase combustion and the periodically transient reheating of the billets in one steady-state simulation. This is done by treating the billets as a highly viscous fluid, which is justified due to the arrangement of the billets in this type of furnace. With this approach, and in combination with the SFM, the calculation time is dramatically reduced in comparison to a fully transient simulation. The calculated gas temperatures and billet temperatures showed close agreement to the measured values recorded by the furnace's control system. Furthermore, the CFD simulation revealed an asymmetrical temperature distribution in the billets, which is caused by the flow structure in the furnace as induced by the swirl of the swirl burners. This was also confirmed by the operator of the furnace. The simulations also revealed the high influence of the skids, located at the beginning of the furnace, on the temperature distribution of the billets.

Based on the experiments and the CFD simulations, a simple 0-D/1-D thermodynamic model was developed in order to determine the influence of oxygen enrichment on the heat flux, gas temperatures, and wall temperatures in the furnace. This model is based on simple thermodynamic and heat transfer correlations, and can therefore be calculated using a simple program, such as Microsoft Excel. Because of the simplicity of this thermodynamic model, the calculation time is very low, and it can be used to quickly determine the influence of different oxygen enrichments on the heat transfer in a furnace. This thermodynamic model was used to calculate the furnaces that had been previously investigated by experiments and CFD simulations. The simplified model predicted nearly the same values and the same trends for the heat flux and the gas temperature; greater deviations were only observed for the wall temperatures. The higher deviations for the wall temperatures can be accounted for by the fact that the simple model neglects the three-dimensional heat conduction effects in the corners of the refractory lining. Considering the simplicity of the thermodynamic model, these results can be seen as very good. This model can be used to estimate the influence of OEC on heat transfer in a furnace with very little effort.

Outlook

Further investigations should be carried out on the applicability of new combustion models, such as the Flamelet Generated Manifold (FGM), for OEC and oxy-fuel combustion. The newly proposed FGM is a promising model for the calculation of oxy-fuel and OEC. The FGM is able to overcome the limitations of the SFM, such as the calculation of flame ignition/extinction and the calculation of flames with low shear rates, making it of interest to future studies in this area.

In industrial furnaces, scale formation on billets and slabs is an important issue, and the influence parameters are difficult to determine using experiments, due to difficulty of conduction experiments on large-scale furnaces. Therefore, the development of numerical models which can predict scale formation is urgently need. With such a model, the main parameters influencing scale formation could be determined, and measures could be developed to reduce the scale formation.

Further work is also needed on the transient simulation of reheating furnaces in order to simulate the transient behaviour of furnace during a load change as well as its influence on product quality. Such simulations would allow new control strategies to be developed, and thus, the efficiency of the furnace could be increased.

Bibliography

[1] B. Mayr, R. Prieler, M. Demuth, M. Potesser, and C. Hochenauer. “CFD and experimental analysis of a 115 kW natural gas fired lab-scale furnace under oxy-fuel and air–fuel conditions.” In: *Fuel* 159 (2015), pp. 864–875.

[2] B. Mayr, R. Prieler, M. Demuth, and C. Hochenauer. “The usability and limits of the steady flamelet approach in oxy-fuel combustions.” In: *Energy* 90 (2015), pp. 1478–1489.

[3] B. Mayr, R. Prieler, M. Demuth, L. Moderer, and C. Hochenauer. “CFD analysis of a pusher type reheating furnace and the billet heating characteristic.” In: *Applied Thermal Engineering* 115 (2017), pp. 986–994.

[4] B. Mayr, R. Prieler, M. Demuth, M. Potesser, and C. Hochenauer. “Computational analysis of a semi-industrial furnace fired by a flat flame burner under different O_2/N_2 ratios using the steady laminar flamelet approach.” In: *Journal of the Energy Institute* 90.4 (2017), pp. 602–612.

[5] B. Mayr, R. Prieler, M. Demuth, and C. Hochenauer. “Comparison between solid body and gas radiation in high temperature furnaces under different oxygen enrichments.” In: *Applied Thermal Engineering* 127 (2017), pp. 679–688.

[6] J. Davison. “Performance and costs of power plants with capture and storage of CO2.” In: *Energy* 32.7 (2007), pp. 1163–1176.

[7] IEA. “World Energy Outlook 2014.” In: (2014).

[8] B. Manickam, F. Dinkelacker, T. Lobe, and M. Tertychnyy. “Enriched oxygen combustion simulation for rotary klin application.” 4th European combustion meeting. Vienna, 2009.

[9] M. Falcitelli, S. Pasini, and L. Tognotti. “Modelling practical combustion systems and predicting NOx emissions with an integrated CFD based approach.” In: *Computers & chemical engineering* 26.9 (2002), pp. 1171–1183.

[10] B. Metz and Intergovernmental Panel on Climate Change, eds. *IPCC special report on carbon dioxide capture and storage.* OCLC: ocm64949778. Cambridge: Cambridge University Press, for the Intergovernmental Panel on Climate Change, 2005. 431 pp.

[11] M. Rabensteiner, G. Kinger, M. Koller, and C. Hochenauer. “Three Years of Working Experience with Different Solvents at a Realistic Post Combustion Capture Pilot Plant.” In: *Energy Procedia* 63 (2014), pp. 1578–1584.

[12] M. Rabensteiner, G. Kinger, M. Koller, G. Gronald, and C. Hochenauer. “Investigation of carbon dioxide capture with aqueous piperazine on a post combustion pilot plant Part II: Parameter study and emission measurement.” In: *International Journal of Greenhouse Gas Control* 37 (2015), pp. 471–480.

[13] M. Rabensteiner, G. Kinger, M. Koller, G. Gronald, and C. Hochenauer. “Pilot plant study of ethylenediamine as a solvent for post combustion carbon dioxide capture and comparison to monoethanolamine.” In: *International Journal of Greenhouse Gas Control* 27 (2014), pp. 1–14.

[14] P. Pak, Y. Lee, and K. Ahn. “Characteristics and economic evaluation of a power plant applying oxy-fuel combustion to increase power output and decrease CO2 emission.” In: *Energy* 35.8 (2010), pp. 3230–3238.

[15] M. B. Toftegaard, J. Brix, P. A. Jensen, P. Glarborg, and A. D. Jensen. “Oxy-fuel combustion of solid fuels.” In: *Progress in Energy and Combustion Science* 36.5 (2010), pp. 581–625.

[16] G.P. Hammond, S.S. Ondo Akwe, and S. Williams. “Techno-economic appraisal of fossil-fuelled power generation systems with carbon dioxide capture and storage.” In: *Energy* 36.2 (2011), pp. 975–984.

[17] A. A. Bhuiyan and J. Naser. “Thermal characterization of coal/straw combustion under air/oxy-fuel conditions in a swirl-stabilized furnace: A CFD modelling.” In: *Applied Thermal Engineering* 93 (2016), pp. 639–651.

[18] A. A. Bhuiyan and J. Naser. “Computational modelling of co-firing of biomass with coal under oxy-fuel condition in a small scale furnace.” In: *Fuel* 143 (2015), pp. 455–466.

[19] A. A. Bhuiyan and J. Naser. “CFD modelling of co-firing of biomass with coal under oxy-fuel combustion in a large scale power plant.” In: *Fuel* 159 (2015), pp. 150–168.

[20] L. Álvarez, C. Yin, J. Riaza, C. Pevida, J.J. Pis, and F. Rubiera. “Biomass co-firing under oxy-fuel conditions: A computational fluid dynamics modelling study and experimental validation.” In: *Fuel Processing Technology* 120 (2014), pp. 22–33.

[21] R. Prieler. "Numerical Modelling of Chemistry, Radiation and Transient Heating Characteristics in High Temperature Processes." PhD thesis. Graz: Graz University of Technology, 2016.

[22] C. E. Baukal, ed. *Oxygen-enhanced combustion.* Boca Raton, Fla: CRC Press, 1998. 369 pp.

[23] BM Abraham, JG Asbury, EP Lynch, and APS Teotia. "Coal-oxygen process provides CO2 for enhanced recovery." In: *Oil Gas Journal* 80 (1982), pp. 68–75.

[24] T. Wall et al. "An overview on oxyfuel coal combustion—State of the art research and technology development." In: *Chemical Engineering Research and Design* 87.8 (2009), pp. 1003–1016.

[25] L. Chen, S. Z. Yong, and A. F. Ghoniem. "Oxy-fuel combustion of pulverized coal: Characterization, fundamentals, stabilization and CFD modeling." In: *Progress in Energy and Combustion Science* 38.2 (2012), pp. 156–214.

[26] G. Scheffknecht, L. Al-Makhadmeh, U. Schnell, and J. Maier. "Oxy-fuel coal combustion—A review of the current state-of-the-art." In: *International Journal of Greenhouse Gas Control* 5 (2011), S16–S35.

[27] C. Yin and J. Yan. "Oxy-fuel combustion of pulverized fuels: Combustion fundamentals and modeling." In: *Applied Energy* 162 (2016), pp. 742–762.

[28] F. A.D. Oliveira, J. A. Carvalho, P. M. Sobrinho, and A. de Castro. "Analysis of oxy-fuel combustion as an alternative to combustion with air in metal reheating furnaces." In: *Energy* 78 (2014), pp. 290–297.

[29] P. Bělohradsky, P. Skryja, and I. Hudák. "Experimental study on the influence of oxygen content in the combustion air on the combustion characteristics." In: *Energy* 75 (2014), pp. 116–126.

[30] P. Bělohradsky, P. Skryja, and I. Hudák. "The influence of oxygen-enhanced combustion methods on NOx emissions, in-flame temperatures and heat flux distribution." In: *10th Int. Conference on Industrial Furnaces and Boilers.* 2015.

[31] R. Prieler, M. Demuth, D. Spoljaric, and C. Hochenauer. "Numerical investigation of the steady flamelet approach under different combustion environments." In: *Fuel* 140 (2015), pp. 731–743.

[32] R. Prieler, B. Mayr, M. Demuth, B. Holleis, and C. Hochenauer. "Numerical analysis of the transient heating of steel billets and the combustion process under air-fired and oxygen enriched conditions." In: *Applied Thermal Engineering* 103 (2016), pp. 252–263.

[33] K. Wu, Y. Chang, C. Chen, and Y. Chen. “High-efficiency combustion of natural gas with 21–30% oxygen-enriched air.” In: *Fuel* 89.9 (2010), pp. 2455–2462.

[34] P.-M. Geffroy, J. Fouletier, N. Richet, and T. Chartier. “Rational selection of MIEC materials in energy production processes.” In: *Chemical Engineering Science* 87 (2013), pp. 408–433.

[35] K. Qiu and A.C.S. Hayden. “Increasing the efficiency of radiant burners by using polymer membranes.” In: *Applied Energy* 86.3 (2009), pp. 349–354.

[36] D. Biernatzki. “Erzeugung von Reinsauerstoff mit Membranverfahren.” Master thesis. Graz: Graz University of Technology, 2014.

[37] A. Ponsich, C. Azzaro-Pantel, S. Domenech, L. Pibouleau, and F. Pigeonneau. “A systemic approach for glass manufacturing process modeling.” In: *Chemical Engineering and Processing: Process Intensification* 48.8 (2009), pp. 1310–1320.

[38] J. Leicher and A. Giese. *O2-Glaswanne: Untersuchungen zur Verbesserung der Energieeffizienz und der Wärmeübertragung in Oxy-Fuel-Glasschmelzwannen (AiF-Nr. 15987 N)*. Würzburg: GWI, 2012.

[39] J. Furu, A. Buchholz, T. H. Bergstrom, and K. Marthinsen. “Numerical modeling of oxy-fuel and air-fuel burners for aluminium melting.” In: *Light Metals 2012*. Hoboken, NJ, USA: John Wiley & Sons, Inc., 2012, pp. 1037–1042.

[40] C. Yin, L. A. Rosendahl, and S. K. Kær. “Chemistry and radiation in oxy-fuel combustion: A computational fluid dynamics modeling study.” In: *Fuel* 90.7 (2011), pp. 2519–2529.

[41] R. Prieler, M. Demuth, D. Spoljaric, and C. Hochenauer. “Evaluation of a steady flamelet approach for use in oxy-fuel combustion.” In: *Fuel* 118 (2014), pp. 55–68.

[42] S. H. Han and D. Chang. “Optimum residence time analysis for a walking beam type reheating furnace.” In: *International Journal of Heat and Mass Transfer* 55.15 (2012), pp. 4079–4087.

[43] Y. Sakamoto, Y. Tonooka, and Y. Yanagisawa. “Estimation of energy consumption for each process in the Japanese steel industry: a process analysis.” In: *Energy conversion and management* 40.11 (1999), pp. 1129–1140.

[44] C. Zhang, T. Ishii, and S. Sugiyama. “Numerical modelling of the thermal performace of regenerative slab reheat furnaces.” In: *Numerical Heat Transfer, Part A: Applications* 32.6 (1997), pp. 613–631.

[45] C. Zhang, T. Ishii, Y. Hino, and S. Sugiyama. "The numerical and experimental study of non-premixed combustion flames in regenerative furnaces." In: *journal of Heat Transfer* 122.2 (2000), pp. 287–293.

[46] J. Kim, K. Huh, and I. Kim. "Three-dimensional analysis of the walking-beam-type slab reheating furnace in hot strip mills." In: *Numerical Heat Transfer, Part A: Applications* 38.6 (2000), pp. 589–609.

[47] J. G. Kim and K. Y. Huh. "Prediction of Transient Slab Temperature Distribution in the Re-heating Furnace of a Walking-beam Type for Rolling of Steel Slabs." In: *ISIJ international* 40.11 (2000), pp. 1115–1123.

[48] C.T. Hsieh, M. J. Huang, S. T. Lee, and C. H. Wang. "Numerical Modeling of a Walking-Beam-Type Slab Reheating Furnace." In: *Numerical Heat Transfer, Part A: Applications* 53.9 (2008), pp. 966–981.

[49] M. Y. Kim. "A heat transfer model for the analysis of transient heating of the slab in a direct-fired walking beam type reheating furnace." en. In: *International Journal of Heat and Mass Transfer* 50.19-20 (Sept. 2007), pp. 3740–3748.

[50] S. H. Han, D. Chang, and C. Y. Kim. "A numerical analysis of slab heating characteristics in a walking beam type reheating furnace." en. In: *International Journal of Heat and Mass Transfer* 53.19-20 (Sept. 2010), pp. 3855–3861.

[51] E. Martín, M. Meis, C. Mourenza, D. Rivas, and F. Varas. "Fast solution of direct and inverse design problems concerning furnace operation conditions in steel industry." en. In: *Applied Thermal Engineering* 47 (Dec. 2012), pp. 41–53.

[52] R. Prieler, B. Mayr, M. Demuth, B. Holleis, and C. Hochenauer. "Prediction of the heating characteristic of billets in a walking hearth type reheating furnace using CFD." In: *International Journal of Heat and Mass Transfer* 92 (2016), pp. 675–688.

[53] J. M. Casal, J. Porteiro, J. L. Míguez, and A. Vázquez. "New methodology for CFD three-dimensional simulation of a walking beam type reheating furnace in steady state." en. In: *Applied Thermal Engineering* 86 (July 2015), pp. 69–80.

[54] C. K. Tan, J. Jenkins, J. Ward, J. Broughton, and A. Heeley. "Zone modelling of the thermal performances of a large-scale bloom reheating furnace." en. In: *Applied Thermal Engineering* 50.1 (Jan. 2013), pp. 1111–1118.

[55] A. Emadi, A. Saboonchi, M. Taheri, and S. Hassanpour. "Heating characteristics of billet in a walking hearth type reheating furnace." en. In: *Applied Thermal Engineering* 63.1 (Feb. 2014), pp. 396–405.

[56] Y. Li, G. Wang, and H. Chen. “Simultaneously estimation for surface heat fluxes of steel slab in a reheating furnace based on DMC predictive control.” en. In: *Applied Thermal Engineering* 80 (Apr. 2015), pp. 396–403.

[57] J. H. Ferziger and M. Falcitelli. *Computational Methods for Fluid Dynamics.* 3rd Edition. Berlin, Heidelberg, New York: Springer, 2002.

[58] T. Poinsot and D. Veynante. *Theoretical and Numerical Combustion.* 2nd Edition. Philadelphia: US: R.T. Edwards Inc., 2005.

[59] F Moukalled, L Mangani, and M Darwish. *The Finite Volume Method in Computational Fluid Dynamics.* Cham, Switzerland: Springer International Publishing Switzerland, 2016.

[60] F. Joos. *Technische Verbrennung: Verbrennungstechnik, Verbrennungsmodellierung, Emissionen ; mit 65 Tabellen.* Berlin: Springer, 2006. 907 pp.

[61] B.E. Launder and D.B. Spalding. “The numerical computation of turbulent flows.” In: *Computer Methods in Applied Mechanics and Engineering* 3.2 (1974), pp. 269–289.

[62] *ANSYS Fluent User Guide 13.0.* 2010.

[63] T.-H. Shih, W. W. Liou, A. Shabbir, Z. Yang, and J. Zhu. “A new k-ϵ eddy viscosity model for high reynolds number turbulent flows.” In: *Computers & Fluids* 24.3 (1995), pp. 227–238.

[64] N. C. Reynolds. *Fundamentals of turbulence for turbulence modeling and simulation.* Report No.755. Von Karman Institute Agard, 1987.

[65] B. E. Launder, G. J. Reece, and W. Rodi. “Progress in the development of a Reynolds-stress turbulence closure.” In: *Journal of Fluid Mechanics* 68.3 (1975), pp. 537–566.

[66] B. E. Launder. “Second-moment closure: present... and future?” In: *International Journal of Heat and Fluid Flow* 10.4 (1989), pp. 282–300.

[67] D. Spalding. “Mixing and chemical reaction in steady confined turbulent flames.” In: *13th Symposium (Int) on combustion. The Combust Inst.* 1970.

[68] B. Magnussen and B. Hjertager. “On mathematical modeling of turbulent combustion with special emphasie on soot formation and combustion.” In: *16th Symposium (Int) on combustion. The Combust Inst.* 1976.

[69] B. Magnussen. “On the structure of turbulence and geralized eddy dissipation concept for chemical reaction in turbulent flow.” In: *19th AIAA meeting.* St. Louis, USA, 1981.

[70] J. Andersen, C. L. Rasmussen, T. Giselsson, and P. Glarborg. “Global Combustion Mechanisms for Use in CFD Modeling under Oxy-Fuel Conditions.” In: *Energy & Fuels* 23.3 (2009), pp. 1379–1389.

[71] C. Galletti, G. Coraggio, and L. Tognotti. “Numerical investigation of oxy-natural-gas combustion in a semi-industrial furnace: Validation of CFD sub-models.” In: *Fuel* 109 (2013), pp. 445–460.

[72] I. R. Gran and B. F. Magnussen. “A Numerical Study of a Bluff-Body Stabilized Diffusion Flame. Part 2. Influence of Combustion Modeling And Finite-Rate Chemistry.” In: *Combustion Science and Technology* 119.1 (1996), pp. 191–217.

[73] S. B. Pope. “Computationally efficient implementation of combustion chemistry using in situ adaptive tabulation.” In: *Combustion Theory Modeling* 1 (1997), pp. 41–63.

[74] N. Peters. “Laminar diffusion flamelet models in non-premixed turbulent combustion.” In: *Progress in Energy and Combustion Science* 10.3 (1984), pp. 319–339.

[75] N. Peters. *Turbulent combustion.* OCLC: 56066895. Cambridge [England]; New York: Cambridge University Press, 2000.

[76] GP Smith et al. *GRI-Mech 3.0.* 2000. URL: `http://www.me.berkeley.edu/gri_mech/` (visited on 2008).

[77] A. Kazakov and M Frenklach. *DRM19 mech.* URL: `http://www.me.berkeley.edu/drm/`.

[78] M. Smooke, I. Puri, and K. Seshadri. “A comparision between numerical calculations and experimental measurements of the structure of a counterflow diffusion flame burning diluted methanin diluted air.” In: *21 st Symposium (Int) on Combustion. The Combust Inst.* 1986, pp. 1783–1792.

[79] T. Peeters. “Numerical modeling of turbulence natural-gas diffusion flames.” PhD thesis. Delft: Delft Technical University, 1995.

[80] MD Smooke and V Giovangigli. “Reduced kinetic mechanisms and asymptotic approximations for methane air flames.” Lecture notes in physics 1991. 384 pp.

[81] W. Jones and R. Lindstedt. “Global reaction schemes for hydrocarbon combustion.” In: *Combustion and Flame* 73.3 (1988), pp. 233–249.

[82] N. Marinov, C. Westbrook, and W. Pitz. “Detailed and global chemical kinetics model for hydrogen.” In: *Chan SH. editor. Transport phenomena in combustion.* Washington, DC: Taylor and Francis, 1996.

[83] R Siegel and JR Howell. *Thermal radiation heat transfer.* 3rd Edition. Washington D.C.: Hemisphere Publishing Corporation, 1992.

[84] P. CHENG. "Two-dimensional radiating gas flow by a moment method." In: *AIAA Journal* 2.9 (1964), pp. 1662–1664.

[85] E. H. Chui and G. D. Raithby. "Computation of radiant heat transfer on a nonorthogonal mesh using the finite-volume method." In: *Numerical Heat Transfer, Part B: Fundamentals* 23.3 (1993), pp. 269–288.

[86] G. D. Raithby and E. H. Chui. "A Finite-Volume Method for Predicting a Radiant Heat Transfer in Enclosures With Participating Media." In: *Journal of Heat Transfer* 112.2 (1990), pp. 415–423.

[87] M. F. Modest. *Radiative Heat transfer.* 3rd Edition. Amsterdam, Boston: Academic Press, 2013.

[88] R. Porter, F. Liu, M. Pourkashanian, A. Williams, and D. Smith. "Evaluation of solution methods for radiative heat transfer in gaseous oxy-fuel combustion environments." In: *Journal of Quantitative Spectroscopy and Radiative Transfer* 111.14 (2010), pp. 2084–2094.

[89] L. Rothman, R. Wattson, R. Gamache, J. Schroeder, and A. McCann. *HITRAN, HAWKS and HITEMP: high-temperature molecular database: SPIE.* Dainty, J.C., (Ed.), Atmospheric Propagation and Remote Sensing IV. Dainty, J.C., (Ed.), Atmospheric Propagation and Remote Sensing IV, SPIE, 1995.

[90] L.S. Rothman et al. "The HITRAN 2004 molecular spectroscopic database." In: *Journal of Quantitative Spectroscopy and Radiative Transfer* 96.2 (2005), pp. 139–204.

[91] L. S. Rothman et al. "The HITRAN 2008 molecular spectroscopic database." In: *Journal of Quantitative Spectroscopy and Radiative Transfer* 110.9 (2009), pp. 533–572.

[92] L.S. Rothman, I.E. Gordon, R.J. Barber, H. Dothe, R.R. Gamache, A. Goldman, V.I. Perevalov, S.A. Tashkun, and J. Tennyson. "HITEMP, the high-temperature molecular spectroscopic database." In: *Journal of Quantitative Spectroscopy and Radiative Transfer* 111.15 (2010), pp. 2139–2150.

[93] V. Becher, S. Clausen, A. Fateev, and H. Spliethoff. "Validation of spectral gas radiation models under oxyfuel conditions. Part A: Gas cell experiments." In: *International Journal of Greenhouse Gas Control* 5 (2011), S76–S99.

[94] A. Soufani and J. Taine. “High temperature gas radiative property parameters of statistical narrow-band model for H20, CO2 and CO, and correlated-K model for H20 and CO2.” In: *International Journal of Heat and Mass Transfer* 40.4 (1997), pp. 987–991.

[95] W. Grosshandler. *RADCAL: A Narrow-Band Model for Radiation Calculations in a combustion environment.* Gaitherburg: National Institute of Standards and Technology, 1993.

[96] D. Edwards. “Molecular gas band radiation.” In: *Advances in Heat Transfer* 12 (1976), pp. 115–193.

[97] H. Hottel and A. Sarofim. *Radiative transfer.* New York: McGraw-Hill, 1967.

[98] T. F. Smith, Z. F. Shen, and J. N. Friedman. “Evaluation of Coefficients for the Weighted Sum of Gray Gases Model.” In: *Journal of Heat Transfer* 104.4 (1982), pp. 602–608.

[99] C. Yin. “Refined Weighted Sum of Gray Gases Model for Air-Fuel Combustion and Its Impacts.” In: *Energy & Fuels* 27.10 (2013), pp. 6287–6294.

[100] C. Yin, L. Johansen, L. Rosendahl, and S. Kær. “New weighted sum of gray gases model applicable to computational fluid dynamics (CFD) modeling of oxy-fuel combustion: derivation, validation and implimentation.” In: *Enegy & Fuels* 24.12 (2010), pp. 6275–6282.

[101] V. Becher, A. Goanta, and H. Spliethoff. “Validation of spectral gas radiation models under oxyfuel conditions – Part C: Validation of simplified models.” In: *International Journal of Greenhouse Gas Control* 11 (2012), pp. 34–51.

[102] T. Kangwanpongpan, F. H.R. França, R. Corrêa da Silva, P. S. Schneider, and H. J. Krautz. “New correlations for the weighted-sum-of-gray-gases model in oxy-fuel conditions based on HITEMP 2010 database.” In: *International Journal of Heat and Mass Transfer* 55.25 (2012), pp. 7419–7433.

[103] R. Johansson, K. Andersson, B. Leckner, and H. Thunman. “Models for gaseous radiative heat transfer applied to oxy-fuel conditions in boilers.” In: *International Journal of Heat and Mass Transfer* 53.1 (2010), pp. 220–230.

[104] R. Johansson, B. Leckner, K. Andersson, and F. Johnsson. “Account for variations in the H2O to CO2 molar ratio when modelling gaseous radiative heat transfer with the weighted-sum-of-grey-gases model.” In: *Combustion and Flame* 158.5 (2011), pp. 893–901.

[105] M. H. Bordbar, G. Wecel, and T. Hyppänen. “A line by line based weighted sum of gray gases model for inhomogeneous CO2–H2O mixture in oxy-fired combustion.” In: *Combustion and Flame* 161.9 (2014), pp. 2435–2445.

[106] S. Rehfeldt, C. Kuhr, M. Ehmann, and C. Bergins. “Modeling of radiative properties of an Oxyfuel atmosphere with a weighted sum of gray gases for variable carbon dioxide and water vapor concentrations.” In: *Energy Procedia* 4 (2011), pp. 980–987.

[107] G. Krishnamoorthy. “A new weighted-sum-of-gray-gases model for CO2–H2O gas mixtures.” In: *International Communications in Heat and Mass Transfer* 37.9 (2010), pp. 1182–1186.

[108] C. Yin. “Nongray-Gas Effects in Modeling of Large-Scale Oxy–Fuel Combustion Processes.” In: *Energy & Fuels* 26.6 (2012), pp. 3349–3356.

[109] J. Kim, U. Schnell, and G. Scheffknecht. “Comparison of different global reaction mechanisms for mild combustion of natural gas.” In: *Combustion Science and Technology* 180.4 (2008), pp. 565–592.

[110] N. Lallemant, J. Dugué, and R. Weber. *Analysis of the experimental data collected during OXYFLAM-1 and OXYFLAM-2 experiments*. IFRF Doc No F 85/y/4. Ijmuiden, 1997.

[111] N. Lallemant, F. Breussin, R. Weber, T. Ekman, J. Dugué, and J. Samaniego et al. “Flame structure, heat transfer and pollutant emission chracteristics of oxy-natural gas flames in the 0.7-1 MW thermal input range.” In: *Journal of the Institut of Energy* 73.496 (2000), pp. 169–182.

[112] C. Yin. *Advanced modeling of oxy-fuel combustion of natural gas*. Project summary ForskEL 2009-1-0256. Aalborg University: Department of Energy Technology, 2011.

[113] N. Lallemant, J. Dugué, and R. Weber. “Measurment techniques for studying oxy-natural gas flames.” In: *Journal of the Institut of Energy* 76.507 (2003), pp. 38–53.

[114] U. Bollettini, F. Breussin, N. Lallemant, and R. Weber. *Mathematical modeling of oxy-natural gas flames*. IFRF Doc No F 85/y/6. Ijmuiden, 1997.

[115] F. Breussin, N. Lallemant, and R. Weber. “Computing of oxy-natural gas flames usingboth a global combustion schme and a chemical equilibrium procedure.” In: *Combustion Science and Technology* 160.1 (2000), pp. 369–397.

[116] F. Dryer and I. Glassman. “High-temperature oxidation of CO and CH4.” In: *14th Symposium (Int) on combustion. The Combustion Inst.* 1972.

[117] Sente Software Ltd. *JMatPro User’s Guide*. English. Version 4.0. 2005.

[118] F-Chart Software. *EES User Manual*. English. Version V10.091-3D. 2016.

[119] A. Jaklič, F. Vode, and T. Kolenko. “Online simulation model of the slab-reheating process in a pusher-type furnace.” In: *Applied Thermal Engineering* 27.5 (2007), pp. 1105–1114.

Appendix

Appendix A.

Reaction mechanisms

A.1. Smooke46 mechanism

Table A.1.: Kinetic parameters for the smooke46 mechanism [78] with units cm, mole, s, cal

Reaction no.	Reaction	k_0	b	E_A
1	$CH_4 + M \longrightarrow CH_3 + H + M$	1.00E+17	0	86000
2	$CH_4 + O_2 \longrightarrow CH_3 + HO_2$	7.90E+13	0	56000
3	$CH_4 + H \longrightarrow CH_3 + H_2$	2.2E+04	3	8750
4	$CH_4 + O \longrightarrow CH_3 + OH$	1.60E+06	2.36	7400
5	$CH_4 + OH \longrightarrow CH_3 + H_2O$	1.60E+06	2.1	2460
6	$CH_2O + OH \longrightarrow HCO + H_2O$	7.53E+12	0	167
7	$CH_2O + H \longrightarrow HCO + H_2$	3.31E+14	0	10500
8	$CH_2O + M \longrightarrow HCO + H + M$	3.31E+16	0	81000
9	$CH_2O + O \longrightarrow HCO + OH$	1.81E+13	0	3082
10	$HCO + OH \longrightarrow CO + H_2O$	5.00E+12	0	0
11	$HCO + M \longrightarrow H + CO + M$	1.60E+14	0	14700
12	$HCO + H \longrightarrow CO + H_2$	4.00E+13	0	0
13	$HCO + O \longrightarrow OH + CO$	1.00E+13	0	0
14	$HCO + O_2 \longrightarrow HO_2 + CO$	3.00E+12	0	0
15	$CO + O + M \longrightarrow CO_2 + M$	3.20E+13	0	-4200
16	$CO + OH \longrightarrow CO_2 + H$	1.51E+07	1.3	-758
17	$CO + O_2 \longrightarrow CO_2 + O$	1.60E+13	0	41000
18	$CH_3 + O_2 \longrightarrow CH_3O + O$	7.00E+12	0	25652
19	$CH_3O + M \longrightarrow CH_2O + H + M$	2.40E+13	0	28812
20	$CH_3O + H \longrightarrow CH_2O + H_2$	2.00E+13	0	0
21	$CH_3O + OH \longrightarrow CH_2O + H_2O$	1.00E+13	0	0

22	$CH_3O + O \longrightarrow CH_2O + OH$	1.00E+13	0	0
23	$CH_3O + O_2 \longrightarrow CH_2O + HO_2$	6.30E+10	0	2600
24	$CH_3 + O_2 \longrightarrow CH_2O + OH$	5.20E+13	0	34574
25	$CH_3 + O \longrightarrow CH_2O + H$	6.80E+13	0	0
26	$CH_3 + OH \longrightarrow CH_2O + H_2$	7.50E+12	0	0
27	$HO_2 + CO \longrightarrow CO_2 + OH$	5.80E+13	0	22934
28	$H_2 + O_2 \longrightarrow 2,\ OH$	1.70E+13	0	47780
29	$OH + H_2 \longrightarrow H_2O + H$	1.17E+09	1.3	3626
30	$H + O_2 \longrightarrow OH + O$	2.20E+14	0	16800
31	$O + H_2 \longrightarrow OH + H$	1.80E+10	1	8826
32	$H + O_2 + M \longrightarrow HO_2 + M$	2.10E+18	-1	0
	$H_2O/21.00/H_2/3.30/N_2/0.00/O_2/0.00/$			
33	$H + O_2 + O_2 \longrightarrow HO_2 + O_2$	6.70E+19	-1.42	0
34	$H + O_2 + N_2 \longrightarrow HO_2 + N_2$	6.70E+19	-1.42	0
35	$OH + HO_2 + N_2 \longrightarrow H_2O + O_2$	5.00E+13	0	1000
36	$H + HO_2 \longrightarrow 2,\ OH$	2.50E+14	0	1900
37	$O + HO_2 \longrightarrow O_2 + OH$	4.80E+13	0	1000
38	$2,\ OH \longrightarrow O + H_2O$	6.00E+08	1.3	0
39	$H_2 + M \longrightarrow H + H + M$	2.23E+12	0.5	92600
	$H_2O/6.00/H/2.00/H_2/3.00/$			
40	$O_2 + M \longrightarrow O + O + M$	1.85E+11	0.5	95560
41	$H + OH + M \longrightarrow H_2O + M$	7.50E+23	-2.6	0
	$H_2O/20.00/$			
42	$H + HO_2 \longrightarrow H_2 + O_2$	2.50E+13	0	700
43	$HO_2 + HO_2 \longrightarrow H_2O_2 + O_2$	2.00E+12	0	0
44	$H_2O_2 + M \longrightarrow OH + OH + M$	1.30E+17	0	45500
45	$H_2O_2 + H \longrightarrow HO_2 + H_2$	1.60E+12	0	3800
46	$H_2O_2 + OH \longrightarrow H_2O + HO_2$	1.00E+13	0	1800

A.2. Skeletal25 mechanism

Table A.2.: Kinetic parameters for the skeletal25 mechanism [79] with units cm, mole, s, cal

Reaction no.	Reaction	k_0	b	E_A
1	$H + O_2 \longrightarrow O + OH$	2.00E+14	0	16800
2	$O + OH \longrightarrow O_2 + H$	1.58E+13	0	690
3	$O + H_2 \longrightarrow OH + H$	1.80E+10	1	8826

4	$OH + H \longrightarrow O + H_2$	8.00E+09	1	6760
5	$H_2 + OH \longrightarrow H_2O + H$	1.17E+09	1.3	3626
6	$H_2O + H \longrightarrow H_2 + OH$	5.09E+09	1.3	18588
7	$OH + OH \longrightarrow H_2O + O$	6.00E+08	1.3	0
8	$H_2O + O \longrightarrow OH + OH$	5.90E+09	1.3	17029
9	$H + O_2 + M \longrightarrow HO_2 + M$	2.30E+18	-0.8	0
	$CH_4/6.50/H_2O/6.50/CO_2/1.50/CO/0.75/O_2/0.40/N_2/0.40/$			
10	$H + HO_2 \longrightarrow OH + OH + M$	1.50E+14	0	1004
11	$H + HO_2 \longrightarrow H_2 + O_2$	2.50E+13	0	700
12	$OH + HO_2 \longrightarrow H_2O + O_2$	2.00E+13	0	1000
13	$CO + OH \longrightarrow CO_2 + H$	1.51E+07	1.3	-758
14	$CO_2 + H \longrightarrow CO + OH$	1.57E+09	1.3	22337
15	$CH_4 \longrightarrow CH_3 + H$	2.30E+38	-7	114360
16	$CH_3 + H \longrightarrow CH_4$	1.90E+36	-7	9050
17	$CH_4 + H \longrightarrow CH_3 + H_2$	2.20E+04	3	8750
18	$CH_3 + H_2 \longrightarrow CH_4 + H$	9.57E+02	3	8750
19	$CH_4 + OH \longrightarrow CH_3 + H_2O$	1.60E+06	2.1	2460
20	$CH_3 + H_2O \longrightarrow CH_4 + OH$	3.02E+05	2.1	17422
21	$CH_3 + O \longrightarrow CH_2O + H$	6.80E+13	0	0
22	$CH_2O + H \longrightarrow HCO + H_2$	2.50E+13	0	3991
23	$CH_2O + OH \longrightarrow HCO + H_2O$	3.00E+13	0	1195
24	$HCO + H \longrightarrow CO + H_2$	4.00E+13	0	0
25	$HCO + M \longrightarrow CO + H + M$	6.00E+14	0	14700
	$CH_4/6.50/H_2O/6.50/CO_2/1.50/CO/0.75/O_2/0.40/N_2/0.40/$			
26	$CH_3 + O_2 \longrightarrow CH_3O + O$	7.00E+12	0	25652
27	$CH_3O + H \longrightarrow CH_2O + H_2$	2.00E+13	0	0
28	$CH_3O + M \longrightarrow CH_2O + H + M$	2.40E+13	0	28812
	$CH_4/6.50/H_2O/6.50/CO_2/1.50/CO/0.75/O_2/0.40/N_2/0.40$			
29	$HO_2 + HO_2 \longrightarrow H_2O_2 + O_2$	2.00E+12	0	0
30	$H_2O_2 + M \longrightarrow OH + OH + M$	1.30E+17	0	45500
	$CH_4/6.50/H_2O/6.50/CO_2/1.50/CO/0.75/O_2/0.40/N_2/0.40/$			
31	$OH + OH + M \longrightarrow H_2O_2 + M$	9.86E+14	0	-5070
	$CH_4/6.50/H_2O/6.50/CO_2/1.50/CO/0.75/O_2/0.40/N_2/0.40/$			
32	$H_2O_2 + OH \longrightarrow H_2O + HO_2$	1.00E+13	0	1800
33	$H_2O + HO_2 \longrightarrow H_2O_2 + OH$	2.86E+13	0	32790
34	$OH + H + M \longrightarrow H_2O + M$	2.20E+22	-2	0
	$CH_4/6.50/H_2O/6.50/CO_2/1.50/CO/0.75/O_2/0.40/N_2/0.40/$			

35	$H + H + M \longrightarrow H_2 + M$	1.80E+18	-1	0
	$CH_4/6.50/H_2O/6.50/CO_2/1.50/CO/0.75/O_2/0.40/N_2/0.40/$			

A.3. GRI3.0 mechanism

The GRI3.0 reaction mechanism can be found under: `http://combustion.berkeley.edu/gri-mech/version30/text30.html`

Appendix B.

Numerical settings CFD simulations

B.1. Lab-scale furnace VO2

Table B.1.: Numerical settings for the CFD simulations of the lab-scale furnace VO2

Spatial discretization	Settings
Gradient	Least squares cell-based
Pressure	PRESTO!
Momentum	Second order upwind
Turbulent kinetic energy	Second order upwind
Turbulent dissipation rate	Second order upwind
Energy	Second order upwind
Discrete Ordinates	First order upwind
Mean mixture fraction	Second order upwind
Mixture fraction variance	Second order upwind
Pressure-velocity coupling	SIMPLE

Table B.2.: Under-relaxation factors for the CFD simulations of the lab-scale furnace VO2

Pressure	0.6
Density	0.5
Body forces	0.5
Momentum	0.25
Turbulent kinetic energy	0.6
Turbulent dissipation rate	0.6
Turbulent viscosity	0.7
Energy	0.98
Temperature	0.98
Discrete Ordinates	0.95
Mixture fraction	1
Mixture fraction variance	0.9

B.2. IFRF furnace

Table B.3.: Numerical settings for the CFD simulations of the IFRF furnace

Spatial discretization	Settings
Gradient	Least squares cell-based
Pressure	PRESTO!
Momentum	Second order upwind
Turbulent kinetic energy	Second order upwind
Turbulent dissipation rate	Second order upwind
Energy	Second order upwind
Discrete Ordinates	Second order upwind
Mean mixture fraction	Second order upwind
Mixture fraction variance	Second order upwind
Pressure-velocity coupling	SIMPLE

Table B.4.: Under-relaxation factors for the CFD simulations of the IFRF furnace

Pressure	0.7
Density	1
Body forces	1
Momentum	0.2
Turbulent kinetic energy	0.8
Turbulent dissipation rate	0.8
Turbulent viscosity	1
Energy	1
Temperature	1
Discrete Ordinates	1
Mixture fraction	1
Mixture fraction variance	0.9

B.3. Burner Chamber

Table B.5.: Numerical settings for the CFD simulations of the furnace Burner Chamber

Spatial discretization	Settings
Gradient	Least squares cell-based
Pressure	PRESTO!
Momentum	Second order upwind
Turbulent kinetic energy	Second order upwind
Turbulent dissipation rate	Second order upwind
Energy	Second order upwind
Discrete Ordinates	First order upwind
Mean mixture fraction	Second order upwind
Mixture fraction variance	Second order upwind
Pressure-velocity coupling	SIMPLE

Table B.6.: Under-relaxation factors for the CFD simulations of the furnace Burner Chamber

Pressure	0.6
Density	0.5
Body forces	0.5
Momentum	0.25
Turbulent kinetic energy	0.6
Turbulent dissipation rate	0.6
Turbulent viscosity	0.7
Energy	0.99
Temperature	0.99
Discrete Ordinates	0.98
Mixture fraction	1
Mixture fraction variance	0.9

B.4. Aluminium melting furnace

Table B.7.: Numerical settings for the CFD simulations of the aluminium melting furnace

Spatial discretization	Settings
Gradient	Least squares cell-based
Pressure	PRESTO!
Momentum	Second order upwind
Turbulent kinetic energy	Second order upwind
Turbulent dissipation rate	Second order upwind
Energy	Second order upwind
Discrete Ordinates	First order upwind
Mean mixture fraction	Second order upwind
Mixture fraction variance	Second order upwind
Pressure-velocity coupling	SIMPLE

Table B.8.: Under-relaxation factors for the CFD simulations of the aluminium melting furnace

Pressure	0.7
Density	1
Body forces	1
Momentum	0.25
Turbulent kinetic energy	0.8
Turbulent dissipation rate	0.8
Turbulent viscosity	1
Energy	1
Temperature	1
Discrete Ordinates	1
Mixture fraction	1
Mixture fraction variance	0.9

B.5. Pusher-type reheating furnace

Table B.9.: Numerical settings for the CFD simulations of the pusher-type reheating furnace

Spatial discretization	Settings
Gradient	Least squares cell-based
Pressure	PRESTO!
Momentum	Second order upwind
Turbulent kinetic energy	Second order upwind
Turbulent dissipation rate	Second order upwind
Energy	Second order upwind
Discrete Ordinates	First order upwind
Mean mixture fraction	Second order upwind
Mixture fraction variance	Second order upwind
Pressure-velocity coupling	SIMPLE

Table B.10.: Under-relaxation factors for the CFD simulations of the pusher-type reheating furnace

Pressure	0.4
Density	0.9
Body forces	0.9
Momentum	0.3
Turbulent kinetic energy	0.7
Turbulent dissipation rate	0.7
Turbulent viscosity	0.9
Energy	0.98
Temperature	0.97
Discrete Ordinates	0.95
Mixture fraction	0.98
Mixture fraction variance	0.9